Utrecht University
Faculty of Geosciences
Department of Earth Sciences

Sabine Haalboom – Monitoring strategies of suspended matter after natural and deep-sea mining disturbances

USES 308

ISSN 2211-4335

Monitoring strategies of suspended matter after natural and deep-sea mining disturbances

Sabine Haalboom

308 UTRECHT STUDIES IN EARTH SCIENCES

Monitoring Strategies of Suspended Matter after Natural and Deep-Sea Mining Disturbances

By Sabine Haalboom

Cover design: Margot Stoete
Cover picture: Photo by Dan Cristian Păduret on Unsplash
Layout: Sabine Haalboom

ISBN: 978-90-6266-681-2

Printed in the Netherlands by Ipskamp Printing

Monitoring Strategies of Suspended Matter after Natural and Deep-Sea Mining Disturbances

Monitoring strategieën van gesuspendeerd materiaal na natuurlijke en aan diepzeemijnbouw gerelateerde verstoringen
(met een samenvatting in het Nederlands)

Proefschrift

ter verkrijging van de graad van doctor aan de
Universiteit Utrecht
op gezag van de
rector magnificus, prof. H.R.B.M. Kummeling,
ingevolge het besluit van het college voor promoties
in het openbaar te verdedigen op

vrijdag 31 mei 2024 des middags te 2.15 uur

door

Sabine Haalboom

geboren op 1 juni 1992
te Ede

Promotor:

Prof. dr. G.J. Reichart

Copromotoren:

Dr. H.C. de Stigter

Dr. F. Mienis

Beoordelingscommissie:

Prof. dr. J. Greinert

Prof. dr. H. Niemann

Prof. dr. ir. J. Pietrzak

Dr. P. Puig

Prof. dr. L. Villanueva

The work presented in this thesis was performed in the scope of the Blue Nodules project, which received funding from the European Union's Horizon2020 research and innovation programme under Grant Agreement no. 688975.

Table of contents

Co-author affiliations 6

Summary 9

Nederlandse samenvatting 17

Chapter 1: Introduction 25

Chapter 2: Suspended particulate matter in a submarine canyon (Whittard Canyon, Bay of Biscay, NE Atlantic Ocean): Assessment of commonly used instrument to record turbidity 43

Chapter 3: Suspended particulate organic matter transport and deposition along the thalweg of the easternmost branch of Whittard Canyon, NE Atlantic Ocean 79

Chapter 4: Patterns of (trace) metals and microorganisms in the Rainbow hydrothermal vent plume at the Mid-Atlantic Ridge 101

Chapter 5: Monitoring of a sediment plume produced by a deep-sea mining test in shallow water, Málaga Bight, Alboran Sea (southwestern Mediterranean Sea) 141

Chapter 6: Monitoring of Anthropogenic Sediment Plumes in the Clarion-Clipperton Zone, NE Equatorial Pacific Ocean 191

References 237

About the author 275

Bibliography 276

Acknowledgements 277

Co-author affiliations

Matthias Baeye	Royal Belgian Institute of Natural Sciences, Brussels, Belgium.
Judith van Bleijswijk	NIOZ Royal Netherlands Institute for Sea Research, Department of Ocean Systems, Texel, The Netherlands.
Gerard Duineveld	NIOZ Royal Netherlands Institute for Sea Research, Department of Ocean Systems, Texel, The Netherlands.
Iason-Zois Gazis	GEOMAR Helmholtz Centre for Ocean Research Kiel, Kiel, Germany.
Benjamin Gillard	Jacobs University, Bremen, Germany.
Jens Greinert	GEOMAR Helmholtz Centre for Ocean Research Kiel, Kiel, Germany.
Matthias Haeckel	GEOMAR Helmholtz Centre for Ocean Research Kiel, Kiel, Germany.
Hans van Haren	NIOZ Royal Netherlands Institute for Sea Research, Department of Ocean Systems, Texel, The Netherlands.
Martina Hollstein	Bundesanstalt für Geowissenschaften und Rohstoffe (BGR), Hannover, Germany.
Laurens de Jonge	Royal IHC Mining, Kinderdijk, The Netherlands.
Jonathan Kranenburg	NIOZ Royal Netherlands Institute for Sea Research, Department of Ocean Systems, Texel, The Netherlands.
Marc Lavaleye	NIOZ Royal Netherlands Institute for Sea Research, Department of Ocean Systems, Texel, The Netherlands.
Furu Mienis	NIOZ Royal Netherlands Institute for Sea Research, Department of Ocean Systems, Texel, The Netherlands.
Christian Mohn	Aarhus University, Department of Bioscience, Roskilde, Denmark.
David Price	NIOZ Royal Netherlands Institute for Sea Research, Department of Ocean Systems, Texel, The Netherlands.
Kaveh Purkiani	MARUM – Center for Marine Environmental Sciences, University of Bremen, Bremen, Germany.
Gert-Jan Reichart	NIOZ Royal Netherlands Institute for Sea Research, Department of Ocean Systems, Texel, The Netherlands. Utrecht University, Faculty of Geosciences, Utrecht, The Netherlands.
Timm Schoening	GEOMAR Helmholtz Centre for Ocean Research Kiel, Kiel, Germany.

Marck Smit	NIOZ Royal Netherlands Institute for Sea Research, Department of Ocean Systems, Texel, The Netherlands.
Henko de Stigter	NIOZ Royal Netherlands Institute for Sea Research, Department of Ocean Systems, Texel, The Netherlands.
Laurens Thomsen	Jacobs University, Bremen, Germany.
Peter Urban	GEOMAR Helmholtz Centre for Ocean Research Kiel, Kiel, Germany.
Thomas Vandorpe	Flander Marine Institute (VLIZ), Oostende, Belgium.
	Ghent University, Department of Geology, Gent, Belgium.
Annemiek Vink	Bundesanstalt für Geowissenschaften und Rohstoffe (BGR), Hannover, Germany.
Harry Witte	NIOZ Royal Netherlands Institute for Sea Research, Department of Ocean Systems, Texel, The Netherlands.

Summary

While the world's oceans are already increasingly under pressure as a result of anthropogenic carbon dioxide emissions leading to ocean warming and acidification, and from overexploitations of fish stocks and massive input of plastic litter and other pollutants, the advance of deep-sea mining poses yet another threat, especially on the unique, vulnerable and largely unknown deep-sea life. Apart from the removal of hard substrate essential for settlement of sessile benthic fauna, sediment plumes produced in the process of mining and dispersed by currents are expected to affect deep-sea life over a much wider area beyond the actually mined area.

If despite the existing uncertainty about the environmental impacts deep-sea mining will be given green light, strict monitoring of these sediment plumes will be a prerequisite to prevent that these exceed prescribed thresholds in concentration of suspended solids or extend beyond agreed limits. For continuous measurement of concentration of suspended particulate matter (SPM) for the purpose of water quality monitoring, various types of turbidity sensors are commonly used, the operation of which is based on the degree of backscatter, dispersion, or transmission of a light or sound beam in the medium to be measured. The different types of optical and acoustic turbidity sensors available each have certain merits and drawbacks. This thesis describes the results of a number of field experiments in which the performance of various commonly used turbidity sensors was tested in different setups. The experiments were carried out in the Whittard Canyon and the Rainbow hydrothermal vent field in the Atlantic Ocean, where enhanced suspended particle concentrations occur naturally, and in the Mediterranean Sea offshore southern Spain and the Clarion-Clipperton Zone in the Pacific Ocean, where sediment plumes were produced artificially.

The sites with naturally elevated SPM mass concentration served as "natural laboratories" for monitoring suspended sediment plumes, while at the same time the studies contributed to the understanding of natural particle transport processes in these environments. In Chapters

Image: Manganese nodules on the seafloor in the Clarion-Clipperton Zone. Photo taken with ROV KIEL 6000 during cruise SO239 with RV Sonne in April 2015 (ROV KIEL 6000, GEOMAR).

2 and 3, results are given from the Whittard Canyon, a large branching submarine canyon incised in the Atlantic continental shelf and slope west of France. In the upper and middle reaches of this canyon bottom and intermediate nepheloid layers are permanently present, due to the tide-driven cycle of sediment resuspension and redeposition.

Chapter 2 accounts how optical backscatter sensors, transmissometers and low- and high-frequency ADCPs may produce different estimates of SPM mass concentration. Simultaneous with the deployment of these sensors, water samples were collected for quantification of SPM mass concentration and to determine some of the particle's characteristics, like particle size and composition. It was found that the 650 nm laser beam of the transmissometer was more strongly absorbed by chlorophyll-bearing phytoplankton in the biologically productive surface ocean layers than by suspended detritic sediment particles in the deep near-bottom water. Conversely, the 700-880 nm light of the OBS was more strongly backscattered by suspended sediment than by phytoplankton. If this sensor-specific sensitivity for different types of SPM is not accounted for, this can lead to a mis-quantification of the SPM mass concentration. It was also found that patterns in temporal variation in backscatter from OBSs and high-frequency ADCPs differed substantially from those recorded by simultaneously deployed low-frequency ADCPs. This is due to the different response of these sensors to the wide range in SPM particle size found in the Whittard Canyon. The OBSs and high-frequency ADCPs are more sensitive to finer particles and hardly detect larger aggregates and zooplankton/nekton, whereas conversely, the latter particles are detected by the low-frequency ADCPs, while these do not detect the finer-grained material. It is therefore recommended to use a combination of different sensors which complement each other with regards to the range of particle sizes they detect. The use of only one type of sensors could lead to an observational bias and hence incomplete understanding of particle transport processes.

In Chapter 3, a more in-depth analysis of SPM distribution is presented, focussing on the organic matter content and composition of suspended particulate matter and surface sediments in the Whittard Canyon. Samples and data were collected along the easternmost branch of the canyon, using a CTD-Rosette, a bottom lander equipped with current meter, turbidity sensors and in situ particle pump, as well as mono- and multicorer, revealed conspicuous short-term temporal variation in suspended particulate organic matter (SPOM)

concentration and composition along the canyon, as well as variation in content and composition of organic matter in sediment on the canyon floor. Low SPOM concentrations were found in the bottom water of the upper reaches of the canyon. In the middle reaches of the canyon, where most active resuspension takes place, SPOM was more degraded compared to the upper reaches, but was present in higher concentrations. In the lower canyon, SPOM concentrations were low and the SPOM was found to be slightly less degraded. Time series data showed that particles are resuspended during peaks in current speed, when the tidal flow is directed up-canyon, resulting in higher concentrations of organic carbon, nitrogen and chlorophyl (C_{org}, N_{tot} and Chl-*a*). It was also found that older and more degraded organic matter incorporated in the surface sediment was entrained during the repeated resuspension by internal tides, as shown by the low Chl-*a*/C_{org} ratio of the SPOM. High SPOM concentrations in the middle reaches of the canyon did not seem to result in enhanced organic matter deposition in that part of the canyon; in fact, the highest concentrations of (relatively degraded) organic matter were found in the lower reaches of the canyon. It is therefore thought that the continuous cycle of resuspension, combined with down-canyon transport by intermittent gravity flows, result in the winnowing of the fine-grained organic-rich particulate fraction from the upper and middle reaches of the canyon, and transport and ultimate deposition of the more refractory organic compounds in the lower reaches. The lateral transport of SPOM via the bottom nepheloid layer affects carbon cycling on a local scale, enhancing remineralisation of the organic matter rich fine-grained sediment and fuelling rich benthic fauna. The depocenters of the organic matter rich fine-grained sediment in the lower canyon reaches should best remain excluded from anthropogenic disturbance, as remobilisation of the sediment would expose the organic matter to conditions favourable for its further remineralisation and consequent release of carbon dioxide.

Chapter 4 accounts of a study carried out in another “natural laboratory”, the Rainbow hydrothermal vent field located on the Mid-Atlantic Ridge southwest of the Azores. Here, chemical composition and microbial assemblages in suspended particulate matter in the hydrothermal plume were studied along the plume as it disperses away from the vent field. Knowledge of the natural state of the plume and how it affects the deep water and seafloor environments in the surrounding of the vent field is essential for assessing the potential impact of future mining of seafloor massive sulphide deposits surrounding the vents. During mining,

surface sediment and massive sulphide fines will be dispersed in the deep water where they could potentially interact with the naturally occurring hydrothermal plume.

To investigate how (trace) metal composition and microbial communities of plume SPM change in a natural plume with distance, the Rainbow hydrothermal vent plume was followed up to 25 km downstream from the vent site, using optical backscatter sensors mounted on a CTD-Rosette to detect the plume. Water samples from within and above the plume were collected with the Rosette sampler, and surface sediment samples from the seabed below the plume were collected with a box corer. Both vertically in the water column and horizontally along the neutrally buoyant plume, geochemical and microbial changes were evident, with the plume showing enrichments in (trace) metals and REE, compared to the ambient water above the plume. As the plume dispersed, the concentrations of these elements changed, which was also reflected in the changes in microbial communities within the plume. These results show that the Rainbow hydrothermal plume represents a unique chemically enriched environment where distinct and spatially variable microbial habitats are present. This study provides a baseline of geochemical and biological heterogeneity, needed to assess the environmental impacts of deep-sea mining.

To better predict the impacts that deep-sea mining will have on the environment surrounding mining sites, and to give guidance for mitigating these impacts, model predictions of the dispersion of resuspended sediment and fine-grained metalliferous minerals are needed. Until the beginning of the previous decade, the majority of these models were focussed on the quantification of redeposited sediment and only in a few models suspended sediment loads in the water column were accounted for. In the past few years however, great progress has been made in this regard, when industry field tests with pre-prototype mining equipment were carried out, offering opportunities for extensive investigation of environmental effects. Even though these mining tests may be of limited extent compared to full-scale industrial mining, the observations on sediment plume dispersion are highly valuable to improve and validate plume dispersion models. This is addressed in Chapters 5 and 6, which describe how knowledge gained from the studies in the "natural laboratories" was applied to design setups for monitoring of sediment plumes generated during small-scale disturbance tests.

In Chapter 5, different experimental designs for monitoring of sediment plumes produced by deep-sea mining are presented. These setups were tested during two industry field tests with Royal IHC's pre-prototype deep-sea mining vehicle *Apollo II*, in relatively shallow water of around 300 m depth offshore southern Spain. During the performance tests of the mining vehicle, carried out on gently sloping muddy seabed, the plume of mobilised suspended sediment was monitored with turbidity sensors deployed on a ship-operated CTD system and on a static array of moorings placed along the path of the vehicle. Additionally, visual observations were carried out using a ROV. It was shown that the generated sediment plume initially did not extend more than 2 m above the seafloor in the first 100 m from the source but increased in height at greater distance. SPM mass concentrations decreased rapidly with increasing distance to the source, from around 100 mg L^{-1} directly behind the vehicle to around 5 mg L^{-1} at 100 m behind the vehicle. Despite the relatively high and variable SPM background concentration at the test site, the generated sediment plume could still be traced up to 350 m away from its source. The average particle size within the generated plume, measured with a LISST-200X in-situ particle sizer mounted on the CTD, was 37 µm, distinctly smaller than the average particle size of the suspended matter in the ambient bottom water (67 µm). If unaccounted for, this difference in particle size can have implications on the estimates of SPM mass concentration. The monitoring setups applied in this study in shallow water, with a combination of sensors operated from both moving and moored platforms, proved to be well-suited for monitoring of anthropogenic sediment plumes, which (on a larger scale) can be applied in the deep sea.

In Chapter 6, the results of a small-scale disturbance experiment, carried out in the Clarion-Clipperton Zone in the NE equatorial Pacific Ocean, are presented and discussed. In this experiment, a dredge was towed back and forth over the seabed at 4120 m depth, for a total duration of 12 hours to disturb the surface sediment layer and to generate a sediment plume. The plume was monitored using an extensive array of optical and acoustic turbidity sensors and current meters, while sediment redeposition from the plume was assessed afterwards from seafloor imagery collected with a towed video system. It was found that redeposited sediment could be visually discerned up to 100 m away from the source. However, the turbidity sensors proved to be a more sensitive tool, as the dispersing plume still stood out clearly from the background waters at 300 m away from the source, with SPM concentration

still up to 60 times higher (~ 1 mg L^{-1} compared to 0.017 mg L^{-1}). Vertical profiles of acoustic backscatter as recorded by different types of ADCPs gave insight in the vertical extent of the generated plume, of which the densest part stayed within 2 m above the seafloor (mab), but which occasionally rose to 6 mab. The monitoring setup applied in this study proved to be useful for the monitoring of this small-scale experiment and the collected data improved understanding of sediment plume dispersion and supported the development of plume dispersion models in this specific deep-sea area (see Purkiani et al., 2021). For future monitoring of mining trials, it is recommended that the monitoring setup presented in this study will be applied on a larger scale, to cover greater distances and to additionally use AUVs for repeated seafloor imaging and water column plume mapping, as well as in situ particle sizers or particle cameras to better understand the effect that particle aggregation within the plume may have on the optical and acoustic backscatter characteristics.

Image: Manganese nodules on the seafloor in the Clarion-Clipperton Zone, with a dredge track in between. The photo also shows a chumed-up sediment lump in the middle of the track and an octopus behind. Photo taken with ROV KIEL during cruise SO268 with RV Sonne in April 2019 (ROV KIEL 6000, GEOMAR).

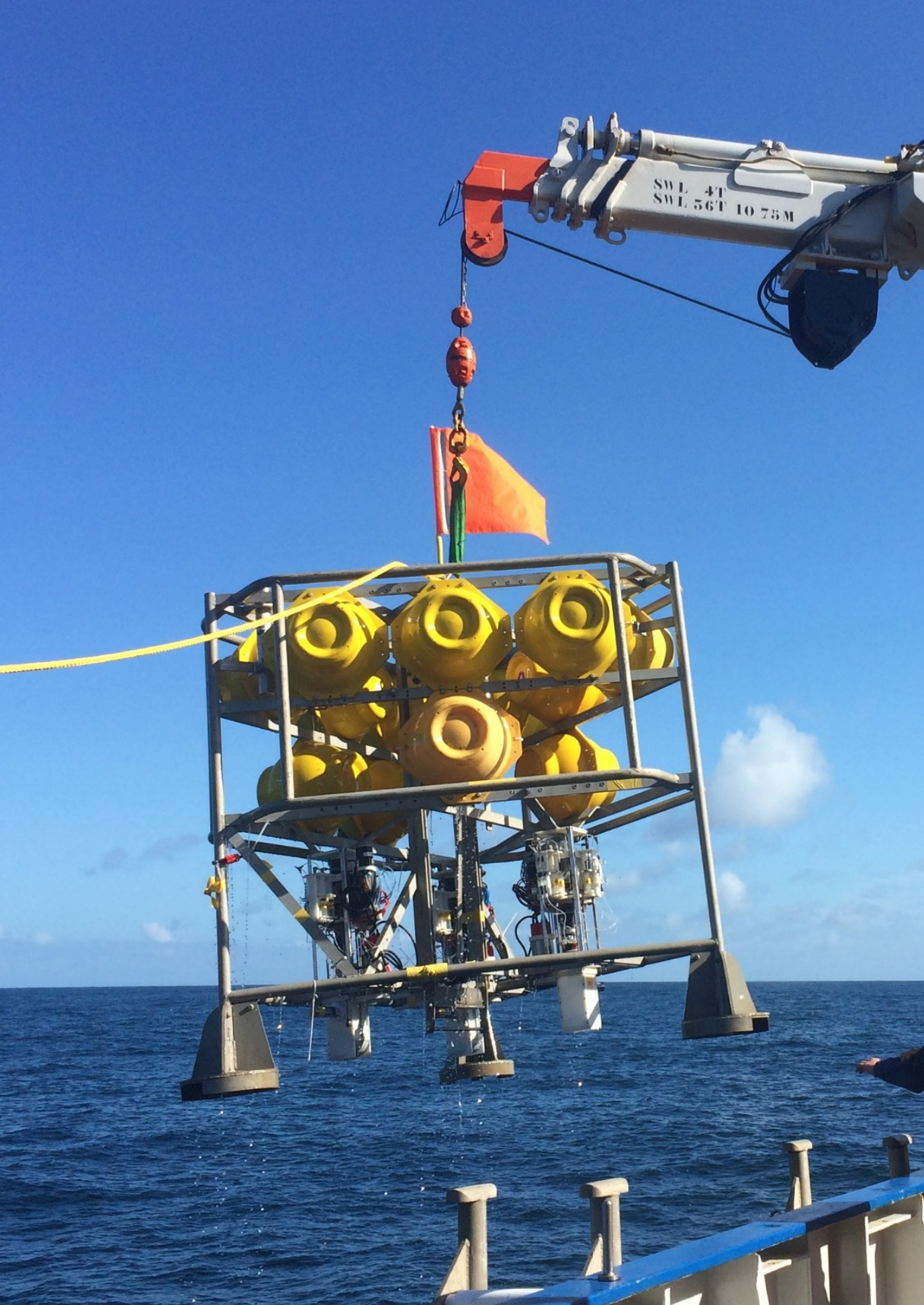
SWL 4T
SWL 36T 10.75M

Nederlandse samenvatting

Onze oceanen staan in toenemende mate onder druk door invloeden van menselijke activiteit. Naast de sterk verhoogde uitstoot van CO_2 sinds het begin van de industriële revolutie, met opwarming en verzuring van het zeewater als gevolg, hebben we te maken met overbevissing en de toevoer van grote hoeveelheden plastic en andere verontreinigingen in de oceanen. De opkomst van diepzeemijnbouw vormt een nieuwe bedreiging voor het unieke, kwetsbare en nog grotendeels onbekende leven in de diepzee. Tijdens het mijnen zal het harde substraat, dat sessiele bodemfauna als sponzen en koralen nodig hebben om op te leven worden verwijderd, en worden wolken van bodemsediment opgewerveld die door stromingen verspreid worden over een groter gebied dan waar de diepzeemijnbouw daadwerkelijk plaatsvindt. Dit met mogelijke gevolgen voor het diepzeeleven in het pad van de sedimentwolk.

Als diepzeemijnbouw ondanks de nog bestaande onzekerheid over de gevolgen voor het milieu zal worden toegestaan, is het van belang dat de verspreiding van de hierbij geproduceerde sedimentwolken goed gemonitord gaat worden, om te voorkomen dat concentraties aan gesuspendeerd materiaal (ook wel afgekort als SPM; "*suspended particulate matter"*) niet over vooraf vastgestelde grenswaarden gaan. Voor continue meting van SPM-concentratie ten behoeve van monitoring van waterkwaliteit wordt doorgaans gebruik gemaakt van turbiditeitssensoren, waarvan de werking berust op de mate van terugkaatsing, verstrooiing of doorlating van een licht- of geluidsbundel in het te meten medium. De verschillende soorten optische en akoestische turbiditeitssensoren die beschikbaar zijn hebben elk bepaalde voordelen en nadelen. In dit proefschrift worden de resultaten beschreven van een aantal veldexperimenten, waarin de werking van verschillende veelgebruikte turbiditeitssensoren is getest in verschillende opstellingen. De experimenten zijn uitgevoerd in de Whittard Canyon en bij het Rainbow hydrothermale veld in de Atlantische Oceaan, waar verhoogde concentraties gesuspendeerd materiaal in de waterkolom van nature voorkomen, en in de Middellandse Zee voor de kust van Zuid-Spanje en in de Clarion-

Image: Deployment of a bottom lander onboard of the RV *Pelagia* in the Whittard Canyon in spring 2017, during cruise 64PE421. Photo by: Sabine Haalboom.

Clipperton Zone in de Stille Oceaan, waar sedimentwolken kunstmatig werden geproduceerd.

De locaties met van nature verhoogde SPM-concentraties dienden als "natuurlijke laboratoria" voor het monitoren van sedimentwolken, terwijl de studies tegelijkertijd ook bijdroegen aan het verkrijgen van inzicht in natuurlijke processen van SPM-transport in deze gebieden. In hoofdstukken 2 en 3 worden de resultaten gepresenteerd van het onderzoek in de Whittard Canyon, een grote, zich vertakkende onderzeese canyon, ingesneden in de Atlantische continentale marge ten westen van Frankrijk. In de bovenloop en het middengedeelte van deze canyon zijn er zowel nabij de bodem als hoger in de waterkolom permanent lagen aanwezig met een verhoogde SPM-concentratie, ook wel nefeloïde lagen genoemd, als gevolg van getij-gerelateerde cycli van resuspensie en depositie van het bodemsediment.

Hoofdstuk 2 beschrijft hoe verschillende turbiditeitssensoren, zoals optische *backscatter* sensoren (OBS'en), transmissometers, en laag- en hoogfrequente *Acoustic Doppler Current Profilers* (ADCP's), verschillende inschattingen van SPM-concentraties opleveren. Gelijktijdig met de inzet van deze sensoren zijn watermonsters genomen om de concentratie van gesuspendeerd materiaal te kwantificeren en om karakteristieken van deze deeltjes zoals korrelgrootte en samenstelling te bepalen. De resultaten lieten zien dat de laserstraal van de transmissometer, met een golflengte van 650 nm, sterker werd geabsorbeerd door chlorofyl-houdend fytoplankton, aanwezig in het biologisch productieve oppervlaktewater van de oceaan, vergeleken met detritisch sediment in het bodemwater van de canyon. Omgekeerd bleek het licht van een OBS met een golflengte van 700-880 nm sterker te worden gereflecteerd door gesuspendeerd sediment dan door fytoplankton. Als er geen rekening wordt gehouden met deze sensor-specifieke gevoeligheden voor verschillende soorten gesuspendeerd materiaal kan dit leiden tot een verkeerde kwantificering van de SPM-concentratie. Ook bleek dat patronen van variatie van turbiditeit zoals opgenomen door de OBS'en en hoogfrequente ADCP's sterk verschilden van die welke gelijktijdig opgenomen werden opgenomen door de laagfrequente ADCP's. Deze verschillen zijn toe te schrijven aan de verschillende gevoeligheid van deze sensoren voor het brede scala aan deeltjesgroottes van het gesuspendeerde materiaal aanwezig in de Whittard Canyon. De OBS'en en de hoogfrequente ADCP's zijn het meest gevoelig voor zeer kleine deeltjes maar kunnen grotere

aggregaten of zoöplankton/nekton slecht detecteren. Grotere aggregaten of zoöplankton/nekton worden daarentegen wel goed gedetecteerd door de laagfrequente ADCP's die op hun beurt juist de kleine deeltjes slecht zien. Het is daarom aan te bevelen om een combinatie van sensoren te gebruiken die elkaar aanvullen wat betreft detectie van gesuspendeerd materiaal met verschillende deeltjesgroottes. Het gebruik van slechts één soort sensor kan door dit inherente onvermogen om een deel van het deeltjesgroottespectrum waar te nemen resulteren in onvolledig inzicht in sediment transport processen.

In hoofdstuk 3 wordt een meer uitgebreide analyse gepresenteerd van de concentratie en samenstelling van organisch materiaal dat zich in suspensie en in het bodemsediment in de Whittard Canyon bevindt. Data en water- en bodemmonsters werden verzameld in de meest oostelijk tak van de canyon, gebruikmakend van een CTD-Rosette, een bodemlander uitgerust met een stromingsmeter, turbiditeitssensoren en een in situ deeltjespomp, alsmede een mono- en multicorer. De resultaten onthulden een opvallende variatie in de tijd in de concentratie en samenstelling van zwevend organisch materiaal (SPOM; *"suspended particulate organic matter"*) langs de as van de canyon, en ook een variatie in concentratie en samenstelling van het organisch materiaal in het sediment op de bodem van canyon. Lage concentraties van relatief vers SPOM werden gevonden in het bodemwater in de bovenloop van de canyon. In het middengedeelte van de canyon, waar de meest actieve resuspensie plaatsvindt, was het SPOM meer gedegradeerd vergeleken met dat van de bovenloop van de canyon, maar het was wel aanwezig in hogere concentraties. In de benedenloop van de canyon was de SPOM-concentraties laag, maar het SPOM was minder sterk gedegradeerd dan in het middengedeelte van de canyon. Opnames van stroming en turbiditeit lieten zien dat sediment van de bodem van de canyon in suspensie wordt gebracht tijdens pieken en stroomsnelheid wanneer de getijdestroom van dieper naar ondieper in de canyon beweegt, wat dan resulteert in hogere concentraties van gesuspendeerd organisch koolstof, stikstof en chlorofyl (C_{org}, N_{tot}, Chl-*a*). Als gevolg van de herhaalde resuspensie door de interne getijstroming wordt ouder en meer gedegradeerd organisch materiaal aanwezig in het bodemsediment in roulatie gehouden en vermengd met verser materiaal, wat resulteert in een opvallend laag Chl-*a*/C_{org} ratio van het SPOM. Hogere SPOM-concentraties in het midden van de canyon bleken niet te leiden tot een verhoogde afzetting van organisch materiaal in dat deel van de canyon;

integendeel, de hoogste concentraties van (matig gedegradeerd) organisch materiaal werden gevonden in de diepere delen van de canyon. Het lijkt aannemelijk dat de continue cyclus van resuspensie, gecombineerd met periodiek transport richting de benedenloop van de canyon door zogenaamde troebelingsstromen, resulteert in verplaatsing van fijnkorrelig organisch-rijk materiaal uit de bovenloop en middengedeelte van de canyon, en transport en uiteindelijke depositie hiervan in meer gedegradeerde vorm in de diepere delen van de canyon. Het laterale transport van het SPOM via de bodemnabije en hogere nefeloïde lagen in de canyon speelt een rol in de koolstofcyclus op lokale schaal, door het versterken van de remineralisatie van organisch materiaal in fijnkorrelig sediment en door voeding te bieden aan bentische fauna. Het lijkt raadzaam om afzettingsgebieden van fijnkorrelig sediment rijk aan organisch materiaal in de diepere delen van de canyon te vrijwaren van antropogene verstoring, omdat remobilisatie van het sediment het organisch materiaal opnieuw kan blootstellen aan omstandigheden die gunstig zijn voor verdere remineralisatie en daarmee het vrijkomen van koolstofdioxide.

Het onderzoek gepresenteerd in hoofdstuk 4 is ook uitgevoerd in een "natuurlijk laboratorium", het Rainbow hydrothermale veld, op de Mid-Atlantische Rug ten zuidwesten van de Azoren. In dit onderzoek werden chemische samenstelling en microbiële leefgemeenschappen van het gesuspendeerde materiaal in de hydrothermale pluim onderzocht, en hoe deze veranderen terwijl de pluim met de stroming meegevoerd wordt. Kennis van de natuurlijke staat van de pluim en welke invloed deze heeft op het omringende zeewater en de zeebodem in de omgeving van het hydrothermale veld is van belang voor het inschatten van de mogelijke gevolgen van toekomstige mijnbouw van massieve sulfide-afzettingen (SMS; "*seafloor massive sulphides*") die aanwezig zijn rond de hydrothermale bronnen. Tijdens het mijnen van deze SMS-afzettingen zullen bodemsediment en fijnkorrelige, metaalrijke sulfide-deeltjes in het water vrijkomen en mogelijk mengen met de natuurlijk voorkomende hydrothermale pluim.

Veranderingen in (spoor)metaal samenstelling en microbiële leefgemeenschappen in de Rainbow hydrothermale pluim werden vanaf de bron stroomafwaarts gevolgd over een afstand van 25 km, waarbij optische *backscatter* sensoren gemonteerd op een CTD-Rosette werden gebruikt voor het detecteren van de pluim. Daarnaast zijn er watermonsters

verzameld in en boven de pluim met een Rosette-waterbemonsteringssysteem en ook sedimentmonsters van de zeebodem onder de pluim met behulp van een box corer. De pluim onderscheidde zich van het omringende zeewater door aanrijking in (spoor)metalen en zeldzame aardmeten (REE; "*rare earth elements*"). Naarmate de pluim verder van de bron afdreef, veranderen ook de concentraties van deze elementen, wat ook weerspiegeld werd in een verandering in microbiële groepen in de pluim. De resultaten laten zien dat de Rainbow hydrothermale pluim een unieke, chemisch verrijkte omgeving is gekenmerkt door een opeenvolging van verschillende microbiële habitats. Deze studie kan bijdragen aan het referentiekader van natuurlijke geochemische en biologische heterogeniteit aan de hand waarvan de milieueffecten van diepzeemijnbouw beoordeeld kunnen worden.

Om beter te kunnen voorspellen welk effect diepzeemijnbouw gaat hebben op de omgeving rondom de te mijnen gebieden, maar ook om sturing te geven voor het beperken van negatieve gevolgen, zijn modelvoorspellingen nodig van de verspreiding van door mijnbouw geproduceerde sedimentwolken. Tot het begin van het vorige decennium waren modellen vooral gebaseerd op waarnemingen van uit de sedimentwolken neergeslagen sediment. Slechts in een paar modellen was er rekening gehouden met gemeten verspreiding van het gesuspendeerde sediment in de waterkolom. In de laatste jaren is er echter goede vooruitgang geboekt op dit gebied doordat er veldtesten hebben plaatsgevonden waarbij door de industrie pre-prototype mijnbouwapparatuur getest werd. Deze testen boden mogelijkheden voor uitgebreidere studies naar de effecten van diepzeemijnbouw op het marine milieu. Hoewel deze mijnbouwtesten op veel kleinere schaal uitgevoerd worden dan voorzien voor de toekomstige commerciële mijnbouw, zijn de observaties van de verspreiding van sedimentwolken van groot belang om modellen hiervan te verbeteren en te valideren. Dit is het onderwerp van hoofdstukken 5 en 6, waarin beschreven wordt hoe kennis opgedaan tijdens die studies in de "natuurlijke laboratoria" kan worden toegepast om opstellingen te ontwerpen voor het monitoren van de sedimentwolken gegenereerd tijdens kleinschalige verstoringsexperimenten.

In hoofdstuk 5 worden verschillende opstellingen voor het monitoren van sedimentwolken gepresenteerd. Deze opstellingen werden getest tijdens twee industriële veldtesten met het pre-prototype diepzeemijnbouwvoertuig *Apollo II* van Koninklijke IHC, uitgevoerd in relatief

ondiep water op ongeveer 300 m diepte voor de kust van Zuid-Spanje. Tijdens de prestatietesten van het mijnbouwvoertuig, uitgevoerd op een licht hellende modderige zeebodem, werd de wolk van gesuspendeerd sediment gemonitord met turbiditeitssensoren gemonteerd op een CTD-systeem en op verankeringen geplaatst langs het pad dat met het voertuig werd gereden. Daarnaast werd een onderwaterrobot (ROV; "*remotely operated vehicle*") gebruikt voor de visuele observaties. De resultaten lieten zien dat de gegenereerde sedimentwolk in eerste instantie in de eerste 100 m achter het voertuig niet hoger dan 2 meter boven de zeebodem kwam, maar daarna met toenemende afstand in hoogte toenam. SPM-concentraties namen snel af met de toenemende afstand, van ongeveer 100 mg L^{-1} direct achter het voertuig, tot ongeveer 5 mg L^{-1} op 100 m achter het voertuig. Ondanks de relatief hoge en variabele achtergrondconcentratie van SPM op de testlocatie, kon de gegenereerde sedimentwolk nog worden gedetecteerd tot op 350 m afstand. De gemiddelde deeltjesgrootte in de sedimentwolk, gemeten met een LISST-200X in-situ deeltjesgroottemeter gemonteerd op de CTD, was met 37 µm duidelijk kleiner dan de deeltjesgrootte van het gesuspendeerde materiaal in het omringende water (67 µm). Als met deze verschillen in deeltjesgrootte geen rekening wordt gehouden kan dit consequenties hebben voor de bepaling van de SPM-concentratie. De monitoringsopstellingen toegepast in deze studie in relatief ondiep water, waarin gewerkt werd met een combinatie van sensoren op mobiele platformen en sensoren op verankerde platformen op de zeebodem, bleek een geschikte strategie voor het monitoren van antropogene sedimentwolken die ook (op een grotere schaal) kan worden toegepast in de diepzee.

In **hoofdstuk 6** worden de resultaten gepresenteerd van een kleinschalig verstoringsexperiment, uitgevoerd in de Clarion-Clipperton Zone in de noordoostelijke equatoriale Stille Oceaan. Tijdens dit experiment werd op 4120 m diepte een dreg gedurende 12 uur over de zeebodem heen en weer gesleept, om het bodemsediment te verstoren en een sedimentwolk te genereren. De verspreiding van deze wolk werd gemonitord met een groot aantal optische en akoestische turbiditeitssensoren en stroomsnelheidsmeters die op de zeebodem rond het verstoorde gebied waren geplaatst. Neerslag van sediment vanuit de wolk terug op de zeebodem werd onderzocht aan de hand van beelden van de zeebodem verzameld met een gesleept videosysteem. Het neergeslagen sediment kon tot een afstand van ca. 100 m van de verstoring nog visueel onderscheiden worden in de videobeelden, maar

de turbiditeitssensoren bleken een veel gevoeliger instrument, waarmee de wolk van gesuspendeerd materiaal nog op 300 m afstand duidelijk kon worden onderscheiden, met SPM-concentraties van bijna 60 keer hoger dan in het omringende water (~ 1 mg L^{-1} vergeleken met 0.017 mg L^{-1}). Akoestische *backscatter* profielen opgenomen met verschillende soorten ADCP's gaven een beter inzicht in de verticale omvang van de gegenereerde sedimentwolk, waarvan het dichtste deel binnen 2 meter boven de bodem bleef, maar de top geregeld steeg tot 6 meter. De opstelling toegepast in deze studie bleek bruikbaar voor het monitoren van dit kleinschalige verstoringsexperiment en de verzamelde data heeft ons inzicht in de verspreiding van de sedimentwolk verbeterd en droeg bij aan de verfijning van verspreidingsmodellen van gesuspendeerd sediment in dit specifieke diepzeegebied (zie Purkiani et al., 2021). Voor toekomstige monitoring van diepzeemijnbouw testen wordt aanbevolen om de opstelling zoals toegepast in deze studie op te schalen, om zo verspreiding van sedimentwolken over grotere afstanden te kunnen volgen. Daarnaast wordt aanbevolen om autonome onderwaterrobots (AUV's; *"autonomous unmanned vehicle"*) te gebruiken voor het interactief volgen van de verspreiding van sedimentwolken en het in kaart brengen van de neerslag van sediment en ook om gebruik te maken van in situ deeltjesgroottemeters of deeltjescamera's, om beter inzicht te krijgen in aggregatie van deeltjes in de sedimentwolk, en het mogelijk effect daarvan op optische en akoestische turbiditeitsmetingen.

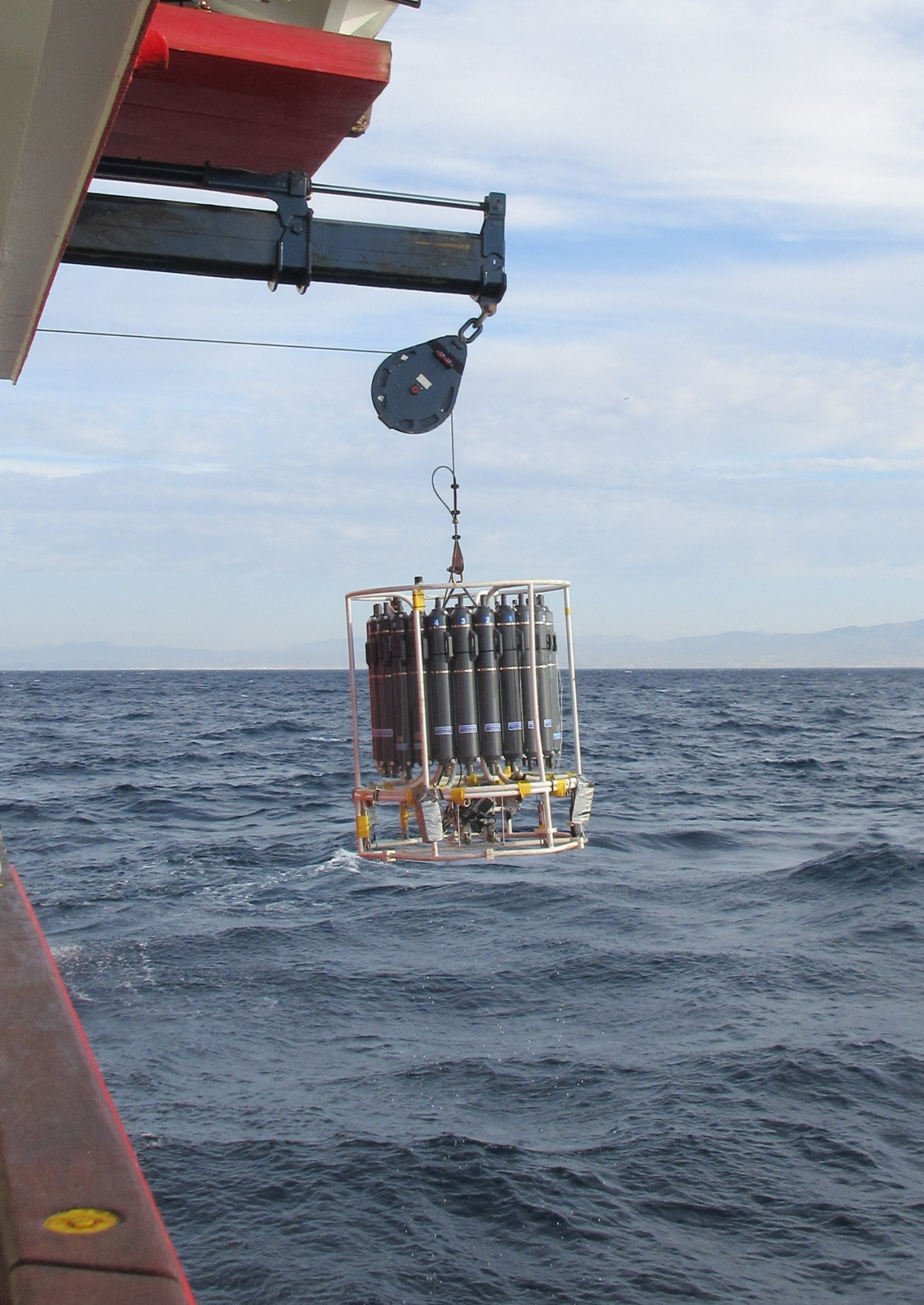

Chapter 1: Introduction

Our oceans host unique ecosystems and play an important role in regulating the global climate. The oceans are the largest carbon dioxide reservoir by taking up atmospheric CO_2 in the seawater and storing carbon in seafloor sediments. Furthermore, ocean currents distribute nutrients and influence global temperatures. However, our oceans are increasingly under pressure as a result of a wide variety of human activities. On a global scale, the increase in carbon dioxide in the earth's atmosphere due to combustion of fossil carbon and changes in land use have resulted in increased amounts of CO_2 stored in the world's oceans, furthering the warming and acidification of oceans waters (Allison and Basset, 2015). Toxic substances and pollutants of all kinds reach the ocean via continental runoff and atmospheric transport, accumulating in marine organisms and sediment (e.g. Willford et al., 1987). Of special concern because of their massive abundance and slow degradation in the environment are plastics (e.g. Alimba and Fagio, 2019).

On a regional scale, reduced deep water ventilation in combination with increased nutrient supply from lands leads to depletion of oxygen in bottom water masses (e.g. Stramma et al., 2010). The seafloor of many continental shelves and slopes is subject to disturbance by demersal fishing, dredging and dumping of dredging spoils, trenching of cables and pipelines, and mining of granulates and minerals, resulting in increased mobility of seabed sediments and increasing suspended particle loads in the overlying water (e.g. Ramirez-Llodra et al., 2011). This leads to changes in transport and deposition of sediment and associated substances, release of carbon from resuspended sediments, changes in transparency of water masses in shallow waters potentially reduce primary production with knock-on effects in subsequent compartments of the marine food chain, and pressure, in particular, on suspension and filter feeding fauna (e.g. Kutti et al., 2015; Sala et al., 2019).

A completely new threat emerging in recent years is the development of mineral mining in the deep sea, which is spurred by the increasing global demand for raw materials used for high-tech applications and the global energy transition (Glover and Smith, 2003; van de Eynde

Image: CTD-Rosette sampler on board of the *RV Sarmiento de Gamboa* off the coast of Málaga (August 2019). Photo by: Sabine Haalboom.

et al., 2014). Unlike shallow marine environments, which are naturally exposed to physical disturbance by storms and tides, most deep-sea environments by comparison are characterised by their stability over long time spans. Disturbances of a magnitude comparable to those caused by mining, such as turbidity currents and sediment transport triggered by seismic events or subsea volcanic eruptions, only occur on geological timescales. Concerns that deep-sea mining will have profound and long-lasting impacts in the mined, as well as in surrounding areas subject to sediment fallout from mining plumes, seem therefore justified.

The aim of this PhD research was to develop strategies for the detection of sediment plumes in the deep sea and to improve quantification of their suspended particle loads. This would be achieved by studying both settings where enhanced particle concentrations occur naturally, such as submarine canyons and hydrothermal vent fields, as well as where enhanced particle concentrations are due to anthropogenic disturbances, such as deep-sea mining.

1.1. Deep-sea mineral resources, prospective deep-sea mining, and potential environmental impacts

The increasing demand for raw materials in the last decades, together with their distribution on land which has major geopolitical consequences, have led to concerns in industrialised nations about the future access to strategic raw materials (e.g. Mero, 1965; Hoagland, 2010). These concerns resulted in an increasing interest in the possible future exploitation of deep-sea minerals, such as concentrated in e.g. deep-sea polymetallic nodules. These nodules, which are currently one of the main targeted resources, were first discovered in the 1870s during the HMS Challenger expedition (Murray and Renard, 1891). At that time, they were considered a natural curiosity of scientific interest but without economic value. It was almost a hundred years later that the possibility of industrial deep-sea mining was first introduced by Mero (1965), leading to a global interest in marine mineral resources in the 1970's. After a decade with several deep-sea exploration initiatives, interest dwindled, as deep-sea mining did not seem to be economically viable. However, with the increase in raw material prices, there was a renewed interest in metal-rich mineral deposits found in the deep ocean (Glover and Smith, 2003; Hoagland, 2010; Hein et al., 2013). These deep-sea resources can be divided into three different deposits and include (1) seafloor massive sulphide deposits at

hydrothermal vent fields, (2) polymetallic nodules at abyssal plains and (3) ferromanganese crusts at the slopes of seamounts (Fig. 1.1).

Figure 1.1: The three main types of minerals targeted by deep-sea mining:

A) Seafloor massive sulphides
Seafloor massive sulphide (SMS) deposits are found along mid-ocean ridges and back-arc basins (Figure 1.2). Here, seawater enters the oceanic crust (e.g., through faults), is heated to several hundred degrees C where it comes into contact with hot volcanic rock and is emitted into the water column as metal-rich hydrothermal fluids. From these hydrothermal plumes, metals precipitate at the seabed, forming polymetallic SMS deposits, which contain high grades of metals like Cu, Co, Zn and rare earth elements (REE) (Cave et al., 2002; Chavagnac et al., 2005).

B) Polymetallic nodules
Polymetallic nodules occur throughout the world's oceans at abyssal plains between 3500 and 6500 m water depth (Halbach and Fellerer, 1980; Hein et al., 2013). These nodules are of great economic interest because they are rich in metals such as Co, Cu, Mn, Ni and REE (Wedding et al., 2015). They form as a result of metal precipitation around a nucleus (e.g. shark's teeth) from ambient seawater and from the interstitial water within the sediment with very slow growth rates in the range of millimetres per million years (Halbach et al., 1988). The largest polymetallic nodule deposit is found in the Clarion-Clipperton Zone (CCZ) in the NE equatorial Pacific Ocean between Hawaii and Mexico (Figure 2). It covers an area of many thousand of square kilometres, roughly the size of Europe, and is likely targeted for future deep-sea mining.

C) Ferromanganese crusts
Ferromanganese crusts are mainly found on the slopes of seamounts between 800 to 2500 m water depth (Figure 1.2; Hein et al., 2000, 2009). They form as dissolved metals are adsorbed onto manganese- and iron oxides and precipitate as a thin crust on sediment-free rock surfaces. They are mainly enriched in cobalt, nickel and manganese, but also host other (rare earth) elements (Baker and Beaudion, 2013).

With the first surge in global interest in deep-sea mining in the 1970's and 1980's, some experiments for collecting minerals from the deep sea were undertaken. However, as the interest in the deep-sea minerals ceased, these attempts never reached sufficient technological maturity. When interest in deep-sea mining was revived at the beginning of the present millennium, several companies and consortia revived the development of deep-sea mining equipment. Among those, Nautilus Minerals Inc. was the first company to develop equipment for mining of seafloor massive sulphide deposits (SMS). The company acquired a license to mine SMS deposits at the *Solwara I* site in the national waters of Papua New Guinea, but resistance from the local community, legal challenges, and lack of funding led to the bankruptcy of Nautilus Minerals Inc. in 2019 before actual mining began. Other companies mainly focussed on the mining of polymetallic nodules, such as Royal IHC, DEME-GSR and The Metals Company (TMC). Where Royal IHC has been working on optimising the functioning of its nodule collector and transport systems to bring the nodules from the seafloor to the

surface, DEME-GSR was the first to actually deploy a pre-prototype mining vehicle in the deep sea. After a failed trial in 2019, it was successfully deployed in the Pacific Ocean in spring 2021. While the pre-prototype mining vehicle of DEME-GSR effectively collected nodules from the seabed, it still lacked a vertical transport system (VTS) to bring the collected nodules to the surface. TMC on the other hand had a successful trial in autumn 2022, including a working vertical transport system. However, techniques for ship-to-shore transport are still being developed, as well as the processing of these ores on land. Hence it is currently still highly unlikely that commercial deep-sea mining will start this decade.

As most of the deep-sea mineral deposits of interest for mining occur beyond the boundaries of national jurisdiction (i.e., exclusive economic zone (EEZ) and extended continental shelf, Fig. 1.2), the call for international protection regulations for the area beyond EEZs began shortly after the concept of deep-sea mining was introduced.

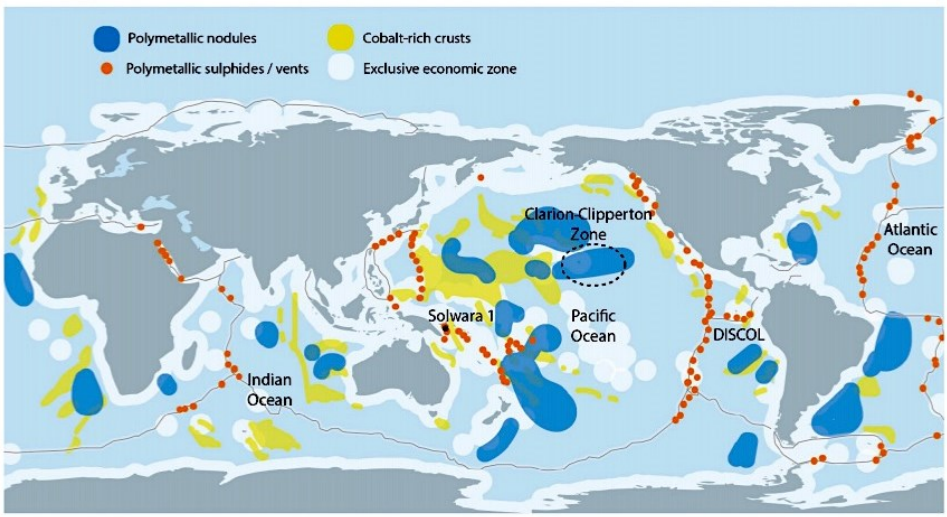

Figure 1.2: Distribution of mineral resources potentially targeted by deep-sea mining. Copyright: Miller et al., 2018; Hein et al., 2013.

Under the United Nations convention on the Law of the Sea (UNCLOS) in 1982, the International Seabed Authority (ISA) was established as an autonomous organisation responsible for regulating deep-sea exploitation and to ensure a fair distribution of the raw materials, as well as preventing serious harm to the marine environment in areas beyond the

EEZs (Article 145 UNCLOS). For exploration of raw materials, as well as technology tests, the ISA had by early 2024 granted 17 contract areas in the Clarion-Clipperton Zone (CCZ) and 14 in other ocean areas to national governments and consortia (ISA, 2024). For the ongoing development of a legally binding framework focussing on the minimisation of the environmental impacts in the framework of an environmental management plan, it is mandatory for the contract holder to assess the environmental impacts of their mining activities and to report their findings to the ISA.

Associated with the deep-sea mineral deposits, a wealth of unique, vulnerable, and largely unknown marine life is found. This gives rise to many questions about the potential environmental impacts caused by future large-scale deep-sea mining activities (e.g. Boschen et al., 2013; Collins et al., 2013; Vanreusel et al., 2016; Boetius and Haeckel, 2018).

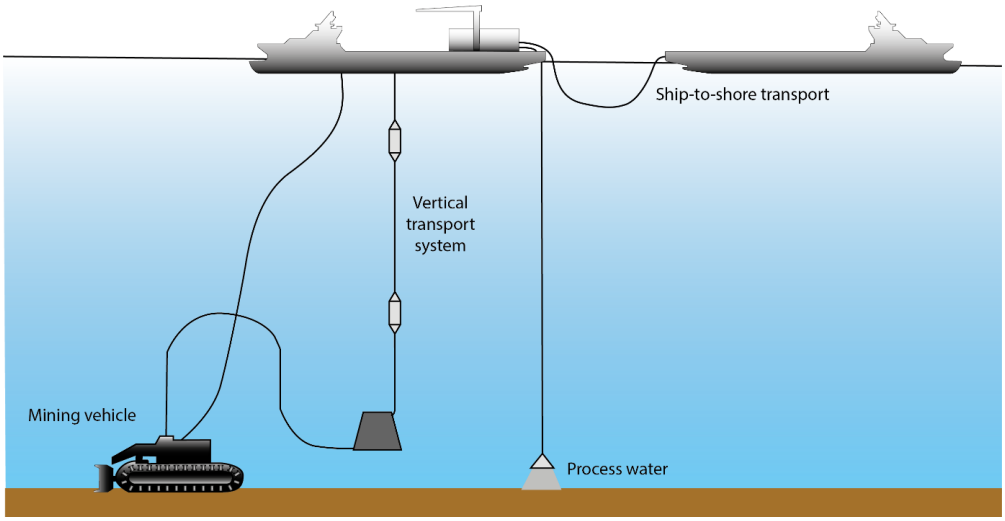

Figure 1.3: Overview of a deep-sea mining operation with mining vehicle, vertical transport system, ship-to-shore transport and the disposal of process water consisting of water, sediment, and nodule fines. (After Blue Nodules, 2016).

During the excavation of mineral deposits, such as polymetallic nodules, the hard substrate essential for sessile benthic fauna to settle on, along with the attached fauna, are removed (Fig. 1.4). Furthermore, depending on the mining techniques, the surface sediment layer will be removed and will thereby likely be dispersed as sediment plumes. Most of the mobilised sediment is expected to settle near the sites directly impacted by the mining vehicle (e.g.

Nakata et al., 1997; Fukushima, 1995; Jankowski and Zielke, 2001; Aleynik et al., 2017; Gillard et al., 2019), thereby smothering benthic fauna. However, a fraction of the mobilised sediment is expected to spread over a much wider area beyond the area actually mined, affecting benthic and pelagic life (e.g. Berelson et al., 1997; Smith and Demopoulos, 2003; Ramirez-Llodra et al., 2011; Levin et al., 2016a; Jones et al., 2017; Vare et al., 2018; Drazen et al., 2020). These far-spreading sediment plumes might disperse over several kilometres to tens of kilometres, with particle concentrations still sufficient to clog the feeding and respiratory surfaces of suspension and filter feeders, especially when they are exposed to elevated sediment concentrations during months or even years (Kutti et al., 2015; Washburn et al., 2019).

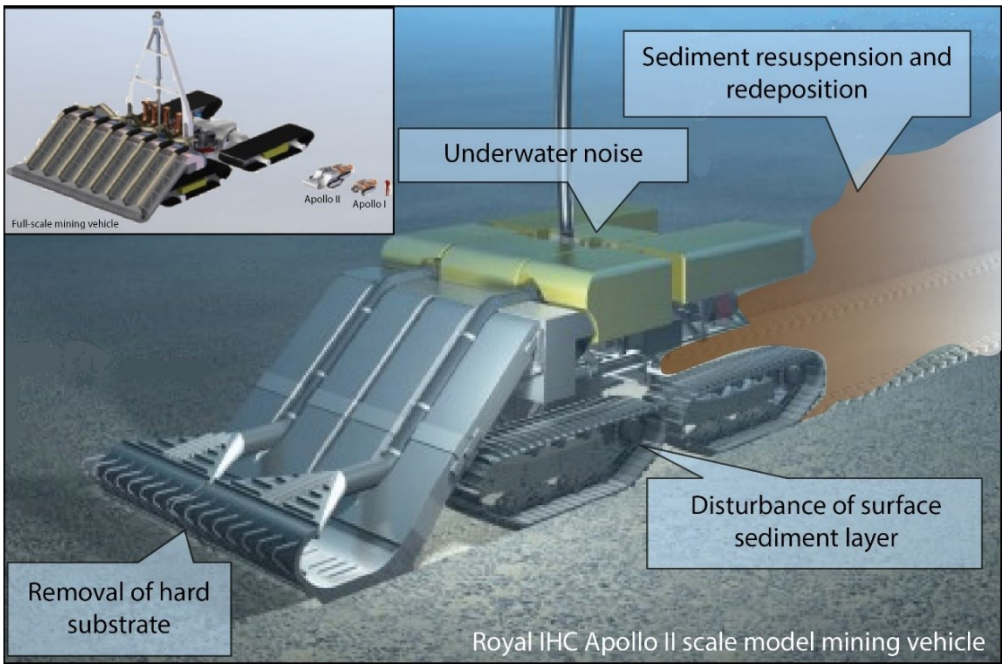

Figure 1.4: Artist impression of the Royal IHC's Apollo II pre-prototype mining vehicle, with potential environmental pressures. Top left inset also shows how the pre-prototype Apollo I and II compare in scale with a full-scale mining vehicle (Copyright: Blue Nodules, 2016).

As deep-sea mining is not yet conducted on full industrial scale, the behaviour of large-scale mining-induced sediment plumes and the impact of these plumes on the deep-sea ecosystem are difficult to assess. Furthermore, to provide reliable recommendations for monitoring schemes of (man-made) particle plumes, it is necessary to extensively test appropriate

technological equipment, which should ideally be standardized for future monitoring purposes.

In order to provide scientific information on the environmental impacts of mining activities at the seafloor and to develop a framework for impact prediction, acceptance criteria and responsible deep-sea mining practices, multiple studies have previously been performed. For example, mainly focussing on the mining of polymetallic nodules, several studies have been performed in the CCZ as well as in other areas rich in polymetallic nodules, such as the Peru Basin. During these studies, trial mining sites were revisited, or the effects of deep-sea mining were simulated by dredging, ploughing, or dragging an epibenthic sledge over the seafloor. During the Deep Ocean Mining Environmental Study (*DOMES*, Burns, 1980), for example, the environmental impacts of the mining trials performed in the CCZ by the Ocean Mining Associates (OMA) consortium, Ocean Management Inc. (OMI), and the Ocean Minerals Company (OMCO) in 1975 and 1978 were investigated. The OMCO site was subsequently revisited by the French Institute IFREMER in 1988 and 2004 (e.g. Khripounoff et al., 2006), during the EU-funded MIDAS project, 26 years after the initial disturbance (e.g. Muljutin et al., 2011), and in 2015 during the JPIO *Mining Impact* project (Martínez Arbizu and Haeckel, 2015). Mining effects were simulated during the Japanese Benthic Impact Experiment (JET; Fukushima, 1995) in 1994 and the Benthic Impact Experiments (BIE) performed in 1993 (BIE-II) and 1995 (OIM-BIE) (e.g. Trueblood and Ozturgut, 1997; Radziejewska, 2002). Another mining impact simulation project was the German *DISCOL* (Disturbance and Recolonization Experiment) project, performed in the Peru Basin in 1989, during which 78 disturbance tracks were made with a plough-harrow (Thiel and Schiever, 1989; Thiel et al., 2001). The site has since been visited multiple times, and it has been shown that even 26 years after the disturbance, the created tracks were still visible (Gausepohl et al., 2020) and that there still was a significant reduction in number of filter- and suspension feeders (e.g. Stratmann et al., 2018; Simon-Lledó et al., 2019).

More recently, environmental impact studies have been performed with actual pre-prototype mining equipment. The *Blue Nodules* project focussed on the development of deep-sea mining equipment for collecting of polymetallic nodules by Royal IHC (*Apollo II*), with as low as possible environmental impact. During this project, two field tests with a pre-prototype

mining vehicle were performed offshore Málaga, Spain, which was closely monitored by the other project partners. The second phase of the *Mining Impact* project started in 2018 with the aim to independently monitor an industrial mining test in the CCZ with the pre-prototype *Patania II* nodule collector vehicle by the Belgian contractor DEME-GSR. The *Patania II* mining test was scheduled for 2019, however, due to technical difficulties, the test had to be postponed to 2021 and could not be studied as part of this thesis. In the framework of these projects, we had the unique chance to gather and evaluate environmental data and to provide scientific knowledge to policy makers for the protection of the environment before deep-sea mining starts.

1.2. Natural particle dynamics in the marine realm and occurrence of nepheloid layers

An important consideration when assessing the potential impact from anthropogenic sediment plumes, is the natural background variability in suspended particle loads in the environment. The particle load in natural aquatic systems is usually referred to as suspended particulate matter (SPM), which consists of lithogenic material derived from the erosion of rocks, biogenic material produced by living organisms, comprising both organic and inorganic matter (e.g. calcium carbonate, biogenic silica, and apatite), and authigenic minerals formed by chemical precipitation. The SPM mass concentration in the marine water column is determined on one hand by the input of matter from land via runoff, atmospheric transport, biological production in the surface ocean, chemical precipitation, and resuspension of material from the seabed by waves and currents. On the other hand, it is defined by loss of suspended particles by sedimentation and dilution via mixing of water with different SPM mass concentration. The highest near-bottom (<10 m above bottom) SPM mass concentrations are generally found in coastal and continental shelf systems, due to the combination of high supply of detritic material from land, high biological production, tidal and wind-driven current that keep particulate matter in suspension, and mobilisation of sediments by human activities. In rivers and estuaries, near-bottom SPM mass concentrations reach >100 mg L^{-1} (e.g. Downing et al., 1981; Nittrouer et al., 1986), and are often further increased by different human activities, such as trawl fishing and dredging. Towards the deep ocean, near-bottom SPM mass concentrations rapidly decrease to generally <10 mg L^{-1} at continental shelves (e.g. Drake, 1976), and decrease further down into the open oceans with

SPM mass concentrations of 0.04 mg L^{-1} in the deep Atlantic Ocean (e.g. German et al., 1998; Wilson et al., 2015b) and 0.02 mg L^{-1} in the deep Pacific Ocean (e.g. Lavelle et al., 1981).

In the open ocean, elevated SPM mass concentrations are commonly referred to as nepheloid layers (Gardner et al., 2018b). These nepheloid layers are common on continental shelves and slopes, in particular in submarine canyons where the steep topography leads to focused sedimentation and where internal tidal currents accelerated by the canyon topography result in frequent resuspension of settling material (Durrieu de Madron, 1994; Amin and Huthnance, 1999; Gardner et al., 2018a; Fig. 1.5). As internal waves frequently break on the canyon's slopes (Quaresma et al., 2007; Puig et al., 2014; van Haren et al., 2015), particles from the seafloor are resuspended and form permanent nepheloid layers, consisting of a mixture of organic and inorganic matter (e.g. Puig and Palanques, 1998; Amin and Huthnance, 1999). As submarine canyons connect the continental shelves with the deep sea, they likely play a major role in particle transport processes (Puig et al., 2014; Davison et al., 2019; Maier et al. 2019b; Fig. 1.5). To aid to the understanding of food supply to the deep sea and transport and burial or carbon it is important to properly quantify these particle loads (Thomsen, 1999; Duineveld et al., 2001; Epping et al., 2002; García and Thomsen, 2008; Amaro et al., 2015).

At hydrothermal vents, nepheloid layers are produced by the release of hot (up to 365 °C) mineral-loaded fluids from fissures in the seafloor into the water column (e.g. Severmann, 2004). Due to their high temperature, these hydrothermal fluids are initially lower in density than the surrounding water, so that they rise to several hundred metres above the seafloor until they have cooled down and reach a density layer in which they are neutrally buoyant (Fig. 1.5). The hydrothermal fluids mixed with ambient seawater are then dispersed by the currents as hydrothermal plumes and can be traced up to tens of kilometres away from their source. These plumes are enriched in metals like Cu, Co, Zn, and rare earth elements, both as dissolved and suspended particulates (Cave et al., 2002; Chavagnac et al., 2005). Together with the hydrothermal deposits on the seafloor, they represent a unique ecosystem hosting a variety of microbial and metazoan life (Levin et al., 2016b).

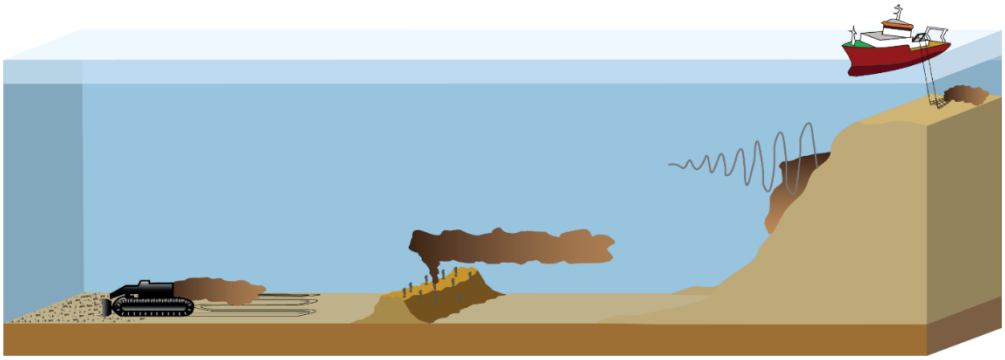

Figure 1.5: Overview of natural processes and anthropogenic activities in the world's oceans addressed in this thesis, that lead to elevated particle concentrations in the water column. From left to right: deep-sea mining of polymetallic nodules found on the abyssal plains, hydrothermal vent fields found at mid-ocean ridges emitting hydrothermal plumes, formation of nepheloid layers in submarine canyons, as incoming internal waves resuspend surface sediments and lastly, fishermen trawling over the continental shelves.

While opportunities to investigate sediment plumes produced by deep-sea mining are scarce, submarine canyons and hydrothermal vents provide "natural laboratories" for monitoring plumes, while at the same time improve the understanding of natural particle transport processes in these environments.

1.3. Prediction and monitoring of deep-sea mining plumes

As anthropogenic sediment plumes are expected to affect benthic and pelagic life in the vicinity of the disturbance sites, various plume dispersion studies have been performed making use of small-scale experiments, in which the effect of mining gear producing a sediment plume was simulated (e.g. Jones et al., 2017). Based on the observations made during these studies, model predictions for the dispersion of resuspended sediment plumes were made (e.g. Jankowski et al., 1996; Nakate et al., 1997; Jankowski and Zielke, 2001). These models are required to better understand the environmental impacts of mining activities and to give guidance for future activities in the deep sea. However, the majority of these studies focussed on the quantification of redeposited sediment, qualitatively assessed by means of photo/video surveys (Barnett and Suzuku, 1997; Yamazaki et al., 1997; Rolinski et al., 2001; Peukert et al., 2018; Gausepohl et al., 2020) and only a few studies also monitored suspended sediment loads in the water column (e.g. Lavelle et al., 1982; Brockett and Richards, 1994). Therefore, these models can be further improved when more observational data is available for model validation and calibration.

At the time that these studies were carried out, the available deep-sea technology was still limited compared to current standards and therefore plume monitoring arrays were not as spatially large and diverse as would be required for meaningful observations (Spearman et al., 2020; Baeye et al., 2022). Moreover, in most of the previous plume dispersion models, particle aggregation processes have not been considered, which has important implications on the results. Based on results from laboratory experiments, particle aggregation is expected to occur in deep-sea mining plumes, speeding up sediment settling and therefore restricting the spatial dispersion of the plumes (Gillard et al., 2019). Therefore, to improve and validate plume dispersion models, both in situ baseline data, as well as data gathered during mining equipment tests, such as data on SPM mass concentration and particle size distributions are needed (Gjerde et al., 2016; Purkiani et al., 2021). Even though these mining tests may be of limited extent compared to full-scale industrial mining, the observations on sediment plume dispersion are highly valuable to improve and validate plume dispersion models.

For the monitoring of deep-sea mining plumes, a variety of sensor types are available. Most commonly used sensors for measuring suspended particle loads in seawater as well as in terrestrial water bodies are optical backscatter sensors (OBSs) and transmissometers. The optical backscatter sensors measure relative turbidity based on changes in the intensity of light backscattered or diffracted by particles suspended in water, whereas transmissometers measure turbidity based on changes in intensity of a light beam transmitted through the water with suspended particles (Fig. 1.6). Instead of backscattered light, backscattered sound may also be used for assessing suspended particle loads. Acoustic backscatter sensors are specifically designed for this purpose, but acoustic Doppler current profilers (ADCPs) designed for measuring current velocity also record intensity of backscattered sound over a vertical or horizontal profile, and therefore are also commonly used to assess variation in suspended particle loads.

Depending on the specific wavelength of light or acoustic frequencies used, these optical and acoustic sensors differ with regards to their sensitivity to certain particle size ranges and other physical characteristics of the particles. Generally, optical sensors as well as high-frequency acoustic devices are more sensitive for finer-grained material, whereas low-frequency ADCPs

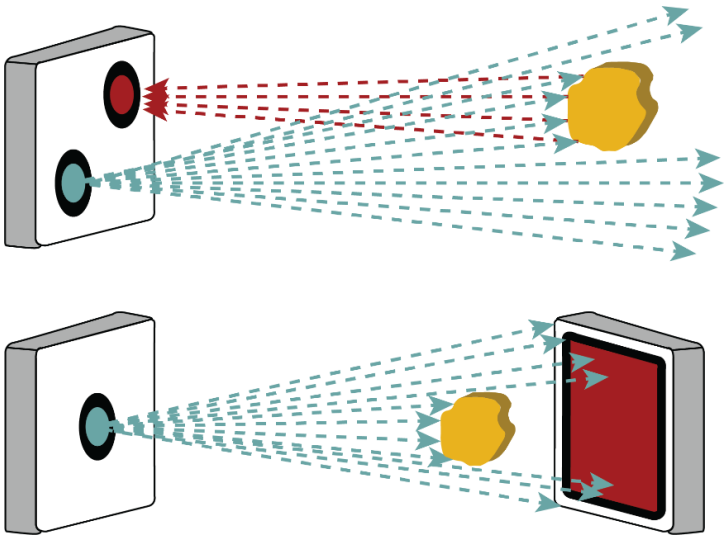

Figure 1.6: Top: Illustration of sensor recording backscattered light or sound. Bottom: Illustration of a transmissometer.

primarily detect material of a few hundred µm or larger (e.g. Bunt et al., 1999; Lohrmann, 2001).

Although the different types of sensors have a physically well-understood relationship between sensor response and SPM mass concentration, the quantification of the recorded turbidity signal is often not straightforward (e.g. Guillén et al., 2000; Downing, 2006; Fettweis et al., 2019). The quantification of the recorded turbidity signal is complicated due to the fact that the signal is dependent on both the concentration of suspended particles and their inherent physical characteristics, such as size (Baker and Lavelle, 1984; Bunt et al., 1999; Hatcher et al., 2001; Gruber et al., 2016; Sahin et al., 2020; Fig. 1.7), shape (Gibbs, 1978; Schaafsma and Hay, 1997), composition (Maa et al., 1992; Moate and Thorne, 2012; Ohnemus et al., 2018) and colour (Hatcher et al., 2000).

Field studies addressing the merits and potential drawbacks of commonly used turbidity sensors often only considered one specific type of sensor (e.g. Bischop, 1986; Merkelbach and Ridderinkhof, 2005; Perkey et al., 2010; Guerrero et al., 2011; Boss et al., 2015; Santos et al., 2020), and sensor inter-comparison studies were mainly performed in onshore and near-shore settings (e.g. Osborne et al., 1994; Hawley, 2004; Lewis et al., 2007; Rymzsewicz et al., 2017; Fettweis et al., 2019; Lin et al., 2020).

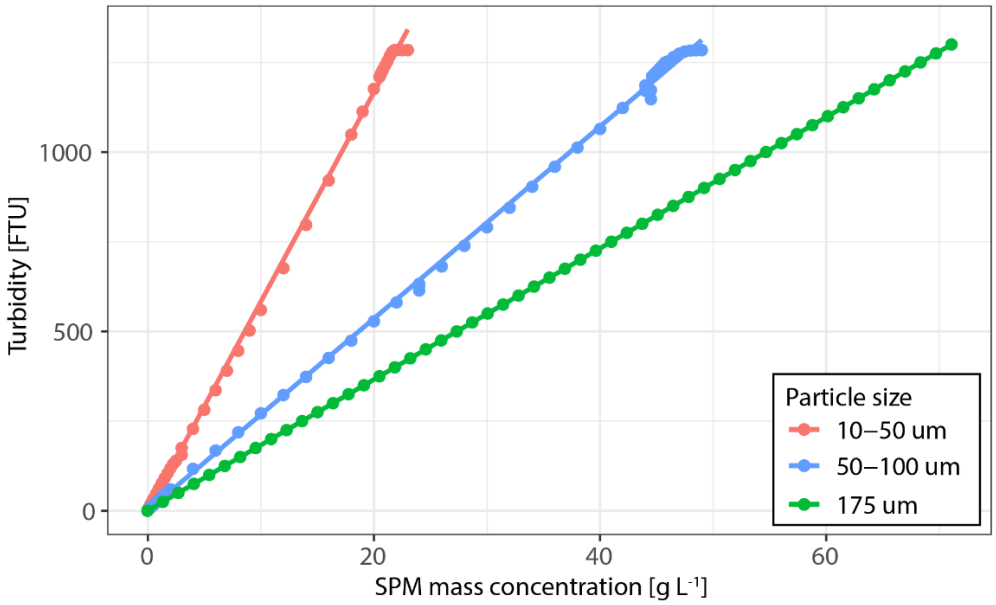

Figure 1.7: Results of a laboratory experiment demonstrating the influence of particle size on OBS sensor response. The OBS sensors response was found to be inversely proportional to the size of the suspended particles (e.g. Gibbs and Wolanski, 1992; Bunt et al., 1999; Downing, 2006). This is because the amount of backscattered light is proportional to the total cross-sectional area of the illuminated particles, which decreases with increasing particle size, assuming a constant total volume of particle (Hatcher et al., 2001). In other words, a certain volume of suspended particles of a small size will produce a stronger backscatter of light than the same volume of particles of a larger size.

In these settings SPM mass concentrations are high, and varying contributions of sand-sized particles and the formation of aggregates complicated quantification of the turbidity signal. However, the deep sea poses different challenges to the quantification of SPM. The larger depth prevents frequent water sampling to determine the SPM mass concentration, and the composition of the SPM is way more heterogeneous compared to material used in the laboratory. Moreover, unlike the glass beads and quartz sand used in the laboratory experiments, the fine-grained particles tend to aggregate into larger aggregates, which possess different optical and acoustic scattering properties. In the studies presented in this thesis different optical and acoustic sensors and different arrangements of sensors have been used to assess natural variability in suspended particle load in different marine environments, and to test their application in the monitoring of deep-sea mining plumes.

1.4. Scope of the thesis

In Chapters 2 and 3, variability of suspended particle load in nepheloid layers in the Whittard Canyon (northern Bay of Biscay, NE Atlantic Ocean) is studied. Submarine canyons, characterised in their upper reaches by pronounced nepheloid layers with tide-driven cycles of sediment resuspension and redeposition, provide a suitable natural laboratory to perform field experiments with different commonly used commercial optical and acoustic sensors. In Chapter 2 a comparative study is presented, in which it is assessed how simultaneously deployed sensors including optical backscatter sensors, transmissometers and both low- and high-frequency ADCPs influence the estimates of SPM mass concentration. Additionally, discrete water samples were collected in situ to quantify the SPM mass concentration. As the study area was visited during spring, it was possible to compare sensor response in the biologically productive surface water with the response of the same sensor in near-bottom waters. It was found that chlorophyll-bearing phytoplankton in the biologically productive surface layer absorb more of the transmitted light signal of the transmissometer compared to suspended detritic particles in the near-bottom water, resulting in a misestimation of the SPM mass concentrations as inferred from the transmissometer's response. Furthermore, it was demonstrated that the detection of suspended particles is affected by the type of sensor, due to the diverse range of particle sizes found in Whittard Canyon. The low-frequency ADCPs were most sensitive for larger aggregated particles and did not detect the finer-grained material. Conversely, the high-frequency ADCPs and OBSs were most sensitive for finer particles and hardly detected the larger aggregates. Therefore, it is suggested to use a combination of different sensors which complement each other with regards to the range of particle sizes they detect, since the use of only one type of sensor could lead to an observational bias and hence understanding of particle transport processes.

Chapter 3 presents a more in-depth analysis of SPM distribution and deposition in the Whittard Canyon, focussing on its organic content. Both SPM and surface sediments were collected along a depth transect along the canyon axis, using a CTD-Rosette and a mono- and multi corer, respectively. To determine temporal changes in suspended particulate organic matter (SPOM) concentration and composition over a tidal cycle, bottom landers were deployed equipped with in situ particle pumps. The results demonstrate the heterogeneity of SPOM present in the bottom water in both space and time. In the bottom water in the upper

reaches of the canyon, SPOM concentrations were relatively low, whereas in the middle reaches of the canyon, where most active resuspension takes place, SPOM concentrations were higher, but the SPOM was more degraded compared to the upper reaches. The lower canyon comprised slightly less degraded SPOM in low concentrations. Temporal data recorded in the mid-canyon reaches showed that particles are resuspended during peaks in current speeds when the tidal flow is directed up-canyon, resulting in higher concentration of C_{org}, N_{tot} and Chl-*a*. Furthermore, the low Chl-*a*/C_{org} ratio of the SPOM at this location suggests that older and more degraded organic matter incorporated in the surface sediments is also entrained during the repeated resuspension by internal tides. As for the surface sediments, the highest concentrations of (more degraded) organic matter are found in the lower reaches of the canyon. It therefore seems that the continuous cycles of resuspension, combined with down-canyon transport by intermittent gravity flows, result in the winnowing of the fine-grained organic-rich particulate fraction from the upper and middle reaches of the canyon, and transport and ultimate deposition of the more refractory organic compounds in the lower reaches. While the organic matter transport in the canyon primarily affects carbon cycling on local scale, it might be worth protecting these depocenters rich in reactive organic matter from anthropogenic activities, as remobilisation would expose the organic matter to conditions favourable for its decay, leading to the release of carbon dioxide from currently trapped carbon.

Chapter 4 is dedicated to the plume of the Rainbow hydrothermal vent field located on the Mid-Atlantic Ridge SW of the Azores. Seafloor massive sulphide deposits around hydrothermal vents are a potential target for deep-sea mining. During mining, surface sediment will be resuspended and will potentially interact with the naturally occurring hydrothermal plume. However, little is known about the natural state of the plume, especially concerning the changes in chemical composition and microbial assemblages as the neutrally buoyant plume disperses. This understanding of the natural state of the plume and how it affects the environment is essential to study potential impact of deep-sea mining. In the case of the Rainbow hydrothermal vent field, the extensive plume was observed up to 25 km downstream from the vent field, using optical backscatter sensors. Furthermore, both water column and sediment samples from the area were collected, to investigate how (trace) metal composition and microbial communities change in the hydrothermal plume with distance to

its source. Geochemical and microbial changes along the neutrally buoyant plume were evident, with the plume showing enrichments in (trace) metals and REE, compared to above-plume water samples. Furthermore, element concentrations changed over distance, as the plume dispersed, which was also reflected in the background pelagic systems within the plume. This study shows that the Rainbow hydrothermal plume is a geochemically enriched environment representing a heterogeneous, dynamic habitat and it provides a baseline study on the geochemical and biological heterogeneity, needed to assess the environmental impacts of deep-sea mining.

Chapters 5 and 6 address approaches for future monitoring of sediment plumes generated during deep-sea mining of polymetallic nodules. Plumes of sediment generated during mining will potentially spread up to tens of kilometres outside of the mined area.

In Chapter 5 different types of monitoring setup are presented, tested during two industry field tests of Royal IHC's pre-prototype deep-sea mining vehicle *Apollo II* offshore southern Spain. Even though the tests were performed in relatively shallow water, on a muddy seabed without polymetallic nodules, they provided valuable insights for the monitoring of deep-sea mining activities in the deep Pacific, and the collected data is currently used for numerical modelling of the sediment plume dispersion. During the performance tests of the mining vehicle, the dispersion of the suspended sediment was monitored with turbidity sensors deployed on a CTD system and on a mooring array. Furthermore, visual observations were carried out using a ROV. The results show that with the applied monitoring setup, the generated sediment plume could still be detected up to 350 m away from its source. It was also shown that the generated plume did not extend more than 2 m above the seafloor in the first 100 m to the source, but increased in height with distance away from source, with turbidity values rapidly decreasing with the increasing distance to the source. The applied monitoring setup, where both moving and moored platforms were combined, proved to be a suitable strategy for monitoring anthropogenic sediment plumes.

In Chapter 6, the results of a small-scale disturbance experiment, carried out in the Clarion-Clipperton Zone in the NE equatorial Pacific Ocean, are presented and discussed. The collected data improved our understanding of sediment plume dispersion and supported the

development of plume dispersion models in this specific deep-sea area (Purkiani et al., 2021). In this experiment, a dredge was used for generating a sediment plume, and sediment plume dispersion and deposition were monitored using an extensive array of both optical and acoustic turbidity sensors and current meters, as well as by visual inspection of the seafloor. Visually, sediment redeposition from the plume could be distinguished to a distance of about 100 m away from the source. The turbidity sensors proved to be a more sensitive tool, as the dispersing plume was still clearly visible in the records on the sensors placed 300 m away from the source. Furthermore, the response of the OBSs could be converted into absolute SPM mass concentration, thereby providing quantitative data on sediment load. The acoustic turbidity sensors also provided vertical profiles of acoustic backscatter, giving insight in the vertical extent of the generated sediment plumes. The monitoring setup applied in this study proved to be suitable to monitor the sediment plumes generated during the small-scale experiment. For an upscaled setup for future plume monitoring it would be recommended that AUVs are used for repeated seafloor imaging and dynamic water column turbidity mapping. Also, in situ particle sizers or particle cameras are needed to better understand ongoing particle aggregation, as this will affect the response of the optical and acoustic turbidity sensors. Elements of the monitoring setup proposed in **Chapter 6** have already been tested in practice during the monitoring of the deep-sea trial of DEME-GSR's pre-prototype mining vehicle *Patania II* in spring 2021.

Chapter 2: Suspended particulate matter in a submarine canyon (Whittard Canyon, Bay of Biscay, NE Atlantic Ocean): Assessment of commonly used instrument to record turbidity

Sabine Haalboom, Henko de Stigter, Gerard Duineveld, Hans van Haren, Gert-Jan Reichart & Furu Mienis

Published as:

Haalboom, S., de Stigter, H.C., Duineveld, G.C.A, van Haren, H., Reichart, G.-J., & Mienis, F., 2021. Suspended particulate matter in a submarine canyon (Whittard Canyon, Bay of Biscay, NE Atlantic Ocean): Assessment of commonly used instruments to record turbidity. Marine Geology, v. 434, 106439. https://doi.org/10.1016/j.margeo.2021.106439

Image: Recovery of the Bottom Boundary (BoBo) lander on board of the RV *Pelagia* during cruise 64PE437 (May 2018). Photo by: Sabine Haalboom.

Abstract

Nepheloid layers with elevated concentrations of suspended particulate matter (SPM) are found throughout the world's oceans. They are generated by both natural processes, involving resuspension of seabed sediment by bottom currents, and anthropogenic sediment resuspension due to bottom trawling, dredging and in the future potentially due to deep-sea mining. These nepheloid layers represent pathways of lateral SPM transport, including lithogenic and biogenic sediment, organic matter, (trace) metals, organic pollutants, and plastics. For assessment of the dispersion of these materials, it is essential that SPM mass concentrations can be accurately quantified. However, this is not straightforward as the detected turbidity signal, which is used as a proxy for SPM mass concentration, not only depends on the concentration of particles, but also on physical characteristics of these particles, such as particle size, substance, and shape. Here we present a comparative study of turbidity data to assess the potential implications different sensors have on the estimates of SPM mass concentration. Optical backscatter sensors (OBSs), transmissometers and both low- and high-frequency ADCPs were deployed simultaneously in the Whittard Canyon (North Atlantic Ocean), and water samples were collected for quantification of SPM mass concentration and ex-situ particle size analysis. We found that SPM mass concentrations inferred from the transmissometer are easily overestimated in the biologically productive surface layer due to higher light absorption by chlorophyll-bearing phytoplankton, compared to suspended detritic particles. Furthermore, we observed that depending on sensor type some particles are not, or less well, detected. This is due to differences in particle size sensitivities of these sensors towards the diverse range of particle sizes found in the Whittard Canyon, whereby the low-frequency ADCP was most sensitive for coarse-grained material and the high-frequency ADCP and OBSs most sensitive for fine-grained material. In future studies, we suggest to use a combination of different sensors as the use of only one type of sensor could potentially lead to misinterpretation and misquantification of particle transport processes and fluxes.

2.1. Introduction

Throughout the world's oceans, and in particular along continental slopes, suspended particulate matter (SPM) is found in elevated concentrations in so-called nepheloid layers (McCave, 1986; Durrieu de Madron, 1994; Amin and Huthnance, 1999; Gardner et al., 2018a). Generally these nepheloid layers occur in areas where the hydrography interacts with the topography (Gardner et al., 2018b), which is often related to the incidence of internal waves in areas with a (super-)critical slope (Quaresma et al., 2007; Puig et al., 2014; van Haren et al., 2015). These energetic hydrodynamics result in resuspension and dispersal of (food) particles (Dickson and Mccave, 1986; Amin and Huthnance, 1999), thereby influencing deep-sea ecosystems (Mienis et al., 2007; Davison et al., 2019). In a very different setting, nepheloid layers are also observed along mid-ocean ridges and back-arc basins where they can be traced back to hydrothermal vents emitting plumes rich in very fine-grained particulates. These plumes rise several hundred metres above the seafloor and disperse over vast areas, providing a major source of heat and chemicals to the ocean (German et al., 1998), hereby affecting the local geochemistry and biodiversity (Khripounoff et al., 2001; Haalboom et al., 2020). Anthropogenic disturbances are also recognised as a cause of the formation of nepheloid layers. Bottom trawling (Puig et al., 2012; Daly et al., 2018) and dredging operations (Smith and Friedrichs, 2011) cause resuspension of bottom sediment, often interfering with natural sediment transport processes (Martín et al., 2014). Moreover, in the foreseeable future, anthropogenic nepheloid layers may also make their appearance in hitherto pristine deep-sea environments, as a consequence of the mining of polymetallic nodules and seafloor massive sulphide deposits (Glover and Smith, 2003; van den Eynde et al., 2014).

Submarine canyons, of which almost 6000 have been identified worldwide (Harris and Whiteway, 2011), appear to be hotspots for the generation of nepheloid layers, which makes them ideal locations to study SPM dynamics. Within submarine canyons the formation of these layers is driven by energetic hydrodynamics often associated with intensified internal wave activity, as for example demonstrated in canyons along the Portuguese margin (de Stigter et al., 2007, 2011; Quaresma et al., 2007), US margin (Gardner, 1989a) and the Bay of Biscay (Wilson et al., 2015b; Hall et al., 2017). In submarine canyons, nepheloid layers are thought to serve as a link between the biologically productive continental shelves and the organic matter starved deep sea, thereby playing a prominent role in carbon and nitrogen cycling (Gardner,

1989a; Durrieu de Madron, 1994; Puig and Palanques, 1998; Amin and Huthnance, 1999; Kiriakoulakis et al., 2011; Canals et al., 2013; Puig et al., 2014). Evidence for enhanced organic matter transport from the continental margins to the deep sea via canyons (Jahnke et al., 1990; Walsh, 1991) is the elevated standing stock of benthic fauna found in submarine canyons compared to their adjacent open slopes (De Leo et al., 2010; Huvenne et al., 2011; Robertson et al., 2020).

Nepheloid layers play a major role in particle transport, including detritic, biogenic sediment, organic matter, (trace) metals, organic pollutants adsorbed to particles and plastics. Therefore, it is important that these particle loads are properly quantified. For example, within submarine canyons quantification of fluxes of organic matter will aid to the understanding of food supply to the deep sea and transport and burial of carbon (Thomsen, 1999; Duineveld et al., 2001; Epping et al., 2002; García and Thomsen, 2008; Amaro et al., 2015), and at hydrothermal vent sites it has been shown that the diversity of microorganisms changes within the chemically enriched hydrothermal plumes as they disperse away from the vent site (Haalboom et al., 2020). In the case of anthropogenic plumes, a proper quantification is also important to assess the extent of plumes, as they can potentially smother benthic fauna (Kutti et al., 2015). This is especially the case in deep-sea settings where sediment plumes do not naturally occur, and life is adapted to extremely low suspended particle concentrations (Boschen et al., 2013).

For the detection of SPM and nepheloid layers, optical sensors (optical backscatter sensors (OBSs) and transmissometers) find widespread application. Acoustic devices, like acoustic Doppler current profilers (ADCPs), which are commonly used for recording current speed and direction, do also record turbidity on the basis of intensity of backscattered acoustic signal. These optical and acoustic sensors, operating at different optical wavelengths and acoustic frequencies, are used to detect relative changes in turbidity in the water column. Quantification of turbidity data in terms of mass concentration of SPM so far remains complex (e.g. Guillén et al., 2000; Downing, 2006; Fettweis et al., 2019), as the detected signal is not only dependent on the concentration of particles, but also on particle size distribution and aggregation (Baker and Lavelle, 1984; Bunt et al., 1999; Hatcher et al., 2001; Gruber et al., 2016; Sahin et al., 2020), shape and surface roughness (Gibbs, 1978; Schaafsma and Hay,

1997), composition (Maa et al., 1992; Moate and Thorne, 2012; Ohnemus et al., 2018) and colour of the material (Hatcher et al., 2000).

To date, mainly laboratory studies have been performed to examine the effects of the physical properties of particles on turbidity measurements (e.g. Baker and Lavelle, 1984; Downing and Beach, 1989; Gibbs and Wolanski, 1992; Hatcher et al., 2000; Sahin et al., 2020) and field studies which have directly addressed the merits and potential drawbacks of commonly used turbidity sensors often only considered one type of sensor (e.g. Bishop, 1986; Merckelbach and Ridderinkhof, 2005; Perkey et al., 2010; Guerrero et al., 2011; Boss et al., 2015; Santos et al., 2020). Inter-comparisons of sensors by e.g. Osborne et al. (1994), Hawley (2004), Lewis et al. (2007), Rymszewicz et al. (2017), Fettweis et al. (2019) and Lin et al. (2020) were performed in onshore (rivers and lakes) and near-shore settings, where very high particle loads, varying contribution of sand-sized particles and formation of aggregates proved challenging for quantification of SPM mass concentrations. Open ocean settings pose different challenges to the quantification of SPM due to the large depth preventing frequent sampling for calibration and because of the large contribution to SPM of both living plankton as well as organic and inorganic detritus. Small-sized primary particles have the tendency to aggregate into larger aggregates that have different optical and acoustic properties. In addition, migrating zooplankton can produce a distinct acoustic backscatter signal in low-frequency ADCPs (Flagg and Smith, 1989; Plueddemann and Pinkel, 1989; van Haren, 2007). Given the past and current studies employing turbidity sensors in open ocean settings, and the many studies to come prompted by increasing human disturbance of the seafloor (e.g. dredging, deep-sea mining), a better understanding of what the different types of turbidity sensors are recording in these settings is needed (Ziegler, 2002; Puig et al., 2014; Rymszewicz et al., 2017). Thereby it is of importance that the output of these sensors can be properly quantified in terms of SPM mass concentration and that processes affecting flocculation and disaggregation are understood, which have possible implications on the quantification of turbidity signals.

In this study, turbidity data, obtained with commonly used commercial optical sensors and acoustic devices, are compared. Sensors were deployed simultaneously in the Whittard Canyon (northern Bay of Biscay, NE Atlantic Ocean), which is known for its ubiquitous presence of nepheloid layers over a wide range of concentrations (Wilson et al., 2015b). Furthermore,

the presence of biologically productive surface water during spring, allowed for comparison of sensor output for surface water containing primarily live plankton versus bottom water containing a mixture of detritic lithogenic and biogenic sediment particles. The differences in turbidity records produced by simultaneously deployed sensors and the respective implications on estimates of SPM mass concentration are discussed. Moreover, we apply these findings on a time series collected with these sensors to investigate the near-bed SPM dynamics.

2.2. Regional Setting

The Whittard Canyon (Fig. 2.1) is a dendritic submarine canyon system, incising the Celtic continental margin in the northern Bay of Biscay (Amaro et al., 2016). The four main, NNW-SSE to NNE-SSW oriented branches of the canyon system extend from the continental shelf at approximately 200 m water depth to the abyss at depths exceeding 3500 m, where the branches converge in the so-called Whittard Channel (Amaro et al., 2015).

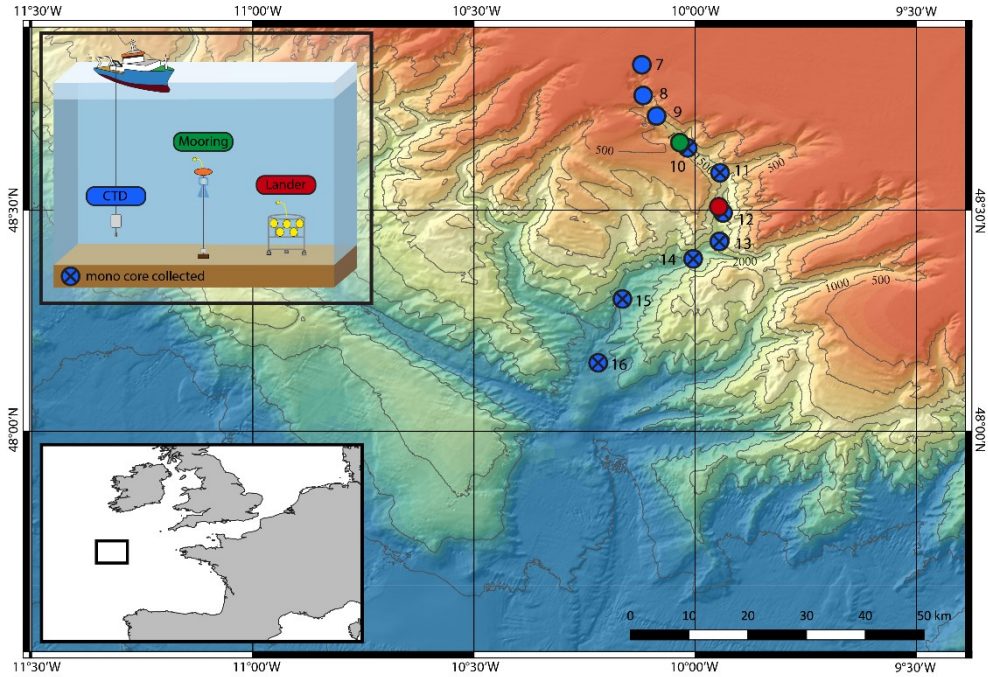

Figure 2.1: Geographical location (lower left inset) and bathymetric map of the Whittard Canyon in the Bay of Biscay, NE Atlantic Ocean (bathymetry from EMOD data base), showing the location of CTD stations 7 to 16 and mooring and lander deployments in the easternmost canyon branch, as well as locations where mono cores were collected (marked with x).

The hydrodynamic regime within the Whittard Canyon is characterised by semi-diurnal tidal currents, dominated by the principal lunar semi-diurnal (M2) component (Pingree, 1980; Holt and Thorpe, 1997; Hall et al., 2017). The complex sloping topography together with the across-slope tidal flow results in the generation and reflection of internal waves and tides at the shelf edge and the upper reaches of the canyon (Hall et al., 2017). These enhanced hydrodynamics cause elevated mixing near the seafloor, resuspending sediment and organic matter and facilitating along-canyon transport by means of intermediate nepheloid layers which are formed as lateral extensions of the bottom nepheloid layers (Wilson et al., 2015b). In addition, gravity flows initiated by trawling at the interfluves in between different branches of the canyon result in sediment laden near-bottom plumes with high concentrations of organic material (Daly et al., 2018), a phenomenon observed previously in the Palamós Canyon in the Western Mediterranean (Puig et al., 2012).

2.3. Material and methods

Sensors discussed in this study were deployed in May 2017 and May 2018 during RV *Pelagia* cruises 64PE421 and 64PE437, in three different configurations (for details see Table S2.1):

1) Two optical backscatter sensors (WetLabs ECO FLNTU and JFE Advantech Infinity, operating at 700 and 880 nm respectively), next to the standard WetLabs C-Star transmissometer, operating at 650 nm, were mounted on a profiling SeaBird 911 CTD-Rosette system. The CTD-Rosette, which among various other sensors also held a fluorometer, was hauled through the water column, allowing comparison of sensor output in productive surface waters with high fluorescence, in clear mid-waters and in a bottom nepheloid layer loaded with fine particulate matter as shown by particle size analysis (see Section 2.5.1).

2) A bottom lander was deployed for two days in the canyon axis at 1915 m water depth, equipped with two optical backscatter sensors (WetLabs ECO FLNTU and JFE Advantech Infinity) and a high-frequency (1 MHz) sideways-looking Nortek Aquadopp ADCP at 1 m above bottom (mab) (with 1 m blanking distance). Sampling frequency was set to five minutes (with data recorded at 1 Hz and averaged over 60 measurements) for all sensors, allowing for comparison of sensor output under highly variable bottom water turbidity produced in a regime of oscillating tidal currents.

3) A 430 m long oceanographic mooring was deployed for nine days in the canyon axis at 1400 m water depth, equipped with a JFE Advantech Infinity OBS at 5 mab, a downward-looking low-frequency (75 kHz) RDI Workhorse Long Ranger ADCP at 410 mab (with a blanking distance of 23.28 m and vertical intervals binned over 5 m), and a string of 200 high-precision thermistors (van Haren et al., 2009). Data from the thermistor string will be published elsewhere, except for a time-series record of vertical isotherm fluctuations. Sampling frequency was set to one minute for the turbidity sensors (with data recorded at 9 pings per ensemble (6 s per ping) for the ADCP and one measurement per minute for the JFE Advantech OBS), allowing for a comparison as under 2, but with a different acoustic frequency. In this study only the data from the lowermost bin which is not affected by interference with the seafloor is shown. The validity of this data was tested by calculating the signal-to-noise ratio (SNR) based on the equation given in the Teledyne RDI application note (Mullison, 2017), which resulted in an average SNR of 39, with less than 6% of the data having a SNR < 10. The data for this bin is located 45 m above the seafloor and therefore 40 m above the JFE OBS.

Backscatter and transmission data produced by the optical sensors mounted on the CTD Rosette were correlated to SPM mass concentration (mg L^{-1}). In parallel with the optical measurements, SPM was collected by filtering duplicate 5 L portions of Niskin water samples over 47 mm 0.4 µm pre-weighed Millipore polycarbonate filters (Table S2.2). The filters were rinsed with Milli-Q to remove salt and stored at -20 °C until further analysis. In the laboratory at NIOZ, the filters were freeze-dried, rinsed once more with Milli-Q to remove any remaining salt, freeze-dried again and then weighed to determine the amount of SPM per volume of filtered seawater. The nature of the collected SPM was investigated by examining a selection of 12 representative filter samples with a Hitachi TM3000 scanning electron microscope (SEM).

The SPM particle size distribution in surface, intermediate and bottom nepheloid layers as well as in clear water was determined from Niskin water samples collected from various depths in the canyons (Table S2.2). The samples were left standing in the dark for over a month at 5 °C in order to make sure all SPM settled, following Stokes' Law for particles with a radius of 1 µm

or larger. The overlying water was carefully siphoned off and the remaining water with SPM was divided equally over two 40 mL bottles. After adding 5 mL 0.1 M Na-pyrophosphate to prevent flocculation of the material, the subsamples were analysed in duplicate with a Beckman Coulter LS 13320 laser particle sizer, using the micro cell measuring mode, with a minimum of three runs for each sample.

Similarly, the particle size distribution of surface sediments (0-0.5 cm) was determined for seven locations along the canyon axis (Fig. 2.1, Table S2.3). Sediment samples were collected using a NIOZ designed mono corer which was suspended 7 m below the CTD-Rosette frame. Collected mono cores were sliced on board in 0.5 cm slices and were subsequently stored at a temperature of -20 °C. Prior to analysis, samples were freeze dried for 3 days to ensure adequate removal of water. For analysis of particle size distribution, a subsample was taken and was suspended in reverse osmosis demineralised water. After adding 10 mL Na-pyrophosphate to prevent flocculation of the material, the subsamples were analysed with a Beckman Coulter LS 13320 laser particle sizer, using the large volume cell, with a minimum of three runs for each sample.

2.4. Theory

Although sensor-specific differences in response to different types of SPM generally hinder a straightforward conversion of measured turbidity to SPM mass concentration, optical and acoustic sensors have in common that they have a physically well-understood relationship between sensor response and concentration and size of the detected particles, within certain limits and for ideal spherical particles.

Optical backscatter sensors such as used and discussed in this paper basically measure relative changes in concentration of particles in a suspension based on changes in intensity of backscattered light. Transmissometers work the opposite and measure relative changes in concentration of particles on the basis of changes in intensity of transmitted light. Within the specified operational range of the sensor, the backscattered or transmitted light intensity is linearly related to the concentration of suspended particles, provided that the physical parameters of the particles remain constant (Baker and Lavelle, 1984; Downing, 2006; Hill et al., 2011). At higher concentrations, beyond the limit where the sensors get saturated, the

increase in backscattered light or decrease in transmitted light with increasing particle concentration flattens off until there is no change in response with increase in particle concentration. With further increase in concentration, backscatter will eventually start to decrease due to the so-called grain shielding effect (Bunt et al., 1999), causing multiple scattering and interference of the backscattered signal (Kineke and Sternberg, 1992; Downing, 2006).

The response of both types of optical sensors is dependent on the particle size distribution of the SPM, complicating the quantification of the detected signal. The response of the OBS is inversely proportional to the size of the particles, as it has been shown that the OBS response is lower for suspensions with coarser particles, than for suspensions of similar mass concentrations with finer grained material (e.g. Gibbs and Wolanski, 1992; Bunt et al., 1999; Hatcher et al., 2001; Downing, 2006). This is explained by the decreased area-to-volume ratio of larger particles and thereby a smaller projected area (Hatcher et al., 2001). The same applies to the transmissometer, of which the response is dependent on the absorption and scattering of particles (c_p) and absorption by water (c_w) (Jerlov, 1976), with c_p being dependent on the total particle cross-sectional area (van de Hulst, 1957). Again, for similar mass concentration of particles, sensor response is stronger for smaller particles than for larger ones.

Acoustic devices such as the ADCPs discussed in this paper, measure relative changes in concentration of particles in a suspension based on changes in intensity of the backscattered acoustic signal, analogous to the principle of optical backscatter. For acoustic devices, however, the sensor response is not linearly related to SPM mass concentration (e.g. Fugate and Friedrichs, 2002). Commonly, the acoustic backscatter is expressed in counts, which is proportional to decibel sound pressure level (*SPL*). In the study of Merckelbach and Ridderinkhof (2005) the following equation (Eq. 1) is given for *SPL*, based on the random phase backscatter model presented by Thorne and Hanes (2002):

$$SPL\ [dB] = 10log_{10}\left(K_R \frac{k^4\langle a_s^6\rangle}{\rho_s\langle a_s^3\rangle} SPM \frac{e^{-4r\alpha}}{r^2}\right) \quad \text{(Eq. 2.1)}$$

In which K_R is the device dependent calibration coefficient, k is the acoustic wave number, a_s is the particle diameter, ρ_s the density of the scattering particles, *SPM* the SPM mass concentration, r the distance from transducer to bin and α the coefficient of attenuation. The acoustic wave number k is defined as:

$$k = \frac{2\pi f}{c} \quad \text{(Eq. 2.2)}$$

In which f is the frequency of the acoustic wave and c the speed of sound. From Eq. 2.1 it follows, with physical characteristics of the particles and water remaining constant, that the *SPL* at any distance within the measuring range is logarithmically proportional to the SPM mass concentration ($SPL \propto 10log_{10}(SPM)$).

The acoustic backscatter response of ADCPs to differently sized particles is dependent on the operating frequency of the ADCP (Wilson and Hay, 2015). This is expressed in different particle size sensitivities for different acoustic frequencies. Peak sensitivity occurs at $k * a = 1$, in which k is the acoustic wave number as defined by Eq. 2.2 and a is the particle radius, and the detection limit is at $k * a = 0.05$, as long as there is no significant concentration of particles with $k * a \approx 1$ (Lohrmann, 2001). Given the mean speed of sound (c) in seawater of 1525 m s^{-1}, a 75 kHz ADCP such as used in the mooring in this study has a peak sensitivity for particles with a diameter of 6475 µm and a lower detection limit for particles with diameter of 323 µm. For the 1 MHz ADCP, such as mounted on the bottom lander, peak sensitivity and lower detection limits are for particle diameters of, respectively, 485 µm and 24 µm. From the above it follows that the 1 MHz ADCP has its peak sensitivity at a particle size for which the 75 kHz ADCP is close to its lower detection limit.

2.5. Results and Discussion

2.5.1. Optical backscatter and light transmission in surface, intermediate and bottom nepheloid layers

A CTD transect along the axis of the easternmost Whittard Canyon branch, covering a depth range of 185 to 3644 m water depth (Fig. 2.1), showed the ubiquitous presence of intermediate and near-bottom nepheloid layers at canyon depths between 900 and 2800 m

water depth, with highest turbidity signals found between 1250 and 1750 m water depth (Fig. 2.2). All three sensors mounted on the CTD, the WetLabs FLNTU and JFE Advantech OBSs and the WetLabs C-Star transmissometer, showed relatively low turbidity at intermediate water depths and increasing values towards the bottom nepheloid layer. The presence of nepheloid layers in the Whittard Canyon is a permanent feature, as it was also observed during previous surveys by Wilson et al. (2015b). In comparison with the two types of OBSs that recorded only modestly elevated turbidity at the surface, the transmissometer also measured distinctly higher turbidity in the surface layer (Fig. 2.2).

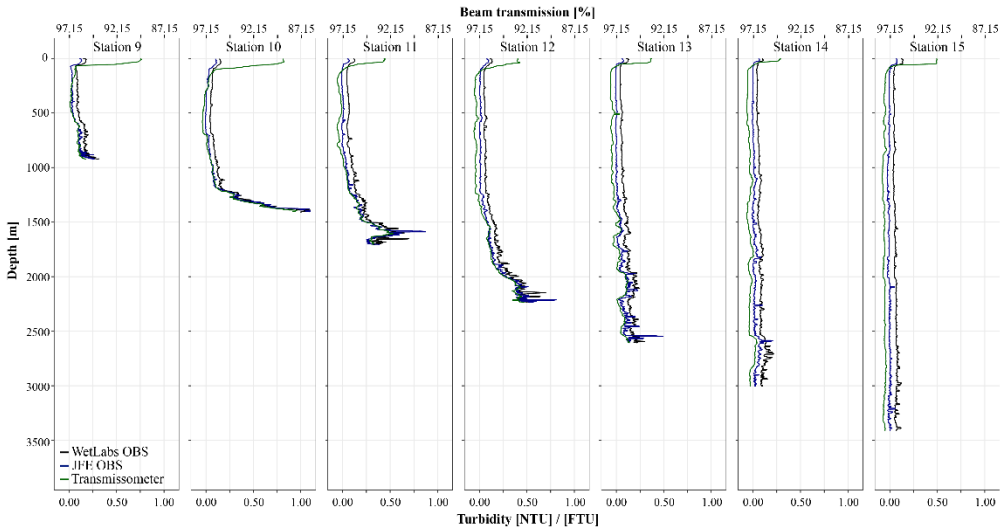

Figure 2.2: CTD profiles showing the turbidity measured by the WetLabs FLNTU OBS (black), JFE Advantech OBS (blue) and WetLabs C-Star transmissometer (green) of station 9 to 15, recorded down to 7 mab.

The deviating sensor response in the surface layer of the transmissometer compared to the OBSs is clearly demonstrated in Fig. 2.3A, where the sensor response of the WetLabs transmissometer is plotted against the response of the WetLabs OBS of all CTD casts. Based on this result and the fact that SPM likely has different characteristics over the water column, two regression lines were calculated for the relationships between sensor output of the WetLabs OBS and WetLabs Transmissometer and the weighed SPM mass concentrations (mg L^{-1}), one for surface samples (<100 m) and one for samples in the lower part of the water column, as shown in Fig. 2.3B and C respectively. The relationships between the JFE Advantech OBS and the response of the transmissometer and the weighed SPM mass concentration are

not shown because of their similarity to the WetLabs OBS. Linear relationships appeared to be an appropriate model for the data with R^2's ranging from 0.70 to 0.95. The relationship between the output of the OBSs does not change significantly when surface and deeper water data are considered separately (ANCOVA, $P = 0.1923$). However, the regression lines clearly illustrate the diverging output of the transmissometer in the surface water (ANCOVA, $P < 0.001$). The slopes of regression lines belonging to the shallow and deep waters are almost the same for the OBS, while they are different in the case of the transmissometer.

The different response of especially the transmissometer to SPM in the surface water and deeper water, as compared to the response of the OBSs, can be explained by the greater sensitivity of the transmissometer to differences in physical properties of the SPM in the surface water and near-bottom water. In the biologically productive surface water, particulate matter detected by the sensors is likely largely composed of living phytoplankton and small zooplankton, as shown by increased fluorescence values in the upper 100 m recorded by the CTD. SPM in bottom nepheloid layer is mostly composed of detritic mineral material and biogenic carbonate and silica. SEM analysis revealed that particulate matter filtered from surface water typically consisted of intact pelagic diatoms, coccolithophores, silicoflagellates and amorphous blots, likely representing organic aggregates. The near-bottom samples were characterised by a mixture of biogenic carbonate, silica and lithogenic material. The stronger response of the transmissometer in the organic-rich surface water may therefore be attributed to a stronger absorption of the emitted light with a wavelength of 650 nm by chlorophyll-bearing phytoplankton (Schoellhamer, 1993; Bunt et al., 1999), compared to the 700 and 880 nm light emitted by the OBSs. This is confirmed by the study of Bricaud et al. (1998), who showed that the absorption coefficient for chlorophyll-bearing material generally increases with decreasing wavelengths.

Although the difference in slopes of the regression lines of the OBS belonging to the shallow and deep water was not significant, the lower response of the OBSs in the surface water could be attributed to the larger average particles sizes (e.g. Gibbs and Wolanski, 1992; Bunt et al., 1999; Hatcher et al., 2001; Downing, 2006), since the particle size of the SPM varied between distinct depths in the water column (Fig. 2.4).

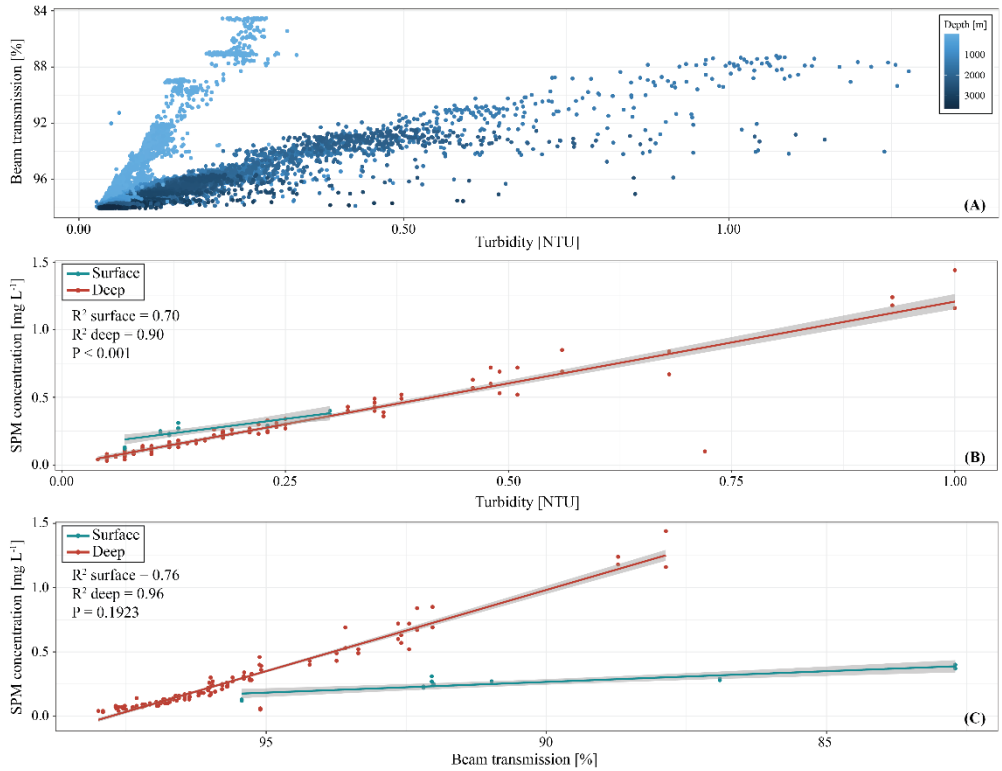

Figure 2.3: A) Relation between sensor responses of the WetLabs FLNTU OBS and the WetLabs C-Star transmissometer of CTD stations 7 to 16, colour-coded by depth. B & C) Relation between the recorded turbidity and weighed SPM mass concentrations of the WetLabs FLNTU OBS and WetLabs C-Star transmissometer respectively, with a 95% confidence interval. Blue lines indicate surface samples collected from the upper 100 m of the water column, red lines indicate samples taken at depths greater than 100 m. Statistical analysis was performed in R (R Core Team, 2020) and P-values are based on an Analysis of Covariance (ANCOVA) test.

The SPM in the surface water had the largest particle size (median of 43 µm), followed by material in the bottom nepheloid layer (median of 34 µm). The SPM found in the clear midwater had the smallest particle size (median of 18 µm). It should be mentioned that these are the particle size distributions for single particles, as aggregates were broken up during sample preparation for particle size analysis. Therefore, to properly quantify the response of optical turbidity sensors, these differences should be accounted for. If only one uniform regression line is calculated in the case of the transmissometer, SPM mass concentration in the surface layer would be overestimated and SPM mass concentration in the lower part of the water column would be underestimated.

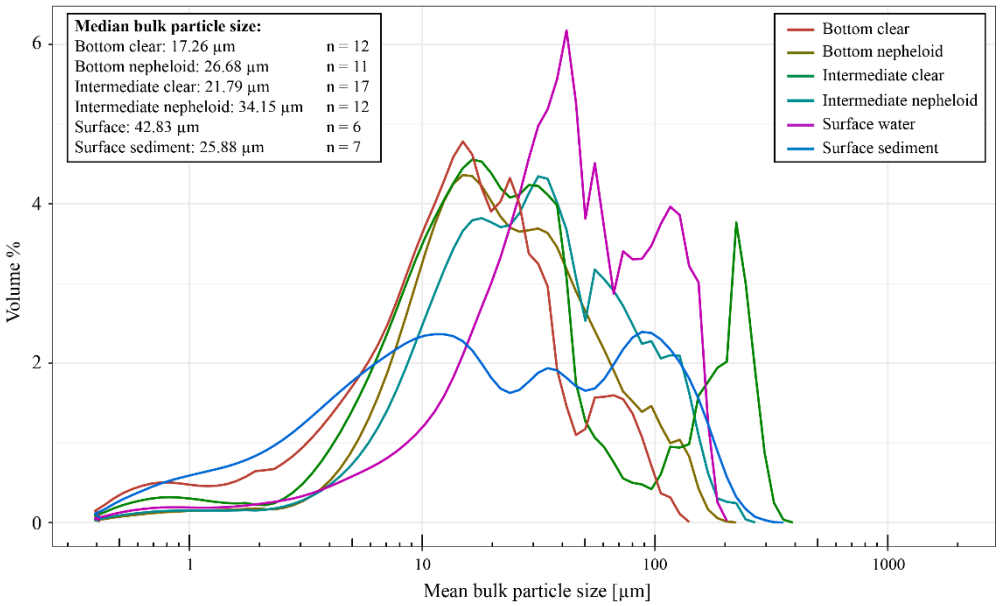

Figure 2.4: Average particle size distribution of suspended particulate matter. "Bottom" samples are taken within 10 m from the seafloor, "Surface" samples represent samples collected from the upper 100 m of the water column and "Intermediate" samples are collected between the surface water and the bottom (nepheloid) layer. "Nepheloid" samples are collected from water with a turbidity distinctively higher (>0.1 FTU) than the background turbidity (<0.1 FTU), which is represented here as "Clear". "Surface sediment" samples refer to the 0–0.5 cm slice of the collected mono cores.

2.5.2. Dynamics of SPM in the bottom boundary layer observed with OBSs and 1 MHz ADCP acoustic backscatter

Lander and mooring deployments, primarily intended for investigating the relationship between current dynamics and suspended sediment transport in the canyon axis, offered an opportunity for comparison of temporal variations in turbidity records obtained by both optical and acoustic sensors. During the two-day deployment of a bottom lander at 1915 m water depth, optical backscatter recorded by the WetLabs and JFE Advantech OBSs and acoustic backscatter recorded by the 1 MHz Nortek ADCP were compared. The near-bottom current regime presented in Figure 2.5 shows a distinct semi-diurnal variation in current speed and direction, with a main flow direction alternating between 15° (up-canyon) and 130° (down-canyon) (Fig. 2.5A), and current speeds ranging from 2 to 20 cm s^{-1}. The OBSs and the 1 MHz ADCP show remarkably comparable patterns in optical and acoustic backscatter (Fig. 2.5C-E), which is especially evident when the time series are normalised and superimposed

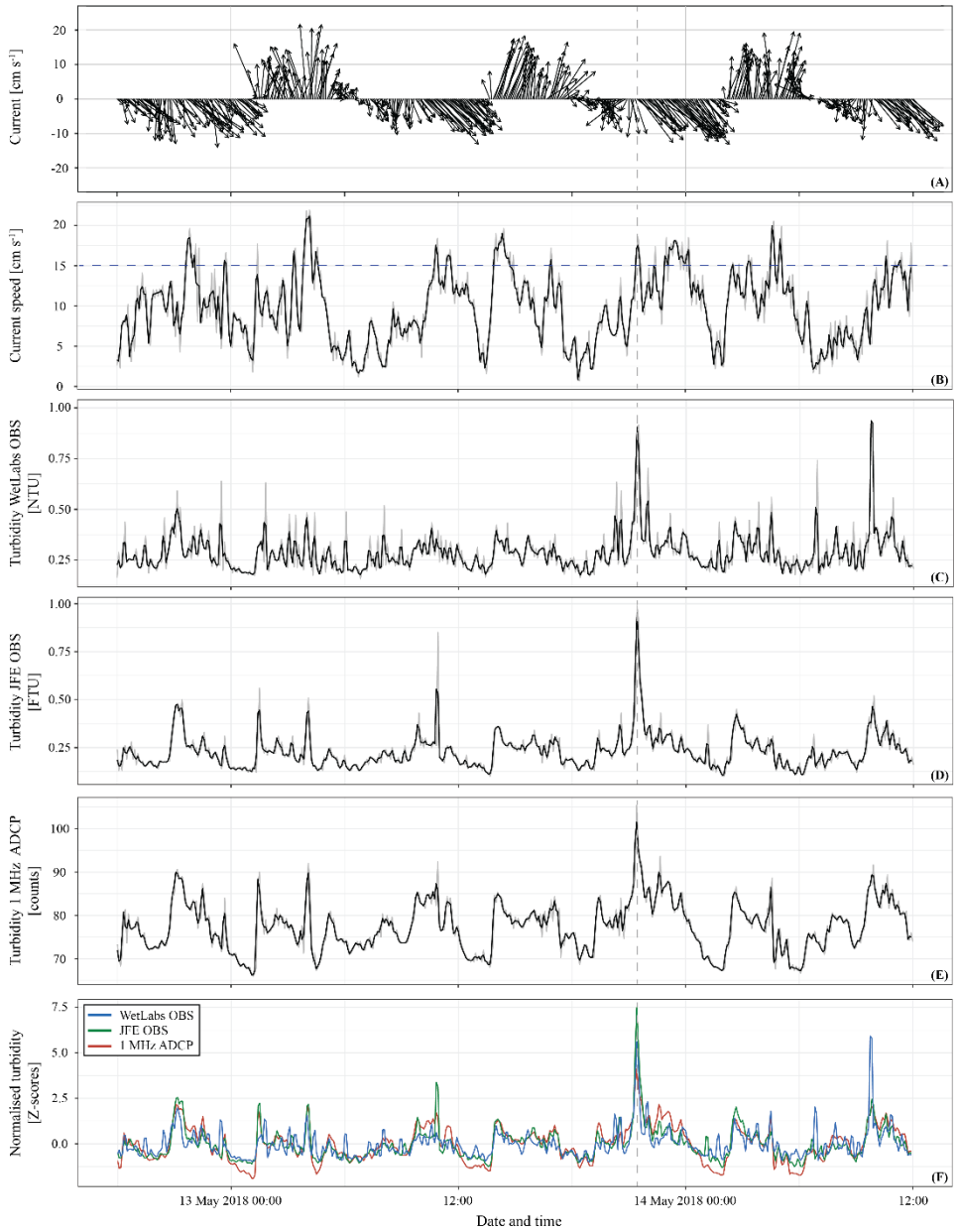

Figure 2.5: Near-bottom (1 mab) time series from the lander deployment at 1915 m water depth showing A) current vectors, B) current speed, with blue dashed line indicating the 15 cm s^{-1} threshold for which resuspension of bottom sediment is expected (Thomsen and Gust, 2000), C) turbidity recorded by the WetLabs OBS, D) turbidity recorded by the JFE Advantech OBS, E) turbidity recorded by the 1 MHz Nortek ADCP and F) normalised (Z-scores) turbidity records of the WetLabs and JFE Advantech OBSs and the Nortek 1 MHz ADCP. Normalisation is needed to allow comparing the different turbidity records by converting them to Z-scores, $Z = \frac{x-\bar{x}}{\sigma}$ in which x is the data point, x is the average over the complete record and σ the standard deviation. Vertical dashed line marks the interval where the conspicuous turbidity peak is noted in all sensors.

(Fig. 2.5F). The good agreement between the optical and 1 MHz acoustic backscatter is also clearly shown in Fig. 2.6A. It demonstrates a logarithmic relationship between the sensor outputs (R^2 = 0.83), showing that the suspended particles present in the bottom water of the canyon fell within the sensitivity range of both the OBS and the 1 MHz ADCP. Particle size analysis of near-bottom water samples along the canyon axis revealed that the median particle size is fining with increasing distance from the canyon head (Fig. S2.1). In general, the majority of the particles found in the bottom nepheloid layer varied from 8 to 60 µm (D_{10} and D_{90}, respectively) in size (Fig. 2.4), and at the depth where the lander was deployed a median particle size of 20 µm was determined (Fig. S2.1). This implies that about half of the suspended particle volume falls below the minimum particle size detection limit (24 µm) of the 1 MHz ADCP. However, it is likely that fine-grained SPM, which in the lab is measured in a fully dispersed suspension, sticks together under natural conditions forming larger-sized organic-mineral aggregates. In such an aggregated form, a larger part of the SPM will fall in the detection range of the 1 MHz ADCP.

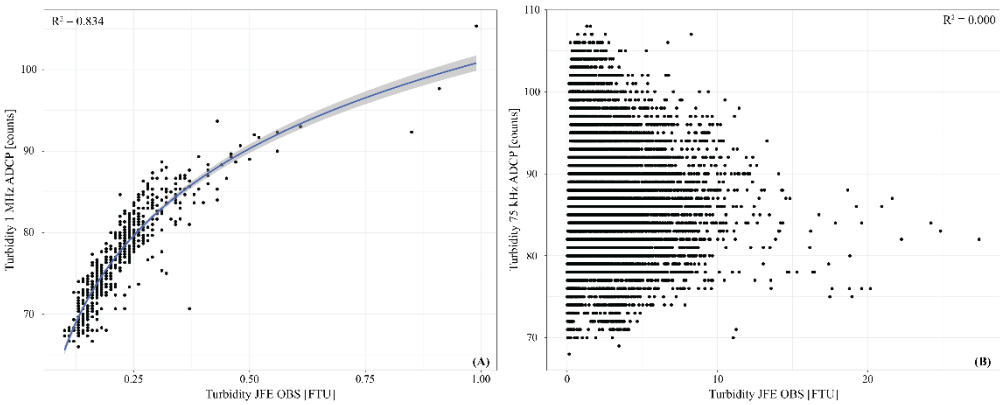

Figure 2.6: Relation between recorded turbidity by the JFE Advantech OBS (x-axis) and the ADCPs (y-axis). A) Relation between JFE OBS and the Nortek 1 MHz ADCP; B) Relation between JFE OBS and the RDI Workhorse 75 kHz ADCP.

The records of both optical and acoustic backscatter from the lander deployment generally show higher values during intervals of higher current speed (Fig. 2.5F). Minimum values occur systematically with the waning of the down-canyon currents and are followed by an abrupt increase in backscatter as the (tidal) flow reverses from down-canyon to up-canyon direction. This associates with the upslope moving tidal bores that have been observed to resuspend matter on more open bottom slopes (Hosegood et al., 2004).

Short-lived peaks in both optical and acoustic backscatter occur mostly, but not exclusively, during intervals of down-canyon flow when current speeds exceed 15 cm s^{-1}. A particularly conspicuous increase in turbidity, recorded by all three sensors, occurred on 13 May between 21:19 and 21:37 h, indicated by the grey dashed lines in Fig. 2.5. Within this 18-min interval, optical backscatter increased by a factor 2-3, and then decreased again to amounts as measured before. The increase in turbidity coincided with a distinct peak in current speed during an interval of variable current direction, suggesting that the peak in turbidity represents resuspension of sediment from the seabed by local turbulence. During the event the current speed recorded was above 15 cm s^{-1} which is the threshold for sediment resuspension for deep-sea sediment on the Western European margin given by Thomsen and Gust (2000). At this site, sediment on the canyon floor was found to have a similar median particle size as the SPM in the near-bottom water (Fig. S2.1). The drop in turbidity at the end of the event seems to occur too fast to be simply explained by settling, given the prevalence of fine-grained SPM at this depth in the canyon. If sediment was only locally stirred up, it is conceivable that the turbid plume was quickly swept off by the down-canyon flow. Alternatively, as discussed in more detail in the next section, the sharp peaks in optical backscatter might reflect break-up of larger aggregates into dispersed smaller particles due to increased shear stresses, followed by re-aggregation, as described by Thomsen and Van Weering (1998).

2.5.3. Bottom boundary layer SPM dynamics observed with OBS and 75 kHz ADCP acoustic backscatter

During the nine-day deployment of the mooring at 1400 m water depth, of which a two-day near-bottom excerpt is presented in Fig. 2.7, a similar semi-diurnal tidal variation in current speed was recorded, with the local main flow direction alternating between 335° (up-canyon) and 155° (down-canyon) (Fig. 2.7A). Current speed was distinctly higher than at 1915 m where the lander was deployed and ranged from 0 to 40 cm s^{-1}, with peak current speeds up to 70 cm s^{-1}.

It should be noted that the current speeds reported here were recorded at 45 mab, which was the depth of the lowermost bin containing valid data, whereas the lander was recording at 1 mab. At this greater height above the seafloor current speeds are likely higher due to a smaller influence of friction with the seafloor. Similar to what was observed during the lander

deployment, intervals with higher turbidity in both optical and acoustic backscatter records appear to correspond with intervals of increased current speed (Fig. 2.7B-D).

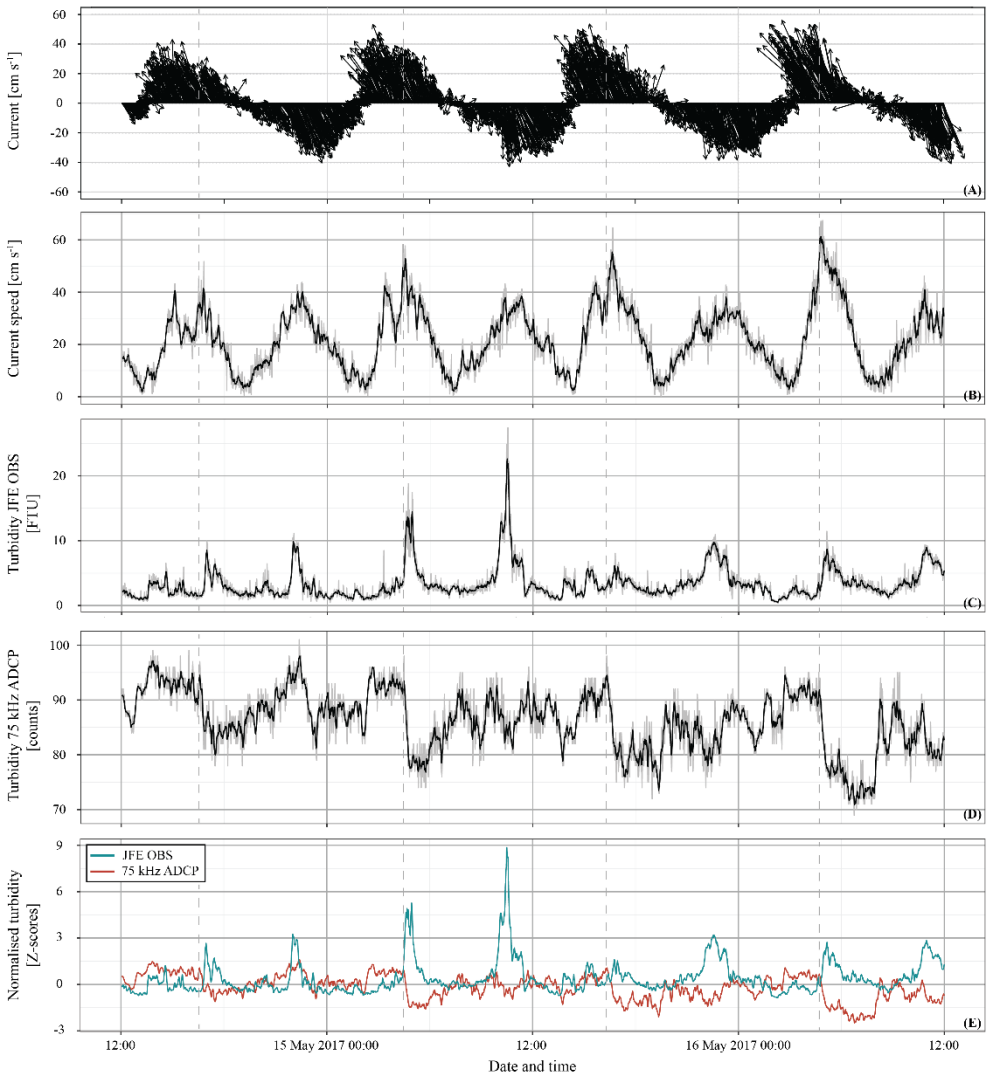

Figure 2.7: Two-day part of a near-bottom (45 mab for 75 kHz ADCP and 5 mab for JFE OBS) time series from the mooring deployment at 1400 m water depth showing A) current vectors, B) current speed, C) turbidity recorded by the JFE Advantech OBS, D) turbidity recorded by the RDI Workhorse 75 kHz ADCP and E) normalised (Z-scores) turbidity records of the JFE Advantech OBS and the RDI Workhorse 75 kHz ADCP. Dashed grid lines indicate the time at which the ADCP signal dropped during up-canyon flow.

However, the records of optical backscatter, produced by the JFE Advantech OBS and acoustic backscatter from the RDI Workhorse 75 kHz ADCP do not even remotely match, but display

distinctly different patterns (Fig. 2.7C-E). This could be due to the fact that the OBS and ADCP data were recorded at different heights of, 5 and 45 m above the seabed, respectively. However, the well-developed and more than 100 m thick bottom nepheloid layer observed at this site (Fig. 2.2, station 10) indicated intense turbulent mixing of the bottom water, allowing comparison, with due caution, of the sensor records. The optical backscatter seemed to respond closely to tidally dominated variations in up-and down-canyon current speed with peaks in backscatter, some representing a five-fold increase in turbidity, coinciding with maxima in current speed. The acoustic backscatter recorded by the 75 kHz ADCP on the other hand displays a broad, irregular saw tooth pattern, repeating itself every cycle of down- to up-canyon flow. Minimum backscatter systematically occurred during the intervals of low current speed when the bottom water flow is turning from up- to down-canyon. From there, acoustic backscatter gradually increased during the interval of down-canyon flow and continued to increase during the subsequent interval of up-canyon flow, to reach a maximum shortly before the up-canyon current was at its maximum strength. When the up-canyon current started to wane, the acoustic backscatter signal steeply dropped to minimum values. Interestingly, and most obvious when the optical and acoustic backscatter records are superimposed (Fig. 2.7F), the peaks in optical backscatter often did not coincide but rather followed just after peaks in acoustic backscatter, where the latter was already plunging down.

The mismatch between optical and acoustic backscatter, which is also illustrated in Fig. 2.6B, is comprehended when taking into account that the optical and acoustic sensors have very different sensitivities regarding particle size. Where the optical backscatter sensor is most sensitive for small particles, the 75 kHz ADCP in contrast has its peak sensitivity for relatively large, millimetre-sized particles, whilst it fails to detect particles smaller than a few hundred micrometre. As shown in Fig. S2.1, the median particle size of SPM collected from the bottom nepheloid layer at the depth where the mooring was deployed, as well as of the surface sediment collected at that depth from the canyon thalweg, was about 30 µm, well below the lower detection limit of 323 µm given for the 75 kHz ADCP. The larger particles apparent in the acoustic backscatter signal of the ADCP are certainly not massive mm-sized sediment particles (i.e. fine gravel), as such gravel is scarcely present at this depth in the canyon (Fig. 2.4) and would require far higher current speeds than measured at this site to be resuspended (Thomsen and Gust, 2000; Duineveld et al., 2001).

One possible explanation for the presence of larger particles that produced the backscatter response in the 75 kHz ADCP is that they represent zooplankton or nekton in the mm- or larger size range. Indeed, commercial and scientific devices for detection of fish and zooplankton typically operate in the 50-200 kHz frequency range overlapping with the frequency of our low-frequency ADCP, and there is ample literature on zooplankton/nekton migration based on backscatter data from ship-based or moored low-frequency ADCPs (e.g. Flagg and Smith, 1989; Plueddemann and Pinkel, 1989; Foote, 2001; van Haren, 2007; De Leo et al., 2018; Yang et al., 2019). Moreover, the conspicuous parabolic patterns seen in the time series profile of echo amplitude (Fig. 2.8), representing the regular vertical oscillation of zones of enhanced backscatter of the ADCP, are reminiscent of acoustic backscatter patterns associated with diel zooplankton migration described by e.g. van Haren and Compton (2013). However, whilst published cases of zooplankton migration typically refer to active diel migration in the upper few tens to hundreds of meters of the water column in response to the day-night cycle, the acoustic backscatter patterns observed in the Whittard Canyon (Fig. 2.8) are closely following vertical water mass motions marked by the oscillating pattern of isotherms recorded with the thermistor string. These vertical water mass motions, with apparent semi-diurnal frequency and with amplitude of over 200 m at the start of the recorded interval but diminishing towards the end of it, are likely associated with upslope moving internal tidal waves as described by Hosegood et al. (2004) and Hall et al. (2017). The zooplankton/nekton in the aphotic zone (1000-1400 m) of the Whittard Canyon, if indeed that is what was producing the observed backscatter patterns, therefore seems not to be actively migrating but passively following the internal tidal motions, as was also inferred in studies by Ibáñez-Tejero et al. (2018) and Burd and Thomson (2019). Unfortunately, in our present dataset from the Whittard Canyon we have no direct observational evidence, from either an underwater camera or plankton net hauls, to verify the nature of the particles producing the low-frequency acoustic backscatter signal. In a number of studies where the relation between recorded ADCP backscatter and in situ measured zooplankton biomass was verified with plankton net hauls (e.g. Ibáñez-Tejero et al., 2018; Fielding et al., 2004; Briseño-Avena et al., 2018) it was found that zooplankton biomass generally explained only 50% or less of the variability in acoustic backscatter. Based on the physical principles of acoustic backscatter, this might be explained by temporal variation in size distribution of the zooplankton/nekton. However, it should also be considered that at least part of the backscattering particles may be non-living, large aggregates settling

out as marine snow through the water column or resuspended from the seabed, possibly in combination with acoustic backscatter of turbulence deformed density stratification.

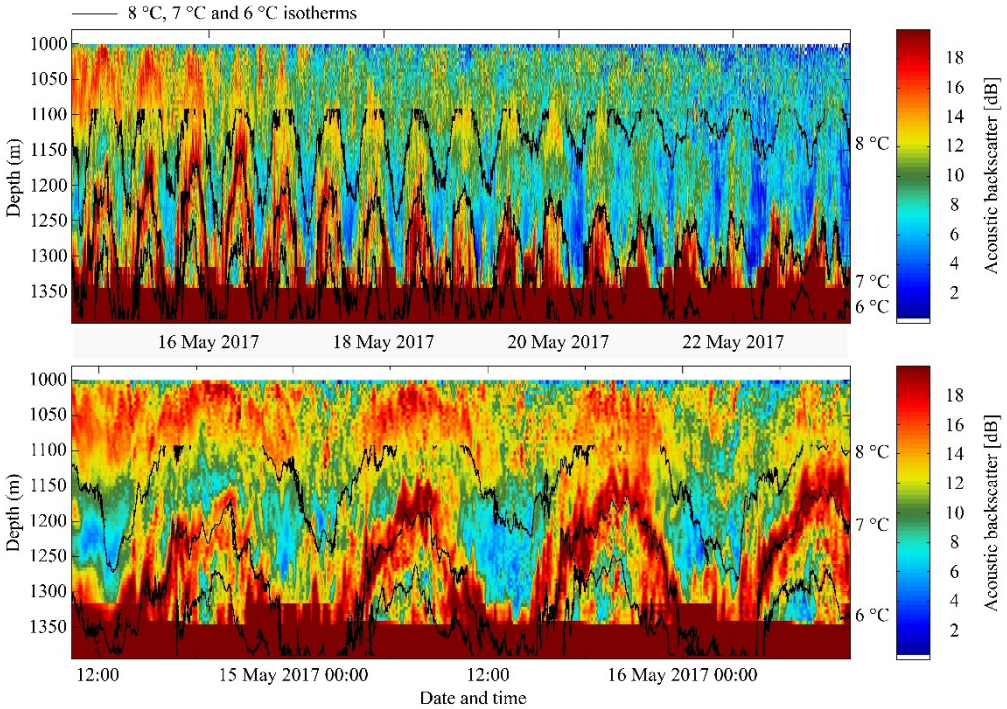

Figure 2.0-8: Time series profile of acoustic backscatter as recorded by the low-frequency (75 kHz) ADCP mounted on the mooring. Echo amplitude counts have been recalculated to dB using the formulas given by Gostiaux and van Haren (2010). Lower end of the profile represents the seafloor. ADCP data shown in Figs. 2.7 and 2.9 is recorded at 1350 m (45 mab). The JFE OBS was recording at 5 mab. The black contours represent, from top to bottom, the 8 °C, 7 °C and 6 °C isotherms as inferred from data recorded by the thermistors. Upper figure shows the entire nine-day time series. Lower figure represents the first two days of the time series.

The importance of particle aggregation and disaggregation processes in fine-grained cohesive sediment dynamics is well-established in the literature (e.g. McAnally and Mehta, 2002), and has been demonstrated both in laboratory studies (e.g. Verney et al., 2011) and in the field (e.g. Markussen and Andersen, 2014). Whilst individual particles in fine-grained cohesive sediment typically are in the size range of a few micrometres, with very slow settling velocities in the order of 0.01 mm s^{-1}, aggregation of these particles may produce large aggregates of up to centimetres in size, with settling velocities orders of magnitude higher than of the individual particles of which the aggregates are made up (e.g. van Leussen, 1988; Manning and Dyer, 1999). In the context of the present study, the relevance of the aggregation process is that

particle suspensions made up of dispersed individual particles may only be detectable with optical sensors and high-frequency acoustic sensors, whereas in aggregated state they may also come in the detection range for low-frequency acoustic sensors. According to theory, particle concentration and turbulence are important factors in determining aggregation rate and the size to which aggregates may grow. Sufficient particle concentration and moderate turbulence are required to promote particle-particle encounters that lead to aggregation. However, under increasing turbulent shear, fragmentation of aggregates becomes prevalent over formation, leading to a decrease in aggregate size.

In resuspension experiments with natural deep-sea sediments, Thomsen and Gust (2000) and Thomsen et al. (2002) demonstrated that with increasing current speed, organic-mineral aggregates, forming a fluffy layer on top of more cohesive sediment, were the first to be resuspended when a critical shear velocity was surpassed. When the current speed was further increased, shear forces at some point led to the break-up of the relatively large organic-mineral aggregates into smaller aggregates and more finely dispersed particles. When current speed was reduced again, the dispersed particles were observed to re-aggregate into larger and relatively fast-sinking flocs (Thomsen and van Weering, 1998). In the Whittard Canyon, and in submarine canyons in general, conditions are favourable for dynamic aggregation processes. Especially in the upper canyon reaches, suspended particle concentrations are relatively high due to the focusing effect of the canyon topography, and due to frequent resuspension of fine-grained material by topographically enhanced tidal currents. These tidal currents are also responsible for a regime of fluctuating turbulent shear, not only at the seafloor but especially also internally, inducing aggregation at low shear and aggregate break-up at high shear. Unpublished underwater time-lapse video imagery collected in spring 2007 at 2076 m water depth in an adjacent branch of the Whittard Canyon confirms the often aggregated nature of particulate matter in the bottom nepheloid layer. On that occasion, but also for the observations of the present study, which were made in approximately the same time of the year, fallout of phytodetritus following the spring bloom may have contributed to stickiness of particulate matter at the bottom of the canyon, favouring aggregation. Applied to the observations in this study, and as an alternative or complementary to the hypothesis of zooplankton/nekton migrations, the variable acoustic backscatter signal recorded by the 75 kHz ADCP could be interpreted in terms of dynamic

aggregation and disaggregation of non-living suspended particulate matter. In this interpretation, the build-up of acoustic backscatter observed during each cycle of down- and up-canyon flow could reflect increasing amounts of large aggregates that were picked up by the current from the canyon floor and entrained in the bottom water flow. The sharp drops in acoustic backscatter that seemed to coincide or even precede the moment that down-and up-canyon current speed reached its maximum could then reflect the fragmentation of larger aggregates. The recurrent peaks in optical backscatter at maximum down- and up-canyon current speed could reflect the moment when more cohesive sediment underlying the fluffy surface layer was also resuspended. However, the fact that optical backscatter on several occasions seemed to peak immediately after acoustic backscatter and already started to decline, may suggest a more direct, causal link between the two signals. In this interpretation, the break-up of larger aggregates at maximum current speed, reflected by a drop in acoustic backscatter, would produce bursts of dispersed finer-grained particles, observed as a sharp increase in optical backscatter. The subsequent steep decrease in optical backscatter and continuing decrease in acoustic backscatter potentially indicates re-aggregation of particles and settling at the waning of the tidal current. Following this hypothesis, the observed vertical pattern in acoustic backscatter (Fig. 2.8) can be explained by resuspension of aggregated particulate matter by internal tidal waves. The upslope moving tidal bores are the driving mechanism behind the resuspension of material (Hosegood et al., 2004), which is then vertically displaced by the internal waves and settles down when the currents start to wane.

After the first two-day time interval on which the discussion above was focused (Fig. 2.7), a marked decrease in overall current speed was noted, and in the last two days peaks in current velocity reached only 20 cm s^{-1} or less (Fig. 2.9A). This trend of decreasing current speed, also reflected in the 12.5 h average of the current speed, is likely associated with the spring-neap tidal cycle (Hall et al., 2017). Turbidity recorded by the OBS followed the trend of decreasing current speed and especially in the last two days showed a marked decrease (Fig. 2.9B). This pattern is consistent with the observation that optical backscatter peaked during intervals of increased current speed, reflecting enhanced concentrations of fine-grained SPM, resulting from sediment resuspension and break-up of larger aggregates. Acoustic backscatter recorded by the 75 kHz ADCP displayed an opposite trend to optical backscatter with decreasing current speed, showing an irregular, but consistent, increase towards the end of the nine-day record

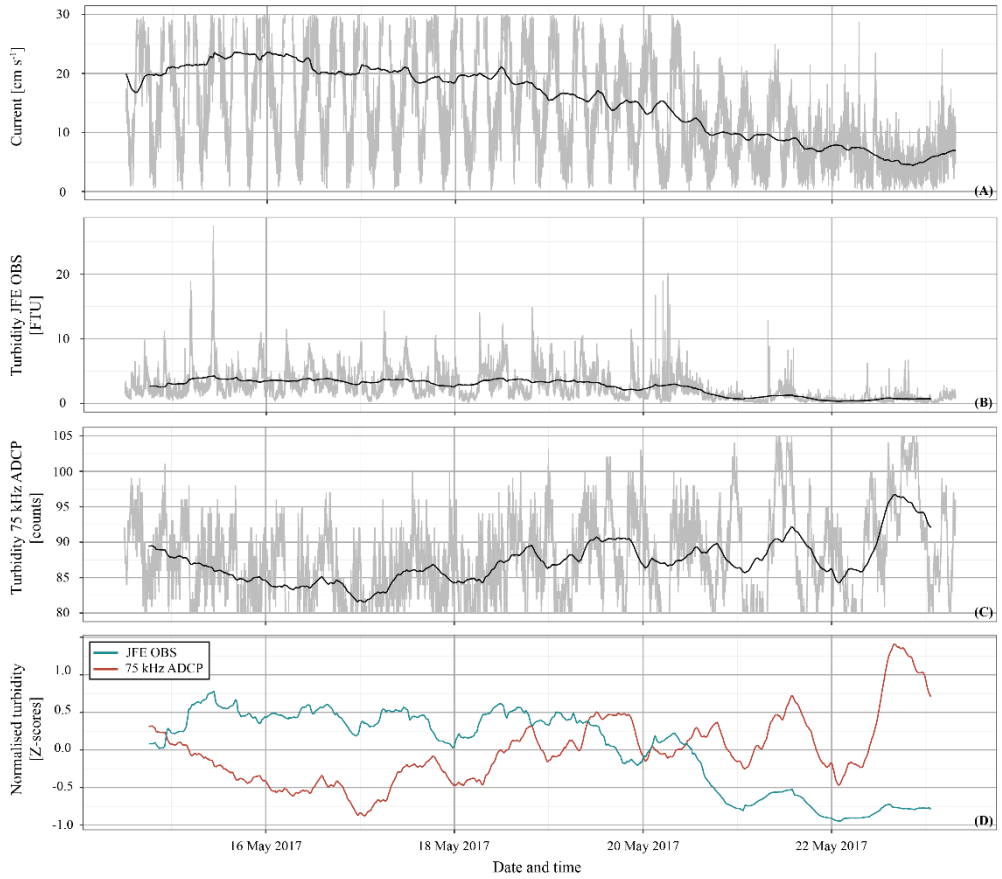

Figure 2.9: Nine-day record of a near-bottom (45 mab for 75 kHz ADCP and 5 mab for JFE OBS) time series from the mooring at 1400 m water depth, showing A) current speed, B) turbidity recorded by the JFE Advantech OBS, C) turbidity recorded by the RDI Workhorse 75 kHz ADCP and D) 12.5 h averaged normalised (Z-scores) turbidity records of the JFE Advantech OBS and the RDI Workhorse 75 kHz ADCP. In panels A-C the grey lines represent the actual data, whereas the black lines represent the 12.5 h averaged values.

(Fig. 2.9C). This is consistent with the interpretation that the acoustic signal is produced by organic-mineral aggregates, large enough to be detected by the 75 kHz ADCP, which increase in abundance and size in a regime of moderate currents, (Thomsen et al., 2002; Fettweis et al., 2006). The observed shorter vertical displacement of both the isotherms as well as the maxima in acoustic backscatter (Fig. 2.8), can also be attributed to the spring-neap tidal cycle. Turbulence induced by breaking of internal waves remained closer to the seafloor which resulted in less vertical displacement of resuspended material. In addition to that, settling out of aggregates from higher water layers may have increased their abundance near the bottom of the canyon. Similar as already noted for the alternative hypothesis, that the 75 kHz acoustic

backscatter signal is reflecting zooplankton/nekton, additional observations that could help to verify the aggregate hypothesis are lacking. The contribution of the different particle sources does deserve to be studied more extensively in future studies, perhaps using particle cameras by which the type of particles can be determined.

2.5.4. Implications for quantification and interpretation of SPM dynamics and recommendations for future studies

The three cases discussed above illustrate how quantification of SPM mass concentration in sea water by means of optical and acoustic sensors may be inherently biased by the choice of sensor in relation to the characteristics of the SPM. Irrespective what type of sensor is used, and within the sensitivity range specific for that sensor, the sensor output will always depend on the concentration of particles, but also on their size and composition. The only truly reliable method for obtaining unbiased SPM mass concentrations seems to be by direct weighing of SPM filtered from representative volumes of water. However, the resolution in space and time of the filtration method is far below what can be achieved with optical and acoustic devices. It is therefore good practice in oceanographic studies to combine the two methods and use SPM mass concentration determined via filtration of discrete water samples for calibration of simultaneously collected optical and acoustic sensor data.

In the case of CTD water column turbidity profiling, a significant correlation was found between the output of the two types of OBSs and the SPM mass concentrations (Fig. 2.3B), despite the fact that the data represented SPM from surface water, mid water and bottom water collected at random moments through the tidal cycle. The SPM in the Whittard Canyon thus appeared to be fairly uniform in its backscattering characteristics through time and space. Water column turbidity profiles obtained by the transmissometer turned out to be biased by stronger absorption of transmitted light by chlorophyll-bearing phytoplankton in the surface water layer than by SPM present in deeper water (Fig. 2.3A). If not accounted for, this might lead to over- or underestimation of SPM mass concentration. When considering transmissometer output separately for surface water and for deep water, a good correlation was found with SPM mass concentration (Fig. 2.3C), allowing for a reliable conversion of transmissometer output to SPM mass concentration. In future studies it could be interesting

to assess the possibility of using this difference in sensor response as means to determine the relative amount of phytodetritus in the SPM.

Compared to optical turbidity sensors, acoustic devices have the advantage that they are less sensitive to biofouling and therefore are better suited for long-term deployments (de Stigter et al., 2011). Additionally, acoustic profilers collect backscatter data not only from a single spot, but over a range that may extend to several meters in the case of high-frequency profilers. From the consistent logarithmic relationship found between acoustic backscatter recorded by the 1 MHz ADCP and optical backscatter recorded by the OBS (Fig. 2.5F and 2.6A), it can be inferred that in that particular case the acoustic and optical sensors were responding to largely overlapping particle size populations. Under such conditions, a quantitative relationship already established between optical backscatter and weighed SPM mass concentration can relatively easily be transferred to a relationship between acoustic backscatter and SPM mass concentration. It should be noted, however, that the sensitivity of the 1 MHz ADCP would increase with an increase of particle size from 24 to 485 µm (lower detection limit to optimum sensitivity), whereas the OBS should decrease in sensitivity over that same particle range. It thus seems preferable, when possible, to calibrate acoustic backscatter directly to SPM from simultaneously collected water samples.

The advantage that high-frequency ADCPs have over optical turbidity sensors, yielding profiles of relative turbidity rather than point measurements, may not apply similarly to low-frequency ADCPs. When operated in downward facing mode to cover the water column up to several hundred of metres above the seafloor, typically the lowermost 25 m above the seafloor, and more in steep terrain, yield unreliable data due to acoustic sidelobe reflections from the seafloor interfering with the signal. However, this could be largely overcome by the usage of ADCPs with a fifth beam, which allows to measure the acoustic backscatter closer to the bottom without interference problems (Wanis, 2013). But even in those ADCPs, data from bins close to the bottom are often compromised by over-reflection. Obviously, for studies of SPM transport in bottom nepheloid layers, the lower tens to hundreds of metres of water column above the seafloor are the most relevant. An even more important disadvantage is that the low-frequency ADCPs are unable to detect dispersed fine-grained SPM, which makes up an important part of the total SPM load. By comparing acoustic backscatter recorded by the 75

kHz ADCP with optical backscatter recorded by the OBS (Fig. 2.6B and 2.7), it is obvious from the lack of a consistent relationship that these sensors respond to very different particle size population. The 75 kHz ADCP records acoustic backscatter from millimetre-sized particles, which may be flocs of aggregated SPM but could also be zooplankton/nekton, or a combination of both, whereas the optical sensors are most sensitive for the dispersed fine-grained SPM particles in the µm size range. For studies focused on quantification of SPM transport, the preferred choice of sensor therefore seems to be optical sensors like OBSs and transmissometers or high-frequency acoustics sensors, as these usually produce output that is consistent with SPM mass concentrations determined by filtration of water samples.

In places where it may be suspected, or where it is known from in situ video footage or net hauls, that acoustic backscatter of the 75 kHz ADCP is for an important part associated to the presence of zooplankton/ nekton, this type of sensor is obviously unsuited for use in sediment transport studies. But what if material recorded by our 75 kHz ADCP at the bottom of the canyon would indeed be composed for a large part of flocs of aggregated SPM, increasing and decreasing in acoustic records by aggregation and disaggregation under influence of variable current shear? Then the 75 kHz ADCP would convey information about SPM dynamics complementary to what is recorded by the optical and high-frequency acoustic sensors. If the conspicuous peaks in optical backscatter shown in Fig. 2.7 were indeed produced by disaggregation of larger aggregates, then from the values presented in this figure we may derive a crude idea of the distribution of SPM over fine-grained dispersed versus aggregated SPM. On top of fluctuating base levels of turbidity of 2-5 FTU, sharp excursions of 10, 15 and up to 25 FTU occurred. This would suggest that these larger aggregates contained the same or up to four times the amount of SPM mass as the background of fine-grained dispersed SPM. This is a substantial amount that should not be overlooked in the quantification of SPM. Quantification of the low-frequency ADCP's backscatter signal in terms of SPM mass concentration remains challenging, however, due to the dependency of the signal on both concentration and particle size.

Independent information on SPM particle size distribution would help to reduce uncertainties. For example, by the use of a Laser In Situ Scattering and Transmission (LISST) sensor for particle sizes up to 500 µm (Sequoia Inc.; Agrawal and Pottsmith, 2000), and a particle camera for

larger particles and aggregates (e.g. Sternberg et al., 1996; Mikkelsen et al., 2005; Davies et al., 2012; Roberts et al., 2018). Whereas particle size distributions of collected water samples measured ex-situ, as illustrated in Figure 2.4, only represent the size distribution of primary particles in disaggregated SPM, the LISST sensor and particle camera have the advantage that they give insight in the in-situ particle size distribution of SPM. Multi-frequency acoustic devices such as AQUAscat (Aquatec; Hunter et al., 2012) also hold promise for a more comprehensive quantification of SPM, covering a broader range of particles. Presently, however, these sensors have a maximum particle detection limit of 500 µm, and with a depth rating of 1000 m the application of this device is limited to shelf and upper slope depths. Furthermore, the use of particle cameras in combination with turbidity sensors is important for determining the nature of backscattering particles, whether it is zooplankton/ nekton or non-living aggregated particulate matter.

Strong variation in particle size distribution of suspended matter, such as we infer from our observations from Whittard Canyon, is a common feature in dynamic marine systems (e.g. Thomsen and van Weering, 1998; Thomsen et al., 2002; de Stigter et al., 2007, 2011; Baeye and Fettweis, 2015), which are subjected to seasonal variation due to variable production of organic matter that favours SPM aggregation. (Fettweis and Lee, 2017). In such dynamic systems the use of multiple sensors covering a wide range of SPM particle sizes has the advantage of providing insight in SPM dynamics, even though full quantification of the SPM mass concentration across the full particle size spectrum remains difficult. Insight in SPM dynamics is relevant for understanding and quantifying natural processes of SPM dispersion such as in bottom nepheloid layers and hydrothermal plumes. If the SPM mass concentration can be quantified in combination with chemical composition analysis of the SPM, improved estimates can be made on e.g. carbon, nutrient and (trace) metal transport in these systems, which have vital implications on biological processes and biogeochemical budgets.

Furthermore, the insight in SPM dynamics is relevant for studying SPM dispersion in plumes produced by bottom trawling, dredging and future deep-sea mining operations. As demonstrated by Gillard et al. (2019) for the case of deep-sea mining in the Clarion-Clipperton Zone, flocculation of fine-grained sediment particles into large, fast-sinking aggregates, is likely a major factor determining dispersion of sediment plumes stirred up by mining. Monitoring

set-ups should therefore be able to record both the dispersed fine-grained SPM and large aggregates and not overlook one or the other, as both may be important pathways of lateral transport (Gardner et al., 2018b).

2.6. Conclusion

We have shown that interpretation and quantification of the responses of different types of turbidity sensors is not straightforward, and that SPM mass concentrations are easily over- or underestimated, potentially leading to misinterpretation of the SPM dynamics with implications on our understanding of ocean systems. In this case study in the Whittard Canyon we have found that:

- The transmissometer has a stronger response to material in the biologically productive surface layer compared to SPM found in the deeper part of the water column, most likely due to higher absorption of the light signal emitted by the transmissometer by chlorophyll-bearing phytoplankton. If in the conversion of the transmissometer's response to SPM mass concentration this is not corrected for, it will lead to mis-quantification of the SPM mass concentration.
- The OBSs and high-frequency ADCP displayed corresponding backscatter records, whereas the low-frequency ADCP had a remarkably different backscatter record. This is attributed to the different ranges in particle size sensitivity of the different sensors with the OBS and high-frequency ADCP being most sensitive for finer grained material and the low-frequency ADCP for coarser grained material, like aggregates and zooplankton/nekton.
- It has to be considered that changing sensor response may not only reflect changes in SPM mass concentrations but is also influenced by changing particle size distribution of the SPM. Even though quantification of the low-frequency ADCP's response remains difficult, the combination of this sensor with an OBS, as on our mooring, can potentially provide qualitative information about the aggregation state of the SPM. This allows studying recurring cycles of resuspension involving aggregation and disaggregation of SPM under different turbulence intensities.
- If it can be verified that the acoustic backscatter recorded by the low-frequency ADCP partially represents aggregated SPM, then it should be considered that these

aggregates may contain a substantial portion of total SPM, which may remain undetected by using optical and high-frequency acoustic sensors only.

- If it can be verified that the low-frequency ADCP's acoustic backscatter response reflects the presence of zooplankton/nekton, the recorded signal is obviously of no use for sediment transport studies, but it would contain relevant biological information on distribution of zooplankton and nekton. With the caveat again that backscatter intensity is not only determined by biomass but also by size distribution of the zooplankton/nekton.

In general, also when applied to other settings than submarine canyons, we recommend combining optical and acoustic devices to obtain records on turbidity and current speed and direction in combination with water sampling to determine SPM mass concentration. Furthermore, it is important to determine what type of material is detected by the different type of sensors in order to determine to which degree the recorded turbidity by a sensor can actually be used in sediment transport studies.

Data availability

CTD, lander and mooring data presented in this work, as well as filter weights for SPM sampling and data on particle size analysis of the SPM and surface sediments are available in PANGAEA (https://doi.pangaea.de/10.1594/PANGAEA.927919) and the NIOZ data portal (http://dataverse.nioz.nl/dataverse/doi under DOI 10.25850/nioz/7b.b.hb).

Acknowledgements

We thank the captain and crew of RV *Pelagia*, as well as the NIOZ technicians, for their essential assistance during cruises 64PE421 and 64PE437. Jonathan Kranenburg performed the particle size distribution analysis of the surface sediment samples. This research has been supported by the Innovational Research Incentives Scheme of the Netherlands Organisation for Scientific Research (NWO-VIDI grant no. 0.16.161.360) and ship time was provided by the Royal Netherlands Institute for Sea Research. Sabine Haalboom received funding from the Blue Nodules project (EC grant agreement no. 688785). Two anonymous reviewers provided constructive criticism which helped to improve the paper.

Supplementary material

Table S2.1: Configuration of sensors.

Type of sensor	Source	Specifications	Settings on CTD	Settings on bottom lander	Settings on mooring
WETLabs C-Star transmissometer (25 cm pathlength)	Optical	Wavelength: 650 nm	Sampling interval: 8 Hz averaged over 1 s		
WETLabs ECO FLNTU	Optical	Wavelength: 700 nm	Sampling interval: 8 Hz averages over 1 s	Sampling interval: 8 Hz averaged over 1 s	
JFE Advantech Infinity series ATUD-USB	Optical	Wavelength: 880 nm	Sampling interval: 1 Hz	Sampling interval: 5 min with 60 measurements at 1 Hz	Sampling interval: 1 measurement every minute
Nortek Aquadopp	Acoustic	Frequency: 1 MHz		Sampling interval: 5 min 60 measurements at 1 Hz Blanking distance: 1 m	
RDI Workhorse Long Ranger ADCP	Acoustic	Frequency: 75 kHz			Sampling interval: 1 min with 9 pings/ensemble Blanking distance: 1 m Bin size: 5 m

Table S2.2: CTD samples taking during cruise 64PE421.

Station	Latitude	Longitude	Depth (m)	SPM	Particle size	Station	Latitude	Longitude	Depth (m)	SPM	Particle size
3	48°32.85756'N	9°55.77096'W	1985	X	X	41	48°44.87424'N	10°6.48324'W	20	X	
3	48°32.85756'N	9°55.77096'W	1700	X	X	46	48°39.49836'N	9°59.42118'W	788	X	
3	48°32.85756'N	9°55.77096'W	1000	X	X	47	48°39.20988'N	10°0.20064'W	958	X	
3	48°32.85756'N	9°55.77096'W	780	X	X	48	48°38.3376'N	10°2.1579'W	1107	X	
3	48°32.85756'N	9°55.77096'W	35	X	X	49	48°38.62854'N	10°1.23468'W	1374	X	
7	48°49.79460'N	10°7.30602'W	185	X	X	49	48°38.62854'N	10°1.23468'W	700	X	
7	48°49.79460'N	10°7.30602'W	34	X	X	54	48°31.97322'N	9°53.2728'W	946	X	
8	48°45.63720'N	10°7.09146'W	547	X	X	55	48°31.99344'N	9°54.9003'W	1426	X	
9	48°42.78606'N	10°5.27112'W	913	X	X	56	48°31.84482'N	9°57.51528'W	1453	X	
9	48°42.78606'N	10°5.27112'W	700	X	X	57	48° 32.088'N	9°59.38422'W	774	X	
10	48°38.45082'N	10°1.01580'W	1405	X	X	58	48° 32.088'N	9°59.38422'W	2041	X	
10	48°38.45082'N	10°1.01580'W	1100	X	X	58	48°31.76904'N	9°56.09826'W	1500	X	
10	48°38.45082'N	10°1.01580'W	498	X	X	58	48°31.76904'N	9°56.09826'W	1000	X	
11	48°35.02608'N	9°56.58168'W	1703	X	X	62	48°38.16726'N	9°57.25788'W	1115	X	
11	48°35.02608'N	9°56.58168'W	1560	X	X	62	48°38.16726'N	9°57.25788'W	1000	X	
11	48°35.02608'N	9°56.58168'W	1340	X	X	62	48°38.16726'N	9°57.25788'W	500	X	
11	48°35.02608'N	9°56.58168'W	1034	X	X	79	48°37.91124'N	10°3.95802'W	503	X	
11	48°35.02608'N	9°56.58168'W	479	X	X	88	48°23.71824'N	9°50.30856'W	2064	X	
12	48°29.54934'N	9°56.23776'W	2233	X	X	88	48°23.71824'N	9°50.30856'W	1677	X	
12	48°29.54934'N	9°56.23776'W	1700	X	X	88	48°23.71824'N	9°50.30856'W	950	X	
12	48°29.54934'N	9°56.23776'W	1000	X	X	88	48°23.71824'N	9°50.30856'W	500	X	
13	48°25.79262'N	9°56.56824'W	2598	X	X	89	48°25.20216'N	9°47.3928'W	1415	X	
14	48°23.46504'N	10°0.18492'W	2995	X	X	89	48°25.20216'N	9°47.3928'W	950	X	
14	48°23.46504'N	10°0.18492'W	2598	X	X	89	48°25.20216'N	9°47.3928'W	499	X	
15	48°17.94606'N	10°9.80646'W	3409	X	X	89	48°25.20216'N	9°47.3928'W	34	X	
15	48°17.94606'N	10°9.80646'W	2806	X	X	90	48°26.49606'N	9°43.68462'W	1246	X	
15	48°17.94606'N	10°9.80646'W	1000	X	X	90	48°26.49606'N	9°43.68462'W	900	X	
15	48°17.94606'N	10°9.80646'W	34	X	X	90	48°26.49606'N	9°43.68462'W	500	X	
16	48°9.271320'N	10°13.07802'W	3644	X	X	91	48°27.4701'N	9° 40.4115'W	1097	X	
31	48°18.04884'N	10°10.06698'W	3433	X		91	48°27.4701'N	9° 40.4115'W	880	X	
37	48°44.76294'N	10°8.76570W'	260	X		91	48°27.4701'N	9° 40.4115'W	501	X	
38	48°44.77158'N	10°7.50054'W	498	X		91	48°27.4701'N	9° 40.4115'W	33	X	
39	48°45.01584'N	10°5.32422'W	430	X		99	48°28.80114'N	9° 37.8081'W	928	X	
40	48°45.34608'N	10°3.84912'W	277	X		99	48°28.80114'N	9° 37.8081'W	500	X	
41	48°44.87424'N	10°6.48324'W	742	X		100	48°30.36306'N	9°34.52172'W	705	X	
41	48°44.87424'N	10°6.48324'W	400	X		100	48°30.36306'N	9°34.52172'W	400	X	

Table S2.3: Mono core samples taking during cruise 64PE421.

Station	Latitude	Longitude	Depth (m)
10	48°38.45082 'N	10°1.01580 'W	1410
11	48°35.02608 'N	9°56.58168 'W	1708
12	48°29.54934 'N	9°56.23776 'W	2238
13	48°25.79262 'N	9°56.56824 'W	2603
14	48°23.46504 'N	10°0.18492 'W	3000
15	48°17.94606 'N	10°9.80646 'W	3413
16	48°9.271320 'N	10°13.07802 'W	3649

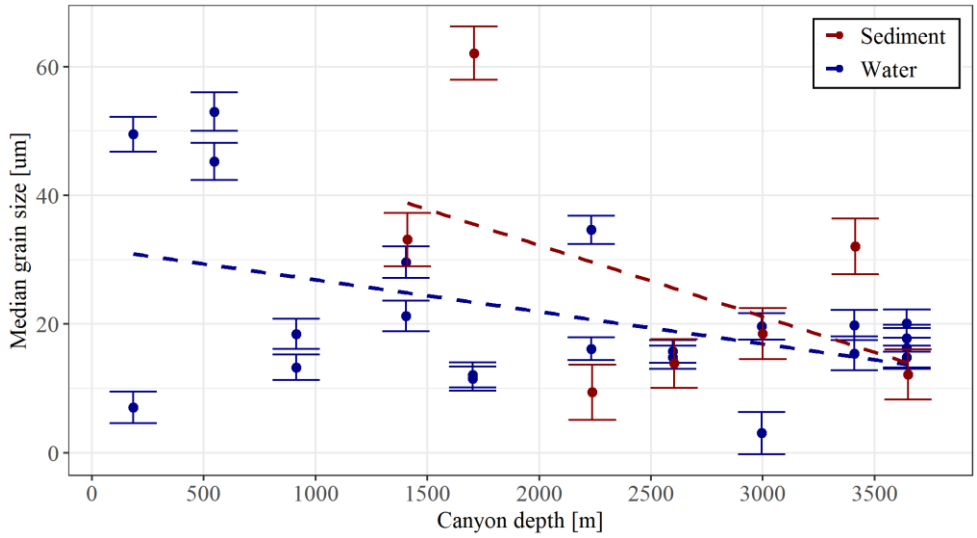

Figure S2.1: Median particle sizes with depth in the easternmost canyon branch for SPM in near-bottom water (blue) as well as for surface sediments (red). Errors bars show the standard deviation. Dashed lines indicate the regression lines.

Image: Deployment of a mooring in the Whittard Canyon during cruise 64PE421 (May 2017) onboard RV *Pelagia*. Photo by: Sabine Haalboom.

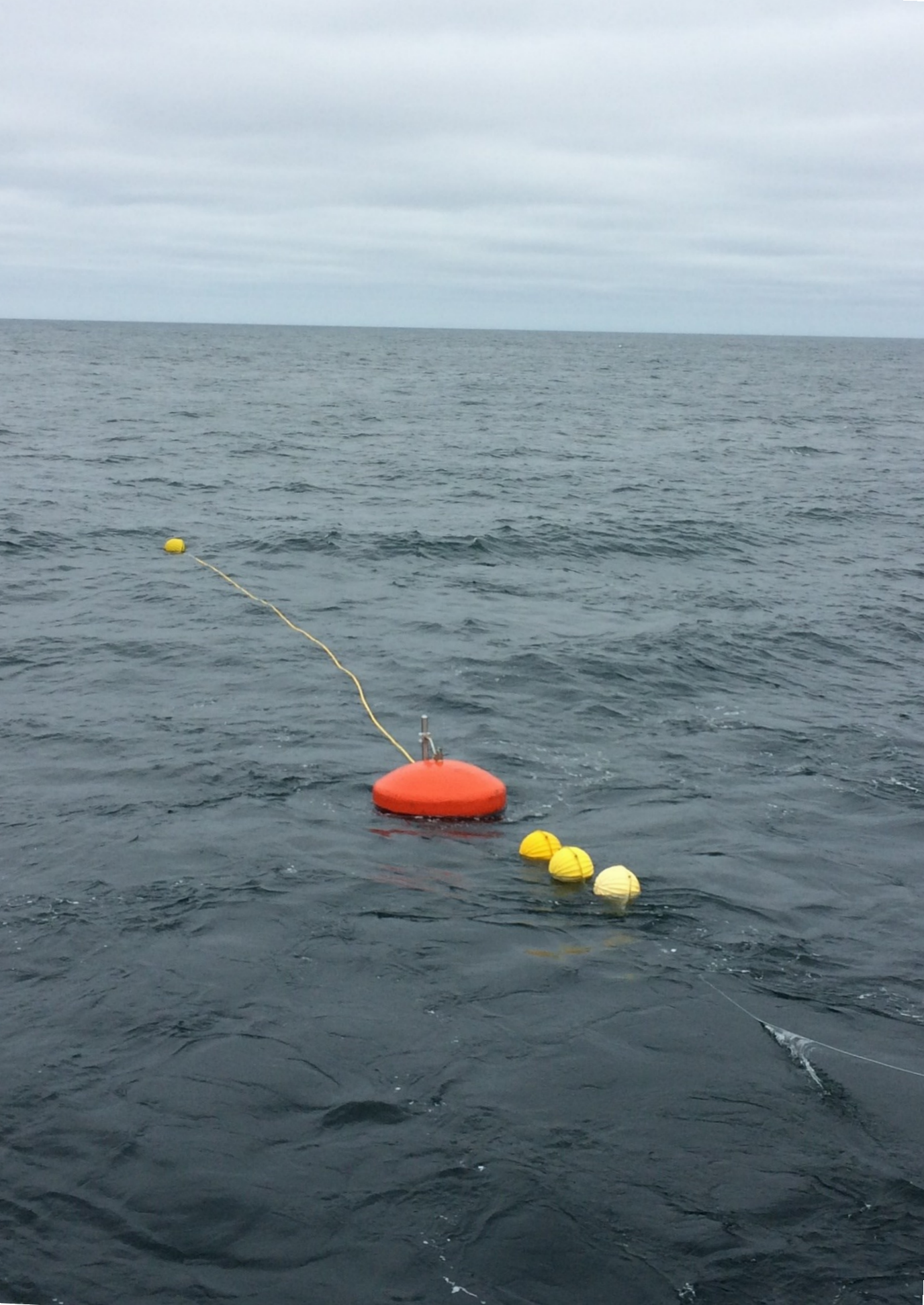

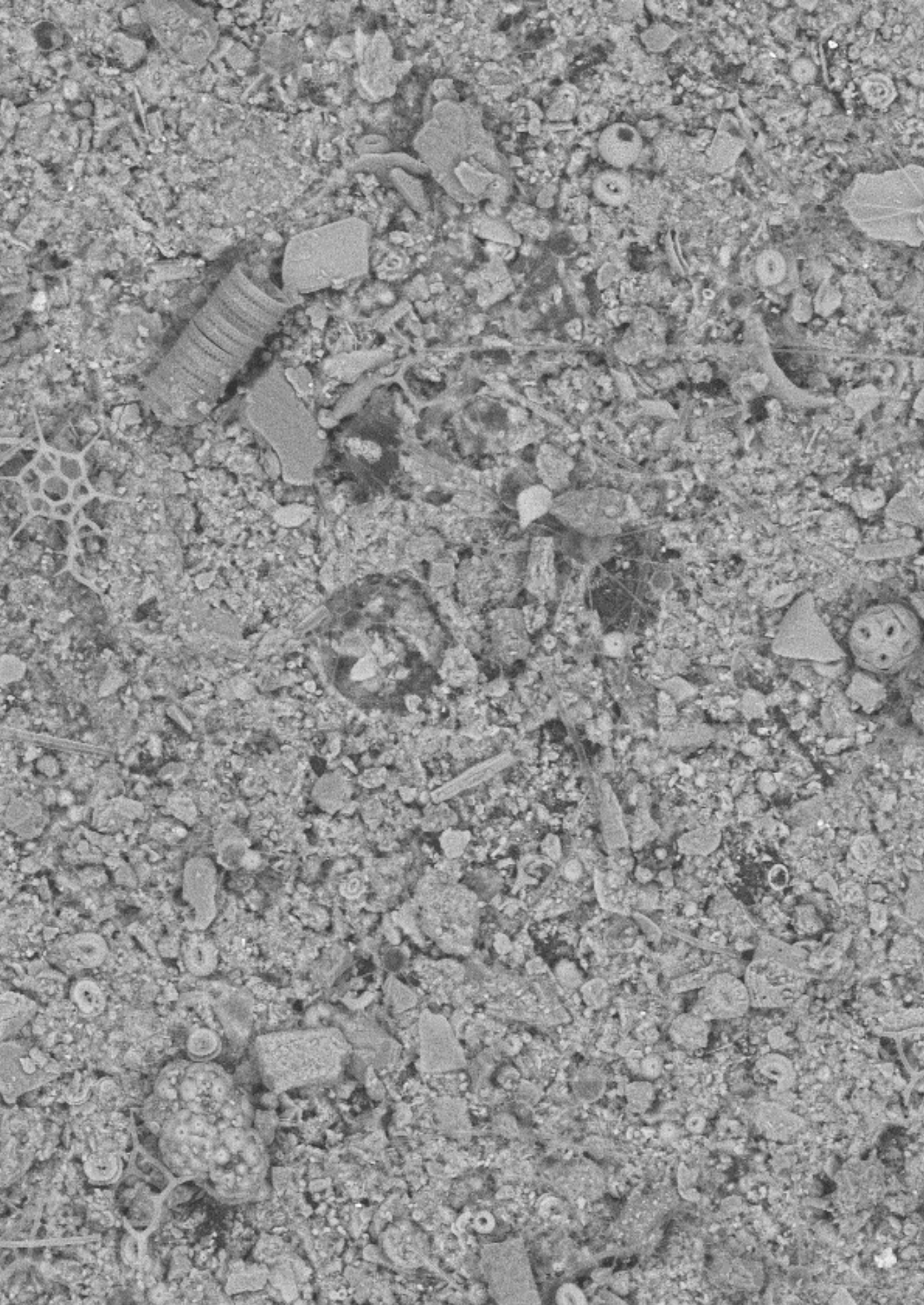

Chapter 3: Suspended particulate organic matter transport and deposition along the thalweg of the easternmost branch of Whittard Canyon, NE Atlantic Ocean

Sabine Haalboom, Henko de Stigter, Jonathan Kranenburg, Marc Lavaleye, Gerard Duineveld, Gert-Jan Reichart & Furu Mienis

In preparation for submission.

Image: Scanning Electron Microscope (SEM) image of a filtered water sample taken in the Whittard Canyon in May 2017 at 1985 m depth, showing all sorts of organic and inorganic particles. Photo by: Sabine Haalboom using the Hitachi TM3000 scanning electron microscope at Royal NIOZ.

Abstract

Submarine canyons are important pathways for the transport of particulate matter from the shelf to deep ocean. Transport is the result of continuous cycles of resuspension and redeposition of matter by internal waves interacting with the steep canyon topography and intermittent gravity flows. While the latter drives matter transport from shelf to deep sea on geological timescales, the first process is more important for organic matter transport and deposition and determines the availability of suspended organic matter for faunal communities. In this study we investigated the organic matter composition of suspended particulate matter and surface sediments along a transect in the easternmost branch of the Whittard Canyon. Surface sediments were collected with a mono corer and multi corer, while suspended particulate matter samples were collected with a CTD-Rosette sampler and in situ particle pumps mounted on bottom landers. The latter allowed to determine temporal changes in suspended organic matter content during several tidal cycles. Results showed that the most active resuspension, as shown by enhanced turbidity in the water column, occurs at sites with strongest bottom currents between 1200 and 2300 m water depth along the canyon thalweg. Different zones were observed along the thalweg with relativity fresh suspended particulate organic matter (SPOM) in low concentration in the bottom water of the upper canyon, more degraded SPOM in higher concentration in the middle canyon with most active resuspension, and slightly less degraded SPOM in low concentration in the lower canyon. Data recorded with a lander at 1650 m depth showed that particles are resuspended during peaks in current speed while tidal flow is directed up-canyon, resulting in higher concentration of C_{org}, N_{tot} and Chl-*a*. The low Chl-*a*/C_{org} ratio of the suspended organic matter at this site suggests that repeated resuspension by internal tides results in the breakdown of the more susceptible compounds and that older and more degraded organic matter incorporated in the surface sediments is also entrained. In the surface sediment of the canyon thalweg, the highest concentrations of organic matter, though of more degraded nature, are found in fine-grained deposits in the lower reaches of the canyon. It thus seems that the continuous cycles of resuspension by tidal currents combined with the down-canyon transport by intermittent gravity flows results in the winnowing of the fine-grained organic-rich sediment fraction from the upper and middle part of the canyon, and transport and ultimate deposition of the more refractory organic components towards the deeper part of the canyon, indicating the potentially important role of submarine canyons as carbon sinks.

3.1. Introduction

Benthic nepheloid layers, near-bottom water layers characterised by enhanced particle concentrations, are a common feature on all ocean margins. A long-term study of the characteristics of nepheloid layers has indicated that the driving processes of erosion and resuspension leading to their formation are persistent features over decadal time spans (Gardner et al., 2018b). Therefore, it is assumed that nepheloid layers play an important role in the lateral transport and mineralisation of (organic) matter (Inthorn et al., 2006; Rabouille et al., 2009). Submarine canyons are areas where benthic nepheloid layers with high particle concentration often occur as was observed in the North Atlantic, along the Mid Atlantic Bight and in the Mediterranean (e.g. de Stigter et al., 2007; Puig et al., 2013; Wilson et al., 2015b; Prouty et al., 2017). Therefore, submarine canyons potentially play an important role in the transport of significant amounts of organic carbon from biologically productive continental shelves towards the organic matter starved deep-sea basins (Canals et al., 2006; García et al., 2008; Harris and Whiteway, 2011; Maier et al., 2019b).

Transport of suspended particulate matter (SPM) and subsequent deposition within canyons is difficult to predict due to hydrographic and topographic differences between canyons that result in multiple processes causing particle resuspension (Puig et al., 2014). Fine-grained particulate lithogenic and biogenic matter settling in the confines of a canyon is subject to continuous cycles of resuspension, transport and deposition by internal wave action driven by tides and meteorological disturbances (Gardner, 1989b; Hall et al., 2017; van Haren et al., 2022), resulting in the permanent presence of nepheloid layers (Dickson and McCave, 1986; Wilson et al., 2015b; Gardner et al., 2018b). Intermittently, gravity flows and dense water cascading resuspend and transport accumulated sediments down the slopes and down the thalweg of the canyon. Major turbidity currents can transport massive amounts of sediment, including organic matter and pollutants, to the deep ocean (Paull et al., 2018). Turbidity currents are often the result of slope failure due to seasonal variations in sediment transport and availability (Maier at al., 2019a; Heijnen et al., 2022), but can also be induced by external triggers such as storms (Puig et al., 2004; Palanques et al., 2011), river floods (Stetten et al., 2015), earthquakes (Goldfinger et al., 2007; Hsu et al., 2008), dense cascading shelf water as observed in the Mediterranean (Palanques et al., 2009; Tesi et al., 2010; Puig et al., 2013) and fishing activities on the canyon flanks and interfluves (Puig et al., 2012: Daly et al., 2018). All

of these processes can initiate temporary enhanced turbidity in the water column and down-slope particulate matter transport. Moreover, due to the steep topography and heterogeneity of habitats provided to organisms, submarine canyons are known hotspots of biodiversity (De Leo et al., 2010; Vetter et al., 2010). The presence of suspension feeders (Huvenne et al., 2011; Morris et al., 2013; Brooke et al., 2017), like scleractinian cold-water corals indicates that fresh phytodetritus is present in these systems, since this is one of main sources of nutrition for these organisms (Maier et al., 2023).

Accordingly, nepheloid layers may provide an important pathway for the transport of organic matter to deeper waters. However, at present organic matter concentrations and composition in nepheloid layers are not well constrained, which hinders developing a process-based understanding of carbon pathways in the deep sea and the role of canyons therein. In order to better constrain the role of nepheloid layers in the (re)distribution of organic matter in submarine canyons, benthic landers were deployed at different depths along the thalweg of the easternmost branch of the Whittard Canyon and a CTD-Rosette systems was used to collect suspended particulate organic matter in the benthic boundary layer. Previous studies in the Whittard Canyon focussed on the quantification of total suspended material in nepheloid layers (Haalboom et al., 2021 and others), however, the organic carbon content and quality of this material were not discussed. The present paper aims to determine whether nepheloid layers in the canyon are enriched in (fresh) organic matter and where this organic matter is ultimately deposited. Surface sediment samples were also collected along the same transect for comparison of the organic matter in sediments with organic matter in suspension, to unravel the effect of resuspension on local organic matter accumulation.

3.2. Methodology

3.2.1. Topographic and hydrographic setting

The Whittard Canyon, situated on the Celtic margin, is a multi-branched system that connects the shallow continental shelf at around 200 m water depth with the abyssal ocean at 4000 m water depth (Amaro et al., 2016). The canyon is a so-called type II canyon, incising the continental margin, but unconnected to any major river system (Harris and Whiteway, 2011). In this study we focus on the easternmost branch of Whittard Canyon (Fig. 3.1) that is characterised by steep walls on the western flanks and multiple tributaries incising the eastern

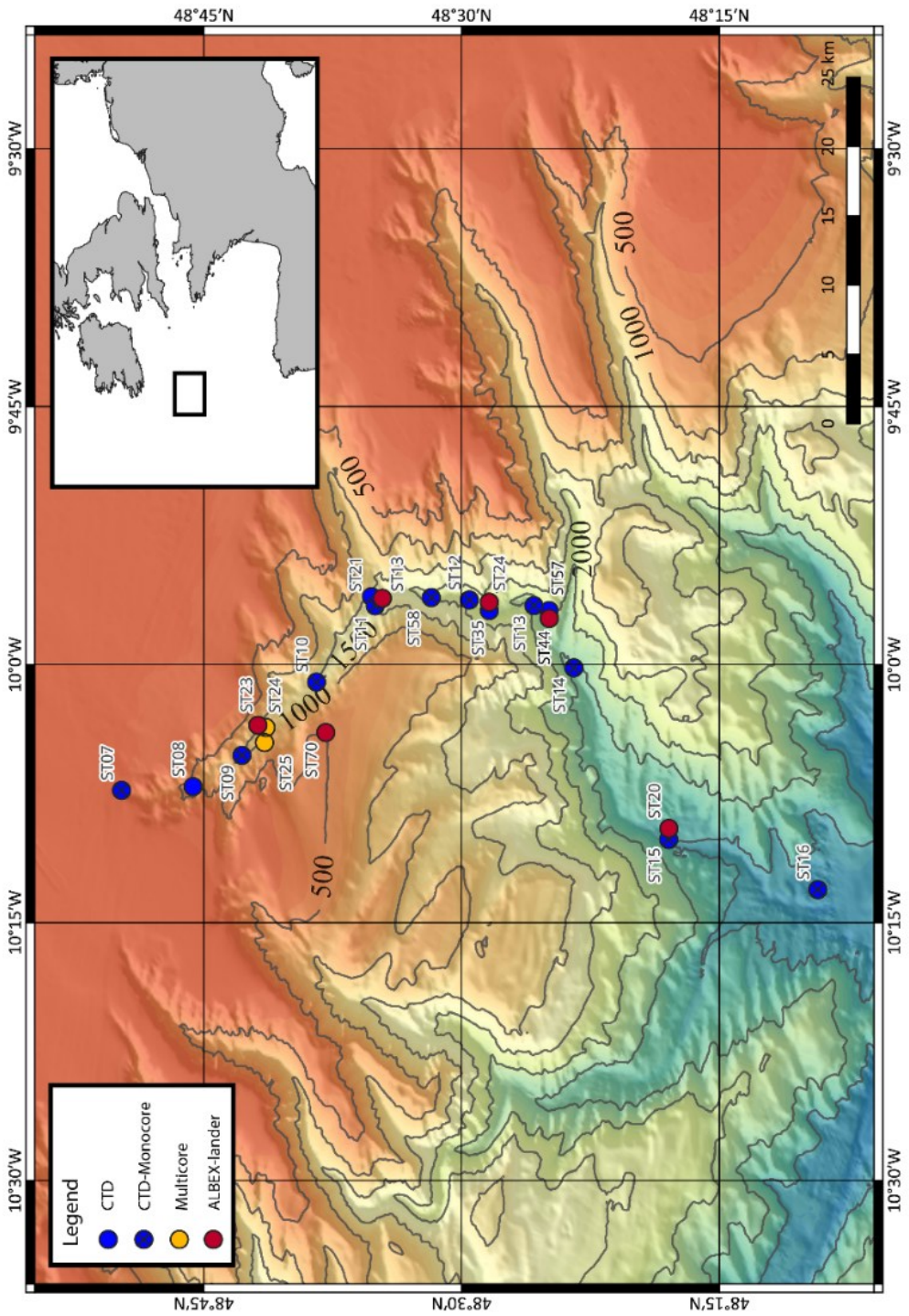

Figure 3.1: Map of the easternmost branch of the Whittard Canyon in the Bay of Biscay. CTD stations with mono corer, multicore, and ALBEX lander locations are indicated.

flank (Huvenne et al., 2011; Lo Iacono et al., 2020). Long-term monitoring studies have shown that the easternmost branch of Whittard Canyon is a particularly active site with regards to particulate matter transport, where on average 7 major turbidity currents flush the canyon in one year (Heijnen et al., 2022). In addition, pronounced nepheloid layers, initiated by continuous resuspension of matter by internal tides, are a permanent feature in this branch of the Whittard Canyon (Hall et al., 2017; Aslam et al., 2018; Haalboom et al., 2021; van Haren et al., 2022).

Glider and lander data collected in the Whittard Canyon showed that these internal tides result in a net headward transport of particulate matter from 2500 m depth towards the shelf break (Amaro et al., 2016; Aslam et al., 2018) and in upwelling of nutrient-rich waters during summertime conditions (Porter et al., 2016). Below 2500 m, bottom current velocities (0.1-0.15 m s^{-1}) were found too low to support significant resuspension of sediments (Amaro et al., 2015).

The upper water masses in Whittard Canyon, originating at sub-tropical latitudes are characterised by the warm Eastern North Atlantic Water (ENAW) that overlies the Mediterranean Outflow water (MOW), characterised by high salinity (van Aken, 2000). The European Slope Currents is carrying the ENAW in a poleward direction with mean flow speeds of 0.05-0.1 m s^{-1}, varying seasonally with lowest strength during the summer months (Pingree et al., 1999). Below the MOW (>1600 m water depth) the less saline Labrador Sea Water (LSW) and North Atlantic Deep Water are observed (van Aken and Becker, 1996).

3.2.2. Field sampling

Samples and data presented in this study were collected during three RV *Pelagia* cruises (64PE421, 64PE437, 64PE453) that all took place in late spring, respectively in 2017, 2018 and 2019 (Fig. 3.1, Table S3.1). To measure water column characteristics conductivity-temperature-depth (CTD) profiles were conducted along a transect following the thalweg of the easternmost branch of Whittard Canyon during RV *Pelagia* cruise 64PE421 (Fig. 3.1). The CTD-Rosette system was equipped with an SBE 9 plus CTD and two different types of turbidity sensors, including a JFE-Advantech and WetLabs FLNTU to measure turbidity. Near-bottom (~10 m above the bottom) and surface suspended particulate matter samples were also

collected with the CTD-Rosette during the upcast. 10 L of seawater collected as close to the bottom as possible, and 5 L of surface waters were immediately filtered on board at ambient temperature conditions over pre-weighed and combusted GF/F filters (47 mm Whatman™). All filters were stored frozen at -20 °C prior to being analysed. Additional CTD casts were carried out during cruises 64PE437 and 64PE543 where water samples were collected from the surface chlorophyll maximum and as close to the seafloor as possible during the upcast. Surface sediment samples were collected along the same transect with a mono corer, a single-tube version of a multi corer that was suspended underneath the CTD-Rosette on a 10 m long line. After retrieval sediments were immediately sliced on board in 0.5 cm slices, which were stored frozen at -20 °C until further analysis.

NIOZ-designed ALBEX landers (Duineveld et al., 2004), equipped with current sensors (Nortek™), turbidity sensors (JFE Advantech™) and a McLane particle pump were deployed for several days at different depths along the thalweg of Whittard Canyon (Fig. 3.1). The McLane particle pump contained 24 filter holders that were loaded with pre-weighed and combusted (3 hours at 450 °C) GF/F filters (47 mm Whatman™) over which 10 litres of seawater were filtered in situ within a 2-hour interval to collect particulate (organic) matter from the bottom water at 40 cm above the seabed. Turbidity values derived from the CTD casts and lander deployments were converted to mass content (mg L^{-1}) using the conversion function as described in Haalboom et al. (2021).

3.2.3. Laboratory analysis

In the laboratory GF/F filters and sediment samples were freeze dried and further prepared for the analysis of the weight percentage and stable isotope composition of organic carbon (C_{org}), total nitrogen (N_{tot}), and content of chlorophyll-*a* (Chl-*a*). The filters were cut into equal parts prior to the analyses and were decarbonated using vapor of hydrochloric acid (2M HCl suprapure). One part was used for organic carbon and nitrogen analysis and their stable isotope ratios. After freeze drying, surface sediment samples were homogenized with a pestle and mortar and split into separate fractions for organic carbon and nitrogen analysis. The fraction for organic carbon analysis was decarbonated with 10% HCl to remove inorganic carbon, followed by several rinses with Milli-Q, and drying and weighing to calculate percentage inorganic carbon. A portion of 5 mg of decarbonated sediment and 50 mg of

untreated sediment were weighed and folded into tin cups for organic carbon and total nitrogen analysis, respectively. The weight percent of organic carbon and total nitrogen relative to total sediment as well as their isotopes were analysed on a Delta V Advantage isotope ratio MS coupled online to an Elemental Analyser (Flash 2000 EA-IRMS). Nitrogen isotopes were determined relative to purified atmospheric N_2. As standards for ^{13}C, certified benzoic acid and acetanilide and for ^{15}N, acetanilide, urea and casein were used. The data are presented versus V-PDB and atmosphere respectively, with a precision and accuracy of 0.15 ‰ for ^{13}C and ^{15}N.

Another fraction of the filters and sediment samples was used for chlorophyll-*a* analysis to assess the freshness of organic material. Chlorophyll-*a* (Chl-*a*) and Pheophytin-*a* (Pheo-*a*) (degradation production of Chl-*a*) were measured by fluorescence spectrophotometry using the F-2500 Hitachi (excitation wavelength 431 nm, emission wavelength 671 nm) (Holm-Hansen and Riemann, 1978). Homogenised sediments (~400 mg) and half GF/F filters were placed in small sample jars. Acetone (10 mL of cold 90% acetone) was added to the samples, and samples were stored in a dark fridge overnight before further extracting the Chl-*a*. Samples were sonicated for 2 minutes in an ultrasonic ice bath followed by a centrifugation phase (10 min at 4000 rpm) to ensure that pigments were separated properly. The spectrophotometer was calibrated using two known Chl-*a* concentrations (50 and 100 µg L^{-1}) and samples were measured in duplicate. For the first measurement 5 mL of sample solution was transferred into a cuvette to measure the fluorescence signal for Chl-*a* and Pheo-*a*. The second measurement involved addition of 50 µL HCl (10%) to degrade all Chl-*a* to Pheo-*a*. A limitation of this method is that wavelength interferences by degradation production of phytoplankton-grazers (faeces) and chlorophyll-*b* (extra pheophytin after acidification) are not corrected for, hence the Chl-*a* concentrations likely will be slightly underestimated (Yentsch and Menzel, 1963; Welschmeyer, 1994). As a measure of the freshness of organic matter, the Chl-*a*/C_{org} ratio was calculated.

3.3. Results

3.3.1. Suspended particulate matter in the surface water

In the surface water layer above the canyon, sampled with CTD-Rosette, total SPM mass concentrations were 0.2-0.4 mg L^{-1}, while the concentration of suspended particulate C_{org} was

0.12-0.2 mg L^{-1}, N_{tot} 0.02-0.04 mg L^{-1}, and Chl-*a* 540-953 ng L^{-1}. In the suspended particulate fraction, the molar C_{org}/N_{tot} ratio was 4.9-5.7, and the ratio of Chl-*a*/C_{org} was 3.6-7.1. For stable isotopes of C_{org} and N_{tot} in the suspended particulate fraction, values of -23.6 to -22.6 ‰ V-PDB were found for $\delta^{13}C$ and 3.4-4.5 ‰ for $^{\delta}15N$, respectively.

3.3.2. Near bed suspended particulate organic matter

A pronounced nepheloid layer was observed along the thalweg of the easternmost branch of Whittard Canyon, with highest turbidity values being measured between 1200-2300 m water depth (Fig. 3.2), the depth interval where highest turbidity and current speed was measured by the bottom landers. Landers along the thalweg recorded near-bottom current speed that displayed a clear semi-diurnal tidal pattern in speed and flow direction, alternating between up-canyon (towards the canyon head) and down-canyon. The highest average and peak current speeds, respectively 0.19 and 0.58 m s^{-1}, were recorded at 1650 m water depth. At 2233 m water depth, average and peak current speeds of, respectively, 0.13 and 0.36 m s^{-1} were recorded (Table 3.1). At these two sites, peaks in current speed in an upstream direction corresponded to notable increases in turbidity (Fig. 3.3). At both shallower (906 m water depth) and deeper parts along the thalweg, lower average current speeds around 0.1 m s^{-1} and peak current speeds up to 0.2 m s^{-1} were recorded (Table 3.1). At these shallower and deeper sites no correlation between current speed and turbidity was observed through time.

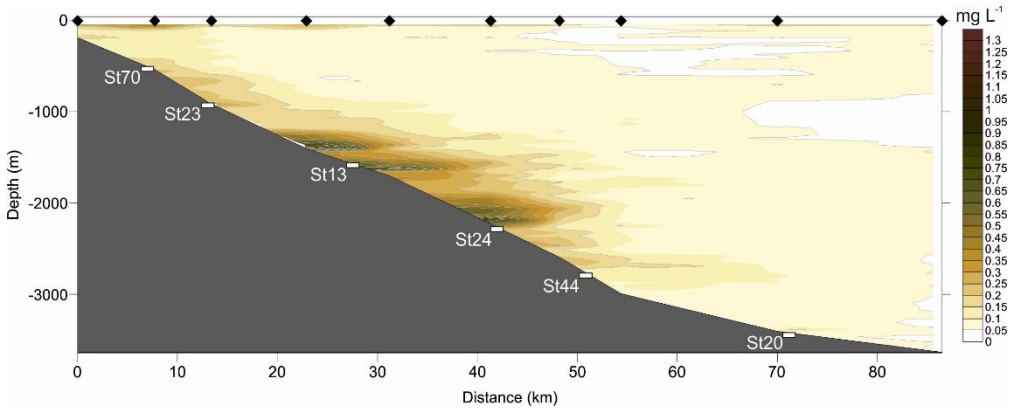

Figure 3.2: CTD transect showing turbidity measurements collected with a CTD along the canyon axis with highest turbidity (in mg L^{-1}) observed between 1600 and 2200 m water depth. Black diamonds at 0 m indicated where CTD stations are located; white symbols are the locations where the bottom landers were deployed.

Table 3.1: Overview of lander metadata and ranges of current speed, C_{org} and Chlorophyll-a. Abbreviations avg and SD stand for average and standard deviation, respectively.

Station	Start	End	Depth (m)	Peak current ($m\ s^{-1}$)	Average current ($m\ s^{-1}$)	C_{org} range ($mg\ L^{-1}$)	C_{org} avg	C_{org} SD	Chl-*a* range ($ng\ L^{-1}$)	Chl-*a* avg	Chl-*a* SD
64PE421-ST70	21-05-2017 21:08	23-05-2017 10:22	516	0.20	0.10	0.007-0.01	0.008	0.001	0.18-2.88	2.12	0.69
64PE437-ST23	15-05-2018 19:00	17-05-2018 11:25	906	0.27	0.08	0.01-0.03	0.015	0.005	0.65-2.65	1.93	0.59
64PE453-ST13	12-06-2019 06:50	11-06-2019 10:25	1650	0.58	0.19	0.02-0.09	0.053	0.020	0.05-5.95	3.70	1.67
64PE453-ST23	12-06-2019 19:35	14-06-2019 06:55	2322	0.36	0.13	0.01-0.04	0.023	0.009	0.41-2.64	1.11	0.59
64PE453-ST44	15-06-2019 21:35	17-06-2019 17:30	2785	0.22	0.08	0.005-0.009	0.007	0.001	0.12-1.1	0.47	0.22
64PE421-ST20	16-05-2017 22:38	18-05-2017 09:14	3420	0.20	0.09	0.004-0.009	0.006	0.001	0.14-0.34	0.25	0.08

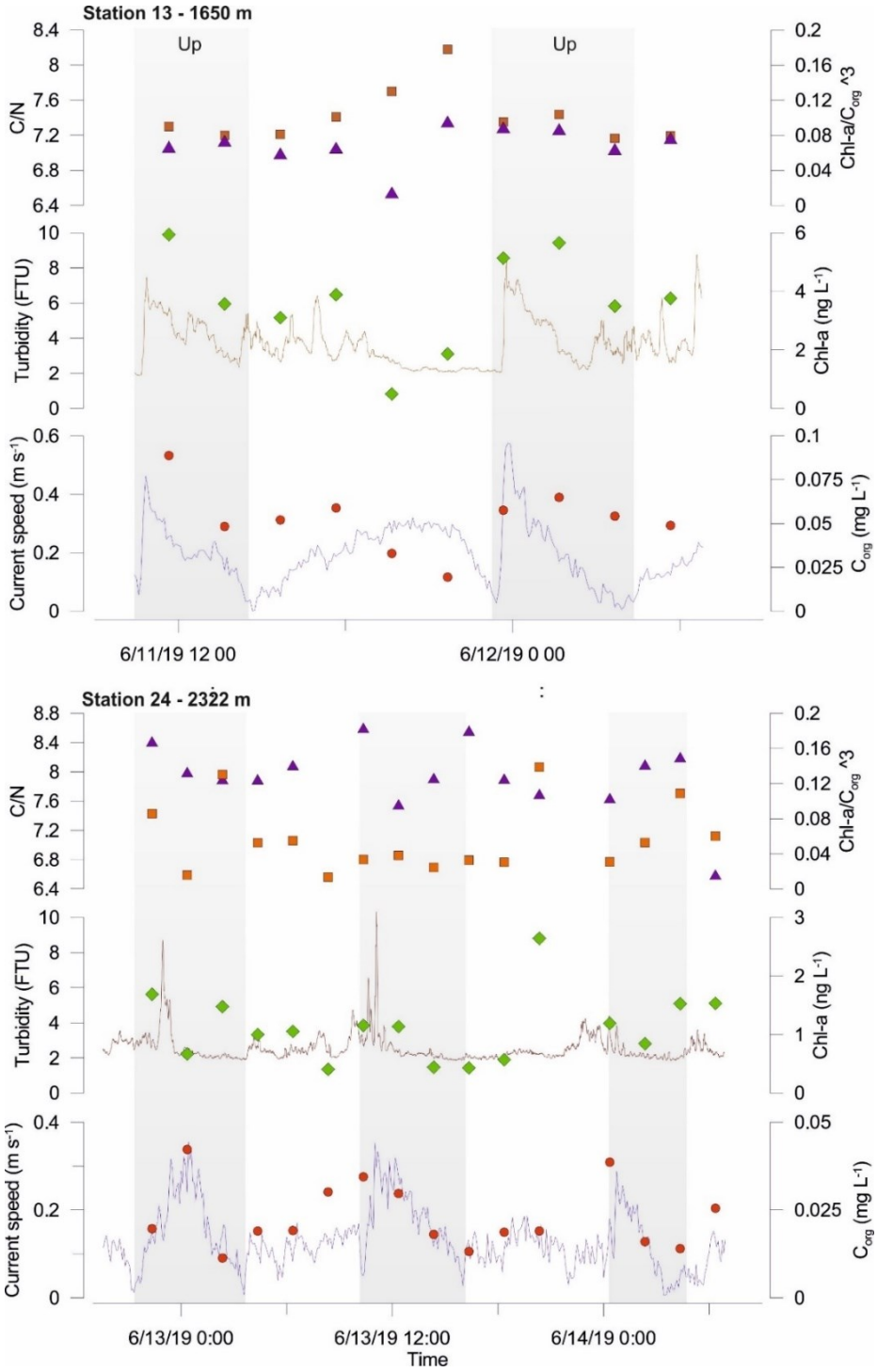

Figure 3.3: Time series of two lander deployments at station 13 (1650 m) and station 24 (2322 m), showing temporal variability in resuspension of matter during a tidal cycle. Highest current speeds correspond to increases in turbidity, resulting in increased C_{org} concentrations.

In bottom water samples collected with CTD-Rosette at 10 m above the canyon thalweg, total SPM mass concentrations ranged from 0.1-1.4 mg L^{-1}. A more comprehensive view of the variability in concentration and composition of the suspended particulate fraction the near-bottom water along the thalweg was obtained from the samples collected with the in situ pump. While characteristics of the SPOM collected with the McLane pump do not appear correlated with current and turbidity dynamics for most of the lander sites along the thalweg, there seems to be a correlation at the 1650 m water depth where marked increases in bottom water turbidity occurred during peaks in tidal current speeds mainly during up-canyon flow (Fig. 3.3). Along with increases in turbidity, the concentration of suspended C_{org}, N_{tot} and Chl-*a* also increased.

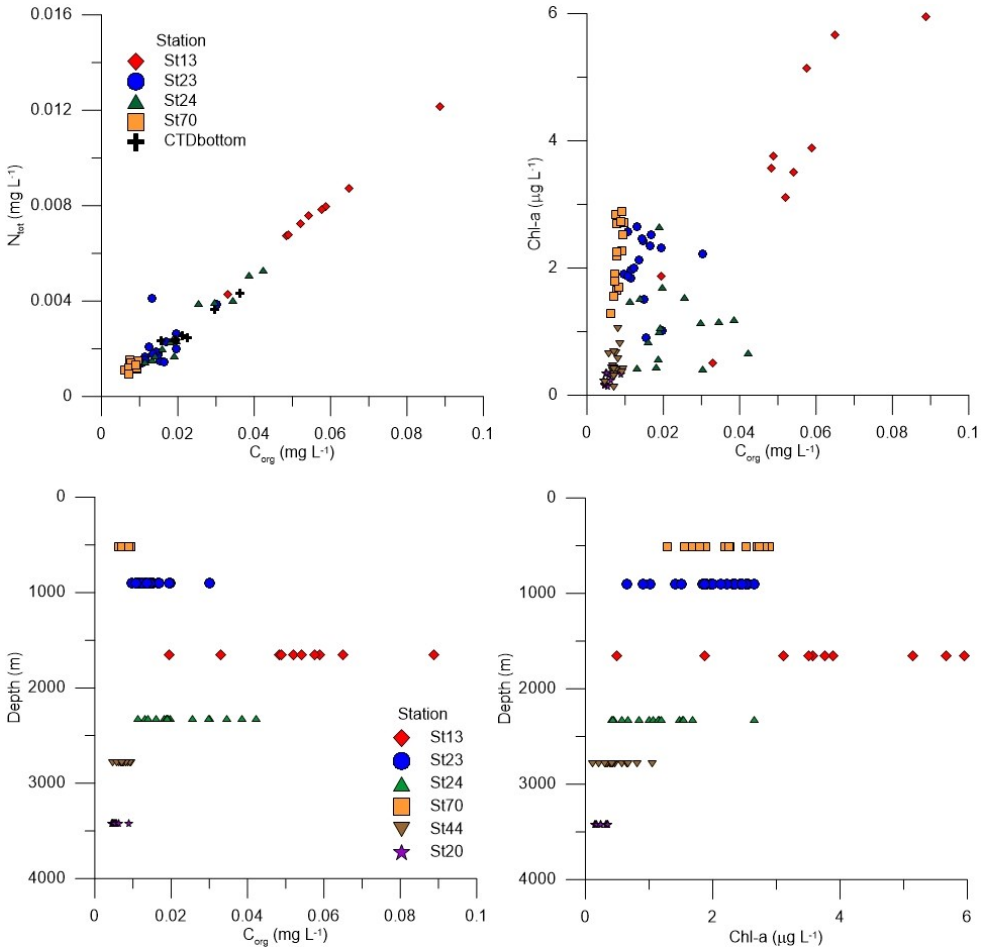

Figure 3.4: Suspended particulate organic matter collected with the McLane pump at 40 cm above the bottom. A) C_{org} vs N_{tot}; B) C_{org} vs Chl-a; C) C_{org} vs depth; D) Chl-a vs depth.

However, Chl-*a*/C_{org} ratios were low during peaks in current speed, while highest values were observed during periods of low current speed (Fig. 3.3). At 2322 m water depth high current speeds corresponded to peaks in turbidity and increased C_{org} concentration. However, increases in C_{org} were not correlated with increasing Chl-*a* concentrations (Fig. 3.3).

The concentration of suspended particulate C_{org} collected with the McLane particle pump ranged from 0.004-0.089 mg L^{-1}. The highest values, but also the greatest variation in values over time, were observed at 1650 m water depth (Fig 3.4). Distinctively lower values, but also lesser variation over time, were observed towards the shallower and deeper parts of the thalweg (respectively at 516 and 3420 m depth). The concentration of suspended particulate N_{tot} ranged from 0.001-0.012 mg L^{-1} (Fig. 3.4). The spatial and temporal variation in N_{tot} values followed the pattern observed in C_{org}, except for the two deepest sites along the thalweg (2785 and 3420 m depth), where the amount of sample collected with the pumps was too low for reliable analysis of N_{tot}. The concentration of suspended Chl-*a* ranged from 0.12-5.95 ng L^{-1}.

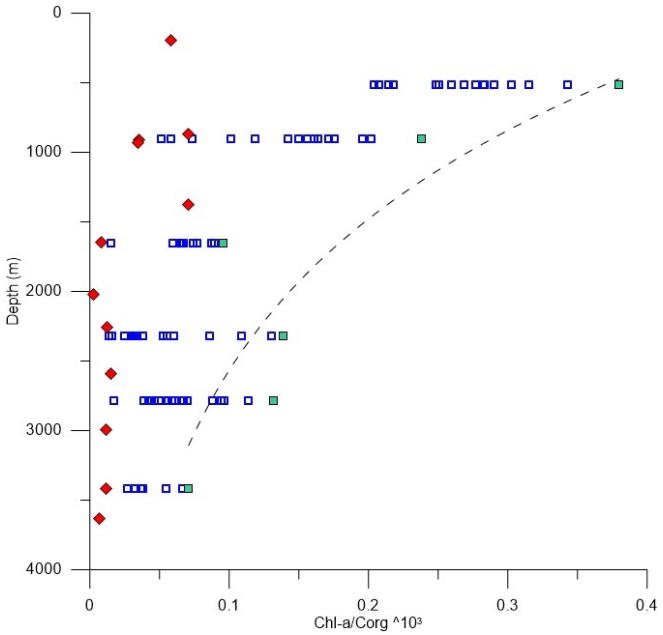

Figure 3.5: Chl-a/C_{org} ratio of SPOM and surface sediment. The blue and green squares represent Chl-a/C_{org} ratio in suspended particulate matter collected in the near-bottom water with an in-situ pump. The dashed line is a logarithmic function fitted on the highest Chl-a/C_{org} ratios, marked with green squares. Red diamonds represent Chl-a/C_{org} ratio in surface sediment of the canyon thalweg.

Similar to suspended C_{org} and N_{tot}, the highest values and the greatest variation in values over time were observed at 1650 m depth, but different from the former two, suspended Chl-*a* values showed a distinct overall decrease with depth along the thalweg (Fig. 3.4). The molar C_{org}/N_{tot} ratio in the suspended particulate fraction ranged from 6.0-11.3 (for as much as N_{tot} could be determined reliably). The Chl-*a*/C_{org} ratio in the suspended particulate fraction showed a distinct decrease in overall values and in variability over time with depth along the thalweg, with the 1650 m site as notable exception. At the latter site, both overall values as well as variability over time fall below the general trend observed along the thalweg (Fig. 3.5). Stable isotopes of C_{org} and N_{tot} in the suspended particulate fraction could be determined reliably only in a number of samples of the sites at 906, 1650 and 2322 m depth. Values of $\delta^{13}C$ ranged between -25.0 and -22.5 ‰, with overall more negative values and the largest variability over time at the 906 and 2322 m sites and in comparison, less negative values, and less variability over time at the 1650 m site. Values of $\delta^{15}N$ ranged between 0.6 and 5.6‰, with overall low values and little variability over time at the 1650 m site.

3.3.2. Surface sediment

Sediment C_{org} and N_{tot} content were found to increase with depth along the canyon thalweg (Fig. 3.6). At depths down to 2000 m C_{org} content was between 0.1 and 0.4%, while further down the thalweg values between 0.4 and 0.9% were found. Overall, the sediments were more enriched in C_{org} compared to N_{tot} in the deep part of the canyon, resulting in an increase in the molar C/N ratio. Content of Chl-*a* appeared highly variable along the thalweg, with both the lowest and the highest values, respectively 0.01 and 0.16 ng g^{-1}, found in the middle reaches of the canyon, and intermediate values at the shallower and deeper end of the thalweg.

The Chl-*a*/C_{org} ratio of the sediments showed a different pattern with highest values in the upper part of the canyon and decreasing values at greater water depths in the lower part of the canyon, but with the lowest values in the middle part where a maximum in bottom water turbidity was found (Fig. 3.4). Stable isotopes in sediment showed little variability in $\delta^{15}N$ (average 5.43‰), which was the same for $\delta^{13}C$ (average -22.5 ‰ V-PDB).

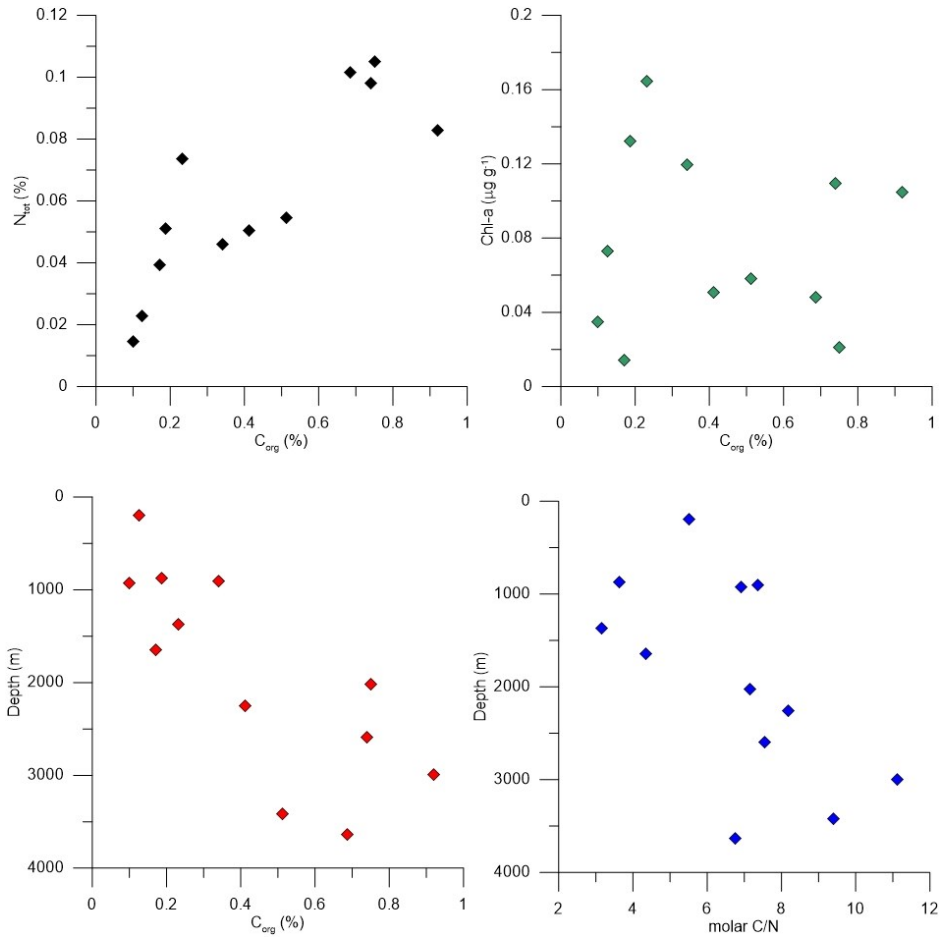

Figure 3.6: Geochemical composition of surface sediment collected with a mono and multi corer. A) C_{org} vs N_{tot}; B) Chl-a vs C_{org}; C) Depth vs. C_{org}; D) Chl-a vs depth.

3.4. Discussion

Submarine canyons are geomorphological features locally affecting the marine carbon cycle (Walsh, 1991). However, the exact role of submarine canyons herein remains poorly constrained. Consequently, marine organic carbon fluxes in Earth System Models are represented by vertical organic carbon transport and do not incorporate lateral transport yet (Moore et al., 2004). Submarine canyons incising continental slopes form important conduits for the transport of organic matter from the biologically productive shelf towards the deep sea. Different processes have been identified that contribute to lateral transport of particulate matter in submarine canyons. The most common are episodic turbidity flows capable of transporting large volumes of sediment from shallower to deeper parts of the canyon, and

tidal currents driving a continuous cycle of resuspension, transport, and deposition of matter (Puig et al., 2014). The first process occurs intermittently at intervals of weeks or months in extremely active canyons and to thousands of years in less active canyons. Due to the long intervals of inactivity that typically occur in between major turbidity current events, this process is most relevant for transport of particulate matter on geological time scales. The second process is of a continuous nature, and for that reason relevant for transport of biologically active organic matter. So far, several studies focussed on the quantification of the particle load in the water column (de Stigter et al., 2007; Dahl et al., 2012; Haalboom et al., 2021), while only few studies addressed organic matter concentrations, fluxes and their variability through time and space (Kiriakoulakis et al., 2011).

Both particle transport processes as described above have been observed in the easternmost branch of Whittard Canyon. Multiple (~7) large turbidity currents were observed during 2019, changing the paradigm that land-detached submarine canyons are inactive during sea level high-stands. During these events large volumes of particulate matter were transported down the easternmost branch of Whittard Canyon within a short time frame of hours to days (Heijnen et al., 2022). In addition, intermediate and bottom nepheloid layers, extending up to several hundreds of meters above the canyon thalweg, were observed in the present study during consecutive years (2017-2019) in the easternmost branch of Whittard Canyon, in particular between 1600 and 2300 m water depth. These nepheloid layers are likely a permanent feature in Whittard Canyon, since they were also observed in other studies (Wilson et al., 2015b), where substantial variability in concentrations was observed following storm events and related to fishery activities (Wilson et al., 2015a; Wilson et al., 2015b; Daly et al., 2018). Nepheloid layers are produced by the interaction of the steep canyon topography and internal wave action, resulting in continuous cycles of resuspension of bottom sediments (Hall et al., 2017; Haalboom et al., 2021; van Haren et al., 2022). Semi-diurnal internal tides in Whittard Canyon are produced at the shelf break and travel along and across the canyon slopes with highest energy dissipation mid canyon (Aslam et al., 2018). This is in line with our observations in the easternmost canyon branch, showing highest current speeds, highest turbidity and highest SPOM concentrations in the middle reaches of the canyon. At these depths, peak current speeds were strong enough to resuspended fine sediments, surpassing the critical erosion threshold (Thomsen and Gust, 2000).

Different zones can be distinguished based on differences in SPOM composition observed along the canyon axis. In the upper reaches of the canyon, relatively low concentration of suspended C_{org} were measured, but the relatively high content of Chl-*a* indicates that it comprised more labile material in comparison to the SPOM sampled at greater depth down the canyon thalweg. The higher content of labile organic matter may be explained by the shallower water through which the SPOM had settled and shorter horizontal distance over which it had been transported through the canyon. At mid-canyon depth the continuous process of resuspension, transport and redeposition of sediment was reflected in the highest yet also most variable concentrations of suspended C_{org} during a tidal cycle, while the lowest Chl-*a*/C_{org} ratio in the SPOM suggests that the suspended matter comprised not only freshly settled organic matter, but that also older and more degraded organic matter incorporated in seabed sediment is resuspended during each tidal cycle. The lander data showed that particles are resuspended during periods of highest current speed in one tidal cycle, which were mainly observed during up-canyon flow, resulting in increasing concentrations of total particles, C_{org} and Chl-*a* (Figure 3.3). This was only observed at mid-canyon sites, while at shallower and deeper depths no correlation between current speed and C_{org} concentrations was observed. In the deeper parts of the canyon relatively low concentrations of suspended C_{org} were measured, while based on the Chl-*a*/C_{org} ratio the SPOM appeared more degraded than the SPOM collected in the upper reaches of the canyon. This is likely related to degradation by zooplankton and oxic remineralisation by microbes during settling of the organic matter through the deep water column (Frischknecht et al., 2018). However, the Chl-*a*/C_{org} ratio was not as low as in the SPOM in the middle part of the canyon, where fine particulate matter is held longer in suspension by dynamic tidal currents and exposed to more intense degradation, and where more sedimentary organic matter is admixed. Similar spatial trends were observed earlier in a canyon along the Portuguese margin, where suspended organic matter derived from multiple sources underwent significant alteration before being deposited (Kiriakoulakis et al., 2011).

Overall, organic matter being transported through the canyon via nepheloid layers may not be consistently recorded in the sediment, due to low burial efficiency of marine derived organic matter that in suspension is more readily consumed by micro- to megafauna (Maier et al., 2019b). Nevertheless, the trend of progressive state of degradation of bottom water SPOM as

noted in decreasing Chl-*a*/C_{org} ratio with increasing depth down the canyon, with a minimum at mid-canyon depth, seems to be reflected also in the underlying sediment of the thalweg. However, while progressive degradation should result in loss of OM, the sediment shows a clear increase in C_{org} content with depth. Grainsize analyses of the surface sediments along the canyon axis have shown that sediment become finer with increasing water depth (Haalboom et al., 2021), which is explained by winnowing of fines from sediment in the upper canyon and deposition of fines further down the canyon. This fining can explain (part of the) observed increased in C_{org} towards the deepest parts of the canyon, since organic matter mainly adsorbs to the silt and clay fraction (Mayer, 1994). The adsorption to clay particles shields the organic matter from degradation as the enzymes used by microorganisms can no longer access the organic matter, which is needed for their metabolic breakdown (Hedges and Keil, 1995). Still, such a shielding is probably only effective for the first few organic molecular monolayers and excess organic matter adhered to the suspended matter would still become increasingly degraded. That way the continued addition of new organic matter settling through the water column would enrich the particles with C_{org}, albeit degraded organic matter. Over time this results in a zone rich in degraded organic matter. Consequently, the organic matter would also become increasingly depleted in nitrogen as was observed in the surface sediments with depth, as amino acids are preferentially remineralised by suspension and filter feeding fauna, as well as bacterial activity (Hunter et al., 2013). As marine organic matter generally contains more amino acids whereas terrestrial organic matter is more characterised by refractory compounds, poor in nitrogen, this ultimately results in the deposition of organic matter with a more terrestrial signature, as was also observed in the Monterey and Nazaré Canyon (Kiriakoulakis et al., 2011; Maier et al., 2019b).

While winnowing of fines from upper canyon sediments and their redistribution towards deeper reaches of the canyon may explain the observed fining of surface sediment and increase in C_{org} content with increasing depth along the thalweg, it does not match with the notion of maximum resuspension activity in the middle part of the canyon as derived from bottom water turbidity records from CTD and landers, and the observations that sediment resuspension in the middle canyon seemed mostly associated with up-canyon flow of the bottom water. Resuspension and up-canyon flow would on the long run produce winnowed, relatively coarse-grained sediment in the middle canyon, while moving fines towards

shallower area. From the actual trends in sediment characteristics we can thus infer that other processes such as the mentioned sediment gravity flows must play an important role too in shaping of the sediment cover. Each individual gravity flow, whether only small and localised, or large and traversing different depth zones of the canyon, will along its path down the canyon preferentially pick up the finer sediment while leaving the coarser part behind, and when decelerating loose the coarser part of its suspended load first and the finer part only later. Larger gravity flows such as documented by Heijnen et al. (2022), originating in the upper canyon and running out until the lower canyon, may effectively pass through the middle canyon area of intense reworking, and bring relatively fresh organic matter directly to the lower canyon.

The lateral transport of organic matter not only influences the redistribution and deposition of organic carbon, but also impacts faunal community distribution patterns. Submarine canyons have been recognised as hotspots of biodiversity due to habitat heterogeneity and higher particulate organic carbon content when compared to the open slope environments (Duineveld et al., 2001). Bottom dwelling fauna in zones with highest organic matter deposition in Nazaré and Baltimore Canyon seem highly specialised with high biomass and low biodiversity (Cunha et al., 2011; Robertson et al., 2020). Similar patterns are thus expected in Whittard Canyon since a similar zonation in organic matter deposition was observed. Canyon walls on the other hand have shown to be hotspots of biodiversity and biomass likely related to the continuous resuspension and delivery of (fresh) organic matter with each tidal cycle (Huvenne et al., 2011; Pearman et al., 2023). Cold-water corals that are known to mainly feed on fresh phytodetritus are mainly observed in the shallow parts of Whittard Canyon (Morris et al., 2013).

To conclude, lateral transport via nepheloid layers will not result in rapid deposition of organic matter as the continuous resuspension also enhances remineralisation and fuels the rich benthic fauna. However, intermittent gravity flows can play a major role in this, releasing high amounts of degraded material from the upper canyon and slopes towards the deeper parts, essentially bypassing the processes of continuous resuspension in the middle canyon described above. Also, Whittard Canyon experiences multiple turbidity currents each year, as was observed by long term mooring deployments. At the moment it is still unclear what

triggers these intermittent turbidity currents that can be related to natural or anthropogenic processes like trawling on the interfluves (Heijnen et al., 2022). These episodes of fast transport and subsequent burial under low oxygen conditions rapidly removes organic matter out of the zone of oxic degradation, reducing the oxygen exposure time. This results in a shift of the depocenter of organic matter, making submarine canyons a carbon sink in some places (Masson et al., 2010). Ultimately the impact on global carbon cycling is most likely limited due to the rather restricted area involved. Also, on a geological time scale, the impact on the carbon cycle is probably limited as the zones characterised by high turbidity probably varied. Still on time scales relevant for our current anthropogenic disturbance of the carbon cycle and in view of the large amounts of organic carbon involved it might be worth protecting depocenters rich in highly reactive organic matter from anthropogenic activities as this potentially would expose the organic matter to conditions favourable for their rapid decay and release of currently trapped carbon.

Acknowledgements

The authors would like to thank the captain and crew of the RV *Pelagia* as well as NIOZ technicians for their help during cruises 64PE421, 64PE437 and 64PE453. We greatly acknowledge the help of Ronald van Bommel, Sharyn Ossebaar and Jort Ossebaar with the carbon and nitrogen analyses. Moreover, we thank Ilsa Posthuma for the assistance during the chlorophyll analyses. This study was funded by the innovational research scheme of NWO under grant agreement 0.16.161.360. SH and HdS received funding from the Blue Nodules project (EC grant agreement 688785).

Supplementary material

Table S3.1: List of stations.

Cruise	Station	Datum	Sampling method	Longitude	Latitude	Depth (m)
64PE421	ST07	15/05/2017 10:43	CTD-Mono core	-10.1218	48.8299	195
64PE421	ST08	15/05/2017 11:59	CTD	-10.1182	48.7606	542
64PE421	ST09	15/05/2017 13:32	CTD-Mono core	-10.0879	48.7131	871
64PE421	ST10	15/05/2017 15:26	CTD-Mono core	-10.0169	48.6408	1372
64PE421	ST11	15/05/2017 17:47	CTD-Mono core	-9.9430	48.5838	1644
64PE421	ST12	15/05/2017 20:19	CTD-Mono core	-9.9373	48.4925	2254
64PE421	ST13	15/05/2017 22:45	CTD-Mono core	-9.9428	48.4299	2593
64PE421	ST14	16/05/2017 01:23	CTD-Mono core	-10.0031	48.3911	2995
64PE421	ST15	16/05/2017 05:09	CTD-Mono core	-10.1634	48.2991	3419
64PE421	ST16	16/05/2017 08:50	CTD-Mono core	-10.2180	48.1545	3634
64PE421	ST20	16/05/2017 21:32	ALBEX-lander	-10.1632	48.2990	3420
64PE421	ST24	17/05/2017 10:27	Multicore	-10.0594	48.6943	907
64PE421	ST25	17/05/2017 11:40	Multicore	-10.0755	48.6912	928
64PE421	ST58	20/05/2017 16:11	CTD-Mono core	-9.9350	48.5295	2023
64PE421	ST70	21/05/2017 20:41	ALBEX-lander	-10.0658	48.6318	516
64PE437	ST23	15/05/2018 18:07	ALBEX-lander	-10.0587	48.6946	906
64PE453	ST13	11/06/2019 09:55	ALBEX-lander	-9.9387	48.5830	1650
64PE453	ST21	12/06/2019 08:39	CTD	-9.9387	48.5830	1668
64PE453	ST24	12/06/2019 18:46	ALBEX-lander	-9.9440	48.4733	2322
64PE453	ST35	14/06/2019 09:03	CTD	-9.9445	48.4732	2338
64PE453	ST44	15/06/2019 20:20	ALBEX-lander	-9.9507	48.4165	2785
64PE453	ST57	18/06/2019 09:27	CTD	-9.9506	48.4152	2452

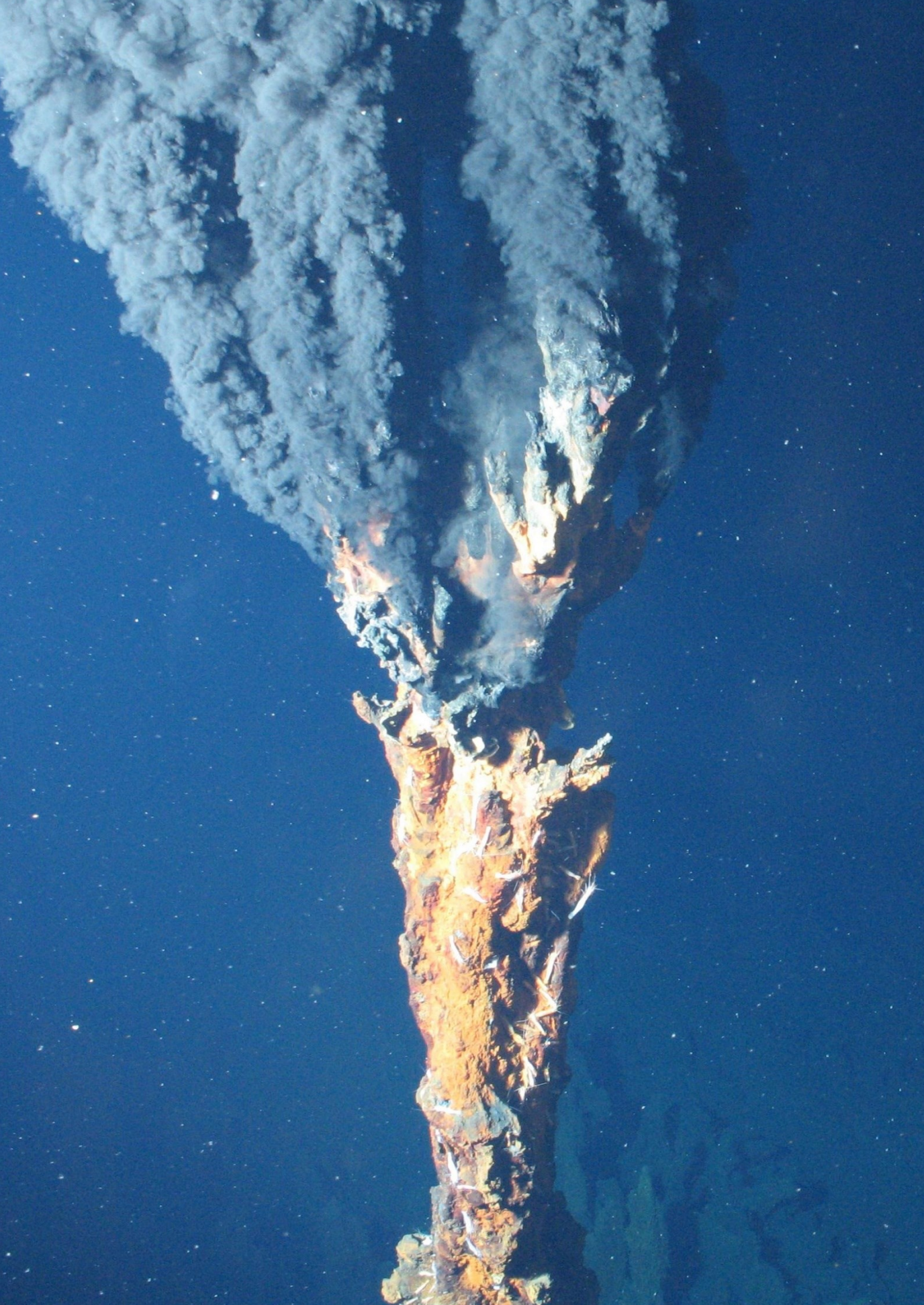

Chapter 4: Patterns of (trace) metals and microorganisms in the Rainbow hydrothermal vent plume at the Mid-Atlantic Ridge

Sabine Haalboom*, David Price*, Furu Mienis, Judith van Bleijswijk, Henko de Stigter, Harry Witte, Gert-Jan Reichart & Gerard Duineveld

*These authors contributed equally to this work.

Published as:

Haalboom, S., Price, D.M., Mienis, F., van Bleijswijk, J.D.L., de Stigter, H.C., Witte, H.J., Reichart, G.-J., & Duineveld, G.C.A., 2020. Pattern of (trace) metals and microorganisms in the Rainbow hydrothermal vent plume at the Mid-Atlantic Ridge. Biogeosciences, v. 17, 2499-2519. https://doi.org/10.5194/bg-17-2499-2020

Image: A hydrothermal vent from the Rainbow hydrothermal vent field. Image taken by the ROV Victor 6000 during the Biobaz cruise in 2013. Photo courtesy: Ifremer (2013).

Abstract

Hydrothermal vent fields found at mid-ocean ridges emit hydrothermal fluids that disperse as neutrally buoyant plumes. From these fluids seafloor massive sulphides (SMS) deposits are formed, which are being explored as possible new mining sites for (trace) metals and rare earth elements (REEs). It has been suggested that during mining activities large amounts of suspended matter will appear in the water column due to excavation processes and discharge of mining waste from the surface vessel. Understanding how hydrothermal plumes can be characterised by means of geochemistry and microbiology as they spread away from their source and how they affect their surrounding environment may help in characterising the behaviour of the dilute distal part of chemically enriched mining plumes.

This study on the extensive Rainbow hydrothermal plume, observed up to 25 km downstream from the vent site, enabled us to investigate how microbial communities and (trace) metal composition change in a natural plume with distance. The (trace) metal and REE content of suspended particulate matter (SPM) was determined using sector field inductively coupled plasma mass spectrometry (SF-ICP-MS) with high resolution (HR), and the microbial communities of the neutrally buoyant plume, above-plume, below-plume, and near-bottom water and sediment were characterised by using 16S rRNA amplicon sequencing methods. Both vertically in the water column and horizontally along the neutrally buoyant plume, geochemical and biological changes were evident, as the neutrally buoyant plume stood out by its enrichments in (trace) metals and REEs, as, for example, Fe, Cu, V, Mn and REEs were enriched by factors of up to ~80, ~90, ~52, ~2.5 and ~40, respectively, compared to above-plume water samples taken at 1000 m water depth. The concentrations of these elements changed as the plume aged, shown by the decrease in element/Fe molar ratios of chalcophile elements (Cu, Co, Zn), indicative of rapid removal from the hydrothermal plume or removal from the solid phase. Conversely, increasing REE/Fe molar ratios imply uptake of REEs from the ambient seawater onto Fe-oxyhydroxides. This was also reflected in the background pelagic system, as Epsilonproteobacteria started to dominate, and univariate microbial biodiversity declined with distance away from the Rainbow hydrothermal vent field. The Rainbow hydrothermal plume provides a geochemically enriched natural environment, which is a heterogeneous, dynamic habitat that is conducive to ecological changes in a short time

span. This study of a hydrothermal plume provides a baseline study to characterise the natural plume before the interference of deep-sea mining.

4.1. Introduction

Hydrothermal vent fields found at mid-ocean ridges and back-arc basins are known for discharging fluids rich in potential microbial energy sources, such as H_2, H_2S, CH_4, NH_4 and Fe (Jannasch and Mottl, 1985; McCollom, 2000). In addition, they are characterised by the presence of polymetallic sulphide deposits containing high grades of metals like Cu, Co, Zn, and rare earth elements (REEs) (Cave et al., 2002; Chavagnac et al., 2005). Because of the steadily increasing demand for these metals and their geopolitical distribution on land, hydrothermal vent deposits are explored as new mining sites (Hoagland, 2010). Since such areas accommodate unique and vulnerable marine life, serious concerns exist about the environmental sustainability of seafloor massive sulphide (SMS) deposit mining (Boschen et al., 2013; Collins et al., 2013), especially with regard to the effects of the different plumes, which are generated during the excavation of ores and by the return flow of wastes in the vicinity of hydrothermal vents (Ramirez-Llodra et al., 2011; Vare et al., 2018). As SMS mining will concentrate on deposits around hydrothermal vents and not on active vents or chimneys due to technical risks associated with high temperatures (Gwyther et al., 2008), it is likely that the background and extinct vent communities (from microorganisms to megafauna) will be impacted through habitat loss, mechanical destruction, noise, smothering and bioaccumulation of toxic substances (Levin et al., 2016a). However, knowledge about the background ecosystem and natural plume is sparse, as the vents and their proximal fauna have attracted most of the attention in, for example, microbiology (e.g. Han et al., 2018; Cerqueira et al., 2018).

To fill this gap, the Dutch TREASURE project (STWNWO) was focussed on describing the structure of the background pelagic and benthic communities of an active hydrothermal vent site with SMS deposits on the Mid-Atlantic Ridge (MAR). The Rainbow hydrothermal vent (36° 14” N on the MAR) was selected for this study as it ejects one of the most prominent and persistent natural plumes on the MAR. Hydrothermal plumes represent a distinct natural ecosystem in itself, which under the influence of currents may extend tens of kilometres away from its point of origin. Basic knowledge of natural plumes is essential to be able to discern

impacts arising from future SMS mining plumes created in the vicinity of the hydrothermal vent, which are likely to interfere with the natural hydrothermal plume. Though mining plumes will have a higher initial density and therefore tend to sink rather than maintain buoyancy (Gwyther et al., 2008; Boschen et al., 2013), the finest and slowest-sinking fraction of suspended solids in the mining plume may interfere with the natural plume during its dispersal, especially when released above the seafloor.

Since the discovery of the Rainbow hydrothermal vent field in 1996 by German et al. (1996), several studies concerning the composition of the hydrothermal fluid and the sediment influenced by fallout of particulates from the Rainbow and other hydrothermal plumes have been published. These showed, for example, that the underlying host rock influences the hydrothermal fluid composition (Wetzel and Shock, 2000; Marques et al., 2006). Geochemical investigation of sediment by Cave et al. (2002) at distances of 2 to 25 km from the Rainbow hydrothermal vent field showed enrichments of Fe, Cu, Mn, V, As and P, as well as REEs (Chavagnac et al., 2005), as a result of fallout from the hydrothermal plume. It has further been shown that microbial activity influences geochemical processes in the plume (Breier et al., 2012; Dick et al., 2013), such as scavenging and oxidation of metals (Cowen and Bruland, 1985; Cowen et al., 1990; Mandernack and Tebo, 1993; Dick et al., 2009), influencing the local ocean geochemistry.

Microbial activity within the plume is fuelled by redox reactions that provide energy for chemolithoautotrophic microbial taxa. The abundance of energy sources within plumes and hydrothermal systems supports a plethora of chemolithoautotrophic microbial communities (e.g. Orcutt et al., 2011; Frank et al., 2013; Anantharaman et al., 2016). Plume microbial communities can be distinct or relatively similar to background communities (Dick and Tebo et al., 2010; Sheik et al., 2015; Olins et al., 2017), with plume associated bacteria originating from either seafloor communities, background seawater communities or from growth within the plume (Dick et al., 2013). Djurhuus et al. (2017) observed the reduction in dominance of vent-associated microorganisms with increased redox potential, suggesting that communities associated with the initial rising plume become diluted on a scale of metres. Comparatively little is known about changes in chemical composition and microbial assemblages in the hydrothermal plume after its initial rise, when it becomes neutrally buoyant and is dispersed

by currents, remaining traceable in particulate form at least 50 km away from its source (Severmann et al., 2004) and even up to 4000 km in dissolved form (Resing et al., 2015). Considering the majority of microbial growth is predicted to occur in the neutrally buoyant portion of the plume (Reed et al., 2015), further efforts should be concentrated on sampling this portion of the plume.

In order to address this gap, water column and sediment samples from the Rainbow hydrothermal vent area were investigated during the TREASURE cruise. Geochemical and biological changes were explored vertically in the water column and horizontally along the neutrally buoyant plume using sector field inductively coupled plasma mass spectrometry (SF-ICP-MS) with high resolution (HR) to determine the (trace) metal and REE content of the suspended particulate matter (SPM). Next-generation sequencing methods were used to quantify the microbial diversity in the pelagic system, which was influenced by the hydrothermal plume. Whilst mechanical understanding of microbial and geochemical interactions in the plume would have required a different experimental setup, which was beyond the scope of the TREASURE project, this paper aims to contribute to knowledge of geochemical and biological heterogeneity in the surroundings of an SMS site, induced by the presence of an active hydrothermal plume, which should be taken into account in environmental impact assessments of SMS mining.

4.2. Material and methods

4.2.1. Study site

The Rainbow hydrothermal vent field (Fig. 4.1) is located on the Mid-Atlantic Ridge (MAR) at 36° 13.80 N, 33° 54.14W, at approximately 2300 m water depth, southwest of the Azores. The vent field is located on the western flank on the non-volcanic Rainbow Ridge, in an offset between the South Alvin Mid-Atlantic Ridge (AMAR) and AMAR segments of the MAR (German et al., 1996; Fouquet et al., 1998; Douville et al., 2002). It is located at the intersection between the non-transform fault system and the ridge faults (Charlou et al., 2002), making this vent field tectonically controlled. The vent field, which is approximately 100 m by 250 m in size, is underlain by a basement composed of ultramafic rocks (Edmonds and German, 2004; Marques et al., 2006). The ultramafic setting of Rainbow is atypical for the region, which is dominated by basalt-hosted vent systems (Douville et al., 2002). Due to serpentinization

reactions during the circulation of the hydrothermal fluid in the peridotite basement rocks, the Rainbow vent field produces plumes particularly enriched in transition metals (notably Fe, Mn, and Cu) and REEs (Douville et al., 2002; Findlay et al., 2015). On the contrary, the plumes are depleted in hydrogen sulphides (Charlou et al., 2002; Douville et al., 2002), resulting in relatively high metal/sulphide ratios. Consequently, the chimneys and the SMS deposits of the Rainbow hydrothermal field are enriched in Cu, Zn, Co, and Ni when compared to vent systems with a basaltic host rock (Charlou et al., 2002).

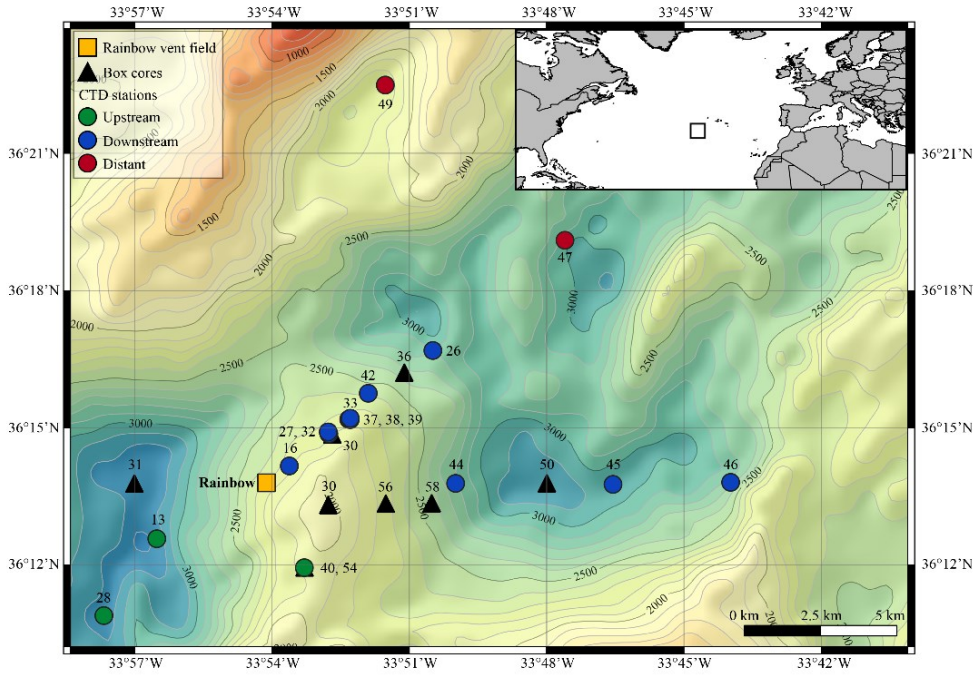

Figure 4.1: Geographical location (inset) and bathymetric map of the Rainbow study site of the Mid-Atlantic Ridge (from the European Marine Observations and Data Network, EMOD, database), with sampling locations depicted.

The vent field consists of 10 active, high-temperature (365 °C), black smokers and emits an extensive plume with a distinct chemical composition compared to the ambient seawater (Severmann et al., 2004). The plume is considered the largest and widest spreading in the region (German et al., 1996), rising up to 200 m above its source and traceable over at least 50 km (Severmann et al., 2004). Controlled by the local hydrodynamic regime and topography (Thurnherr and Richards, 2001; Thurnherr et al., 2002), the neutrally buoyant plume moves

predominantly to the north and east around the Rainbow Ridge with an average current speed of 5–6 cm s^{-1} and continues in a northward direction along the southern and eastern side of the rift valley of the AMAR segments (Edmonds and German, 2004). Characteristics and behaviour of the Rainbow plume are relatively well studied, which make the Rainbow vent field a suitable site to study neutrally buoyant plumes.

4.2.2. Water column and sediment sampling

Water samples and sediment cores were collected along the path of the plume during RV *Pelagia* cruise 64PE398 in April 2015. Five putatively distinct biotopes were sampled: (i) above-plume (1000 m water depth), (ii) plume, (iii) below-plume (10 m above the bottom), (iv) near-bottom water and (v) sediment.

Using conductivity, temperature, and depth (CTD) casts with a Seabird 911 CTD rosette system, the plume was traced in real time using turbidity as an indicator, measured in Nepheloid Turbidity Units (NTUs) with a WetLabs turbidity sensor. Other variables measured included temperature (°C), salinity, density (σ-θ, kg m^{-3}), dissolved oxygen (ml L^{-1}) and chlorophyll (µg L^{-1}). At five stations, continuous yo-yo CTD casts were taken over the course of 12 h to study the temporal changes of the hydrothermal plume.

A total of 41 water samples were collected using 12 L Niskin bottles from 11 downstream stations, 2 distal downstream stations and 3 upstream stations. Once the CTD was back on deck, three distinct water samples were immediately taken for SPM, trace metals and the microbial community. Depths for sampling SPM were chosen to comprise the largest variation in turbidity measured by the WetLabs turbidity sensor in a vertical profile so that the sensor could be reliably calibrated, and readings converted to milligrams per litre. If possible, trace metal and microbial community samples were taken at the same stations and/or same depth.

Sediment and near-bottom water samples were collected with a NIOZ-designed box corer of 50 cm diameter equipped with a top valve to prevent flushing, subsequently trapping near-bottom water (van Bleijswijk et al., 2015). In total, eight cores were collected (Table 4.1). Due to unsuitable coring substrates, CTD locations and coring sites did not always follow the same track. Box cores were taken on the eastern part of the Rainbow Ridge, continuing in the basin

Table 4.1: Metadata of samples taken.

Station	Latitude	Longitude	Biotope	Sample type	Depth (m)	Micro-biology	SPM	(Trace) metals
30	36°13'19"N	33°52'46"W	Sediment and near-bottom water	Box core	1970	x		
31	36°13'47"N	33°57'00"W	Sediment and near-bottom water	Box core	3190	x		
33	36°14'51"N	33°52'41"W	Sediment and near-bottom water	Box core	2223	x		
36	36°16'13"N	33°51'06"W	Sediment and near-bottom water	Box core	2857	x		
50	36°13'47"N	33°47'60"W	Sediment and near-bottom water	Box core	3157	x		
54	36°11'57"N	33°53'46"W	Sediment and near-bottom water	Box core	2129	x		
56	36°13'21"N	33°51'31"W	Sediment and near-bottom water	Box core	2198	x		
58	36°13'21"N	33°50'31"W	Sediment and near-bottom water	Box core	2514	x		
13	36°12'35"N	33°56'31"W	Above plume	CTD	125	x		
13	36°12'35"N	33°56'31"W	Below plume	CTD	3220	x		
13	36°12'35"N	33°56'31"W	Plume	CTD	2000	x		
16	36°14'10"N	33°53'37"W	Plume	CTD	1944	x		
16	36°14'10"N	33°53'37"W	Above plume	CTD	998	x		
26	36°16'41"N	33°50'29"W	Below plume	CTD	2756	x	x	x
26	36°16'41"N	33°50'29"W	Plume	CTD	2150	x	x	x
26	36°16'41"N	33°50'29"W	Plume	CTD	2000		x	x
26	36°16'41"N	33°50'29"W	Above plume	CTD	999	x	x	x
27	36°16'52"N	33°52'45"W	Below plume	CTD	2191	x		x
27	36°16'52"N	33°52'45"W	Plume	CTD	2077	x		x
27	36°16'52"N	33°52'45"W	Plume	CTD	1996			x
27	36°16'52"N	33°52'45"W	Above plume	CTD	994	x		x
28	36°10'54"N	33°57'40"W	Below plume	CTD	3170	x	x	x
28	36°10'54"N	33°57'40"W	Plume	CTD	1975	x	x	x
32	36°14'55"N	33°52'46"W	Plume	CTD	2192		x	
32	36°14'55"N	33°52'46"W	Plume	CTD	2088		x	
37	36°15'11"N	33°52'19"W	Plume	CTD	2190			x
38	36°15'11"N	33°52'17"W	Plume	CTD	2040			x
39	36°15'13"N	33°52'17"W	Plume	CTD	2019			x
40	36°11'57"N	33°53'18"W	No plume	CTD	2120			x
42	36°15'45"N	33°51'54"W	Plume	CTD	2291	x	x	x
42	36°15'45"N	33°51'54"W	Plume	CTD	2209	x	x	x
42	36°15'45"N	33°51'54"W	Plume	CTD	2037		x	x
42	36°15'45"N	33°51'54"W	Above plume	CTD	999	x	x	x
44	36°13'47"N	33°49'59"W	Below plume	CTD	2623	x		
44	36°13'47"N	33°49'59"W	Plume	CTD	2202		x	x
44	36°13'47"N	33°49'59"W	Plume	CTD	2002	x	x	x
44	36°13'47"N	33°49'59"W	Above plume	CTD	995	x		
45	36°13'46"N	33°46'33"W	Below plume	CTD	3004	x		
45	36°13'46"N	33°46'33"W	Plume	CTD	2166		x	x
45	36°13'46"N	33°46'33"W	Plume	CTD	2002	x	x	x
45	36°13'46"N	33°46'33"W	Above plume	CTD	996	x		
46	36°13'49"N	33°43'59"W	Below plume	CTD	2622	x		
46	36°13'49"N	33°43'59"W	Plume	CTD	2280	x	x	x
46	36°13'49"N	33°43'59"W	Plume	CTD	2145		x	x
46	36°13'49"N	33°43'59"W	Above plume	CTD	1000	x		
47	36°19'06"N	33°47'36"W	Below plume	CTD	2850			
47	36°19'06"N	33°47'36"W	Plume	CTD	2200	x		x
49	36°22'19"N	33°51'31"W	Plume	CTD	2260	x	x	x
49	36°22'19"N	33°51'31"W	Plume	CTD	1902		x	x

east of the ridge, while two cores were taken on the northwestern flank of the ridge, following the path of the plume.

4.2.3. Suspended particulate matter analysis

From each 12 L Niskin bottle, two 5 L subsamples were collected to determine the concentration of SPM. The subsamples were filtered on board over pre-weighed 0.4 µm polycarbonate filters. The filters were rinsed with ~10mL of Milli-Q water to remove salt while still applying under pressure and subsequently stored at -20 °C on board. In the laboratory, the filters were freeze dried and then weighed in duplicate, or in triplicate if the difference between the first two measurements was more than 0.03 mg. To yield SPM mass concentrations, the net dry weight of the SPM collected on the filters (average of 0.25 mg), corrected by the average weight change of all blank filters (0.04 mg), was divided by the volume of filtered seawater (5 L). Subsequently, the filters were examined using a Hitachi TM3000 tabletop scanning electron microscope (SEM) connected to an energy-dispersive spectroscopy (EDS) detector to visualise content of the SPM and to qualitatively analyse the chemical composition. The SEM was operated under an acceleration voltage of 15 kV and a filament current of 1850 mA.

4.2.4. Chemical analysis

For analysis of major and trace metals present in particulate form in and around the hydrothermal plume, water samples were filtered on board over acid-cleaned 0.45 µm polysulfone filters directly from the Niskin bottle at ambient temperature while applying under pressure. A water barrel in between the filtration holder and pump allowed for volume measurements of filtered water. The filters were subsequently stored at -20 °C until further examination. Filters were dried in the laboratory in an Interflow laminar flow bench at room temperature prior to analysis. Subsequently, the filters were placed in acid-cleaned Teflon vials and were subjected to a total digestion method. For this purpose a mixture of 6.5 mL HNO_3 (ultrapure)/HF (suprapure) (10:1) solution, 1 mL HCl (ultrapure) and 1mL $HClO_4$ (ultrapure) was added to the vials, after which the vials were covered and placed in an Analab HotBlock for 48 h at 125 °C. After the filters were completely dissolved, the covers were taken off from the vials and the vials were left for 24 h in order to evaporate the acids. Finally, the residue was taken up again in 10 mL 1M ultra grade HNO_3, and pre-spiked with 5 ppb scandium and 5 ppb rhodium as internal standards. Furthermore, 10 procedural blanks were performed. Half of them were empty acid cleaned Teflon vials, the other five contained an acid-cleaned blank filter in order to correct for the dissolved filters. These blanks were subjected to the same total

digestion method as described above. A SF-ICP-MS (Thermo Element II) at the Royal Netherlands Institute for Sea Research (NIOZ) was used to analyse the concentrations of major and trace metals, as well as REEs. The concentrations were calculated using external calibration lines made from a multi-stock solution, which was prepared by mixing Fluka TraceCert standards for ICP. Rh was used as an internal standard for all elements. The machine drift was measured before, halfway and after each series of samples and was monitored by using an external drift solution. Precision (relative standard deviation, RSD) of these analyses was generally < 2% for major and trace metals, apart from ^{115}In, where the RSD values generally are between 4% and 8%, with maximum values going up to 12.48 %. For REEs, the RSD values were generally < 3%, apart from a few measurements where RSD values reached maximums up to 12.48 %. The accuracy could not be determined as no certified reference material was analysed. A blank correction was applied to the sample data by subtracting average values measured for five dissolved blank filters, which for the majority of the measured elements accounted for less than 10% of the sample values. Subsequently, the data were recalculated to account for the dilution of the samples during the total digestion and the amount of seawater that was filtered to yield the true concentration of each element.

4.2.5. Microbial community

Three distinct samples of 2 L of water were collected from three different Niskin bottles for next-generation sequencing (NGS). The water was filtered immediately after collection through a 0.2 µm polycarbonate filter (Nuclepore), facilitated by a vacuum of 0.2 bar, in a climate-controlled room at 4 °C to limit DNA degradation. From the box cores > 0.25 g of surface sediment was scraped off with a sterilised spatula, whilst 1.5 L of overlying (near-bottom) water was filtered as above. Filters were stored in a 2 mL cryo-vial and all samples were stored at -80 °C on board.

DNA was extracted using a Power Soil DNA Isolation Kit (MoBio, now Qiagen) according to the manufacturer's protocol. Each DNA extract concentration was quantified using a Qubit 3.0 fluorimeter (Qiagen, Inc.) and stored at -20 °C before amplification. Extracts were combined with Phusion Taq (Thermo Scientific), High-Fidelity Phusion polymerase buffer and universal primers to amplify the V4 region of 16S rDNA of bacteria and archaea (Table 4.2), with unique molecular identifier (MID) combinations to identify the different samples. All negative controls

from all polymerase chain reaction (PCR) series were labelled with the same unique MID. The PCR settings were as follows: 30 s at 98 °C, 29 cycles (10 s at 98 °C, 20 s at 53 °C, 30 s at 72 °C) and 7 min at 72 °C. Four and three samples were rerun at 30 and 32 cycles, respectively, in order to yield enough product. Each sample was subjected to the PCR protocol in triplicate and processed independently to avoid bias. A total of 5 µL of product was used to screen the products on an agarose gel. The remaining 25 µL of each triplicate was pooled to evenly distribute the DNA, split into two slots, and run on a 2% agarose gel at 75 volts for 50 min. Sybergold stain was applied post-run for 20-30 min before cutting the 380 bp bands out with a sterilised scalpel over a blue light to avoid UV damage. The two bands of mixed triplicates were pooled, purified using the Qiaquick Gel Extraction Kit (Qiagen, Inc.) and quantified with a Qubit™ 3.0 fluorometer (Qiagen, Inc.). Samples were pooled in equimolar quantities together with blank PCR controls. The pooled sample was concentrated using MinElute™ PCR Purification columns (Qiagen Inc.) as described by the manufacturer and sent to Macrogen (South Korea) for sequencing. Sequencing was undertaken with a Roches GS FLX instrument using Titanium chemistry on an eight-region gasket and Roche GS FLX instruments. Sequence processing was undertaken as described by van Bleijswijk et al. (2015), using a QIIME pipeline. Sequences shorter than 250 bases and average Q scores below 25 were removed. The OTU sequences (> 98% similarity) were classified (> 93% similarity) based on a recent SILVA SSU database (release 132; Yilmaz et al., 2014). Single reads were excluded, and all data were standardised to remove any disproportionate sampling bias.

Table 4.2: Primers used for sequencing.

Forward primer name	Forward primer sequence 5'-3'	Reverse primer name	Reverse primer sequence 5'-3'	Ratio in mix	Reference
Arch-0519-a-S-1 (universal)	CAGCMGCCGCGGTAA	Bact-0785-b-A-18 (universal)	TACNVGGGTATCTAATCC	3/9 + 3/9	Klindworth et al. (2013)
Bact-0519F (targets WS6, TM7, OP11 groups)	CAGCAGCATCGGTVA			1/9	This paper
Nano-0519F (targets Nanoarchaea)	CAGTCGCCRCGGGAA	Nano-0785R (targets Nanoachaea)	TACNVGGGTMTCTAATYY	1/9 + 1/9	This paper

4.2.6. Statistics

Unconstrained ordination techniques were utilised to distinguish biotopes and general community patterns. Nonmetric multidimensional scaling plots (NMDS) were created based upon Bray–Curtis similarity matrices of square root-transformed microbial community assemblages. Group average clustering was also utilised in order to quantify similarities between the samples. ANalysis Of SIMilarities (ANOSIM) was subsequently used to statistically test community distinctions based upon presumed biotopes (sediment, near-bottom water, below-plume water, plume water and above-plume water). In addition, all water column samples were plotted in separate NMDS plots to observe patterns in greater detail. Physical properties of all water samples (station, depth, turbidity, and location) were depicted in a NMDS plot to observe sample similarities. These environmental data were normalised, and Euclidean distance was used to create a similarity matrix. The relationship between Fe and turbidity was tested with a linear regression analysis. Trace metals and REEs were normalised to Fe, since it is the primary particle-forming element at all stages of plume dispersion, giving insight into the chemical behaviour. All multivariate statistics were undertaken in Primer™ V6 (Clarke and Gorley, 2006).

The Shannon–Wiener index ($\log_e$) was calculated as a diversity measure. Biodiversity differences between biotopes were tested with the non-parametric Kruskal–Wallis test with pairwise comparisons, as the data did not meet normality or homogeneity assumptions, even after transformation. These statistical tests were undertaken in SPSS.

A SIMililarities PERcentage analysis (SIMPER in Primer v6) was applied on the microbial class level with a cut-off for low contributions at 90% based on Bray–Curtis similarity matrix to characterise the community composition based on groups contributing to intra-biotope similarities. Relationships between environmental variables and microbial classes as a percentage of each composition within the plume were tested with Pearson correlation and hierarchical clustering to identify broad response groups.

4.3. Results

4.3.1. Water column characteristics

Temperature, salinity, and density plots indicated that the water column at each location had similar physical traits, whereby three main different water masses could be distinguished (Fig. S4.1). The surface Eastern North Atlantic Central Water (ENACW) was characterised by a temperature, salinity, and density at the surface of 18 °C, 36.4 and 26.2 kg m^{-3} to 11 °C, 35.5 and 27.2 kg m^{-3} at the bottom of the water mass. The underlying Mediterranean Outflow Water (MOW) was characterised by a temperature of 7.5-11 °C, a salinity of 35.4-35.5 and a density of 27.2-27.75 kg m^{-3}. The North Atlantic Deep Water (NADW) was characterised by temperatures ranging from 4 to 7.5 °C, salinity of 35.0 to 35.4 and a density of 27.75 to 27.825 kg m^{-3} (Emery and Meincke, 1986). The neutrally buoyant plume was centred around the 27.82 kg m^{-3} isopycnal, as illustrated in Figures 4.2 and 4.3.

4.3.2. Turbidity and plume dispersion

Against a background of non-plume-influenced waters, as found in the CTD casts, with typical concentrations of SPM of 0.04 mg L^{-1} (0.015 NTU), the neutrally buoyant plume stands out as a layer with distinctly higher turbidity values (i.e. higher SPM mass concentrations) consistently present in the depth interval of 1750-2400 m at stations located north and east of Rainbow (Fig. 4.2). Except where this turbid water layer was found impinging the seabed, relatively clear waters separated the turbid layer from the underlying seabed.

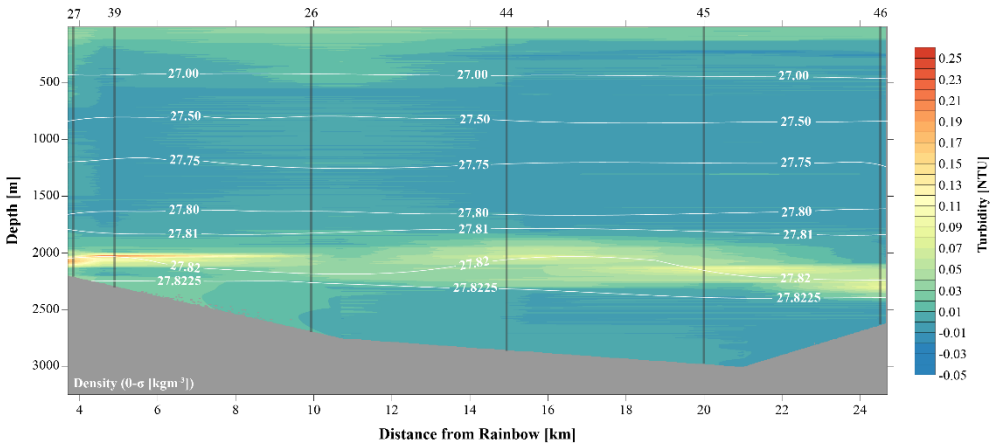

Figure 4.2: Transect along main plume path (indicated in Fig. 4.1 as plume transect), showing turbidity in the water column. The plume is indicated by highest turbidity values and disperses away from the Rainbow vent field.

At downstream stations, a consistent trend of decreasing turbidity and increasing vertical dispersion was noted. At station 27, 3.5 km north of Rainbow, maximum turbidity in the core of the plume was 0.15 NTU (0.09 mg L^{-1}) and plume thickness was about 105 m, whilst at station 46, 15.2 km east of Rainbow, maximum turbidity was only 0.08 NTU (0.06 mg L^{-1}) and plume thickness was 275 m. Away from the main plume path, stations 47 and 49 (13.8 and 16.5 km from Rainbow, respectively) showed a diluted signature similar to that observed at the most distal stations along the main plume path. Despite being most proximal to Rainbow, station 16, located 1.0 km downstream of Rainbow, showed a relatively low turbidity of 0.015 NTU (0.04 mg L^{-1}). Since the plume is more constrained closer to the source, the main body of the narrower plume could have been missed with the CTD. Stations upstream of the vent site (stations 13 and 28, 4.2 and 7.5 km southwest of Rainbow, respectively, and station 40, 3.6 southeast of Rainbow) displayed low turbidity values, ranging between 0.01 and 0.02 NTU (0.04 mg L^{-1}) (Fig. S4.2).

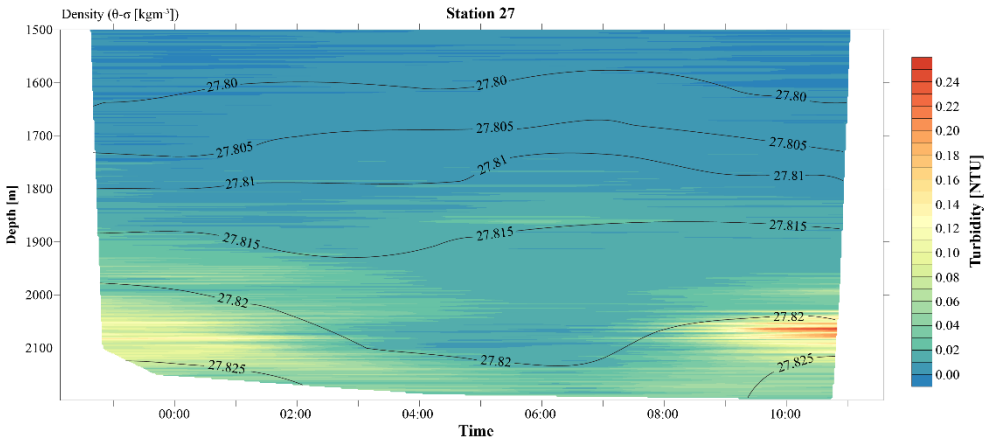

Figure 4.3: A 12 h yo-yo CTD at station 27 showing the temporal evolution of the hydrothermal plume over a tidal cycle.

The CTD profiles from stations 42 and 49 (4.9 and 16.5 km north of Rainbow, respectively) both displayed the highest turbidity in the lower hundreds of metres above the seafloor, with instances of seafloor contact during time of sampling. Therefore, no samples could be taken below the plume at these stations. The assumption that the plume is subject to vertical movement is supported by observations made during 12 h CTD yo-yo casts carried out at station 27 (Fig. 4.3). Along with vertical displacements of the 27.82 kg m^{-3} isopycnal on the

order of 150 m, likely reflecting internal tidal motions, the hydrothermal plume was found to also move up and down and at times touch the seafloor.

4.3.3. Enrichment of (trace) metals compared to the ambient seawater

NMDS ordination (Fig. 4.4) based on Euclidean distance resemblance of normalised element/Fe molar ratio data of all collected water samples (2D stress = 0.03), revealed a clear distinction of the different samples. Most outstanding are the samples from above-plume waters, indicating that the chemical composition is different from the other samples.

The remaining samples showed less variation, nonetheless the samples collected from below the plume and the samples collected away from the main path of the plume can be distinguished. This shows that the hydrothermal plume can be characterised by its chemical composition. When comparing samples taken in the turbidity maximum of the plume to the above-plume water samples taken at 1000 m water depth it is found that Fe, Cu, P, V, and Pb are enriched by factors of 80, 90, 17, 52 and 25, respectively. Elements with a more moderate degree of enrichment are Co, Mn, Zn, Al, and Ni, with enrichment factors of 8.0, 2.5, 10.3, 1.4 and 1.6, respectively. The REEs were enriched by a factor of 5 to 40 relative to the clear water. U, Ti, and Ca are slightly enriched at turbidity maxima, by factors of 1.3, 1.6 and 1.2, respectively. In and Sn are depleted compared to the above-plume water.

4.3.4. Geochemical gradients within the hydrothermal plume

Within the hydrothermal plume, geochemical evolution is found as the plume disperses. Visual examination of the samples with the SEM, coupled with chemical analysis performed with the EDS detector, revealed that the SPM within the plume close to the Rainbow hydrothermal vent at station 32 (2.9 km north of Rainbow) mainly consisted of Fe-sulphides. In the plume samples further downstream, Fe is mainly present as Fe-oxides, Fe-hydroxides or bound in aluminosilicates. Chemical examination of the samples showed gradients in the element/Fe molar ratios along the path of the plume, as well as off the main path of the plume at the upstream and the most distal downstream stations. Since the Fe concentration is linearly related to the turbidity (Fig. 4.5) (R^2 = 0.9356, $P < 0.001$), normalisation to Fe reveals relative enrichments or depletion of common elements. The chalcophile elements Co, Cu and Zn show a partly linear relation steepening with increasing Fe concentration (Fig. 4.6a for Cu), indicating

that the element/Fe molar ratios are elevated close to the source but decrease towards the more distal sites (Fig. 4.7a).

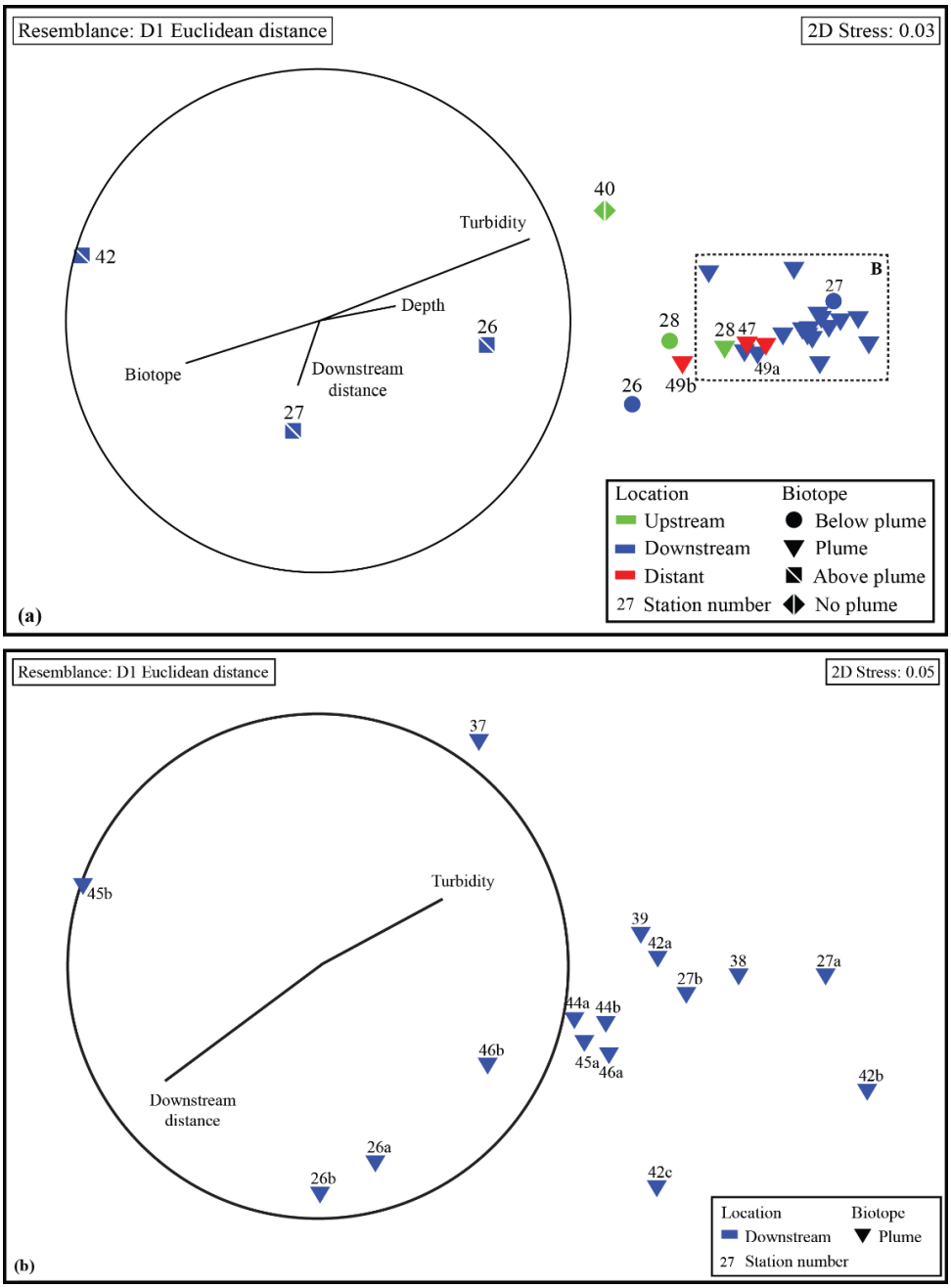

Figure 4.4: A) NMDS ordination showing all water samples based on their resemblance in chemical composition. B) NMDS ordination showing all plume samples from the downstream stations based on their resemblance in chemical composition.

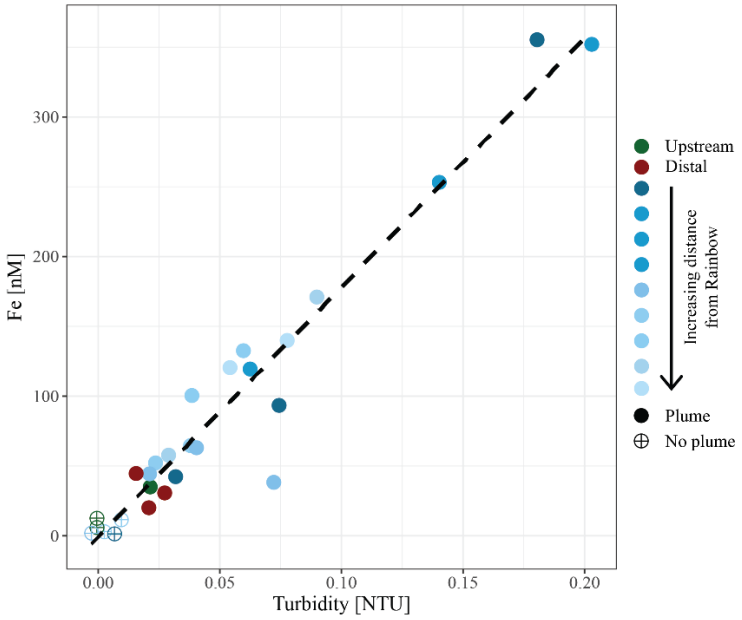

Figure 4.5: Relationship between in situ measured turbidity and molar concentration of particulate iron.

One exception is the Zn/Fe molar ratio, which is elevated at stations 37, 39 and 44. Furthermore, a high Zn/Fe molar ratio is observed at upstream station 40. The oxyanions P and V are linearly related to Fe (Fig. 4.6b for V) and show varying element/Fe molar ratios without a clear trend of increasing or decreasing ratios, both upstream and downstream of Rainbow (Fig. 4.7b). The REEs show a partly linear relation, levelling off with increasing Fe concentrations (Fig. 4.6c for Y). Within the plume this is displayed as increasing element/Fe molar ratios towards station 44, with station 42 as an exception, followed by slightly decreasing molar ratios from station 44 onwards (Fig. 4.7c). The Ca/Fe molar ratios ranged between 0 and 15 for most of the downstream stations, apart from the stations further downstream (47 and 49), which displayed slightly higher Ca/Fe molar ratios. Upstream station 28 had a Ca/Fe molar ratio similar to those found at station 47 and 49, and upstream station 40 was found to have a significantly higher Ca/Fe molar ratio (Fig. 4.7e). Other analysed elements, Mn, Al, Ni, In, Pb, Sn, Ti and U, showed no clear relationship with the Fe concentration (Fig. 4.6d for Sn). However, within the plume it was found that the Mn/Fe molar ratio is lower than at the upstream stations or the more distal downstream stations.

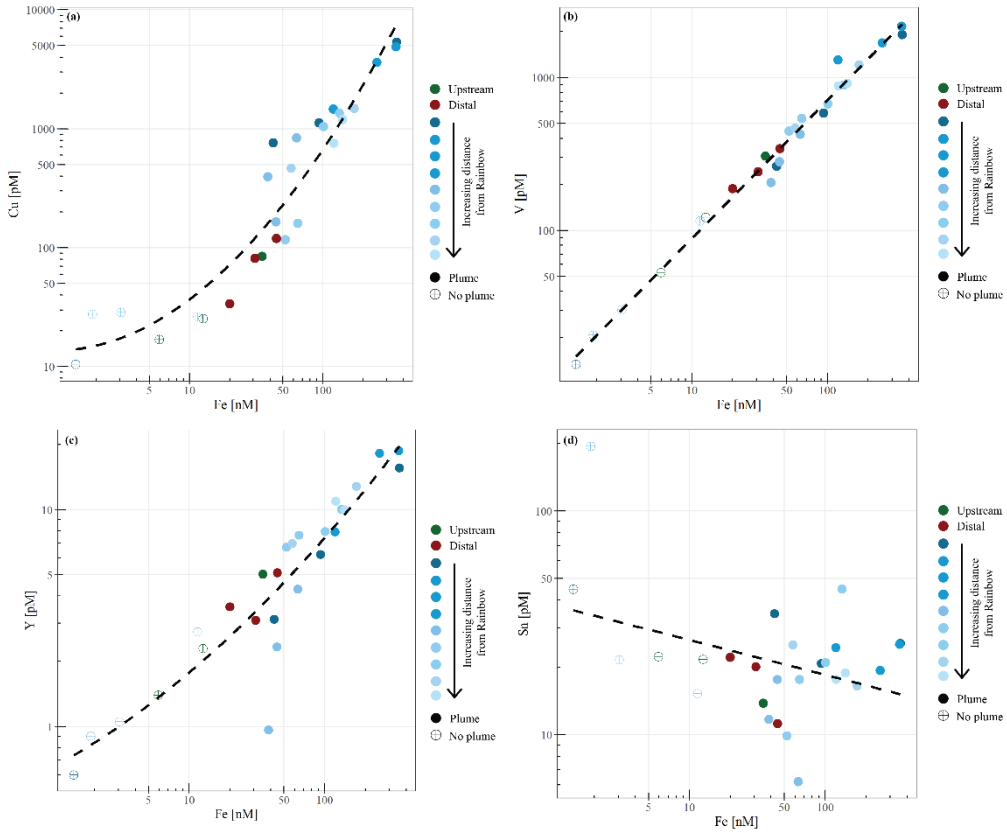

Figure 4.6: Relationships between molar concentration of particulate copper (a), vanadium (b), yttrium (c) and tin (d) to iron.

4.3.5. Microbial assemblages in water column isotopes

Samples from sediment, near-bottom water and no plume water contained microbial communities that clustered distinctly from each other and from plume, below-plume, and above-plume communities (Fig. 4.8). In particular, sediment, near-bottom water and no plume (station 13) samples have communities that are very dissimilar from the overlying water column samples. Sediment samples appeared to cluster in a straight line, suggesting some sort of gradient of similarity along the ordination axis, though no apparent patterns were observed when independently plotted. The near-bottom water samples were relatively dispersed in the NMDS plot, suggesting a more variable community. Samples taken at the upstream station 13 from below-plume and plume depths showed no similarity with samples from corresponding depths in the other stations, whilst the above-plume community at this station is consistent with that of other stations. In general, plume and below-plume communities were more

similar nearer to the vent source, with stations further downstream displaying greater dissimilarity (Figs. 4.9, S4.3).

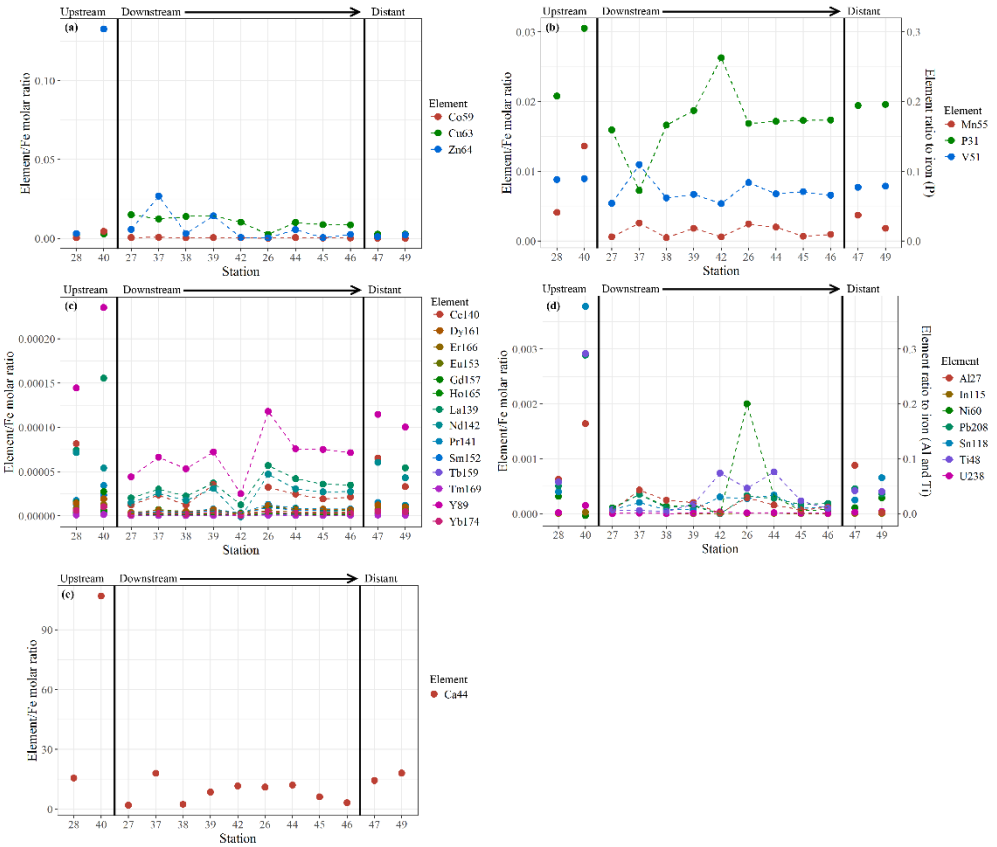

Figure 4.7: Element to iron molar ratios of plume samples of upstream, downstream and distant stations. Downstream station follows the main path of the plume. A) shows the element/Fe molar ratios of the chalcophiles (Co, Cu, and Zn), B) shows the ratios of Mn and the oxyanions (P and V), C) displays the ratios of REEs, D) the ratios of Al, In, Ni, Pb, Sn, Ti, and U and E) shows the Ca/Fe molar ratios.

Group average cluster analysis showed a high level of dissimilarity, i.e. large community variation, between and within biotopes. ANOSIM revealed all putative biotopes that were sampled had distinct communities (global R = 0.738; P < 0.001; 999 permutations), except for plume and below-plume samples, which could not be distinguished statistically (global R = 0.091; P = 0.861). The two seemingly unique samples from station 13 also tested as significantly distinct but with a low number of permutations (< 999) due to low replication (n = 2).

*Table 4.3: SIMPER similarity results of each biotope at class level (*indicates undefined class).*

Biotope	Average similarity (%)	Class	Average proportion (%)	Average similarity	Sim/SD	Contribution (%)	Cumulative %
Above plume	82.34	Nitrososphaeria	27.10	22.79	4.61	27.67	27.67
		Alphaproteobacteria	18.34	15.22	4.15	18.49	46.16
		Gammaproteobacteria	13.44	11.58	5.52	14.07	60.23
		Deltaproteobacteria	10.67	8.46	3.38	10.27	70.50
		Marinimicrobia (SAR406 clade)*	8.22	6.96	6.07	8.46	78.96
		Dehalococcoidia	6.38	5.69	9.19	6.91	85.87
		Thermoplasmata	2.63	2.26	5.68	2.74	88.61
		Acidimicrobiia	2.13	1.89	8.62	2.30	90.91
Plume	76.74	Epsilonproteobacteria	39.59	30.29	2.53	39.47	39.47
		Nitrososphaeria	12.16	10.32	4.05	13.45	52.92
		Gammaproteobacteria	9.69	7.92	4.71	10.32	63.23
		Alphaproteobacteria	9.23	7.22	2.44	9.40	72.64
		Deltaproteobacteria	7.60	5.56	2.75	7.25	79.88
		Dehalococcoidia	4.57	3.55	2.58	4.63	84.51
		Marinimicrobia (SAR406 clade)*	4.02	3.07	3.83	4.00	88.51
		Thermoplasmata	2.56	1.94	3.39	2.53	91.04
Below plume	77.94	Nitrososphaeria	22.35	16.60	3.29	21.30	21.30
		Alphaproteobacteria	13.26	11.43	5.18	14.67	35.97
		Deltaproteobacteria	10.88	9.25	8.31	11.87	47.84
		Gammaproteobacteria	10.60	8.89	7.78	11.40	59.24
		Epsilonproteobacteria	9.65	7.18	2.50	9.22	68.46
		Dehalococcoidia	7.84	6.97	7.89	8.95	77.40
		Marinimicrobia (SAR406 clade)*	6.32	4.49	2.31	5.76	83.16
		Thermoplasmata	4.69	3.04	2.20	3.90	87.07
		Phycisphaerae	1.97	1.75	7.60	2.24	89.31
		Planctomycetacia	2.03	1.50	2.96	1.93	91.23
Near-bottom water	75.71	Gammaproteobacteria	20.79	16.77	3.18	22.15	22.15
		Nitrososphaeria	16.90	13.54	3.79	17.89	40.04
		Alphaproteobacteria	15.55	13.25	5.47	17.50	57.54
		Deltaproteobacteria	6.68	5.89	5.99	7.78	65.32
		Oxyphotobacteria	5.93	4.04	2.18	5.34	70.66
		Dehalococcoidia	4.08	2.99	2.50	3.95	74.61
		Phycisphaerae	3.72	2.57	2.03	3.40	78.01
		Thermoplasmata	2.47	1.70	2.25	2.24	80.25
		Acidimicrobiia	2.06	1.61	2.72	2.13	82.38
		Bacteroidia	2.15	1.57	1.85	2.07	84.45
		Marinimicrobia (SAR406 clade)*	1.75	1.24	2.17	1.64	86.09
		OM190	1.64	1.14	2.02	1.51	87.60
		Planctomycetacia	1.40	1.09	2.76	1.44	89.04
		Epsilonproteobacteria	1.71	0.85	1.08	1.12	90.16
Sediment	82.51	Gammaproteobacteria	29.67	27.17	8.51	32.93	32.93
		Alphaproteobacteria	13.98	12.44	4.88	15.07	48.01
		Deltaproteobacteria	11.98	10.98	10.24	13.30	61.31
		Nitrososphaeria	7.73	5.69	3.74	6.90	68.21
		Phycisphaerae	5.46	5.01	7.85	6.07	74.28
		Dehalococcoidia	3.35	2.48	2.58	3.01	77.29
		BD2-11 terrestrial group	2.36	1.91	2.90	2.31	79.60
		Subgroup 22 (Acidobacteria)	2.10	1.74	3.22	2.11	81.71
		OM190	2.09	1.50	5.50	1.81	83.53
		Nitrospira	1.79	1.49	3.68	1.80	85.33
		Bacteroidia	1.91	1.48	3.66	1.79	87.12
		Acidimicrobiia	1.58	1.24	2.84	1.50	88.62
		Thermoanaerobaculia	1.41	1.07	3.25	1.30	89.92
		Gemmatimonadetes*	1.57	1.06	1.56	1.28	91.21

4.3.6. Univariate biodiversity

Plume and below-plume samples were less diverse than sediment samples, whilst diversity in the plume was lower than in near-bottom water samples (Kruskal–Wallis: $\chi 2$ (4) = 36.127, P < 0.012, P < 0.01). In general, plume diversity was low (Fig. 4.10), but further differences were not statistically significant, likely due to limited replication and intra-biotope variation. The plume microbial community at sites upstream of Rainbow and at the immediate downstream sites (stations 28, 13, 16 and 27) showed similar and relatively high biodiversity (>4.5) (Fig. 4.11). Plume biodiversity at the sites further away from Rainbow gradually decreased until station 46, which displayed the lowest Shannon–Wiener index value of 2.4. Distant stations 47 and 49, showed biodiversity rising to a more moderate index value around 3.5.

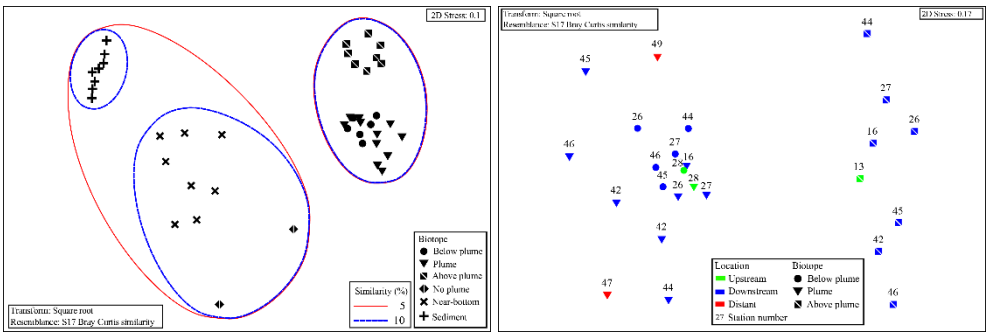

Figure 4.8 (left): Non-metric multidimensional scaling plot of the microbial community composition of all samples based on Operational Taxonomic units. Similarity grouping is based on group average clustering. "No plume" is representative of samples collected from station 13, where there was no indication of a plume.
Figure 4.9 (right): Non-metric multidimensional scaling plot of the microbial community composition of all water column samples based on Operational Taxonomic units. Plume and below-plume depths from station 13 were excluded.

4.3.7. Species composition

Results of the SIMPER analyses, showing the contributions of taxa composition to similarities within biotopes (Table 4.3), mirrored the NMDS and ANOSIM results, whereby the similarity of community composition in each biotope was dominated by a different makeup of the microbial community. The archaeal class Nitrososphaeria (marine group 1 archaea) contributed the most to similarity within the above- and below-plume water communities, while also being very common in all water samples. Alphaproteobacteria, Gammaproteobacteria and Deltaproteobacteria also constituted a large amount of the makeup of all biotopes in the area. The class Epsilonproteobacteria were rare in above-plume

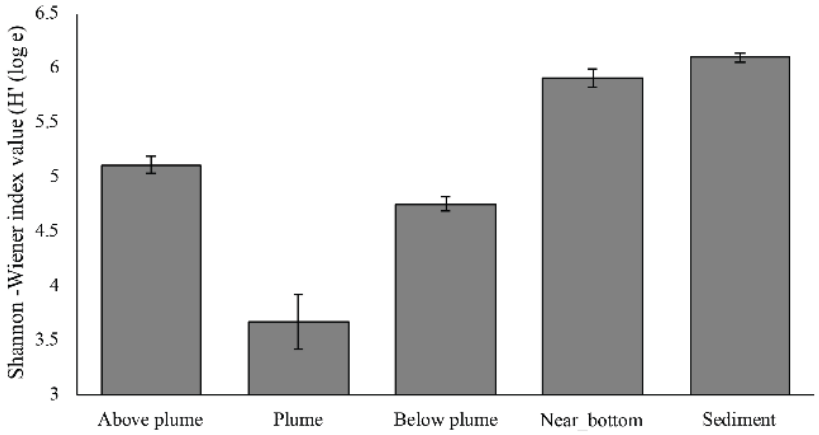

Figure 4.10: Mean Shannon-Wiener diversity index for microorganisms in each biotope. Error bars represent SE.

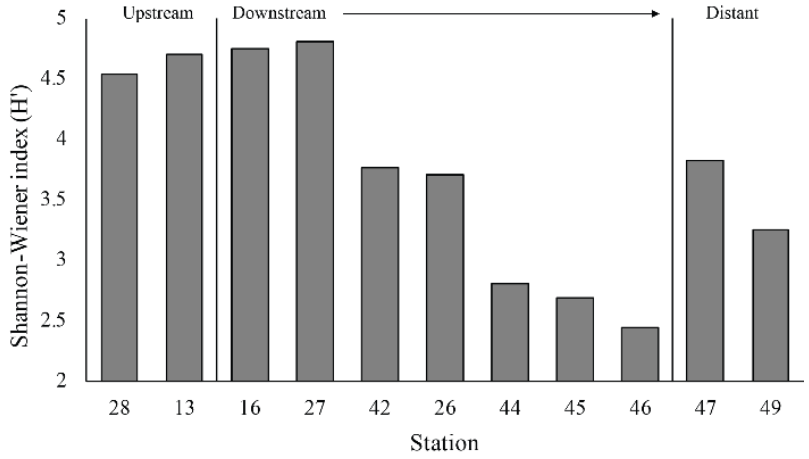

Figure 4.11: Shannon-Wiener index values for microorganisms in each plume sample taken.

samples and only contributed < 2% to near-bottom water communities. By contrast, Epsilonproteobacteria were dominant in plume water samples (accounting for > 35% of the community) and were the fifth most dominant taxon in below-plume water samples contributing 8.9% of the community.

Epsilonproteobacteria accounted for about 20 % of the plume community at stations near the vent. Beyond the near vent stations, an increase in relative abundance of Epsilonproteobacteria with distance from the vent was observed, accounting for 64% of the community at the distant station 46 (Fig. 4.12). Alphaproteobacteria, Deltaproteobacteria and Gammaproteobacteria appeared to become less dominant with distance from the plume

source (Fig. 4.12). The communities at distant stations 47 and 49 were less dominated by Epsilonproteobacteria (around 40 %). Below-plume communities were dominated mostly by Nitrososphaeria (marine group 1 archaea), whereby Nitrososphaeria became more dominant with distance from the plume source similar to the Epsilonproteobacteria in the plume. Correlations between environmental variables (elemental chemistry and physical properties) and all microbial classes observed in the plume were evident and appeared to be class-specific (Fig. S4.4). The hierarchical clustering revealed eight broad response groups, which displayed different relationships with the environmental variables.

4.4. Discussion

Using a multidisciplinary approach in which physical, geochemical, and ecological data were collected from the Rainbow vent neutrally buoyant plume and its underlying sediment, we aimed to expand knowledge and characteristics of the background (i.e. before impact) state of a hydrothermal vent site. Such knowledge is deemed essential to be able to assess (potential) impacts of future deep-sea SMS mining, as it may help in characterising the behaviour of the diluted distal part of chemically enriched mining plumes. We found geochemical and microbial differences between the above-plume, plume, below-plume, and no-plume water, and, in addition, pertinent chemical and biological gradients within the extensive Rainbow hydrothermal vent plume were evident.

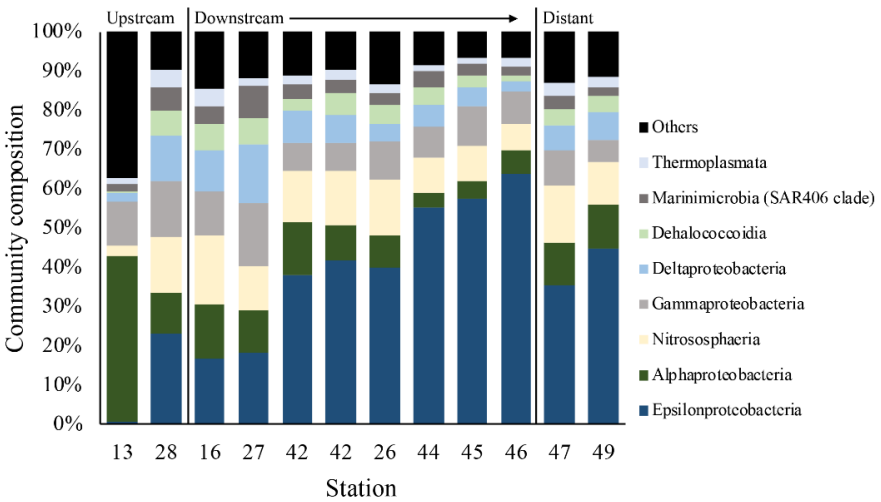

Figure 4.12: Microbial community composition in the plume samples as a percentage of the dominant class groups in accordance with the SIMPER results. The asterisk indicated an undefined class.

4.4.1. Physical constraints of plume location and behaviour

The plume was observed within the NADW mass, constrained to an isopycnal density envelope of 27.82 kg m^{-3} (Figs. 4.2 and 4.3). The apparent continuity of this turbid water layer, especially to the northeast of the Rainbow field, and lack of similarly turbid waters in the bottom waters below the plume, link the plume to Rainbow and preclude local sediment resuspension as an origin. Using turbidity measurements and presumed plume path, we traced the plume up to 25 km away from the vent source. This is within the range mentioned by German et al. (1998), who found that the Rainbow plume extends over 50 km, being controlled by local hydrodynamics and topography. Unexpectedly, in the basin upstream of the Rainbow vent field, a turbidity peak at 1975 m water depth resembling a plume was observed as well (station 28), confounding our assumption of a clear water column at upstream stations and distant downstream stations. This suggests that the plume is distributed much further than previously observed by Thurnherr and Richards (2001) and German et al. (1998). This is exemplified by the local variation in microbial community composition of upstream stations (Fig. 4.12) and is supported by the relatively low Ca/Fe molar ratio at station 28 (Fig. 4.7), indicating hydrothermal influence. In addition, the observed variability of plume strength and vertical position (Fig. 4.3) indicate that local fluctuation in the current regime and tidal motions influence plume behaviour. This dynamic behaviour has implications for survey designs and should be considered when monitoring natural and man-made plumes, such as mining-related plumes. Prior insight into plume extension and behaviour is required for the identification of adequate control sites and for tracking of plume evolution in future impact studies.

4.4.2. Plumes influences on the water column chemical and microbial make-up

The neutrally buoyant plume introduced pelagic heterogeneity in terms of chemical and microbial composition, which is supported by the vertical classification of the different biotopes. The neutrally buoyant plume was evidently enriched in metals and REEs compared to overlying clear water. Element concentrations were found to be in line with those found by German et al. (1991) and Edmond et al. (1995) and Edmonds and German (2004), who studied the Trans-Atlantic Geotraverse (TAG) hydrothermal plume and the Rainbow hydrothermal plume, respectively. Our chemical results from Rainbow also match with those of Ludford et al. (1996), who studied vent fluid samples from the TAG, Mid-Atlantic Ridge at Kane (MARK),

Lucky Strike and Broken Spur vent sites; i.e. our element concentrations were found to be in the same order of magnitude as theirs (Table S4.2).

The distinctive chemical composition of the plume samples (e.g. metal concentrations) affects chemolithoautotrophic microbial growth within the plume, as indicated by the typical microbial community in plume samples. We observed a clear and consistent separation between communities in the plume and those in above-plume samples. The influence of MOW on the above-plume community could also play a role, as water masses can harbour different microbial communities (Agogue et al., 2011). However, the palpable presence of a plume in the turbidity data with supporting chemical measurements and the occurrence of vent-associated Epsilonproteobacteria (Olins et al., 2017; Djurhuus et al., 2017) and other vent-associated groups, such as the Gammaproteobacteria clade SUP05 (Sunamura et al., 2004), point to a unique chemical environment. Here chemosynthetic communities flourish and give rise to independent biotopes in the neutrally buoyant plume kilometres downstream of the vent site.

Below-plume communities were not distinct from the plume biotope, although instead of Epsilonproteobacteria, the ubiquitous class Nitrososphaeria was the most dominant group, reflecting some similarities with above-plume seawater communities. Similarities between plume and proximal habitat communities have also been observed by Olins et al. (2017), whereby intra-field (defined as within vent field between diffuse flows) and diffuse flow microbial communities were alike. In our study, similarities between plume and below-plume water are likely derived from precipitation of mineral and microbial aggregates dragging plume microbes deeper below the plume, as suggested by Dick et al. (2013). In addition, internal wave-induced turbulence causes vertical mixing along the slope of the Rainbow Ridge (van Haren et al., 2017), which may cause the plume and associated communities near the vent field to mix with ambient water communities, leading to assemblage similarities. This indicates the plume and that associated microbial processes could have a larger vertical footprint than previously observed, supporting suggestions by Olins et al. (2017) that proximal non-plume habitats have been overlooked. Interestingly, near-bottom water (and sediment) community assemblages were distinct from the below-plume and other water column communities. This could imply (1) that there is little “fallout” from the plume at distance from the vent, which is

in agreement with sediment trap observations by Khripounoff et al. (2001); that (2) plume-specific bacteria die off due to lack of energy sources and DNA degrades before reaching the seafloor; and that (3) microbes are more abundant in the near-bottom waters, either naturally or through mechanical disturbance resuspending sediment during the coring process, outnumbering groups that have been mixed in from overlaying water. Despite the presence of a plume and precipitation, a difference between the seafloor and the water column biotopes is present, consistent with global broadscale non-vent benthic–pelagic patterns (Zinger et al., 2011). According to Khripounoff et al. (2001), particulate fallout from the Rainbow plume is spatially very limited. This implies that the extended chemical imprint on the sediment (reported by Cave et al., 2002; Chavagnac et al., 2005; and this study) is likely to have formed when the plume is in direct contact with the sediment during its vertical tidal migration. As the plume rises again, the associated distinct communities apparently resume dominance in the near-bottom water. Though Epsilonproteobacteria have been detected in Rainbow vent sediments comprising over 5% of the sediment community (López-García et al., 2003), very few reads of this group in sediment samples were present in our study, probably as our coring samples were collected kilometres away from the vent site. Cave et al. (2002), observed chemical evolution of sediment composition with distance from source, thus we infer a relationship between the sediment dwelling Epsilonproteobacteria with nearby plume precipitates, such as Cu and presumed precipitates Zn and Cd (Trocine and Trefry, 1988). Additionally, extracellular DNA degradation rate can be 7 to 100 times higher in sediment than in the water column (Dell'Anno and Corinaldesi, 2004). Therefore, although our results suggest no microbial plume community imprint on the sediment, we cannot rule out short-lived episodic community changes when the plume is in contact with the sediment.

4.4.3. Geochemical gradients within the hydrothermal plume

Analysis of SPM in water samples taken along the flow path of the plume, as well as off the flow path, showed conspicuous trends of elements, reflecting the chemical evolution of the plume as it drifts away from its hydrothermal source.

The chalcophile elements (Cu, Co, and Zn) were found to have the highest element/Fe molar ratios closest to the vent site, indicating either rapid removal from the hydrothermal plume or removal from the solid phase as the plume drifts away from the vent site. Using SEM-EDS, it

was demonstrated that at the proximal downstream stations mainly Fe-sulphides were found, whereas Fe-(oxyhydr)oxides were found further downstream. This suggests that chalcophile elements are mainly present in the form of sulphide mineral particles at the proximal stations, which are entrained in the flow of hydrothermal water emanating from the Rainbow vents. Subsequently, they are rapidly lost by settling from the plume in sulphide-bearing phases, while a large portion of Fe remains in suspension (Cave et al., 2002; Edmonds and German, 2004), consistent with decreasing concentrations of Cu, Zn and Co in sediment recovered from the Rainbow area with increasing distance to the vent site (Cave et al., 2002).

The oxyanions (V and P) showed slightly varying element/Fe molar ratios with increasing distance away from Rainbow, suggesting co-precipitation with Fe as oxyhydroxides (Edmonds and German, 2004). No additional uptake of these elements was observed with increasing distance from the vent field (German et al., 1991), since these elements are scavenged initially in significant amounts during the buoyant plume phase (Cave et al., 2002).

The trend shown by Mn/Fe molar ratios can be attributed to the slower oxidation kinetics of Mn (Cave et al., 2002). It takes longer for reduced Mn to be oxidised than it would for Fe, resulting in an increase in particulate Mn with increasing distance from the Rainbow hydrothermal vent field, which subsequently settles out from the plume as Mn-oxyhydroxides (Cave et al., 2002).

The observed positive relationship between the REEs and Fe is indicative of continuous scavenging of these elements from the ambient seawater onto Fe-oxyhydroxides (Edmonds and German, 2004; Chavagnac et al., 2005; Caetano et al., 2013). Therefore, the highest element/Fe molar ratios were observed away from the Rainbow hydrothermal vent site, where Fe-(oxyhydr)oxides are dominant more distal to the vent site.

The Ca/Fe molar ratios vary between 0 and 15 for the stations downstream of the Rainbow hydrothermal vent but are higher at the distant downstream station 47 and 49 and upstream stations 28 and 40. Especially at station 40, located on the Rainbow Ridge, the Ca/Fe molar ratio is significantly higher than at the other stations. This is in line with observations by Khripounoff et al. (2001) and Cave et al. (2002), who also found that the relative Ca

concentration in settling particles and the sediments is lower close the Rainbow vent field and increases as the Fe concentration decreases when the plume disperses. Since Ca is naturally present in high abundances in pelagic skeletal carbonate that rains down from the overlying water column and Fe is mainly present as a hydrothermal component, the Ca/Fe molar ratio could be an indicator for the extent of the hydrothermal influence. The high molar ratio at station 40 would then suggest that this station is hardly or not at all influenced by the hydrothermal plume, as the natural abundance of particulate iron is low (e.g. Michard et al., 1984 and this study), whereas stations 28, 47 and 49 are, as expected, influenced in more moderate degrees compared to the stations directly downstream of Rainbow.

4.4.4. Microbial gradients within the hydrothermal plume

The microbial plume community composition and diversity altered with distance from the plume source, showcasing horizontal heterogeneity within the plume. Despite dilution, the vent-associated group Epsilonproteobacteria (specifically the most common genus Sulfurimonas), appeared to dominate the community composition. This is likely due to its flexibility to exploit a range of electron donors and acceptors (Nakagawa et al., 2005), making them suitable inhabitants of dynamic environments (Huber et al., 2003). From the relative abundance data presented here it cannot be determined whether Epsilonproteobacteria dominate by rapid reproduction or if other groups decline in abundance. However, it is evident that Epsilonproteobacteria remain competitive or outcompete other competitors, such as generalist Gammaproteobacteria that are often vent associated (i.e. SUP05). It is unlikely that this pattern is caused by entrainment of Epsilonproteobacteria from background seawater over time. This is based on the lack of significant presence of Epsilonproteobacteria in above-plume water and at remote station 13 and reduced mixing that neutrally buoyant plumes generally experience (McCollom, 2000). This is further supported by the increasing uniqueness of the plume community with distance from the source, suggesting that mixing and entrainment between downstream biotopes is negligible.

The neutrally buoyant plume is likely too chemically enriched for non-adapted microbial taxa to thrive and consequently they are outcompeted by groups that can benefit from, or tolerate, the chemical nature of the plume. Therefore, it is likely that less specialised groups die out due to lack of appropriate resources and interspecies competition, as indicated by the decline in

biodiversity with age of plume (distance) directly mirroring the increasing dominance of Epsilonproteobacteria, a group already known to influence diversity and community structures (Opatkiewicz et al., 2009; Sylvan et al., 2012). In addition, the decrease in concentration of particulate matter may influence microbial diversity (Huber et al., 2003). Temporal succession has been observed within plume environments by Sylvan et al. (2012) and Reed et al. (2015), driven by metabolic energy yield and concentration of the electron donors. These patterns may relate to ecological succession (Connell and Slaytor, 1977) within the plume with change in microbial communities resulting in a low diversity climax plume community. At the distant stations 47 and 49, the community was less dominated by Epsilonproteobacteria and more diverse, indicating a gradual return to what is possibly a non-plume-influenced state of the microbial community. The wide range of correlations within and between microbial classes and water properties, i.e. ranging from chemical to physical variables (Fig. S4.4), indicates a complex array of community drivers within the plume.

In contrast to our results, Sheik et al. (2015) and Djurhuus et al. (2017) observed decreasing Epsilonproteobacteria abundance within hundreds of metres from the source in the rising, buoyant portion of plumes generated by Indian Ocean and South Pacific Ocean vents. Interestingly, in our results Epsilonproteobacteria were least dominant in the neutrally buoyant plume closest to the Rainbow vent site, which may indicate that entrainment of other microbial groups within the rising portion of the plume initially dilutes the contribution of Epsilonproteobacteria (possibly derived from near seafloor communities), whilst the competitive advantage of certain species from this group only becomes evident at a later stage as the plume drifts away from the source. However, Huber et al. (2003) suggested that Epsilonproteobacteria thrive in hydrothermal fluid mixed with seawater due to the lower temperature and high electron acceptor availability, suggesting greater habitat suitability away from the immediate venting orifice. Furthermore, it has been demonstrated that Epsilonproteobacteria (specifically Sulfurimonas) have higher dispersal capabilities than thermophilic vent-associated microbial groups (Mino et al., 2017). A sampling design to follow the continuity of the plume from the buoyant to the neutrally buoyant portion would be a suitable approach to fully trace the evolution of the plume from the orifice to full dilution. However, the term full dilution is ambiguous as it is unknown exactly how far the plume

influences the water properties and how far the plume-associated bacteria will follow, adding water column microbial community heterogeneity beyond our study spatial extent.

4.4.5. Possible effects of SMS mining plumes

Mining of SMS deposits will create additional plumes generated by activities of mining vehicles (resuspension) and by the discharge of solids from the surface vessel (discharge plume). It is yet unknown how these plumes will affect the ecosystem at active and inactive hydrothermal vent sites. Our study showed the influence of a natural hydrothermal plume on the pelagic microbial and chemical composition up to 25 km away from its source. It is not unlikely that the dispersion of sediment and chemically reactive mineral material in the water column may cause similar or larger changes to the background state.

While large particles mobilised by mining are expected to stay close to the seafloor and settle out rapidly, smothering fauna in the immediate surroundings (Jones et al., 2018), smaller particles will disperse further, potentially invoking effects on a larger spatial scale. Modelling the behaviour of the discharge plume generated by the proposed Solwara 1 SMS mining has shown that these plumes can extend up to 10 km from the mining site, resulting in a deposit thickness of up to 50 cm within 1 km of the discharge site (Gwyther et al., 2008; Boschen et al., 2013). Apart from the physical impact that suspended fine-grained solids may have, especially on suspension feeders, the presence of chemically reactive material may give the mining plume a distinct chemical and microbial fingerprint, analogous in a certain context to what we observed in the natural plume.

The extent of the local impact of deep-sea mining will depend on the location where the mining takes place. At an active site like the Rainbow hydrothermal vent field, we showed that even in the distant plume (25 km away from Rainbow) hydrothermal plume microbiota dominate. When a mining discharge plume at an active hydrothermal vent field would be merged with the natural plume, the local effects might be minimal since microbial communities are already adapted to the metal-rich environments (Gwyther et al., 2008). However, a mining plume consisting of a dense suspension of bottom sediment and fine-grained metal sulphides is expected to support an altered microbial community in terms of abundance and composition, impacting the hydrothermal plume community. Moreover, the

effects over larger spatial scales could be multiplied because of the increased export of electron donors by mining activities. Reed et al. (2015), who studied a hydrothermal plume in the Lau Basin, have shown that the export of the chemolithoautotrophs from a plume increases with increasing availability of electron donors. Dispersion of chemolithoautotrophs is variable between groups depending on the energetics of their metabolisms; for example, methanotrophs that can disperse more than 50 km are likely to disperse further than sulphur oxidisers (Reed et al., 2015). Increased export of microbial biomass from plumes may have an impact on other marine systems that are hospitable to chemolithoautotrophs, such as oxygen minimum zones (Dick et al., 2013), and to higher trophic levels (Phillips, 2017). At inactive sites the effect on the background fauna is also potentially large since these are not adapted to the heavy-metal-rich environments and the discharge plume could prove to be toxic to the fauna (Boschen et al., 2013), possibly affecting organisms at all levels of the food chain (Weaver et al., 2018). In addition, in cases of multiple plumes at different depths due to stratification and vertical migration due to tidal regimes, the impacts may not be confined to a single depth band and may affect a large part of the water column, including other habitats, such as benthic habitats (Klunder et al., 2020).

4.5. Conclusions

Our results demonstrate that geochemically enriched plumes provide a dynamic habitat that is conducive to ecological changes over a short time span. Combining microbial and chemical analysis has proven to be a sensitive tool, which enabled us to trace the hydrothermal plume up to 25 km downstream from the vent source and also upstream of the Rainbow vent site, implying that the influence of the hydrothermal vent on the surrounding environment may reach further than previously thought. The neutrally buoyant plume was chemically enriched, which spawned a distinct microbial biotope dominated by vent-associated species. As the plume aged and dispersed, we observed alteration of the chemical composition and microbial community composition of the plume, showcasing a horizontal heterogeneous plume. Overall, we have shown that a hydrothermal plume acts as a unique chemically enriched environment where distinct and variable microbial habitats are present. The plume heterogeneity and its dynamical behaviour would require extensive sampling in order to be able to assess the impacts and interferences by man-made mining plumes on the natural conditions.

Data availability

CTD data presented in this work; filter weights for SPM sampling, geochemical data of the (trace) metals, and REEs; associated calculated enrichment factors and information on the blanks; drift measurements; and detection limits of the SF-ICP-MS analyses are available in the NIOZ data portal (https://dataverse.nioz.nl/dataverse/doi under DOI 10.25850/nioz/7b.b.s, Haalboom and de Stigter, 2019, last access: 26 November 2019) and are also submitted to PANGAEA. Raw sequence data are available via the European Nucleotide Archive (ENA), under accession number PRJEB36848.

Acknowledgements

We thank Evaline van Weerlee for assistance in DNA extraction, Patrick Laan for assistance in the chemical analysis of the collected samples, and Hans Malschaert for maintaining the bioinformatics hardware and software tools. We also thank the crew and captain of the RV *Pelagia*, as well as the NIOZ technicians, for their essential assistance during cruise 64PE398. We thank Valérie Chavagnac and an anonymous reviewer for reviewing the paper and their collective constructive feedback.

Financial support

This research has been supported by the Applied and Engineering Sciences (AES) domain of the Netherlands Organisation for Scientific Research (NWO) (grant no. 13273) and by partners from the Dutch maritime industry. Topsector Water, a collaborative effort of Dutch industry, academia and government, funded ship time. Sabine Haalboom received funding from the Blue Nodules project (EC grant agreement no. 688785). David Price is supported by the Natural Environmental Research Council (grant no. NE/N012070/1). Henko de Stigter received funding from TREASURE. Furu Mienis is supported financially by the Innovational Research Incentives Scheme of the Netherlands Organisation for Scientific Research (NWO-VIDI grant no. 0.16.161.360).

Supplementary material

Tables

Table S4.1: Dissimilarity (%) between biotopes based on SIMPER results of microbial classes.

	Above plume	Plume	Below Plume	Near-bottom water
Above Plume				
Plume	44.83			
Below Plume	25.39	35.37		
Near-bottom water	32.79	47.13	35.47	
Sediment	44.46	56.42	46.60	32.89

Table S4.2-A: Comparison of (trace) metal data with work of German et al. (1991), Edmond et al. (1995) and Edmonds and German (2004).

Location	Sample	Depth [m]	Fe [nM]	Ca [nM]	Al [nM]	Mn [pM]	V [pM]	Cu [pM]	Zn [pM]	Co [pM]	Pb [pM]	Y [pM]	Reference
TAG	14	3477	56	34	1.4	140	260	980		9	15	3.5	German et al. (1991)
TAG	18	3364	87	39	1.2	140	393	620	205	8		6.7	German et al. (1991)
TAG	19	3392	67	35	1.4		323	760	167	6	11	3.7	German et al. (1991)
TAG	22	3337	192	53	1.6	180	888	15440	512	71	21	8.7	German et al. (1991)
TAG	403T	3340	50		0.52	189	239	1405					Edmond et al. (1995)
TAG	403B	3440	38		0.62	193	174	647					Edmond et al. (1995)
TAG	409T	3081	4		1.06	190	32	40					Edmond et al. (1995)
TAG	409B	3231	5		0.3	339	27	20					Edmond et al. (1995)
Rainbow	SAP 05_1	2025	278.8	83.6	0.3	184	1389	2386	287	47.2	24.5	13	Edmonds and German (2004)
Rainbow	SAP 06_1	1940	26.4	51	1	144	143	134	178	4.1	19.4	2.3	Edmonds and German (2004)
Rainbow	SAP 07_1	2150	18	72.2	3.4	216	98	153		5	24.6	2.4	Edmonds and German (2004)
Rainbow	SAP 09_1	2100	128.4	38.6	0.9	45	504	1781	751	43.5	7.2	4.1	Edmonds and German (2004)
Rainbow	27	2077	355.43	700.31	2.15	202.78	1910.64	5355.68	2030.09	117.40	32.97	15.61	This study
Rainbow	42	2209	38.42	446.55	0.04	22.47	205.65	396.33	25.47	15.71		0.97	This study
Rainbow	44	2002	132.73	1605.10	2.14	263.64	894.23	1355.13	729.65	77.71	37.23	10.05	This study
Rainbow	45	2166	171.11	1052.82	1.19	116.28	1213.40	1487.52	81.95	44.95	28.69	12.81	This study
Rainbow	46	2280	139.98	455.14	1.67	129.49	917.24	1195.15	353.27	31.14	26.29	9.99	This study

Table S4.2-B: Comparison of REE data with work of Edmonds and German (2004).

Sample	Depth [m]	La [pM]	Ce [pM]	Pr [pM]	Nd [pM]	Sm [pM]	Eu [pM]	Gd [pM]	Tb [pM]	Dy [pM]	Ho [pM]	Er [pM]	Tm [pM]	Yb [pM]	Lu [pM]	Reference
SAP05_1	2025	6.830	3.630	1.330	5.190	0.951	0.379	0.823	0.150	0.917	0.196	0.543	0.072	0.418	0.061	Edmonds and German (2004)
SAP06_1	1940	1.180	1.290	0.272	1.117	0.217	0.071	0.203	0.035	0.194	0.038	0.108	0.013	0.093	0.013	Edmonds and German (2004)
SAP07_1	2150	1.540	2.380	0.392	1.563	0.293	0.083	0.225	0.041	0.229	0.044	0.121	0.015	0.091	0.012	Edmonds and German (2004)
SAP09_1	2100	2.300	1.380	0.439	1.788	0.330	0.180	0.294	0.050	0.307	0.064	0.174	0.022	0.137	0.018	Edmonds and German (2004)
27	2077	7.179	4.343	1.389	5.250	1.019	0.498	1.149	0.193	1.285	0.274	0.717	0.093	0.521	0.072	This study
42	2209	0.480		0.124		0.090	0.036	0.102	0.010	0.077	0.024	0.054	0.006	0.043	0.003	This study
44	2002	5.562	3.247	1.160	4.037	0.842	0.302	0.984	0.147	0.956	0.228	0.554	0.068	0.410	0.051	This study
45	2166	6.130	3.305	1.308	4.658	0.979	0.375	1.148	0.187	1.252	0.271	0.694	0.089	0.526	0.072	This study
46	2280	4.884	2.972	1.059	3.839	0.803	0.303	0.933	0.155	0.976	0.205	0.537	0.070	0.415	0.059	This study

Figures

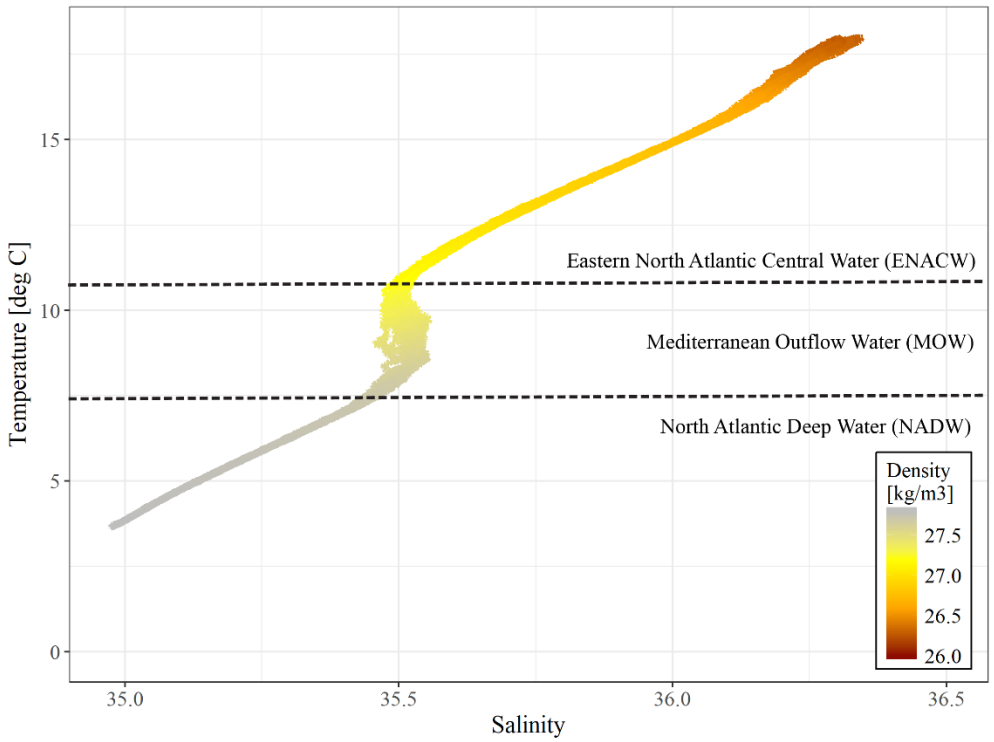

Figure S4.1: Temperature – salinity plot of all CTD casts showing the three distinct water masses found in the Rainbow area.

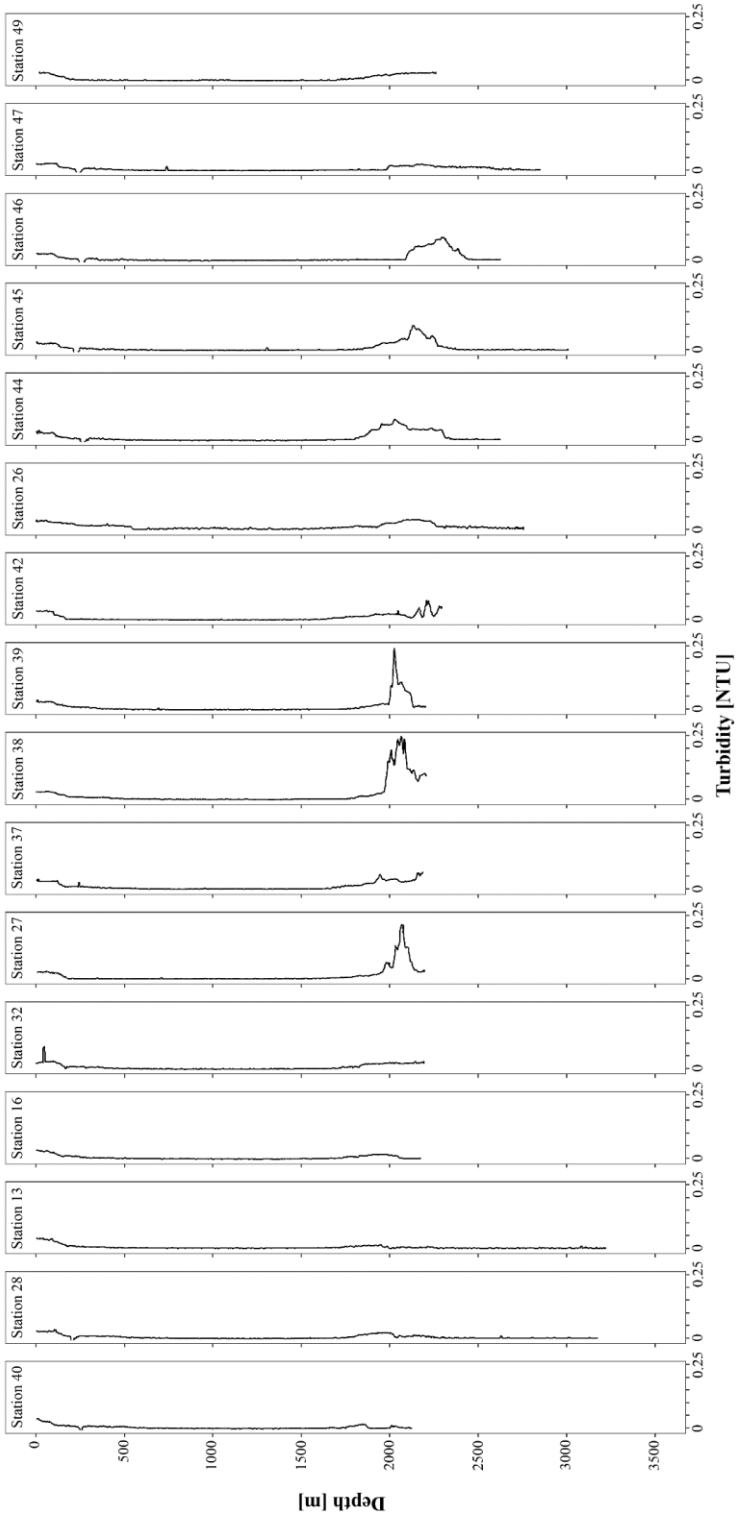

Figure S4.2: CTD casts of discussed stations showing the measured turbidity.

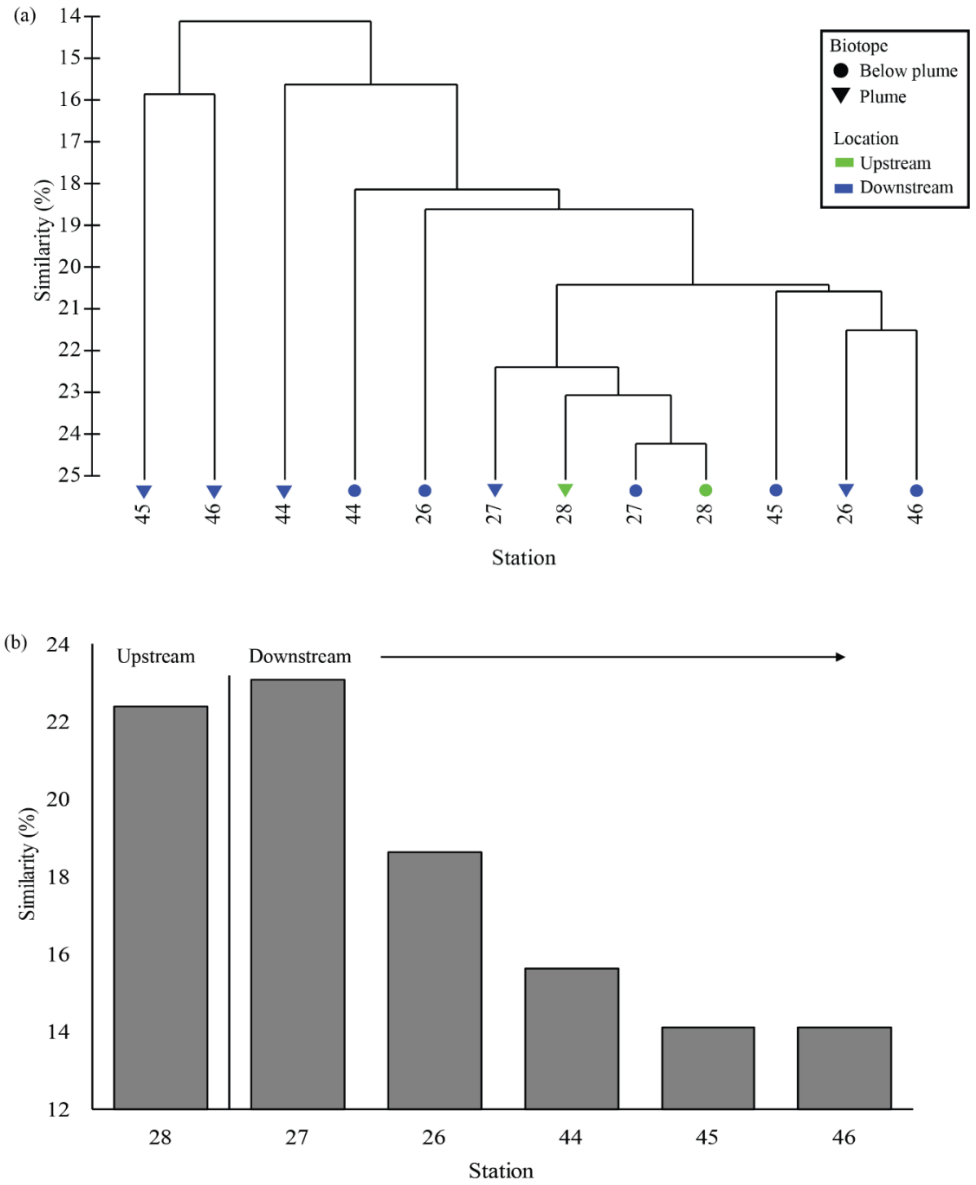

Figure S4.3: Group average clustering of plume and below plume microbial communities. (a) Dendrogram results; (b) Similarity between plume and below plume samples.

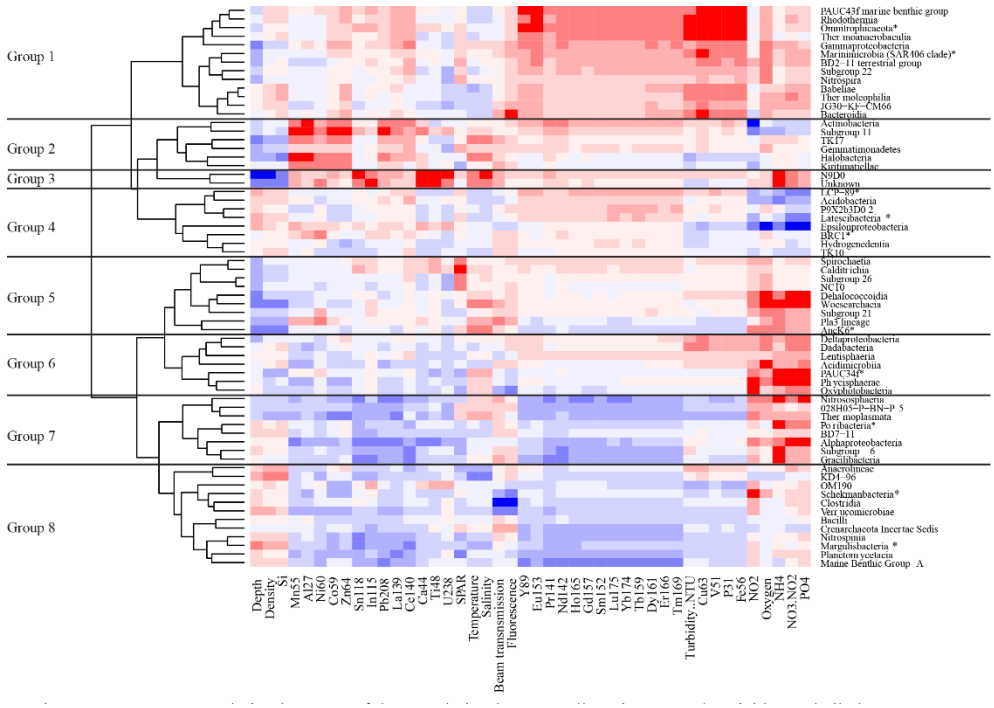

Figure S4.4: Pearson correlation heatmap of the correlation between all environmental variables and all classes that were present in multiple samples within plume samples. Colour intensity refers to the strength of the correlation; red indicates a positive correlation and blue indicates a negative correlation. Dendrograms based on hierarchical clustering and groups based on clustering to 8 distinct groups.

Image: The RV *Pelagia* in the harbour of Horta, Faial, Azores, in June 2016, with the volcano Pico in the back. Photo by: Sabine Haalboom.


PELAGIA
PELAGIA

APOLLO II
IHC

Chapter 5: Monitoring of a sediment plume produced by a deep-sea mining test in shallow water, Málaga Bight, Alboran Sea (southwestern Mediterranean Sea)

Sabine Haalboom, Henko de Stigter, Christian Mohn, Thomas Vandorpe, Marck Smit, Laurens de Jonge & Gert-Jan Reichart

Published as:

Haalboom, S., de Stigter, H.C., Mohn, C., Vandorpe, T., Smit, M., de Jonge, L., Reichart, G.-J., 2023. Monitoring of a sediment plume produced by a deep-sea mining test in shallow water, Málaga Bight, Alboran Sea (southwestern Mediterranean Sea). Marine Geology, v. 456, 106971. https://doi.org/10.1016/j.margeo.2022.106971

Image: Royal IHC's pre-prototype mining vehicle *Apollo II* on the back of the deck of *RV Sarmiento de Gamboa* offshore southern Spain during the Blue Nodules cruise in August 2019. Photo taken by: Laurens de Jonge.

Abstract

In this study different experimental designs for monitoring of sediment plumes produced by deep-sea mining are presented. Plumes of sediment stirred up from the seabed by mining machines are considered to represent a major environmental pressure which may extend far beyond the actual mining area. Two industry field tests with the scaled mining vehicle *Apollo II* of Royal IHC conducted in a relatively shallow setting offshore southern Spain provided valuable insights for anticipated monitoring of nodule mining activities in the deep Pacific. Although the tests were performed in only 300 m water depth, much less than the depth where future deep-sea mining will take place, the weakly stratified bottom water, tide-dominated near-bed currents with mean magnitude of around 5-10 cm s^{-1}, and gently sloping seabed covered with fine muddy sediment provide a good analogue to operational conditions in the deep sea. The plume of suspended sediment mobilised by the mining vehicle was monitored with turbidity sensors deployed on a ship-operated CTD system and on a static array of moored sensors and monitored visually using a ship-operated ROV. It was found that the generated sediment plume extended no >2 m above the seabed close to the source (<100 m) but increased in height at greater distance. Furthermore, turbidity values decreased rapidly with increasing distance to the source. Even though plume monitoring suffered interference from bottom trawling activities in neighbouring areas, a distinct turbidity signal generated by the mining equipment could still be distinguished above background turbidity at 350 m away from the source. From the experience gained in shallow water, recommendations are made on how a combination of sensors operated from moving and moored platforms may be a suitable and successful strategy for monitoring man-made sediment plumes in the deep sea.

5.1. Introduction

Concerns about future access to strategic raw materials for the high-tech industry have led to renewed interest in mining of mineral resources from the deep sea as a potential alternative for land-based mining (e.g. Hoagland et al., 2010). Polymetallic nodules, especially abundant in the eastern equatorial Pacific Ocean in water depths of 4000-6000 m, are a likely target of future deep-sea mining (e.g. Glover and Smith, 2003). Polymetallic nodules contain critical raw materials including nickel, copper, cobalt, and manganese in addition to considerable quantities of rare earth elements (e.g. Hein et al., 2013). Polymetallic nodule harvesting from deep-sea environments at an industrial scale is a technological and environmental challenge.

Until present, no integrated system for nodule extraction from extreme deep-sea environments including nodule collection, vertical transport and surface processing has reached industrial viability. Furthermore, a legally binding framework regulating extraction of deep-sea mineral resources in areas beyond national jurisdiction, including important aspects such as management of waste disposal, minimizing environmental impact, and safeguarding ecological preservation, is still in preparation by the International Seabed Authority (ISA) in line with requirements of UNCLOS (ISA - International Seabed Authority, 2019). Many questions exist about possible environmental impacts of deep-sea mining, as it would involve the removal of hard substrate, disturbance of the surface sediment layer, and dispersion of mobilised sediment over large areas of seabed adjacent to the mining site (Levin et al., 2016a). To date, impacts and effects of deep-sea mining inside the directly mined area are poorly understood. Estimating mining-related impact in open oceanic regions outside mined areas is even more challenging due to uncertainties of the mining impact scale (Gollner et al., 2017). This mainly concerns the fate and dispersal of sediment-laden near-bottom and mid-water plumes from nodule collection and return of excess sedimentary material after nodule separation. Different ecological risks have been previously highlighted (Jones et al., 2017), including burial of organisms, clogging of suspension feeders and masking of bioluminescence (Washburn et al., 2019). The combined effects of nodule removal and sediment plume deposition may reduce biodiversity and standing stock at the landscape scale (Simon-Lledo et al., 2019). Polymetallic nodule mining at an industrial scale and complementary monitoring of the deep-sea ecosystems and plume propagation have not begun anywhere in the world's oceans. Thus, mining tests and associated monitoring inside a small test area provide a vital baseline for determining the full spatial extent and impact of plumes (Gjerde et al., 2016). Previous impact experiments have contributed to the development of sediment plume models (e.g. Lavelle et al., 1982; Brockett and Richards, 1994; Jankowski et al., 1996; Barnett and Suzuki, 1997), but often have mainly focussed on sediment redeposition (e.g. Yamazaki et al., 1997; Rolinski et al., 2001). Plume modelling in deep-sea environments is ambitious due to a shortage of physical data for model validation and interpretation. Thus, both in situ baseline data from prospective mining sites yet undisturbed by deep-sea mining and data from monitoring during mining equipment tests and full-scale mining operations are needed to close the existing data gaps and to improve model skills (Gjerde et al., 2016). This again proves the necessity of smaller-scale impact experiments, from which the observations can be used

to build and validate models of plume behaviour and dispersion. The reliability of these models will depend on realistic boundary conditions and sediment characteristics obtained from in situ near-field tests (particle size distribution, sediment release depth and flux, settling velocities, realistic mining scenario) and environmental conditions in the surrounding far-field (bathymetry, ocean currents). Such a combined observation and model approach was successfully applied in a number of recent deep-sea mining related studies in the Clarion-Clipperton Zone (CCZ) (Aleynik et al., 2017; Gillard et al., 2019; Purkiani et al., 2021; Baeye et al., 2022), Tropic Seamount (Spearman et al., 2020) and the Southern California Bight (Kulkarni et al., 2018). Observations on sediment plume dispersion acquired during tests with industrial mining machinery could help to improve existing numerical models, as well as serving as input for future modelling approaches.

Anticipating full-scale industrial mining tests, of which the nodule collector trials by DEME-GSR in the deep Pacific Ocean in spring 2021 heralded the beginning (DEME Group, 2021), we tested approaches for environmental monitoring of mining activities during two industry field tests in relatively shallow waters (about 300 m water depth) offshore southern Spain, carried out in the framework of the European H2020 Blue Nodules project. These field tests, involving technical validation of the scaled polymetallic nodule mining vehicle *Apollo II* developed by the Dutch shipbuilder and maritime technology provider Royal IHC, provided an opportunity to monitor the dispersion of sediment plumes generated by the vehicle. Data on current regime and turbidity collected during the field tests is currently used for numerical modelling of the dispersion of generated sediment plumes. In this paper, we present the experimental setup consisting of static mooring arrays deployed at the seabed and complementary remotely operated vehicle (ROV), and ship-based measurements in the water column with conductivity, temperature, and depth (CTD) profilers, as well as ship-based acoustic Doppler current profiler (ADCP) measurements. Based on our results we point out advantages and shortcomings of the experimental setup and make recommendations for monitoring of sediment plumes in operational settings in the deep sea.

5.2. Study Area

The test area is located on the northwestern Alboran Sea continental slope, about 10 nm south of Málaga, Spain, where the water depth is around 300 m (Fig. 5.1). The western Alboran Sea

is an area of complex water mass and flow dynamics where the deep outflow of high-saline Mediterranean Sea waters through the Strait of Gibraltar is balanced by the near-surface inflow of less saline and colder water masses from the Atlantic (e.g. Vargas-Yanaz et al., 2002; Ercilla et al., 2016; Millot, 2009). The clockwise western Alboran Gyre is the dominant mesoscale circulation feature in the area, extending from east of the Strait of Gibraltar throughout the entire Alboran Basin (Millot, 1999; Renault et al., 2012; Fig. S5.1). It is a quasi-permanent feature with little seasonal or inter-annual variability (Fig. S5.1). The western Alboran Gyre is most pronounced in the upper 200 m of the water column with maximum current speeds of up to 1 m s^{-1} and is composed of surficial Atlantic Water (AW), modified by mixing with high salinity Mediterranean waters (Millot, 2009). At greater depths, westward propagation of Mediterranean waters in deeper layers compensate the inflow of modified AW. The main deeper water masses are Levantine Intermediate Water (LIW) and Western Mediterranean Deep Water (WMDW). LIW originates in the Levantine Basin in the eastern Mediterranean, flows along the Spanish continental margin in the depth range of 200-600 m and is characterised by salinities exceeding 38.4 in the Western Alboran Sea (Millot, 2009). WMDW has a maximum salinity of 38.4 and is formed in the Western basins of the Mediterranean, spreading along the Moroccan and Spanish continental margin at depths >600 m (Millot, 2009). Tidal currents are generally weak in the Mediterranean Sea (<2 cm s^{-1}) but can be significant in the Alboran Sea with semi-diurnal tidal amplitudes occasionally exceeding 5 cm s^{-1} (Poulin et al., 2018). Other oscillatory motions are associated with internal solitary waves generated over the Camarinal Sill in the Strait of Gibraltar propagating into the western Alboran Sea, which at spring tide may exceed 100 m in vertical amplitude (Sanchez-Garrido et al., 2011). They are well detectable in our field test area but cannot be found eastward of 4 °W (van Haren, 2014). Ercilla et al. (2016) provide a general overview of the geomorphology and sedimentology in the western Alboran Sea and evaluated the role of bottom currents in shaping the Spanish and Moroccan continental margins. Muddy sand and gravel supplied by rivers are the dominant sediment types on the shelf east of Málaga (Bárcenas, 2011), and most likely also on the shelf further to the west. Beyond the shelf break, which is located at 90 m depth in the Málaga Bight, the sediment consists of hemipelagic mud (Baraza et al., 1992; Masqué et al., 2003). The field test area is located on the very gently sloping upper slope (<1 °), away from dynamic sedimentary environments such as canyons and channels. The absence

of uneven and/or steep terrain in combination with gentle background sedimentation rates render the area suitable for driving with *Apollo II*.

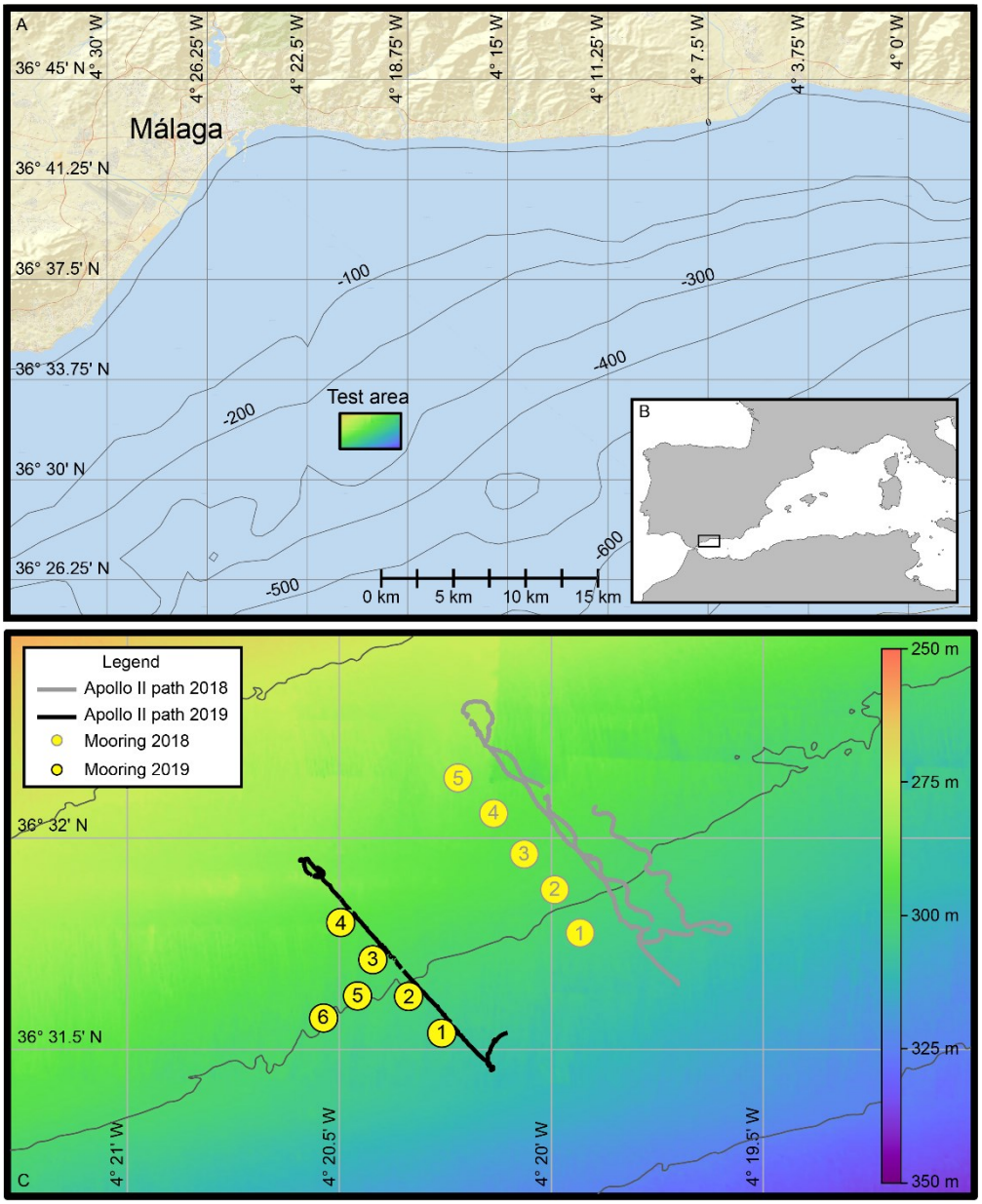

Figure 5.1: A) Bathymetric map of the Málaga Bight, SW Mediterranean Sea, with location of the Blue Nodules test site (Google Maps). Location of the test area in the western Mediterranean Sea is shown in B. C) The location of the moorings and the path driven by Apollo II during the drive-by experiments of 2018 and 2019. The isobath contours are given for 275 m, 300 m, and 325 m depth.

From automatic identification systems (AIS) data, the selected area appeared to have relatively low maritime traffic intensity as compared to more near-shore areas (MarineTraffic – Global Ship Tracking Intelligence; www.marinetraffic.com). However, AIS tracks in the vicinity of the test area parallel to the bathymetric contours, indicate (local) fishing activity, in particular bottom trawling. This was confirmed by our own observations of trawlers active at short distance from our test area and is also supported by observations done by Brennan et al. (2015) who visually observed seabed disturbance by bottom trawlers in the area. The trawling results in substantial sediment resuspension and consequently background turbidity values which are much higher than in the deep-sea areas where no bottom trawling takes place (Puig et al., 2012; Mengual et al., 2016; Daly et al., 2018).

5.3. Experimental design

Two industry field tests of Royal IHC's *Apollo II* scaled polymetallic nodule mining vehicle, carried out onboard RV *Sarmiento de Gamboa* in August 2018 and 2019, provided an opportunity to monitor environmental effects arising from usage of this type of deep-sea mining equipment. Monitoring of the sediment plume generated by *Apollo II* comprised vessel-based measurements using CTD and ROV as mobile sensor platforms, and an array of sensors moored at the seabed. The mooring array was equipped with several sensors to record current speed and direction, as well as turbidity. The ROV provided visual observations of the environmental impacts. Usage of a CTD-Rosette system allowed for profiling of water column properties and collection of water samples. A shipboard ADCP (S-ADCP) provided water column current speed and direction.

5.3.1. The Apollo II scaled mining vehicle

Royal IHC's *Apollo II* is a scaled pre-prototype mining vehicle with a hydraulic nodule collector (Fig. 5.2; Boschen et al., 2020). This mining vehicle is 5.6 × 2.5 × 2.3 m in size and weighs 3800 kg in air and 850 kg in water. The mining vehicle is remotely operated through an umbilical cable, enabling hoisting, power supply and data exchange. Propulsion of the vehicle is by four caterpillar tracks, which exert an average pressure of 2.8 kPa on the seabed.

Figure 5.2: Deployment of the Apollo II pre-prototype nodule collector vehicle from the aft of RV Sarmiento de Gamboa during the 2018 field test in Málaga Bight. Photo courtesy: Alberto Serrano. Note the Nortek Aquadopp current profiler mounted upward-facing on starboard side of the diffuser. Acoustic backscatter data presented in Fig. 5.11E were acquired with the current profiler mounted backward-facing.

During the tests, *Apollo II* was driving at variable speeds up to 0.55 m s^{-1}, with an average speed of 0.25 m s^{-1}. Underwater navigation was done based on propulsion system data and compass readings relayed through the umbilical, whilst a Global Acoustic Positioning System (GAPS) transponder provided underwater position during the tests. The 1 m wide hydraulic nodule collector makes use of powerful jets of seawater to lift the nodules from the seabed. Water flow through the collector is regulated by varying pump rates. The standoff height of the collector relative to the seabed could not be remotely adjusted during the tests but was mechanically adjusted on board the vessel. Since polymetallic nodules are not present in the field test area, only the erosion of the surface sediment layer by the collector could be tested. Sediment taken up by the collector is discharged through the diffuser mounted at the rear of the vehicle. The diffuser is designed to minimise plume development by reducing the discharge flow velocity and aiming the density flow downwards. In order to determine the suspended particulate matter (SPM) mass concentration in the immediate vicinity of *Apollo II*, a JFE Advantech Infinity optical backscatter sensor (OBS) was mounted to the diffuser to record the turbidity at a sampling rate of 1 min. Furthermore, in 2018, a Nortek Aquadopp 2 MHz current profiler was mounted on the diffuser. During the drive-by in front of the moorings on the 18th of August, the sensor was mounted with its head facing backwards, whereby two

of the beams were directed downwards towards the seabed and one beam was directed upwards. This allowed for recording echo amplitude profiles behind the diffuser of the *Apollo II*, at a sampling rate of 5 min.

5.3.2. ROV Zonnebloem

The ROV *Zonnebloem* (formerly called ROV *Genesis*) of the Flanders Marine Institute (VLIZ) was used for performing video surveys of the seabed at the field test site before and after passage of *Apollo II*, for technical inspections during deployments of *Apollo II*, and for observations of the sediment plume generated by *Apollo II*, while it was driving over the seabed. It is a 2000 m depth rated CHEROKEE ROV with a Tether Management System (TMS) built by the company Sub-Atlantic. For video observations, the ROV was equipped with a Luxus HD Zoom forward-looking video camera, mounted on a pan-and-tilt unit and two SD Luxus compact cameras installed at the rear and on front of the ROV.

5.3.3. Underwater positioning

Sub-meter navigation of the *Apollo II* and the ROV and positioning of the box corer used for sediment coring was performed using an IXBLUE GAPS and transponders mounted on each of the platforms. The calibration-free GAPS is a portable Ultra Short Base Line (USBL) with integrated Inertial Navigation System. The GAPS was mounted and deployed from the drop-keel of RV *Sarmiento de Gamboa* and received the ship's onboard GPS signal. Underwater positioning was obtained every second and all positioning data (ship and GAPS) was immediately visualized.

5.3.4. Water column profiling and sampling

5.3.4.1. CTD-Rosette

The SeaBird 911+ CTD-Rosette system of RV *Sarmiento de Gamboa* was lowered through the water column for profiling of water properties, including while the *Apollo II* was driving, targeting the plume generated by the mining vehicle (Fig. 5.3). Water samples for collection of SPM were taken at discrete water depths using the 12 L Niskin bottles integrated in the CTD-Rosette system. The CTD-frame was equipped with two turbidity sensors, a WetLabs ECO FLNTU OBS integrated with the standard sensor package and a JFE Advantech Infinity OBS mounted at the base of the CTD frame. A second JFE Advantech OBS was suspended below

the CTD-frame to record turbidity as close to the seabed as possible (one metre above bed, mab). In 2018, a Sequoia LISST-200X in situ particle sizer was mounted at the base of the CTD frame during three CTD casts for in situ observations of SPM particle size distribution. Additionally, the LISST-200X recorded turbidity using a transmissometer. In total 33 full water column CTD casts were collected, 18 in 2019 and 15 in 2019 (Supplement Table 5.1). Nineteen of the 33 CTD casts were carried out from a moving ship following the mining vehicle, aiming to capture the sediment plume generated by the *Apollo II*. Various approaches, tow-yo-ing the CTD between surface and 4 mab, towing the CTD at 4 mab, tow-yo-ing between 4 and 10 mab, tow-yo-ing between 2 and 15 mab, were done to acquire profiles and water samples from the sediment plume created by *Apollo II*.

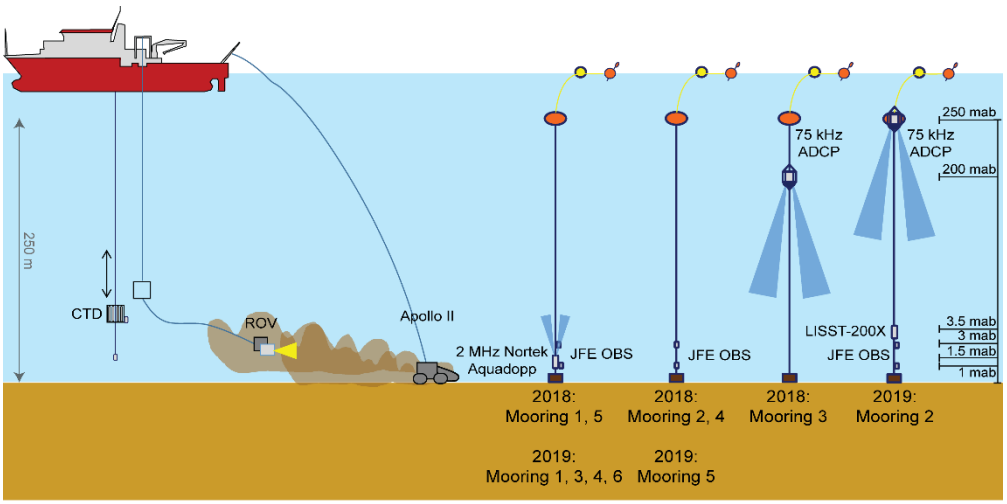

Figure 5.3: Schematic overview of the plume monitoring setup. Apollo II was driven along the mooring array equipped with turbidity sensors, current profilers, sediment traps, LISST and acoustic recorder, while RV Sarmiento de Gamboa was following, moving backwards. During this operation, the CTD or ROV equipped with additional turbidity sensors were alternatingly deployed for monitoring the plume.

Water samples taken during the CTD casts were used for determining the SPM mass concentration inside- and outside of the generated sediment plume, as well as the background turbidity. From each collected 12 L Niskin bottle, two subsamples of maximum 5 L were drawn. These subsamples were vacuum filtered on board over pre-weighed 47 mm polycarbonate filters with a pore size of 0.4 µm, applying 0.3 Bar underpressure. After filtration the filters were rinsed with Milli-Q water, and subsequently left to dry in a Flowtronic laminar flow bench. In the laboratory, the filters were rinsed once more with Milli-Q water to remove any

remaining salt and then freeze-dried. Afterwards the filters were weighed in duplo, or in triplo if the difference between the first two measurements was >0.03 mg. To yield SPM mass concentrations, the net dry weight of the SPM collected on the filters, corrected by the average weight change of all blank filters, was divided by the volume of filtered seawater.

5.3.4.2. Shipboard ADCP

Shipboard ADCP data were collected continuously in 2018 and 2019 throughout the entire survey period (8-19 August 2018, 12-25 August 2019). On-station and underway current velocity components were collected in the water column with a 75 kHz Teledyne RD Instruments (RDI) Ocean Surveyor system mounted in the hull of RV *Sarmiento de Gamboa* along with ancillary data of ship position and motion (pitch, roll and heading). The software RDI VmDAS was used to configure instrument setup, data communication (ship position, ship heading) and data acquisition. The vertical bin size was set to 8 m (first bin at 25 m, transducer depth 9 m) and the total sampling range was 100 bins (800 m). The transducer offset relative to the ship's keel was 46.33°. Repeated underway ADCP surveys were conducted mostly during night-time along a rectangle (6.25 km E-W x 7.78 km N-S) set around the actual test site. On-station time series were collected at the field test site inside the underway rectangle mainly during daytime.

S-ADCP data were processed and analysed daily on board to provide near real-time estimates of structure and variability of currents in support of the in situ monitoring. Processing of single ping S-ADCP data was conducted using the Common Oceanographic Data Access System (CODAS) from the University of Hawaii (Firing et al., 1995; http://currents.soest.hawaii.edu/docs/adcp_doc/index.html) following the GO-SHIP guidelines for S-ADCP measurements (Firing and Hummon, 2010). The main CODAS processing steps included time-averaging of single ping data into 120 s ensembles, water track calibration to estimate any remaining transducer offset and calculating absolute current velocities by removing the ship velocity from the ADCP ensemble velocities. Finally, depth bins with a percent good value <20% of the acoustic return signal were discarded to eliminate effects from strong interference of the acoustic signal with the seabed (Mohn et al., 2018). As a consequence, velocity data from the lower 3 bins (24 m) above bottom were discarded.

5.3.4.3 Sediment sampling

For analysis of particle size distributions in the surface sediment, sediment cores were collected by means of a NIOZ 'HaJa' box corer. The cylindrical coring barrel of 30 cm diameter and height of 55 cm is closed off on both ends upon retrieval from the seabed, preserving the sediment core with overlying water relatively undisturbed. In total 12 successful box corer casts were made and from each of the cores in 2018, and from 5 of the 7 cores taken in 2019, a 6 cm diameter subcore was taken. Sediment particle size distribution was determined for the top 1 cm of each subcore with the Beckman Coulter LS13 320 at NIOZ. About 250 mg of wet sediment was immersed in a beaker with 20 mL of reverse osmosis (RO) water and dispersed without application of ultrasonic or chemical dispersant. The suspension was introduced in the large volume cell of the particle sizer, and particle size distributions were calculated applying an optical model (called: grey), which uses an average of refractive indices of the most common minerals including quartz, calcite, feldspar, and mica, suited for fine-grained sediment. Particle size distribution is reported as volume percentage of particles within logarithmic size classes from 0.4 to 2000 µm, assuming spherical particles.

5.3.5. Mooring array

Different mooring setups were tested for monitoring of the temporal evolution and spatial extent of sediment plumes created by the *Apollo II* test vehicle. The moorings consisted of a 760 kg steel anchor weight, directly attached (2018) or attached via a single IXSea acoustic release (2019) to a 250 m long mooring line, the latter held up in the water column by a 150-250 kg "smartie" float of syntactic foam, to which an additional 50-70 m long floatline with surface floats was attached. Accurate positioning on the desired location, which in 2019 could be confirmed by acoustic ranging of the releases, was done by lowering the mooring string with anchor weight first to the seabed. In 2018, five moorings were distributed with a 200 m interval along a single 800 m SE-NW trending line parallel to the intended driving path of the vehicle and perpendicular to the expected prevailing current directions (Fig. 5.1; Fig. S5.2). By driving *Apollo II* at different distances along the mooring array, the characteristics of the proximal and more distal plume would be recorded. In 2019, six moorings were deployed in a T-shaped array (Fig. 5.1; Fig. S5.2). Four of these on a 600 m long, SE-NW trending line oriented at right angles to the isobaths and parallel to the intended driving path of the vehicle and perpendicular to the expected prevailing current direction, with the moorings 200 m apart

from each other. Two were placed perpendicular to this first line at 150 and 300 m distance, respectively. In this configuration, a single drive-by would suffice to record both the proximal and the more distal plume.

The application of different types of sensors on the moorings and on mobile platforms is illustrated in Fig. 5.3. Sensor settings are given in Table 5.1. To record turbidity and current speed and direction, 4 moorings in 2018 and 6 in 2019 were equipped with JFE Advantech OBSs at 1 and 3 mab, 4 moorings with upward-looking 2 MHz Nortek Aquadopp current profilers at 2 mab and one mooring with a downward-looking 75 kHz RDI Workhorse Long Ranger ADCP mounted at 200 mab (2018) and 250 mab (2019). In addition to that, 2 moorings were equipped with Technicaps PPS4/3 sediment traps during both years (BN18-M2, BN18-M4, BN19-M4 and BN19-M5) for collecting settling particulate material. The sediment traps with cylindroconical shape had their 0.05 m^2 opening at 2.5 mab and were each equipped with a carrousel with 12 sampling bottles of 250 mL. The data of the 2018 moorings is not shown here as the sediment traps sampled material when the *Apollo II* was not being operated. In 2019 the sediment traps were set to sample on the 20th of August. Furthermore, in 2019 mooring 2 (BN19-M2) was equipped with a LISST-200X at 3.5 mab for in situ recording of particle sizes and turbidity and a Develogic Sono Vault deep-sea acoustic recorder at 10 mab for recording underwater noise. The sampling frequency was set to 1 min for the OBSs, Nortek Aquadopp current profilers and LISST. The 75 kHz ADCP had a sampling frequency of 2 min. The Nortek Aquadopp had a sampling range of 10 m, with vertical intervals binned over 0.5 m (20 bins) and a blanking distance of 0.5 m. In 2018, the 75 kHz ADCP had a sampling range of 240 m with vertical intervals binned over 16 m (15 bins) and a blanking distance of 24.8 m. In 2019, the 75 kHz ADCP had a sampling range of 296 m with vertical intervals binned over 4 m (74 bins) and a blanking distance of 12.81 m. Data points collected by the Nortek Aquadopp represent the ensemble average of 60 individual measurements within the sampling interval, for the JFE Advantech OBS this is 15 measurements per ensemble and for the 75 kHz ADCP, respectively for 2018 and 2019, 11 pings per ensemble and 60 pings per ensemble.

Table 5.1: Overview of the used sensors, with specifications on measurements settings and deployment.

Name	Year	Platform	Equipment	Depth	Measuring range	Settings
BN18-L3	2018	Apollo II (L3)	JFE Advantech OBS	1.65 mab	Spot measurement	5 min interval, 30 samples, 1 Hz
			Nortek Aquadopp	2.40 mab	2.9 – 12.9 mab	5 min interval, 60 samples, 1 Hz, 20 bins, 0.5 m bin size, 0.5 m blanking distance
BN18-L5	2018	Apollo II (L5)	JFE Advantech OBS	1.75 mab	Spot measurement	1 min interval, 15 samples, 1 Hz
			Nortek Aquadopp	1.75 mab	0.5 – 10.5 m	1 min interval, 30 samples, 1 Hz, 48 bins, 0.2 m bin size, 0.1 m blanking distance
BN18-M1	2018	M1	JFE Advantech OBS	1 mab	Spot measurement	1 min interval, 15 samples, 1 Hz
			JFE Advantech OBS	3 mab	Spot measurement	1 min interval, 15 samples, 1 Hz
			Nortek Aquadopp	1.5 mab	2 mab – 12 mab	1 min interval, 30 pings, 1 Hz, 20 bins, 0.5 m bin size, 0.5 m blanking distance
BN18-M2	2018	M2	JFE Advantech OBS	1 mab	Spot measurement	1 min interval, 15 samples, 1 Hz
			JFE Advantech OBS	3 mab	Spot measurement	1 min interval, 15 samples, 1 Hz
BN18-M3	2018	M3	RDI Workhorse ADCP	200 mab	0 mab – 175 mab	5 min interval, 11 pings, 0.04 Hz, 15 bins, 16 m bin size, 24.8 m blanking distance
BN18-M4	2018	M4	JFE Advantech OBS	1 mab	Spot measurement	10 min interval, 15 samples, 1 Hz
			JFE Advantech OBS	3 mab	Spot measurement	10 min interval, 15 samples, 1 Hz
BN18-M5	2018	M5	JFE Advantech OBS	1 mab	Spot measurement	10 min interval, 15 samples, 1 Hz
			JFE Advantech OBS	3 mab	Spot measurement	10 min interval, 15 samples, 1 Hz
			Nortek Aquadopp	1.5 mab	2 mab – 12 mab	1 min interval, 30 pings, 1 Hz, 20 bins, 0.5 m bin size, 0.5 m blanking distance
BN19-M1	2019	M1	JFE Advantech OBS	1 mab	Spot measurement	1 min interval, 15 samples, 1 Hz
			JFE Advantech OBS	3 mab	Spot measurement	1 min interval, 15 samples, 1 Hz
			Nortek Aquadopp	2 mab	2.5 mab – 12.5 mab	1 min interval, 60 samples, 1 Hz, 20 bins, 0.5 m bin size, 0.5 m blanking distance
BN19-M2	2019	M2	JFE Advantech OBS	1 mab	Spot measurement	1 min interval, 15 samples, 1 Hz
			JFE Advantech OBS	3 mab	Spot measurement	1 min interval, 15 samples, 1 Hz
			LISST-200X	3.5 mab	Spot measurement	1 min interval, 60 samples, 1 Hz
			RDI Workhorse ADCP	250 mab	0 mab – 237 mab	2 min interval, 60 samples, 2 Hz, 74 bins, 4 m bin size, 12.71 m blanking distance
			Devologic Sono Vault acoustic recorder	10 mab	Spot measurement	Continuous sampling
BN19-M3	2019	M3	JFE Advantech OBS	1 mab	Spot measurement	1 min interval, 15 samples, 1 Hz
			JFE Advantech OBS	3 mab	Spot measurement	1 min interval, 15 samples, 1 Hz
			Nortek Aquadopp	2.5 mab	3 mab – 13 mab	1 min interval, 60 samples, 1 Hz, 20 bins, 0.5 m bin size, 0.5 m blanking distance
BN19-M4	2019	M4	JFE Advantech OBS	1 mab	Spot measurement	1 min interval, 15 samples, 1 Hz
			JFE Advantech OBS	3 mab	Spot measurement	1 min interval, 15 samples, 1 Hz
			Nortek Aquadopp	2.5 mab	3 mab – 13 mab	1 min interval, 60 samples, 1 Hz, 20 bins, 0.5 m bin size, 0.5 m blanking distance
			PPS4/3 Sediment trap	2.5 mab		Start: 20-08-2019 07:45, sampling interval: 1 h
BN19-M5	2019	M5	JFE Advantech OBS	1 mab	Spot measurement	1 min interval, 15 samples, 1 Hz
			JFE Advantech OBS	3 mab	Spot measurement	1 min interval, 15 samples, 1 Hz
			PPS4/3 Sediment trap	2.5 mab		Start: 20-08-2019 08:00, sampling interval: 1h
BN19-M6	2019	M6	JFE Advantech OBS	1 mab	Spot measurement	1 min interval, 15 samples, 1 Hz
			JFE Advantech OBS	3 mab	Spot measurement	1 min interval, 15 samples, 1 Hz
			Nortek Aquadopp	2 mab	2.5 mab – 12.5 mab	1 min interval, 60 samples, 1 Hz, 20 bins, 0.5 m bin size, 0.5 m blanking distance

The linear relationship found between the turbidity signal of WetLabs and JFE Advantech OBSs mounted on the CTD-Rosette system and SPM mass concentration determined by filtration of simultaneously taken Niskin water samples was used to convert the turbidity signal of each individual sensor into SPM mass concentration, following equation (Eq. 5.1):

$$SPM\ [mg\ L^{-1}] = a * Turbidity + b \qquad \text{(Eq. 5.1)}$$

in which *SPM* is the SPM mass concentration in mg L^{-1}, *turbidity* is the output of the OBS sensors in NTU or FTU, and *a* and *b* are constants determined by resolving the relationship between the recorded signal and the determined SPM mass concentration. This was done for each individual sensor, as all of them were lowered on the CTD at least once while during that cast at least 5 Niskin water samples were taken, covering a range of turbidity values. Turbidity values recorded by the LISST-200X (expressed as beam attenuation) have not been converted into SPM mass concentrations.

The echo amplitude (*amp*) recorded by the Nortek Aquadopp current profilers is explored here for information it provides on the near-bottom gradients in SPM mass concentration. The *amp* signal was converted to echo level to account for the attenuation by acoustic spreading and water absorption. This was done by following the equation (Eq. 5.2) given in the technical note by Lohrmann (2001):

$$Echo\ level\ [dB] = 0.43 * amp + 20log_{10}(R) + 2\alpha_w R + 20R \int \alpha_p\, dr \qquad \text{(Eq. 5.2)}$$

in which *R* is the distance along the acoustic beam, α_w the water absorption coefficient and α_p the coefficient of particle attenuation. The water absorption coefficient, α_w, was determined following the model of Ainslie and McColm (1998), with parameters set to an instrument frequency of 2000 kHz, temperature of 13.5 °C, salinity of 38.5 and depth of 300 m, giving an α_w of 1.234 dB m^{-1}.

The particle attenuation coefficient, α_p, dependent on site-specific particle characteristics, was treated as an unknown. In most cases this term can be ignored, especially at lower concentrations as the correction for the loss of attenuation over depth has a far larger effect

than the difference in particle attenuation over the ranged profile (Lohrmann, 2001). Therefore, the acoustic backscatter data shown in this study is only corrected for the loss of attenuation due to acoustic spreading and absorption by water (Eq. 5.3):

$$Echo\ level\ [dB] = 0.43 * amp + 20log_{10}(R) + 2\alpha_w R \quad \text{(Eq. 5.3)}$$

5.4. Results

5.4.1. Hydrography and current dynamics

The core water masses present in the test area can be clearly distinguished in CTD water column profiles and in a T-S plot comprising all temperature and salinity data recorded with the CTD (Fig. 5.4): modified AW in the upper 200 m with temperatures of 17–24 °C and salinities of 36.3-36.6, and at depths exceeding 200 m LIW with temperatures of below 13.4 °C and salinities higher than 38.4. S-ADCP water column current measurements in 2018 and 2019 (Supplement Fig. 5.3 and Fig. 5.5, respectively) show that E-W (u) and N-S (v) velocity components are dominated by semidiurnal internal tides; the resulting currents regularly change from southwest, i.e. along-slope, to northerly, cross-slope, direction (Fig. 5.5A, B). The surface layers (depths <100 m) were largely out of phase with the deeper layers indicating maximum current shear at around 100 m depth (Fig. 5.5A-C). A pronounced amplification of current magnitudes in the upper 100 m was recorded in 2019 after 23 August resulting in intensified SW along-slope flow and weaker cross-slope flow. The predominant semi-diurnal variation of currents was also observed near the bottom in current records obtained with moored Nortek Aquadopp current profilers (Fig. 5.5E). At all depth levels, the semi-diurnal tidal variation is superimposed on a SW along-slope mean flow.

5.4.2. Water column turbidity

Apart from shallow turbidity variations in the upper 50 m of the water column associated with pelagic productivity, most of the water column was relatively transparent, with SPM mass concentrations <0.1 mg L^{-1} (Fig. 5.4). In the lower 10-20 m of the water column, approaching the seabed, a decrease in transparency was observed. Background SPM mass concentration, measured with moored OBSs at 1 mab and excluding intervals when *Apollo II* was active at the bottom, showed conspicuous variation over the few days that the moorings were deployed, generally varying between 0.5 and 2.5 mg L^{-1} in 2018, with occasional peaks up to 5 mg L^{-1} and

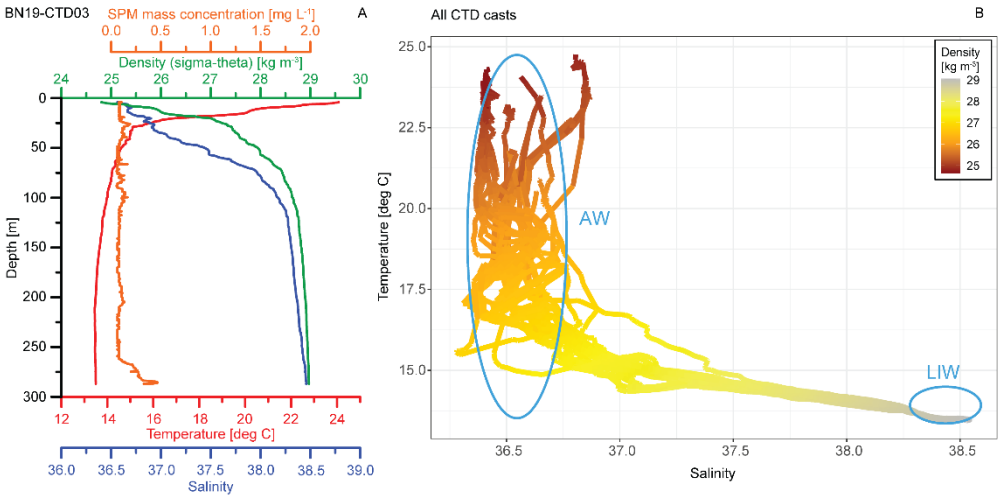

Figure 5.4: Water mass characteristics of the Málaga Bight test site. A) Water column profiles of temperature, salinity, density and SPM mass concentration as observed in CTD cast BN19-CTD03; B) T-S diagram comprising all 2018 and 2019 CTD measurements collected to a maximum depth of 300 m. The observed core water masses are modified Atlantic Water (AW) and Levantine Intermediate Water (LIW). Below 50 m depth AW properties are strongly modified (lower temperature, higher salinities) due to mixing with LIW. Our sampling did not reach water depths where Western Mediterranean Deep Water (WMDW) could be detected.

between 1 and almost 5 mg L^{-1} in 2019 (Fig. 5.6). With the relatively high background turbidity, it was at times difficult to distinguish the turbidity signal of the plume produced by *Apollo II*. During intervals of high turbidity, visibility was often so reduced that navigation of the ROV *Zonnebloem* close to seabed could not be done on sight but only with help of sonar and altimeter. SPM particle size distribution with the LISST-200X, which in 2018 was mounted in the CTD frame and in 2019 mounted at 3.5 mab in BN19-M2, showed highly variable bimodal distribution patterns (Fig. 5.7A). In background water without additional SPM stirred up by *Apollo II*, a relatively fine mode centred around 5 to 10 µm was almost always present, while a more pronounced coarser mode was found to shift back and forth between 50 and 250 µm. The coarsest modes occurred mostly during intervals of high background turbidity.

5.4.3. Seabed characteristics

From seabed video imagery obtained with ROV and *Apollo II* and box coring results, the weakly sloping seabed of the test area (average slope of 0.9°) appeared uniformly covered with soft clayey silt. The surface sediment recovered in box cores had a bimodal particle size distribution, with a fine-grained mode centred around 12-32 µm and a coarser mode centred around 128-185 µm. Median particle size is 16-30 µm (Fig. 5.7B).

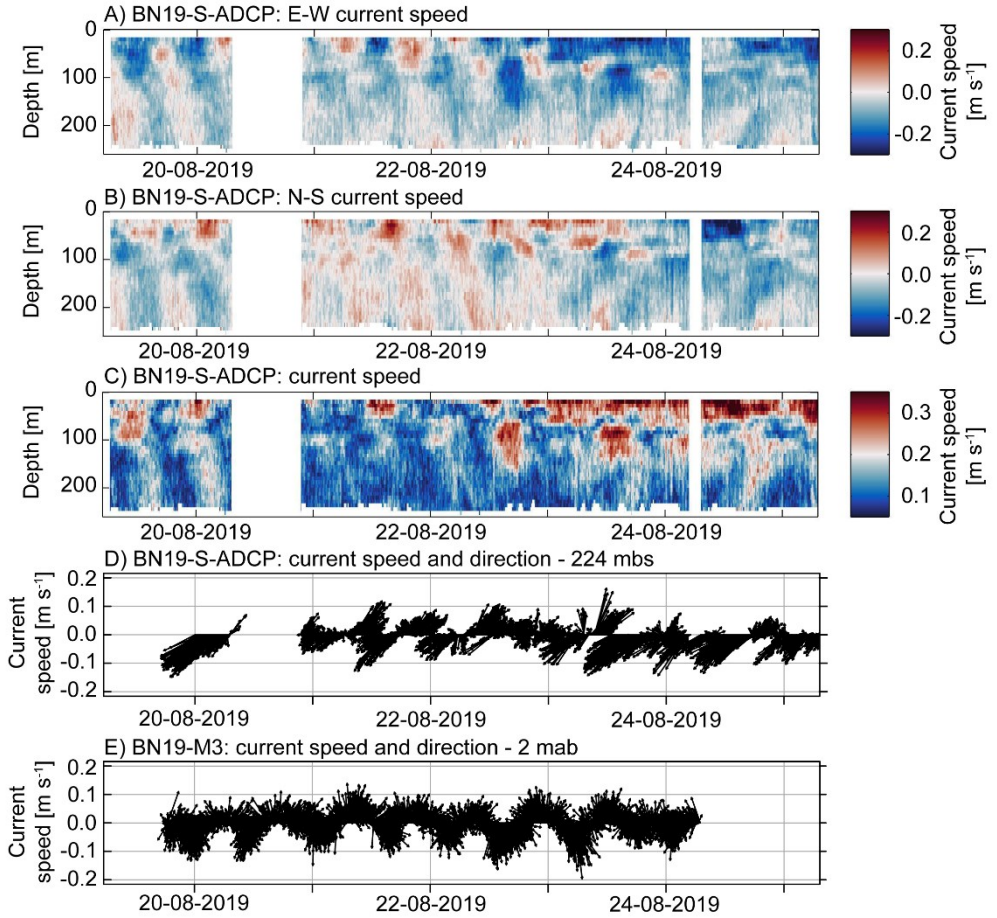

Figure 5.5: Current dynamics of the Málaga Bight test site for the period 20-25 August 2019, when the mooring array was deployed. A-C) Time series of, respectively, E-W current speed, N-S current speed, and total current speed (m s^{-1}) between 25 and 250 m below sea surface (mbs) recorded by the S-ADCP; D and E) Time series of, respectively, current speed recorded at 224 mbs by the S-ADCP and current speed recorded at 2 mab by the Aquadopp current profiler of mooring BN1-M3.

The sand fraction is largely composed of planktonic and benthic foraminifera and rounded glauconite grains, the latter mostly formed as internal casts of foraminifera shells. The sediment surface, as observed with ROV *Zonnebloem* and the forward-looking camera of *Apollo II*, was marked by a conspicuous pit and mound morphology resulting from intense bioturbation by burrowing crustaceans (Fig. 5.8). Large Cerianthus sea anemones were also relatively common (Fig. 5.8B). Upon approach of *Apollo II* these anemones were seen to retract into the sediment within a split second, an escape behaviour which enables these animals to survive in an intensely trawled area. Other sessile benthic fauna appeared scarce, likely under pressure from the intensive trawling. Trawl marks, including elongate striae produced by the

trawl net dragging over the seabed and deep groves ploughed in the seabed by the trawl doors (Fig. 5.8C), were commonly encountered.

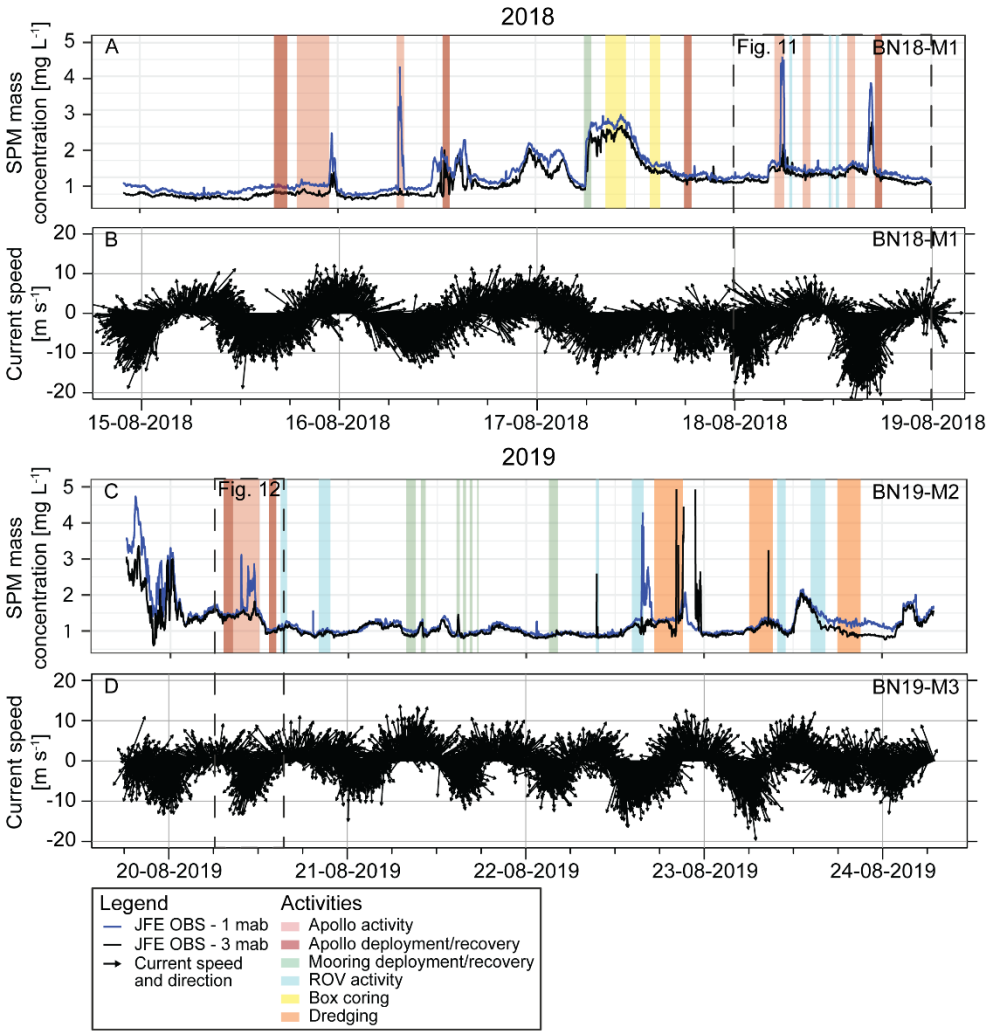

Figure 5.6: Time series of SPM mass concentration and current speed and direction in the near-bottom layer as recorded by the JFE OBSs and Aquadopp current profilers in moorings BN18-M1, BN19-M2 and BN19-M3, deployed, respectively, 15-19 August 2018 and 19-24 August 2019. The different coloured bars represent different activities that might have caused resuspension of surface sediments. Data recorded during Apollo II drive-bys are illustrated in more detail in Figs. 5.11 and 5.12.

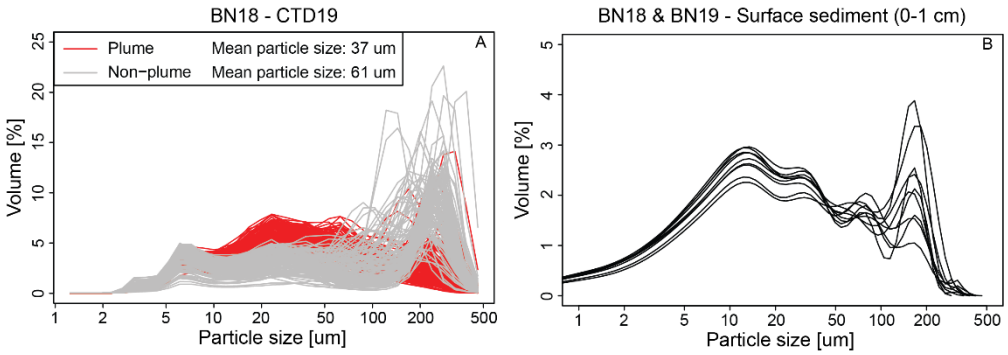

Figure 5.7: A) Particle size distribution curves of, respectively, non-plume background SPM (grey) and plume (red) in near-bottom water recorded by LISST-200X on BN1-CTD19 on the 18th of August 2018. The distinction of plume/non-plume SPM is made on the basis of simultaneously recorded turbidity (beam attenuation) by the LISST-200X (see Supplement Fig. 5.4A). B) Particle size distribution of surface sediment (0-1 cm) of the box cores from 2018 and 2019.

5.4.4. SPM characteristics and sensor calibration

The turbidity signal recorded with the WetLabs and JFE Advantech OBSs mounted on the CTD-Rosette system generally showed a good linear relationship with SPM mass concentration measured in Niskin water samples taken simultaneously (Fig. 5.9). R^2 values for the linear fit ranged from 0.74 to 0.92 in 2018 and from 0.88 and 0.97 in 2019 (Fig. 5.9 and public data in PANGAEA), excluding data from CTD02 of 2019 (red line). Most of the Niskin samples used for sensor calibration probably represent background water. Collecting water samples from the plume turned out to be difficult, because the plume in its initial phase, while it was in reach of the CTD lowered from the ship, did not extend much higher than 2-3 m above the seabed. In order to sample the plume, the CTD-Rosette should have been immersed into the plume, with high risk of hitting the seabed. Only CTD02 in 2019 (red data points in Fig. 5.9A and B) appeared to have successfully sampled water from within the plume, which is reflected by a conspicuously different relationship of SPM mass concentration vs. turbidity measured with the OBSs. For similar SPM mass concentration, the plume SPM would produce a 2- to 3-fold higher optical backscatter than the SPM of background water.

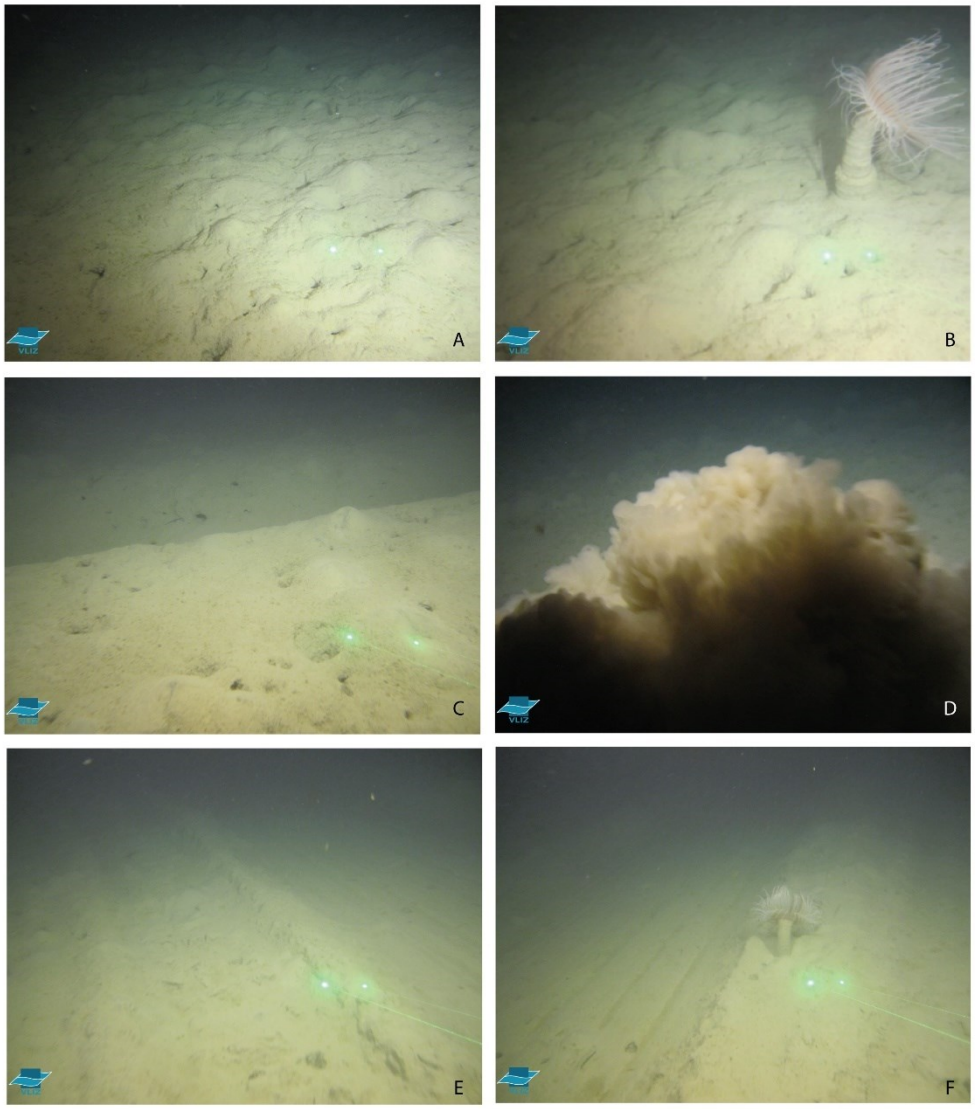

Figure 5.8: Seabed images taken by the ROV Zonnebloem of VLIZ. A) Undisturbed seabed; B) Undisturbed seabed with a sea anemone; C) Trawl door mark; D) Sediment plume produced by Apollo II; E) Imprint by Apollo II caterpillar track; F) Imprint by Apollo II collector. The green laser dots given for scale are 8 cm apart.

A quantitative relationship between acoustic backscatter recorded with the moored Nortek Aquadopp current profilers and SPM mass concentration was established indirectly, using SPM mass concentration inferred from JFE Advantech OBS recordings collected simultaneously within the same depth interval as where the acoustic backscatter was collected (Fig. 5.9). For suspensions with uniform particle composition and size distribution, the relationship between

recorded echo level and SPM mass concentration should conform to a logarithmic function of the form:

$$Echo\ level\ [dB] \propto log_{10}(SPM) \qquad \text{(Eq. 5.4)}$$

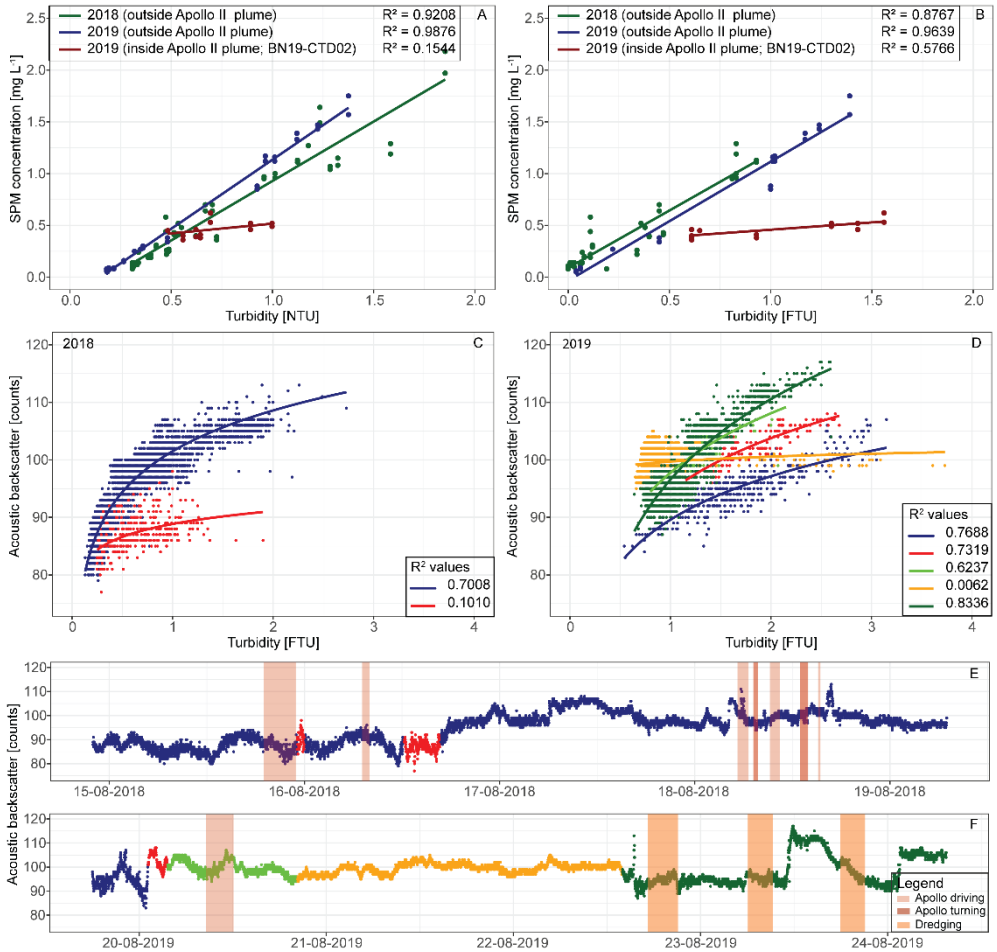

Figure 5.9: Relationship between SPM mass concentration, optical backscatter and acoustic backscatter. A and B) SPM mass concentration measured by filtration of Niskin water samples vs. turbidity measured simultaneously with WetLabs (OBS) (A) and JFE Advantech (B). Green and blue data points represent background samples collected from outside the plume. Red data points represent samples collected from the Apollo II plume (BN19-CTD02). C and D) Acoustic backscatter recorded with Nortek Aquadopp at 3 mab vs. turbidity measured simultaneously with JFE Advantech OBS at 3 mab in, respectively, BN18-M1 (C) and mooring BN19-M1 (D). The different colours represent particle population with different optical-acoustic characteristics, occurring at different time intervals in 2018 and 2019, as respectively shown in E and F. The shaded bars in E and F represent the times Apollo II was driving or turning (red), and when the dredging took place (orange).

However, in the SPM and acoustic backscatter data collected in 2018 and 2019, a broad scatter is observed which cannot be described by a single logarithmic relation as in Eq. 5.4. Rather, in 2018 two main clusters of data can be distinguished, and five clusters in 2019, each conforming to a logarithmic relationship of the general form given in Eq. 5.4 but with different constants (Fig. 5.9). The data clusters, representing SPM with different optical and acoustic backscatter characteristics (Fig. 5.9C and D), correspond to different time intervals in the recorded data (Fig. 5.9E and F). In 2018 (Fig. 5.9B), the majority of the data belong to one cluster characterised by a relatively high acoustic backscatter response. A much smaller part of the data belongs to the second cluster, characterised by relatively low acoustic backscatter response. This second cluster represents two short time intervals (Fig. 5.9E), the first late on August 15th when *Apollo II* landed on the seabed and drove to the start position for a drive-by along the mooring array, the second in the course of August 16th when *Apollo II* performed the actual drive-by which was, however, aborted before completing it. A second, successful, drive-by on 18 August 2018, and the drive-by performed in 2019, do not seem to be reflected in a distinct data cluster (Fig. 5.9C and D). The cluster with lowest acoustic backscatter in the 2019 data (blue cluster; Fig. 5.9D) cannot be linked to *Apollo II* activity (Fig. 5.9F) and must be considered as part of the background variability.

5.4.5. Plume characteristics near the mining vehicle

SPM mass concentrations measured directly at the rear of the *Apollo II* with a JFE Advantech OBS attached to the diffuser, went up to 100 mg L^{-1} when the vehicle was driving with the hydraulic nodule collector switched on (Fig. 5.10A). Tow-yo-ing the CTD while following the *Apollo II* mining vehicle at about 100 m distance, gave insight in SPM mass concentration and maximum height of the created sediment plume in its initial phase (Fig. 5.10B, C and D). The turbidity sensor mounted within the CTD frame, which during this cast, illustrated in Fig. 5.10, only approached the seabed to 4 mab (Fig. 5.10B), did not show any increase in SPM mass concentration above the natural background SPM mass concentration of about 0.75 mg L^{-1}. However, the turbidity sensor suspended 3 m below the CTD frame, which approached the seabed to about 1 mab, recorded enhanced SPM mass concentration near the bottom (Fig. 5.10C, D). While the *Apollo II* was driving with its hydraulic nodule collector switched off, a sediment plume was generated only by interaction of the caterpillar tracks with the seabed

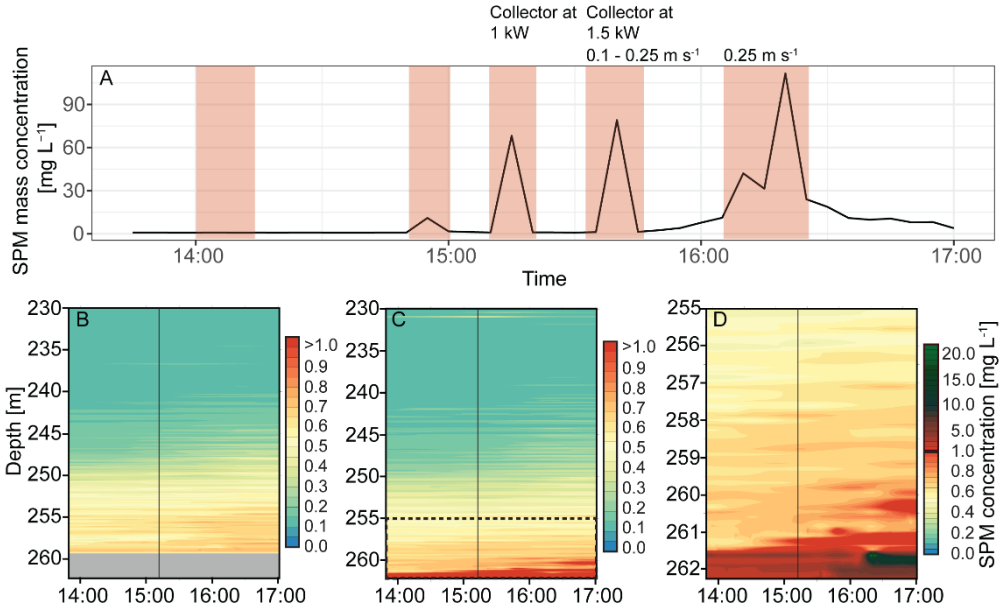

Figure 5.10: Time series of SPM mass concentration recorded in the wake of Apollo II while the vehicle was driving over the seabed on 12 August 2018. A) SPM mass concentration recorded by a JFE OBS mounted at the rear of Apollo II. Shaded areas mark intervals when Apollo II was driving over the seabed, stepwise increasing forward speed, and power of the hydraulic collector pump. B-D) SPM mass concentration recorded by JFE OBSs mounted on the CTD, operated in tow-yo mode while the ship was following Apollo II. Vertical black line marks the time when the hydraulic collector of Apollo II was switched on. B) was recorded by the JFE OBS mounted at the base of the CTD-frame which was lowered until 4 mab, thereby remaining just above the plume. C) was recorded by the OBS suspended 3 m below the CTD-frame, which reached until 1 mab and thereby dipped into the plume. D) same as C), showing the lowest 8 m to the seabed.

and by water displacement and turbulence around the vehicle. The SPM mass concentration within the plume, measured at about 100 m behind the vehicle, was generally around 5 mg L^{-1}. With the hydraulic collector switched on, the additional discharge of sediment-laden seawater through the mining vehicle's diffuser resulted in a marked increase in SPM mass concentration within the plume to around 20 mg L^{-1}. The relatively low height of the plume in its initial phase was visually confirmed by diving ROV *Zonnebloem* into and out of the plume while following *Apollo II* (Fig. 5.8D).

Tow-yo-ing the CTD through the *Apollo II* sediment plume with the LISST-200X in situ particle size analyser mounted within the lower part of the frame gave insight into the contrasting particle size distributions of the *Apollo II* plume (enhanced beam attenuation) compared to background turbidity levels, especially in BN18-CTD19 (Fig. 5.7A and Fig. S5.4A and B). Especially in BN18-CTD19, this is well illustrated, with particle size distributions in the *Apollo II*

plume dominated by very small particles with a broad and flat mode centred around 25 µm, comparable to the fine particle size mode observed in the surface sediment. In the background water, there was a dominance of larger particles with a pronounced mode centred around 250 µm, similar to what was seen in the LISST records of 2019.

5.4.6. Plume dispersion

During the 2018 field test, *Apollo II* made an unsuccessful first attempt to drive along the mooring array on August 16th, but on August 18th, two complete lines of 1000 m at approximately 100 and 150 m distance from the single-line mooring array, and a third incomplete line at 250 m distance (Fig. 5.1; Fig. S5.2) were driven. Unfortunately, due to issues with the pump of the hydraulic collector, only the plume generated by the propulsion of the vehicle was recorded by the moored sensors. Furthermore, due to a malfunctioning compass, navigation of the vehicle was done based on USBL-tracked position, which resulted in a path that was far from straight. What makes interpretation of the recorded plume data even more challenging is the variable bottom current direction. While *Apollo II* was driving its first line at 100 m from the moorings, the current was directed towards the SW, carrying the plume towards the mooring array (Fig. 5.11). However, while the vehicle was making the turn to start driving the second line at 150 m from the moorings, the current had changed direction to NW and N, carrying the plume parallel to or even away from the mooring array. In the following hours the current changed further to NE and then to SE, and it was only after *Apollo II* had come to a halt in the middle of the third line at 250 m from the moorings that the current turned again to SW and carried the plume towards the moorings. The succession of events is readily recognised in the time series of SPM mass concentration recorded by the OBSs at 1 and 3 mab (Fig. 5.11B). The plume produced in the first line showed in the OBS at 1 mab as a sharp increase in SPM mass concentration from about 1.5 to over 6 mg L^{-1}. Only a very weak trace of the plume was recorded by the OBS at 3 mab, confirming what was observed in the CTD tow-yo casts that the plume in its initial phase hardly extended higher than 2 mab. The plume produced in the third line was recorded with some delay in time by the OBS at 1 mab, with a distinct rise in SPM mass concentration from about 1.5 to almost 4 mg L^{-1}. This time, the plume was also clearly recorded by the OBS at 3 mab.

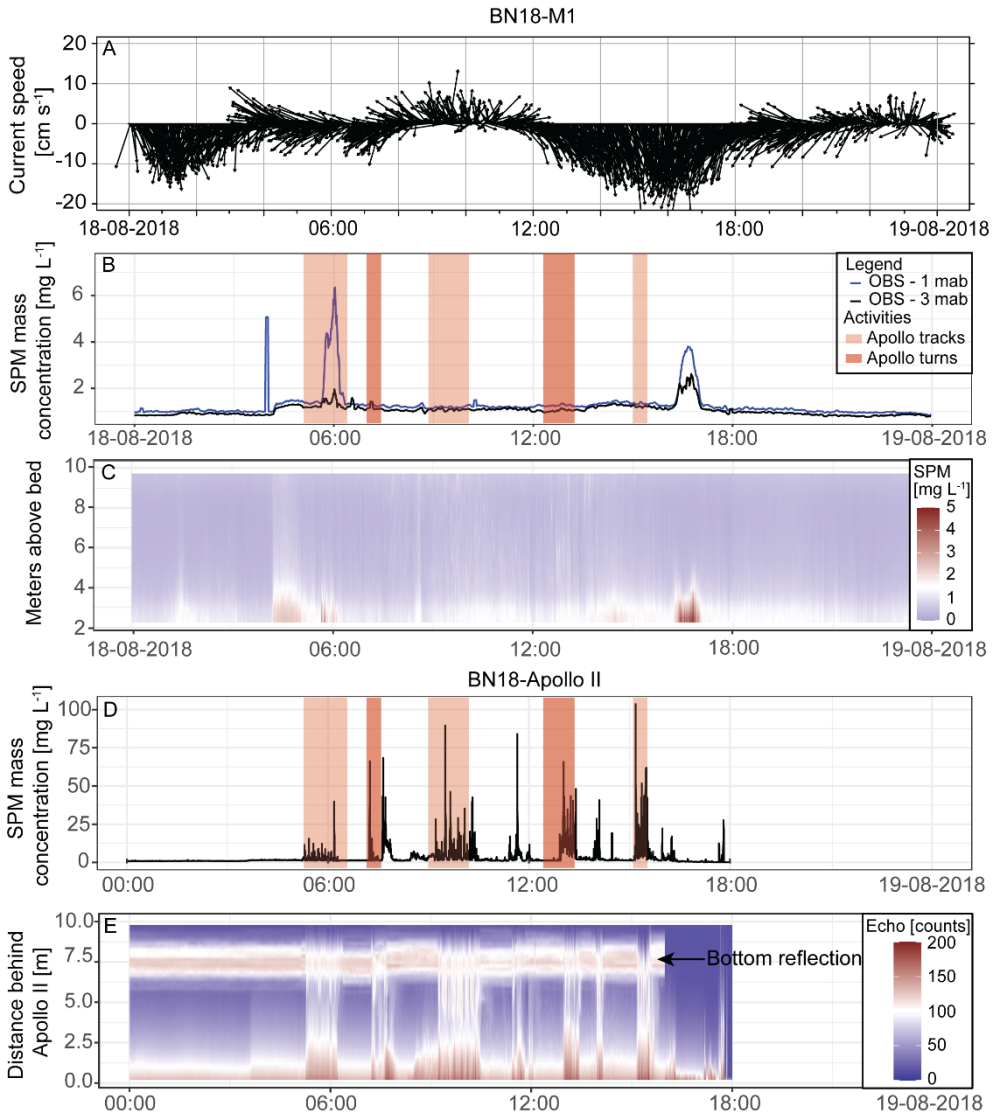

Figure 5.11: SPM mass concentration and current speed and direction recorded during the Apollo II drive-by experiment on 18 August 2018. A) Near-bottom current speed and direction recorded at 2 mab by the 2 MHz Nortek Aquadopp on mooring BN18-M1. B) SPM mass concentration recorded by the JFE OBSs at 1 mab (dark blue) and 3 mab (black) on mooring BN18-M1. Shaded areas mark intervals when Apollo II was driving over the seabed. C) Vertical profile of SPM mass concentration as converted from recorded by the JFE OBS mounted at the rear of Apollo II. E) Profile of acoustic backscatter (raw counts) recorded by the Nortek Aquadopp profiler mounted facing backwards at the rear of Apollo II. The strong reflection at 7.5 m distance is produced by impingement of the acoustic beam with the seabed. The abrupt end of the bottom reflection at 15:33 indicated that the vehicle tilted sideways at that point. Details of experimental configuration are provided in Fig. S5.2.

During the 2019 field test, on August 20th, the *Apollo II* drove one line of 1000 m at 50 m distance from the mooring array (Fig. 5.1; Fig. S5.2) with the hydraulic nodule collector switched on. With the compass working properly, the driven path was impeccably straight this time. Unfortunately, technical issues forced the vehicle to a full stop shortly after starting the second track line at 60 m distance. Considering the current velocity data recorded by the moored current profilers, the timing for driving the first line was not well chosen. When *Apollo II* started driving the first line at 08:01 UTC, the near-bed current was directed NE, carrying the plume away from the mooring array (Fig. 5.12 BN19-M3). Only after 11:00 UTC the current turned to SW, now carrying the plume towards the moorings. In the front line of the mooring array, 50 m away from the path of *Apollo II* (moorings BN19-M1 to BN19-M4), the sediment plume was mainly recorded by sensors at 1 mab, with SPM mass concentrations going up to 5 mg L^{-1}. Approximately one hour later the plume arrived at BN19-M5, 200 m away from the path of *Apollo II*. Here, the SPM mass concentration was higher when compared to the moorings BN19-M1 to BN19-M4, going up to 6 mg L^{-1} at 1 mab and 3 mg L^{-1} at 3 mab. Another 45 min later the plume was also recorded at BN19-M6, 350 m away from the path of *Apollo II* with SPM mass concentrations of 3.5 mg L^{-1} and 2.5 mg L^{-1} at 1 and 3 mab, respectively. The two moorings equipped with sediment traps, sampled settling particles during the *Apollo II* drive-by on the 20th of August. The recorded mass fluxes varied between 200 and 800 mg m^{-2} h^{-1} (Fig. S5.5). Highest mass fluxes were recorded between 11:45-12:45 UTC and 12:00-13:00 UTC at BN19-M4 and BN19-M5, respectively. While the maximum flux at BN19-M5 coincided with the time the plume passed by, the maximum at BN19-M4 occurred only after the plume had passed.

After technical issues had stopped further testing of *Apollo II* in 2019, a plume was generated on 22 and 23 August by means of a steel beam with trailing lengths of chain, which was towed repeatedly over the seabed parallel to the mooring array, at distances of 50 to 180 m. However, even when the current was carrying the plume directly towards the moorings, maximum recorded SPM mass concentrations did not exceed 2.5 mg L^{-1}, apart from some short-lived increases in SPM mass concentration on 22 August 2019, which were hard to distinguish against the variable background SPM mass concentration (Fig. 5.6).

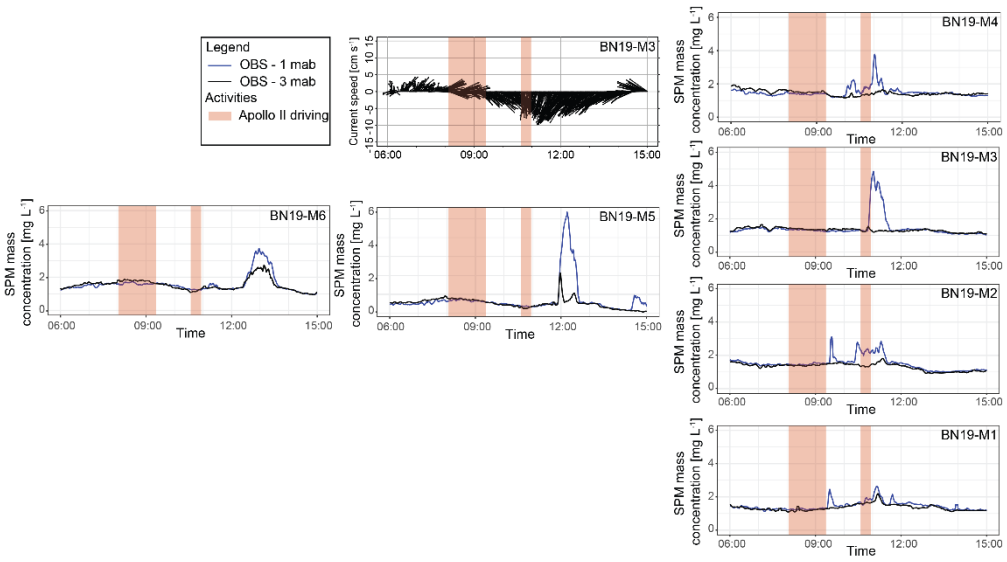

Figure 5.12: SPM mass concentration and current speed and direction recorded with JFE OBS and Nortek Aquadopp on moorings BN19-M1 to M6 during the Apollo II drive-by experiment on 20 August 2019. SPM mass concentration at 1 mab and at 3 mab is indicated with blue and black lines, respectively. Shaded areas mark intervals when Apollo II was driving over the seabed. Details of the experimental configuration are provided in Fig. S5.2.

5.5. Discussion

Environmental management of deep-sea mining activities requires monitoring designs and strategies that are capable of reliably assessing the impact of ongoing mining operations relative to a pre-mining baseline (Jones et al., 2020). In addition, sediment plumes may cause delayed changes to the system, resulting in disturbances far beyond the mining site, in otherwise pristine and undisturbed deep-sea regions (Gardner et al., 2018; Jones et al., 2020). Environmental monitoring of sediment plumes should thus address both physical drivers (currents and their variability) as well as plume response (horizontal and vertical propagation and settling) at different spatial and temporal scales. In this study, we presented different experimental approaches for monitoring sediment plumes which we tried out during two deep-sea mining field tests in the Alboran Sea (western Mediterranean). The adopted designs consisted of both moving, vessel-based, operations (S-ADCP, CTD, ROV, crawler-mounted sensors), and sampling with a static sensor array for measurements of water column and near-bottom currents, sediment characteristics and plume evolution and propagation. Based on our experiences as summarised in the previous section, we will discuss the merits and shortcomings of these designs.

5.5.1. Environmental setting of the field test

Prior to the field tests of the *Apollo II* scaled mining vehicle in 2018 and 2019, various components of the propulsion system and the hydraulic collector had already been tested extensively in a lab environment, submerged in a test tank filled with fresh water and on a substrate composed of fine sand or a mixture of sand and clay (Lucieer et al., 2017). With water and sediment characteristics very different from those encountered in prospected mining sites in the deep sea, the lab results have little value for predicting environmental effects arising when the mining equipment is used in a deep-sea setting. In addition, the test tank offered very limited space for experimenting with a realistic plume monitoring setup. The test area in Málaga Bight, despite of its relatively shallow water depth, offered all the space needed, and a seabed and water column that for a number of relevant aspects provided a good approximation of a deep-sea mining setting.

The weakly sloping seabed covered with soft, muddy sediment provided a good analogy for the abyssal seabed for which the mining is designed. Absence of nodules was the most important 'shortcoming' of the Málaga Bight seabed from a testing perspective, but lab tests of the hydraulic collector had already yielded very satisfying results. For assessment of the sediment plume stirred up by the vehicle, it was more important that the sediment of the Málaga Bight seabed was predominantly composed of clay and silt, which are also the dominant fractions in surface sediment in polymetallic nodule fields of the Pacific Ocean (e.g. BGR Bundanstalt für Geowissenschaften und Rohstoffe, 2018).

The prevalence of fine-grained sediment in the test area, atypical for a relatively shallow near-coast environment, reflects the overall weak bottom current regime in the Málaga Bight. The sluggish current regime in turn is the result of the absence of strong tides in the Mediterranean Basin and the relative shelter in the bight provided by mountainous headlands protruding from the coast. Weak near-bed currents, with magnitude mostly below 10 cm s^{-1} and of a variable direction, in combination with a weak density stratification, provide a good analogy for the hydrodynamic regime found in the abyssal ocean.

The variable tidal current, however, posed a considerable challenge with regards to timing of our drive-by experiments. With improper timing, the plume generated by the test vehicle

would drift away from our moored sensors, and in the best case was recorded only hours later when the current had turned to a more favourable direction. In the time span between generation and detection of the plume, a considerable part of the suspended sediment must have settled out and have been diluted by mixing with ambient non-plume water, as reflected by the relatively low SPM mass concentrations recorded by the moored sensors. Therefore, we used our S-ADCP data, available in real time and processed and analysed on a daily basis, to find the optimal time window for conducting our drive-by experiment. Post-hoc comparison with current data recorded by our moored current profilers revealed that changes in current direction at 3 m above the seabed typically lagged 1–2 h behind (Fig. 5.5D, E) those observed at 25 m and higher above the seabed by the S-ADCP. This can be attributed to the phase shift of the baroclinic tidal current indicating strong vertical shear as a result of Ekman veering in the bottom boundary layer (Perlin et al., 2007). As a result, we started the drive-bys while the currents were still directed away from the moorings, so that we failed to record the plume while it was freshly produced. This initial mismatch in timing would have been compensated if the following lines had been successful, and the current would have carried the plume straight towards the moorings. The challenges posed by variable currents are similarly present in a deep-sea setting, as found in small-scale plume experiments conducted in the abyssal Pacific (DISCOL Experimental Area, Baeye et al., 2022; CCZ, Haalboom et al., 2022; Purkiani et al., 2021). In a future monitoring scenario, it would be advantageous to have near-bottom current data from the mining site in real time, to feed into an operational plume dispersion model.

An aspect in which the bottom water of Málaga Bight was markedly different from that of the typical abyssal ocean setting was in its high and highly variable background SPM mass concentration. Recorded intervals of increased background SPM mass concentration, as shown in Fig. 5.6A and C, did not seem to correlate with periods of increased current speed, precluding sediment resuspension by bottom currents as their cause. A correlation was not found either with the diel migration of pelagic fauna to deep water during daytime, or with ship-based sampling activities that might have stirred up sediment from the seabed. The most likely explanation for the variable turbidity seems to be nearby trawling activity. Whilst fishing vessels operating in the area kept a minimum distance of 1 nautical mile to RV *Sarmiento de Gamboa* and the moorings, the plumes produced by trawling may well have drifted towards

our moorings in a few hours' time. Interference by bottom trawling or other human activity is not an issue in the polymetallic nodule fields in the abyssal Pacific Ocean, where background SPM mass concentration is typically on the order of 0.01 mg L^{-1} (Lal, 1977; Haalboom et al., 2022). Despite indications that bottom currents in this area are periodically enhanced under influence of mesoscale eddies passing by in the surface ocean layer (Aleynik et al., 2017), there are no records yet that these lead to substantial sediment resuspension. Different from Málaga Bight, where the more distal plume produced by *Apollo II* could not be distinguished from background turbidity, any resuspension of sediment in the deep sea will be readily detected and will be traceable to considerable distance away from the source.

5.5.2. Operational settings of mining machinery

The trials with *Apollo II* involved testing of different functions of the vehicle in the field, including driving performance at different speeds, and performance of the hydraulic collector at different settings (i.e. pump rate of the collector pump and stand-off distance of the collector relative to the seabed). Whilst the technical validation was overall successful, the environmental testing was flawed by a lack of replication due to both technical issues and the inherent variability of the environment. Due to the failing compass, driving straight lines at constant speed turned out problematic in 2018, and due to the untimely failure of the hydraulic collector pump only the plume produced by the motion of the vehicle could be observed. In 2019 the hydraulic collector pump worked properly, but there was no good control of the standoff distance of the collector to the seabed. As a result, the collector merely grazed the sediment surface. Our data may thus give a more positive impression of the resulting environmental pressures than when the mining vehicle would have operated with the hydraulic collector on full power and driving at its desired speed. For any future monitoring of deep-sea mining, it seems important that basic operational parameters such as underwater position, driving speed, and collector performance will be continuously logged. In addition, it would also be desirable that plume emission from the diffuser and the plume produced by the propulsion of the vehicle are measured directly, as a source term for operational modelling of plume dispersion, but also to allow a standardised evaluation of the environmental performance of mining gear (Weaver et al., 2022). Our measurement of suspended sediment concentration at the exit of the diffuser, even when not conclusive as the sensors were not located directly in the diffuser flow, showed the feasibility of this approach.

5.5.3. Setup of the plume monitoring array

Our plume monitoring setup, with sensors mounted on the mining vehicle and moored on the seabed at set distances from the source, proved effective to record the progressive spreading of the plume under influence of currents and turbulent mixing, as well as the decrease in SPM mass concentration within the plume resulting from dilution with ambient water and settling out of sediment particles. Even with the variable background SPM mass concentrations, the passage of the plume at different sensor locations within a radius of a few hundred metres from the source was noted by a distinct increase in SPM mass concentration. The recorded data on current velocity and SPM mass concentration would in principle be good for validation and calibration of a numerical model describing the overall dispersion and redeposition of sediment resuspended by the mining vehicle, including in places where no sensor data are available.

Placement of sensors close to the source would be desirable to better constrain the initial concentration and dispersion of the sediment plume. In our experimental setup with moorings, where anchor positions were accurately determined and top floats were clearly visible at the sea surface, 50 m was deemed the absolute minimum for safely driving by with *Apollo II* tethered to the ship. The need for caution was demonstrated by the failed first drive-by on 16 August 2018, when the umbilical of *Apollo II* accidentally crossed one of the mooring lines. The problems involved in the use of mooring lines could be overcome by positioning sensors directly on the seabed by means of an ROV. This approach proved successful in a dredge plume experiment carried out in 2019 in the CCZ (Purkiani et al., 2021; Haalboom et al., 2022), but here a working class deep-sea ROV with extended capacity for handling equipment was available. The small ROV *Zonnebloem* which we used in our experiment in Málaga Bight was more limited in that respect, while finding back equipment might also have been problematic with the sometimes poor visibility near the bottom. The safest option for nearfield plume monitoring after all seems to be to mount acoustic profilers directly on the mining vehicle, with beams directed both backwards and sideways. Results from using one of the 2 MHz Aquadopp profilers for that purpose seem promising (Fig. 5.11C), but a proper calibration of the acoustic backscatter signal received over the full distance range of >10 m would be essential for conversion of the acoustic signal to SPM mass concentration. At high

suspended sediment concentration near the source, sound absorption by suspended sediment may prove to be a factor that needs to be accounted for (Lohrmann, 2001).

For monitoring the more distal plume, our moored sensor layout proved effective. Especially by the combination of acoustic devices, recording vertical profiles of acoustic backscatter extending to >10 m above the seabed, and optical backscatter sensors, which are relatively straightforward to calibrate, and which allow cross-calibration of the acoustic backscatter signal. Both the optical and acoustic devices confirmed what was also observed with the CTD and ROV, that the plume initially stayed very close to the seabed (Fig. 5.10C and D), and only with progress of time and distance from the source extended higher above the seabed, while at the same time developing a clear vertical gradient in concentration (Fig. 5.12). Although sensors could have been placed even closer to the seabed, attached directly to the mooring weights, we chose not to do so to avoid damage to the sensors. We might also have reduced the blind spot in acoustic profiles in the lower 2 mab, resulting from the minimum height of the sensor head at 1.5 mab plus the 0.5 m blanking interval above the sensor head, by mounting the Aquadopp profilers at 10 mab facing downwards. However, in that configuration the most important lower part of the profile close to the seabed would be covered by the more distant depth bins of the profiler, where data may be less reliable and could be influenced by backscatter from the seabed.

The choice to have moorings only on one side of the path driven by *Apollo II* was mainly motivated by the available amount of sensors and mooring equipment. Safe navigation of the ship with tethered *Apollo II* was an additional argument for not placing moorings on both sides of the path. With the good underwater navigation, as achieved in 2019, a drive-through approach might have been an option though, which would have provided good data at times that the current carried the plume away from the main line of moorings. Compared to our single line mooring setup of 2018, our setup of 2019 was significantly improved by the addition of two moorings behind and perpendicular to the first line of moorings, as these additional moorings provided synoptic recordings of the evolution of the plume as it dispersed away from the source. In 2018, insight in the spatial evolution of plume was obtained by driving the vehicle at different distances upstream from the mooring array. In practice, however, the changing tidal currents complicated the comparison of recorded data from consecutive lines.

In view of the rapid decrease in SPM mass concentration in the plume with time and distance to the source, until the point that the plume could no longer be distinguished from the variable background, it seems that a further expansion of the sensor array over distances greater than a few hundred metres from the source would not have had added value. In a deep-sea setting, where bottom waters have a two orders of magnitude lower background SPM mass concentration (e.g. Lal, 1977), a monitoring array may be spread out over longer distances and still be able to detect the plume. This may even be required in an operational scenario where sensors must be placed at sufficient distance from the mining vehicle without the risk of being overrun.

5.5.4. Mobile sensors platforms

Compared to the moored sensors, from which the recorded data could be accessed only after recovery, the standard ship-based CTD-Rosette system offered the advantage that vertical profiles of turbidity and other water column characteristics could be investigated in real-time, and that water samples could be collected at any desired moment by firing Niskin bottles. The CTD frame also offered space for mounting additional sensors such as the LISST for in situ particle sizing. An obvious limitation of operating the CTD-Rosette system from the same ship also used as platform for operating the mining machine was that the plume could only be accessed when currents and navigation of ship and mining machine brought the plume directly below the ship. In practice, with the ship following behind the mining vehicle and at a speed usually higher than the speed of near-bottom currents, it was actually not uncommon that the plume was in reach of the CTD. A more important limitation which we noted was that the CTD could often not be lowered sufficiently close to the seabed to properly sample the low-lying plume. In 300 m water depth, under optimal sea-state conditions, and with a very smooth and gently sloping seabed and reliable altimeter on the CTD, we could confidently approach the seafloor to as low as 2 mab. However, even under such ideal conditions, the sensors mounted within the CTD frame and the vertically mounted Niskin bottles would often only graze the very top of the plume. With sensors suspended below the CTD frame, we could reach deeper into the plume, but at the risk of damage to the sensors and erroneous readings in case the sensors would accidentally hit the seabed. In deep-sea settings the minimum distance of safe approach to the seabed is usually held at 5 m, depending on sea-state, obviously too far to sample a low-lying plume with sensors and Niskin bottles. A ROV, as shown in our field tests,

offers a greater flexibility than a ship-operating CTD-Rosette system in exploring sediment plumes in the vertical and horizontal dimension. With ROV video cameras, the plume can be observed in real-time, and within certain limits of weight and size additional sensors can be added to its payload. Care should be taken, however, that the ROV is not stirring up its own sediment plume. An example of a plume produced by the ROV may be seen in Fig. 5.6C on the 22nd of August, where we observed an increase in the turbidity at 1 mab shortly after the deployment of the ROV. Tether length and risk of entanglement with the mining vehicle's umbilical and riser system remain limitations for use of a ROV in an operational setting. In that respect, autonomous underwater vehicles (AUV) might seem the most promising technology for operational plume monitoring purposes, as they autonomously can cover relatively large distances on the order of tens of kilometres, and therefore can follow plumes from near field to far field. The required minimum safe flying height above seabed may pose limitations to detection of low-lying plumes with optical backscatter sensors, but this limitation may be overcome by use of downward-looking acoustic profiling devices with appropriate frequency to detect fine-grained suspended sediment.

5.5.5. Sediment deposition from the plume

Whereas assessment of blanketing of the seabed by sediment deposition from the plume should be an integral part in monitoring of deep-sea mining impact, our experiment was not successful in this respect. The sediment traps in the mooring array appeared not very effective in sampling sediment deposition from the plume, as their opening at 2.5 mab, the lowest we could possibly mount them, was still too high above the seabed to sample the low-lying plume. The observed variation in settling particle flux in the traps could not be unambiguously correlated with the passage of the sediment plume. If placed at a greater distance from the source, where the plume might rise higher, the traps would still only catch deposition from the upper, most dilute, part of the plume. In plume dispersion experiments in the deep Pacific Ocean (Thiel, 2001; Peukert et al., 2018; Haalboom et al., 2022), the areal distribution and thickness of redeposited sediment was assessed from seabed imagery. However, in these experiments, the dark-coloured polymetallic nodules provided a suitably contrasting background against which resettled plume sediment could be readily distinguished. Such optical contrast was not present in our study area, and besides that, it would have been

impossible to distinguish sediment settled out from the *Apollo II* plume from sediment settled out from plumes produced by nearby trawling.

5.5.6. Conversion of optical backscatter to SPM mass concentration

As demonstrated by our field tests, suspended sediment plumes in deep waters can be reliably detected with both optical and acoustic sensors that record the presence of particles by variation in transmitted, diffracted, or backscattered light or sound. For a quantitative assessment of the mass of sediment dispersed through sediment plumes, optical and acoustic sensor data must be converted to a common unit of dry weight of solids per volume of water. Since the amount of transmission, refraction or backscatter of light or sound depends not only on the concentration of particles in suspension but also on physical characteristics of the particles such as their size distribution, relative density and reflectively (e.g. Baker and Lavelle, 1984; Hatcher et al., 2001; Downing, 2006), there is not a single universally applicable function to do the conversion. The conversion should be made on a case-by-case basis through a function appropriate for the specific suspension under investigation. This was clearly illustrated by CTD02 of 2019, the only CTD cast in which we managed to collect water samples from the plume of *Apollo II*. In this cast we found a relationship between optical backscatter and SPM mass concentration notably different from that found in other CTD casts which only sampled background water (Fig. 5.9). Data obtained with the LISST-200X particle sizer mounted on the CTD demonstrated that dominant particle size within the plume at short range from *Apollo II* was substantially smaller than in the background water outside the plume (Fig. 5.7A). In the freshly mobilised plume, the size distribution of suspended particles appeared to correspond closely with that of the fine fraction of the surface sediment. The much larger particles that dominated in the background water were likely aggregates composed of aggregated fine-grained mineral and organic matter. The difference in dominant particles sizes in plume and background waters may well explain the different relationship between optical backscatter and SPM mass concentration which we observed for fresh plume and background water. As demonstrated by lab experiments and field observations, fine-grained particles have a larger backscattering surface per unit mass than coarser-grained particles, and hence also produce a higher backscatter response than coarser particles (e.g. Downing, 2006). After the initial mobilisation and dispersion of the fine-grained surface sediment by the action of the mining vehicle, the fine-fraction primary particles are likely to

aggregate rapidly into larger particles, by electrostatic attraction of clay particles and probably also favoured by organic material relatively abundant in the near-coast environment. Both field observations in man-made sediment plumes (Durrieu de Madron et al., 2005) and lab experiments (Gillard et al., 2019) demonstrated that aggregation of primary particles of a few µm to tens of µm into larger aggregates of hundreds of µm may occur in a matter of hours.

In this study we have used the regression lines of the majority of samples taken outside the plume to convert all OBS turbidity readings from both the 2018 and the 2019 cruises to SPM mass concentration. We consider the number of samples from within the generated *Apollo II* plume insufficient to establish a reliable conversion specifically for the plume. As a consequence, the SPM mass concentrations reported in this study for the *Apollo II* plume may well be overestimated. As an alternative to our approach of in situ sensor calibration, sensors could be calibrated on-board or in the lab with suspensions produced with local surface sediment and bottom water, as described by e.g. Guillén et al. (2000). This seems a valid approach for dredging and deep-sea mining sediment plumes formed by resuspension of surface sediment, but only if the composition of the material in the plume corresponds with that of the surface sediment. In our case in Málaga Bight the seabed contained a substantial fraction of sandy material, which in a field setting will settle out in a matter of minutes after being brought in suspension according to Stokes' Law, but in a lab calibration setting with continuous stirring will be kept in suspension and thus add to the SPM mass concentration. In this case, using a lab-based conversion function for calculating SPM mass concentration from optical backscatter measured in the field will lead to overestimation of the SPM mass concentration. In the typical polymetallic nodule setting where the sediment is predominantly fine-grained and sand represents only a very minor fraction, lab-based sensor calibration may be a good practice. Especially since in situ calibration of sensors in deep water may be even more difficult than what we experienced in Málaga Bight. However, using a lab-based conversion function for assessing SPM mass concentration in sediment plumes does not account for the effect that particle aggregation may have on optical backscatter. For a monitoring set-up it would therefore be recommended to record not only turbidity but also the particle size at different distances away from the disturbance site.

5.5.7. Conversion of acoustic backscatter to SPM mass concentration

Conversion of the acoustic backscatter signal from acoustic profilers to SPM mass concentration, on the basis of the logarithmic relationship found between echo level and SPM mass concentration derived from simultaneously recorded optical backscatter data, has been previously employed in field studies (e.g. Durrieu de Madron et al., 2005; Tessier et al., 2008; Mengual et al., 2016). As explained in Haalboom et al. (2021), the acoustic backscatter signal, much like what is described above for the optical backscatter, is not only determined by particle concentration but also by the size of the suspended particles. Following hydroacoustic theory as presented in Haalboom et al. (2021), the Nortek Aquadopp 2 MHz profilers which we used in our plume monitoring experiment have a lower detection limit for particles of 12 µm diameter, and maximum sensitivity for particles of 242 µm diameter. These particle sizes are close to what we found, respectively, as fine-grained mode in surface sediment, and as coarse-grained mode of suspended particles in background water as recorded by the LISST-200X. It may thus be expected that different states of particle aggregation occurring in the *Apollo II* sediment plume and in background water would be reflected by different intensities of acoustic backscatter. Sediment freshly mobilised and dispersed by *Apollo II*, forming an unaggregated suspension, would produce a lower acoustic backscatter than the suspension in a more advanced state where the primary sediment particles would have aggregated into larger-sized particles. This would explain the occurrence of the two data clusters observed in the plot of echo level vs. SPM mass concentration for mooring BN18-M1 (Fig. 5.9). It appears puzzling, however, that similar data clusters with low acoustic backscatter were not found associated with other time intervals when *Apollo II* was active near the moorings. Possibly the higher and variable background SPM mass concentration at those times masked the signature of the fresh *Apollo II* plume, or the *Apollo II* plume might itself already have evolved to a more aggregated state. Also, the suspended particles present in trawling plumes advected from adjacent areas, here considered as background to the *Apollo II* plume signal, may also have been in variable states of aggregation. The LISST-200X data recorded in 2019, showing considerable variability in particle size distribution in the background water (Fig. 5.7A and Fig. S5.4), seem to confirm this. In view of the variable relationship between acoustic backscatter and SPM mass concentration, illustrated by the different data clusters in Fig. 5.9, caution seems to be due when using acoustic backscatter for deriving SPM mass concentration. Even

so, this approach may give valuable insight in gradients of SPM mass concentration within mining plumes.

5.6. Concluding remarks – Application to deep-sea mining setting

Plume monitoring in a realistic industrial mining scenario is challenging, when considering the temporal (years to decades) and spatial (hundreds of kilometres) scales, over which measurements and maintenance of instruments may need to be realised. Recent studies have highlighted the importance of smaller-scale experiments for developing mining-related plume monitoring strategies at a time, where deep-sea mining at an industrial scale is waiting in the wings. Monitoring data obtained in the field are essential for validation and calibration of numerical models of plume dispersion. Conversely, numerical models help to better understand monitoring results, and help to identify data gaps. Our own experimental monitoring efforts, even though performed in a relatively shallow marine setting, confirm that robust monitoring can be achieved by combining standard commercial instrumentation on suitable stationary and moving platforms. Most of the monitoring methods presented in this study can be applied also in a deep-sea setting, although sometimes in an adapted form.

- A good control on the plume source, i.e., when and where sediment is being mobilised by the mining machine and the rate of sediment mobilisation and discharge, is important for interpretation of far field sensor recordings, and is essential for numerical modelling of plume dispersion.
- The initial SPM mass concentration of the plume discharged from the mining vehicle may be derived from operational data on navigation of the mining vehicle and erosion depth and pumping rate of the collector but should preferably also be measured directly by sensors mounted on the mining vehicle.
- To allow detection of the low-lying plume in its initial stage near the source, it is important that at least some sensors are placed very close to the seabed. High-frequency acoustic profilers moored close to the seabed in combination with calibrated OBSs are suitable for measuring vertical profiles of suspended sediment concentration above the seabed.
- Mobile sensor platforms like the standard CTD-Rosette system deployed from a ship are limited in the distance to which they can safely approach the seabed, and for that

reason are prone to miss the initial low-lying plume. The same limitation applies when AUVs are employed for plume monitoring. The lower metres of water column directly above the seabed could, however, be in range for a downward-looking high-frequency acoustic profiler.

- Current velocities close to the seabed measured with moored high-frequency current profilers differed substantially from velocities measured higher up in the water column with ship-ADCP and long-range moored ADCP. For predicting the initial dispersion of the sediment plume, near-bottom current velocity records should be used.
- Turbidity sensors used for plume monitoring need to be calibrated in situ by reference to simultaneously collected samples of SPM or in a lab setting using suspensions made from local surface sediment. However, particle aggregation occurring in the sediment plume may affect the optical and acoustic backscatter characteristics of the SPM, resulting in under- or overestimation of SPM mass concentration.
- Assessment of particle size distribution in sediment plumes may contribute to more reliable quantification of SPM mass concentration.

Data availability

CTD data, S-ADCP data, data collected by the turbidity sensors, LISST-200X, and ADCPs mounted on the CTD-frame, *Apollo II* and moorings, as well as filter weights for SPM sampling and data on particle size analysis of the surface sediments, collected during the cruises in 2018 and 2019 are available in the NIOZ database (https://dataverse.nioz.nl/dataverse/doi) under, respectively, DOI 10.25850/nioz/7b.b.vd and 10.25850/nioz/7b.b.wd.

Acknowledgements

We thank the captains and crew of RV *Sarmiento de Gamboa* for their essential assistance during the two field tests. Technical assistance onboard the ship was provided by Arturo Castellón and his team of the Marine Technology Unit of the Spanish Research Council UTM-CSIC. The ROV team of the Flanders Marine Institute (VLIZ) assisted in the field tests by seabed surveys and plume observations with ROV *Zonnebloem* and supporting underwater navigation with the GAPS system. The engineering team of IHC Mining, responsible for driving *Apollo II*,

played a key role in carrying out the field tests. We thank our colleagues from the NIOZ-EDS department for borrowing their LISST-200X and in particular Dr. Karline Soetaert for her assistance with the processing of the data. This research was funded by the Blue Nodules project (EC grant agreement no. 6887851). HdS, CM and LdJ acknowledge additional funding from the Blue Harvesting project (EIT RM grant no. 18138). We thank three anonymous reviewers for insightful comments and constructive criticism which improved the manuscript.

Supplementary material

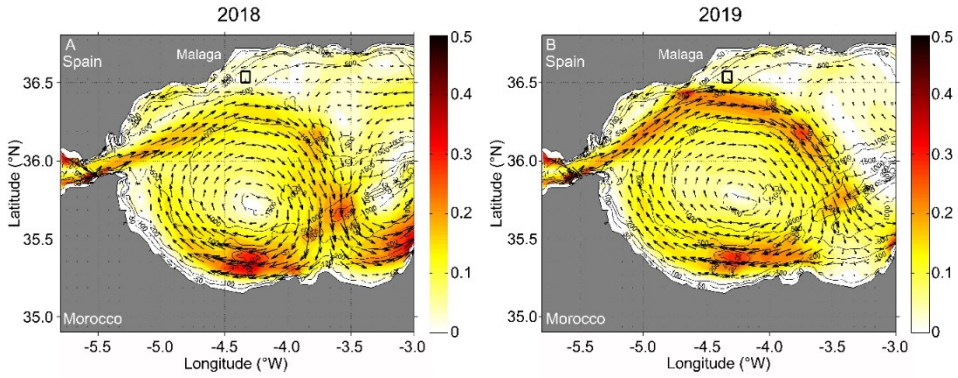

Figure S5.1: General circulation (depth-averaged) in the western Alboran Sea in August 2018 and 2019 from hindcasts of Med-Currents (Mediterranean Forecasting System). Colour contours represent current speed (m s^{-1}). The black rectangle indicates the location of the field test area. The physical component of the Mediterranean Forecasting System (Med-Currents) is a coupled hydrodynamic-wave model implemented over the whole Mediterranean Basin. The model horizontal grid resolution of 1/24' (approximately 4 km) and has 141 unevenly spaced vertical levels. The hydrodynamics are supplied by the Nucleus for European Modelling of the Ocean (NEMO v3.6), while the wave component is provided by Wave Watch-III (marine.copernicus.eu). The currents predicted by this model are used to describe the large-scale physical setting during the time of the local-scale observations in Málaga Bight presented in the main manuscript. The dynamics of the currents in the Málaga Bight test area are described exclusively on the basis of our own measurements.

Table S5.1: Specification of the CTD casts.

Year	Station	Start Longitude (°)	Start Latitude (°)	Sampling depths (m)	LISST	Type
2018	CTD01	-4.365292	36.501373	331, 220, 188, 100, 25	-	Calibration Single cast
2018	CTD02	-4.33394	36.550704	-	-	Tow-yo
2018	CTD03	-4.333866	36.5508	-	-	Tow-yo
2018	CTD04	-4.333962	36.550704	-	-	Tow-yo
2018	CTD05	-4.334208	36.550562	-	-	Tow-yo
2018	CTD06	-4.334222	36.550306	-	-	Tow-yo
2018	CTD07	-4.334139	36.550361	-	-	Tow-yo
2018	CTD08	-4.333726	36.550732	-	-	Tow-yo
2018	CTD09	-4.333709	36.550695	-	-	Tow-yo
2018	CTD10	-4.332514	36.551539	-	-	Tow-yo
2018	CTD11	-4.331919	36.551995	-	-	Tow-yo
2018	CTD12	-4.331924	36.551994	-	-	Tow-yo
2018	CTD14	-4.325014	36.557505	257, 257, 257, 255, 250, 240, 185, 99	-	
2018	CTD15	-4.33167	36.526806	307, 307, 278, 100	X	
2018	CTD16	-4.33042	36.531089	-	X	
2018	CTD17	-4.330255	36.528934	-	X	
2018	CTD18	-4.330208	36.529038	304, 304, 304, 306, 306, 225, 100	X	
2018	CTD19	-4.327554	36.529944	303, 295, 295, 295, 255, 215, 100	X	

Table S5.1 continued: Specification of the CTD casts.

Year	Station	Start Longitude (°)	Start Latitude (°)	Sampling depths (m)	LISST	Type
2019	CTD01	-4.3000823	36.5000077	396, 353, 324, 260, 201	-	Calibration Single cast
2019	CTD02	-4.3186195	36.5436527	288, 284, 283, 281, 277, 273, 273	-	Tow-yo
2019	CTD03	-4.3190368	36.5437562	289, 275, 209, 150	-	Calibration Single cast
2019	CTD04	-4.3360175	36.5244927	308, 305, 303, 302, 301, 299	-	Tow-yo
2019	CTD05	-4.339536	36.52671	-	-	Single cast
2019	CTD06	-4.339538	36.5267108	-	-	Single cast
2019	CTD07	-4.3395515	36.5267088	-	-	Single cast
2019	CTD08	-4.3395393	36.5267033	-	-	Single cast
2019	CTD09	-4.3395335	36.526714	-	-	Single cast
2019	CTD10	-4.339536	36.5266975	-	-	Single cast
2019	CTD11	-4.339539	36.5266933	-	-	Single cast
2019	CTD12	-4.339524	36.5267112	-	-	Single cast
2019	CTD13	-4.3395435	36.5267077	-	-	Single cast
2019	CTD14	-4.3395333	36.5267152	-	-	Single cast
2019	CTD15	-4.3395255	36.526726	-	-	Single cast

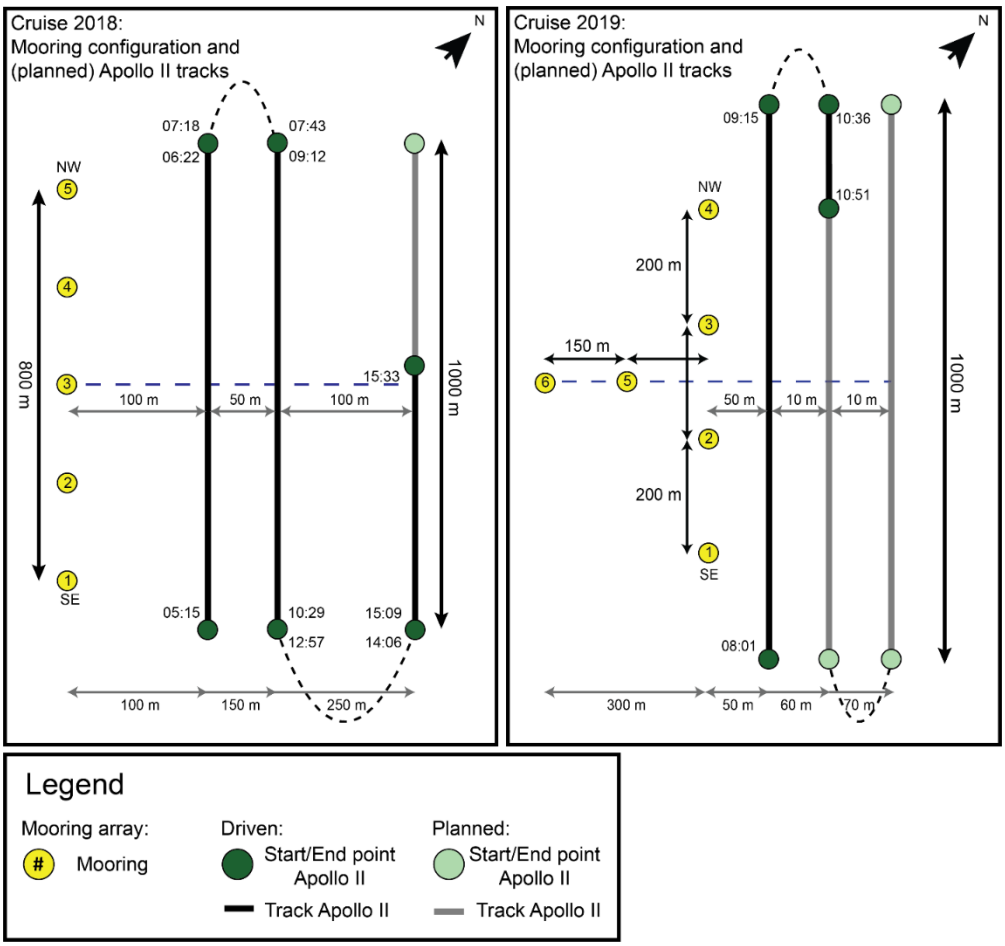

Figure S5.2: Configuration of the Apollo II drive-by experiments on the 18 August 2018 and 20 August 2019, with start- and end times of driving.

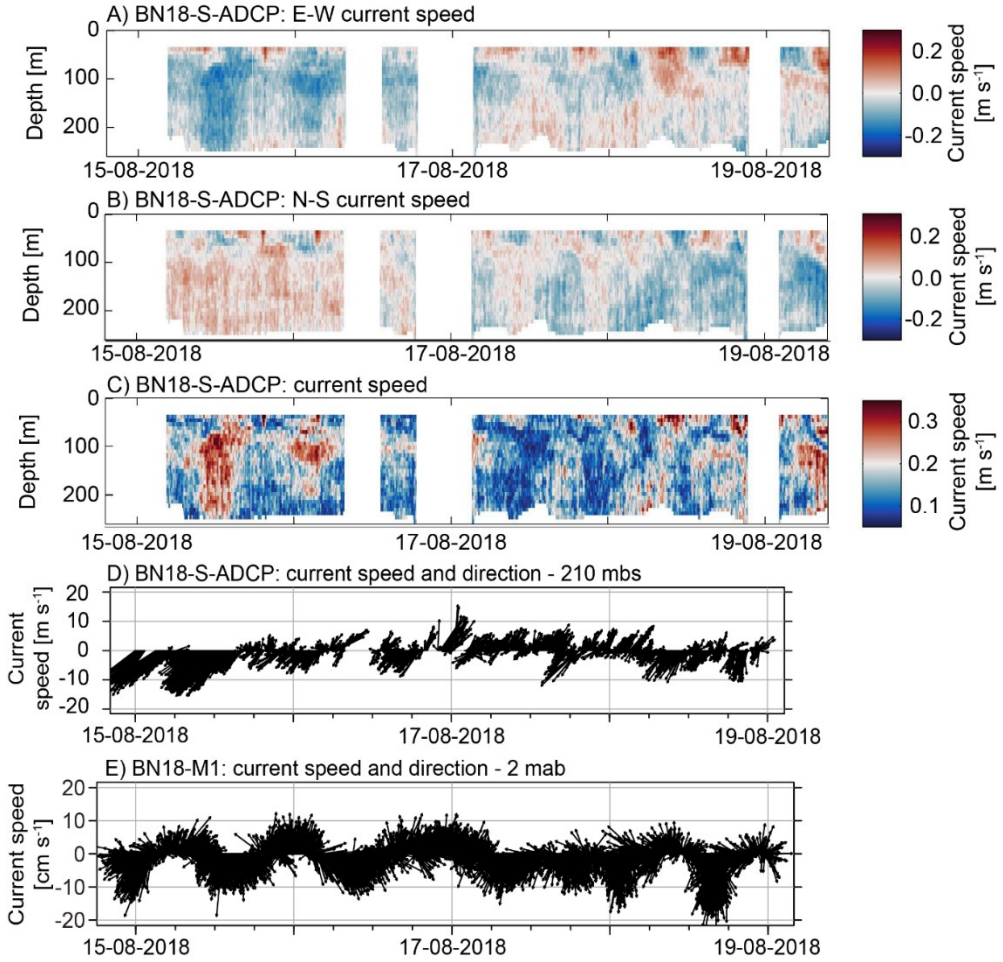

Figure S5.3: Current dynamics of the Málaga Bight test site for the period 15-19 August 2019 when the mooring array was deployed. A-C) Time series of, respectively, E-W velocity, N-S velocity, and total current speed (m s^{-1}) between 25 and 250 m below sea surface (mbs) measured by the S-ADCP. D) Current velocity measured at 210 mbs by S-ADCP. E) Current velocity measured at 2 m above bottom (mab) by the Aquadopp current profiler of mooring BN18-M1.

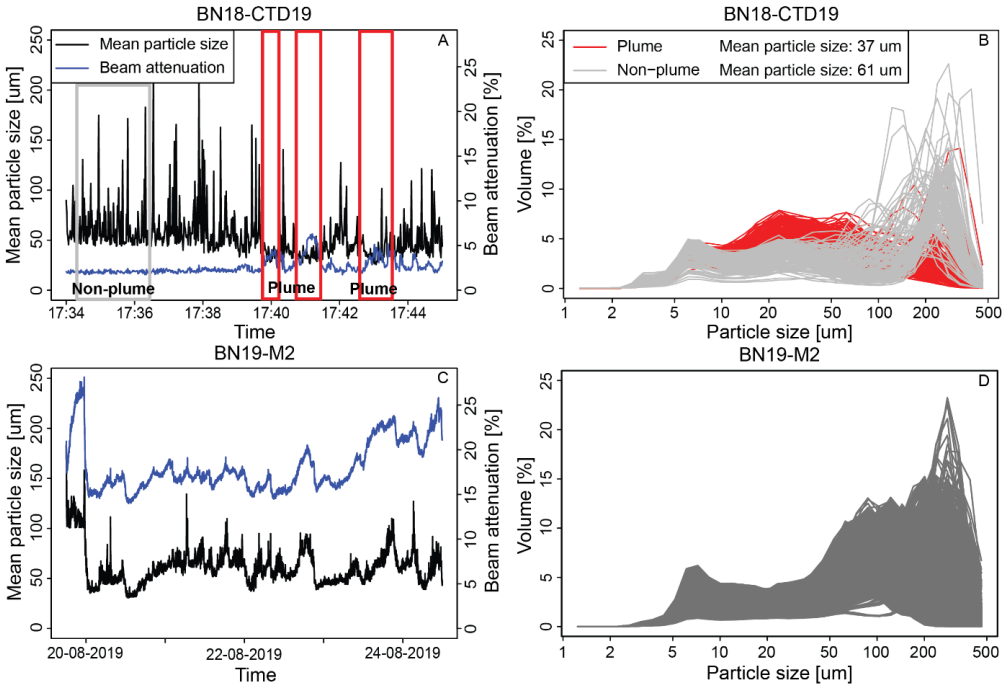

Figure S5.4: Recorded mean particle size and turbidity (beam attenuation) and particle size distribution in the near-bottom water (Fig. A-D). A) Time series of mean suspended particle size and turbidity measured at 2.5 mab with LISST lowered with CTD BN18-CTD19. Particle size distribution curves for non-plume background SPM (interval marked with grey box) and for Apollo II plume SPM (intervals marked with red boxes), are shown in B. C) Time series of mean suspended particle size and turbidity measured by a LISST moored at 3 mab in BN19-M2. Corresponding particle size distribution curves as measured over the entire time interval are shown in D.

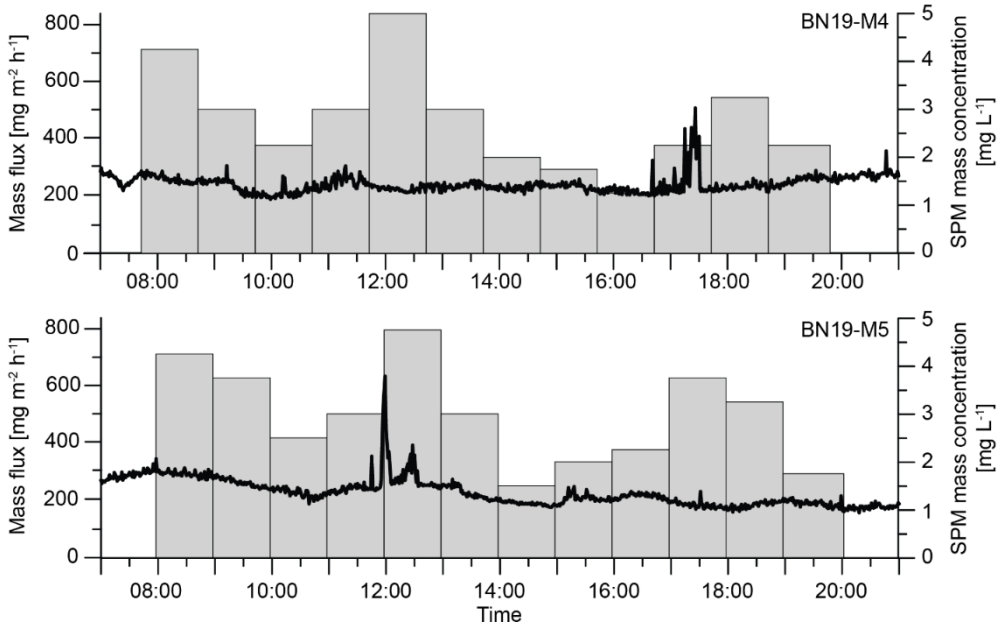

Figure S5.5: Hourly mass fluxes of sinking particles as obtained by the sediment traps on BN19-M4 and M5, and SPM mass concentration at 3 mab recorded with the JFE OBSs (black line), during the Apollo II drive-by experiment on 20 August 2019.

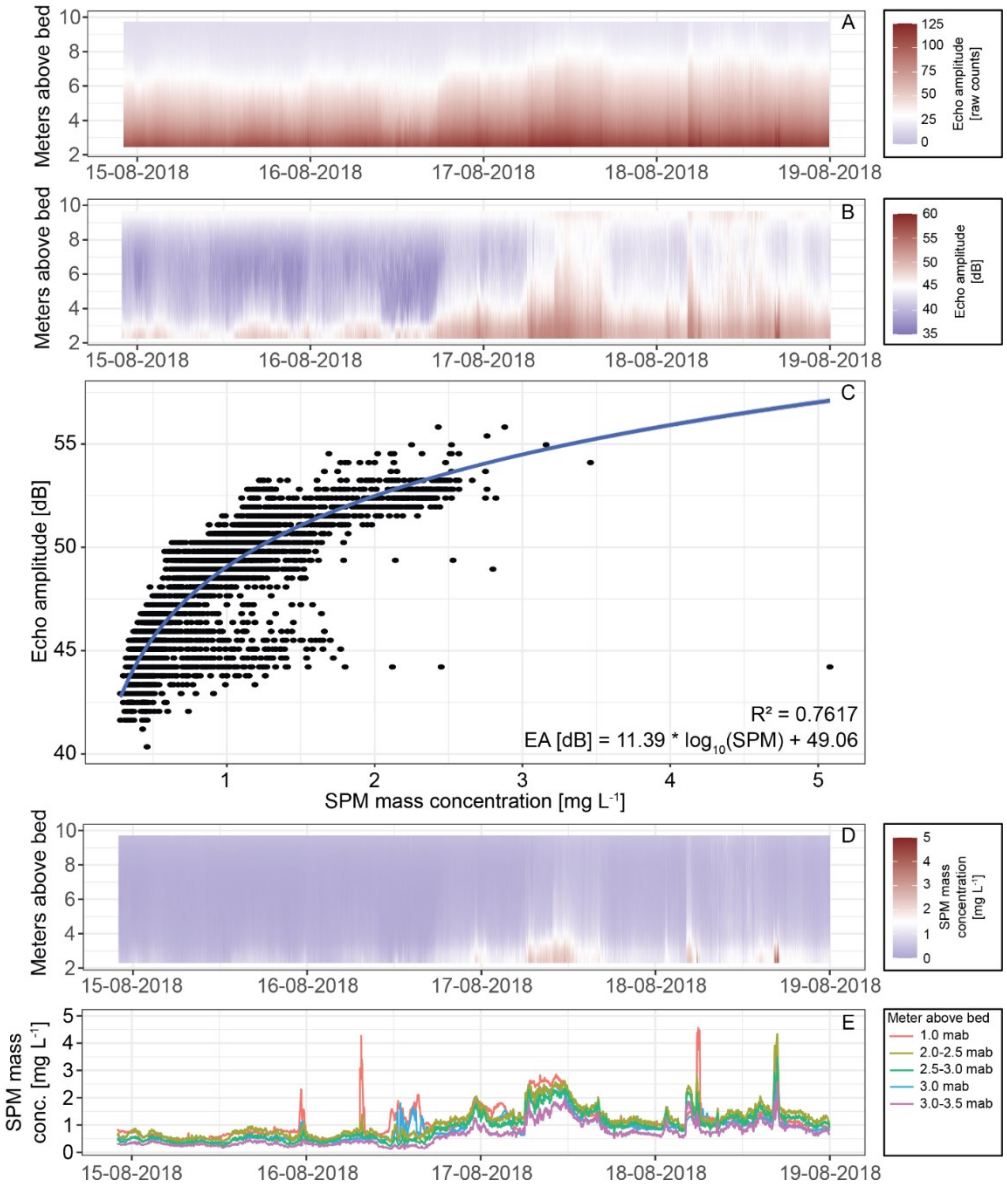

Figure S5.6: Conversion of acoustic backscatter recorded by Nortek Aquadopp to vertical SPM mass concentration profile, as used to produce SPM time-depth section as shown in Fig. 5.11C. A) Raw echo amplitude record, recorded by Nortek Aquadopp in mooring BN18-M1. B) Echo amplitude, after correction of raw data for signal attenuation by geometric spreading and attenuation by water. C) Echo amplitude in bin 2 (2.5-3.0 mab) vs. SPM mass concentration recorded with the JFE OBS at 3 mab, with logarithmic regression and corresponding correlation coefficient. D) SPM mass concentration converted from echo amplitude. E) SPM mass concentration converted from echo amplitude at discrete levels, compared to SPM mass concentration from JFE OBS at 1 and 3 mab.

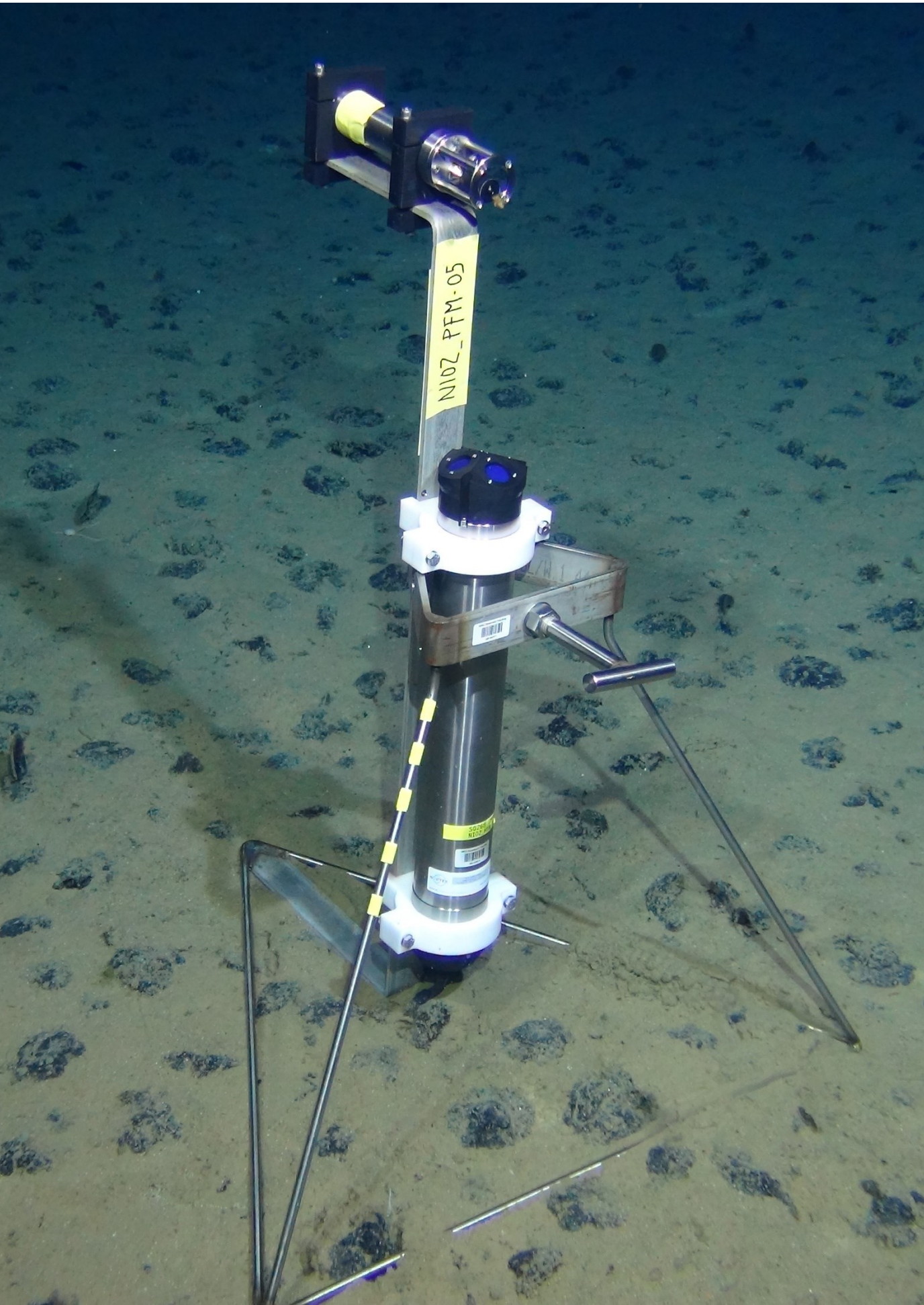
N102_PFM-05

Chapter 6: Monitoring of Anthropogenic Sediment Plumes in the Clarion-Clipperton Zone, NE Equatorial Pacific Ocean

Sabine Haalboom, Timm Schoening, Peter Urban, Iason-Zois Gazis, Henko de Stigter, Benjamin Gillard, Matthias Baeye, Martina Hollstein, Kaveh Purkiani, Gert-Jan Reichart, Laurenz Thomsen, Matthias Haeckel, Annemiek Vink & Jens Greinert

Published as:

Haalboom, S., Schoening, T., Urban, P., Baeye, M., Hollstein, M., Purkiani, K., Reichart, G.-J., Thomsen, L., Haeckel, M., Vink, A., & Greinert, J., 2022. Monitoring of Anthropogenic Sediment Plumes in the Clarion-Clipperton Zone, NE Equatorial Pacific Ocean. Frontiers in Marine Science, v. 9, 882155. https://doi.org/10.3389/fmars.2022.882155

Image: Sensor frame equipped with an OBS and an ADCP deployed in in the Clarion-Clipperton Zonne by ROV KIEL 6000 during cruise SO268 in April 2019 (ROV KIEL 6000, GEOMAR).

Abstract

The abyssal seafloor in the Clarion-Clipperton Zone (CCZ) in the NE Pacific hosts the largest abundance of polymetallic nodules in the deep sea and is being targeted as an area for potential deep-sea mining. During nodule mining, seafloor sediment will be brought into suspension by mining equipment, resulting in the formation of sediment plumes, which will affect benthic and pelagic life not naturally adapted to any major sediment transport and deposition events. To improve our understanding of sediment plume dispersion and to support the development of plume dispersion models in this specific deep-sea area, we conducted a small-scale, 12-hour disturbance experiment in the German exploration contract area in the CCZ using a chain dredge. Sediment plume dispersion and deposition was monitored using an array of optical and acoustic turbidity sensors and current meters placed on platforms on the seafloor, and by visual inspection of the seafloor before and after dredge deployment. We found that seafloor imagery could be used to qualitatively visualise the redeposited sediment up to a distance of 100 m from the source, and that sensors recording optical and acoustic backscatter are sensitive and adequate tools to monitor the horizontal and vertical dispersion of the generated sediment plume. Optical backscatter signals could be converted into absolute mass concentration of suspended sediment to provide quantitative data on sediment dispersion. Vertical profiles of acoustic backscatter recorded by current profilers provided qualitative insight into the vertical extent of the sediment plume. Our monitoring setup proved to be very useful for the monitoring of this small-scale experiment and can be seen as an exemplary strategy for monitoring studies of future, upscaled mining trials. We recommend that such larger trials include the use of AUVs for repeated seafloor imaging and water column plume mapping (optical and acoustical), as well as the use of in situ particle size sensors and/or particle cameras to better constrain the effect of suspended particle aggregation on optical and acoustic backscatter signals.

6.1. Introduction

Due to the increasing demand for raw materials, deep-sea minerals are being explored as potential new mineral resources (Glover and Smith, 2003; Hoagland et al., 2010; Hein et al., 2013). One of these resources are polymetallic nodules, found in the world's oceans on abyssal plains between 3200 and 6500 m water depth (Halbach and Fellerer, 1980; Hein et al., 2013). These polymetallic nodules are rich in metals such as Cu, Co, Ni, and rare earth elements as well as Mn, and are therefore of great economic interest (Wedding et al., 2015). The area with the highest abundance of high-grade nodules is the Clarion-Clipperton Zone (CCZ), located in the north-eastern equatorial Pacific Ocean between Hawaii and Mexico (Halbach and Fellerer, 1980). Mining of these polymetallic nodules will unequivocally result in environmental pressures that will have an impact on the surrounding deep-sea environment. These include mobilisation and compaction of surface sediment, removal of nodules as hard substrate for benthic life, removal of fauna from the seafloor and deposition of suspended sediment in the mined area and its surroundings. Sediment plumes that are produced by the mining vehicle's propulsion and nodule collector system or produced by the discharge of surplus water, sediment and nodule fines from the mining vessel will affect benthic and pelagic life, respectively, over wide areas beyond the actual mined stretches on the seafloor (e.g., Berelson et al., 1997; Smith and Demopoulos, 2003; Drazen et al., 2020). Most of the suspended sediment produced by the mining vehicle is expected to deposit in the vicinity of the disturbance site (Jankowski and Zielke, 2001; Rolinski et al., 2001), smothering benthic fauna under a layer of sediment. Further away, potentially up to several kilometres from the mining site, the suspended sediment concentration in bottom waters may still be sufficient to clog the feeding and respiratory surfaces of filter feeders (Kutti et al., 2015). In addition to the plumes directly produced by the mining process, meso-scale eddies have the potential to resuspend freshly settled sediment and disperse it over an even larger area (Aleynik et al., 2017). Although tolerances of deep-sea fauna in the CCZ to enhanced sediment deposition rates and suspended sediment concentration are currently unknown, it is of great importance that the dispersion of sediment plumes, and the extent of their environmental footprint, can be predicted accurately before the start of any commercial nodule mining, as well as can be verified once the operation has started. Thus, potential impacts observed in deep-sea fauna in the surroundings of the mining site may be linked to levels of exposure to suspended and redeposited sediment.

To date, several plume dispersion studies have been performed during seafloor impact experiments (e.g., Jones et al., 2017; Gausepohl et al., 2020 and references therein), some of these in areas which are licensed for mineral exploration. These studies focused on the resettling of sediment, as inferred from sediment trap data or from seafloor imagery (Barnett and Suzuki, 1997; Yamazaki et al., 1997; Peukert et al., 2018; Gausepohl et al., 2020), as well as on the monitoring of the suspended sediment plumes (e.g., Lavelle et al., 1982; Brockett and Richards, 1994). Based on observations of sediment plume dispersion and plume settlement, model predictions have previously been made (e.g., Nakata et al., 1997; Jankowski; Rolinski et al., 2001; Zielke, 2001). However, comprehensive monitoring of the dispersion of the generated plumes was often limited by the available deep-sea technology at those times (e.g., point sensors rather than profilers; reduced navigational precision of ships and equipment; no AUVs and ROVs). Furthermore, comprehensive plume monitoring requires a spatially large and diverse sensor array around the mining/test site (Spearman et al., 2020; Baeye et al., 2022). Recent plume dispersion studies highlighted the importance of particle aggregation processes within the plume, which speeds up sediment settling and hence restricts the spatial dispersion of the plumes (Gillard et al., 2019). However, plume aggregation processes have not been considered in most of the previous modelling studies.

To better understand the environmental impacts of deep-sea mining activities, comprehensive monitoring experiments and modelling exercises that include field data on plume dispersion and sediment redeposition are urgently required. As part of the European MiningImpact 2 project of the Joint Programming Initiative Healthy and Productive Seas and Oceans (2018-2022), we aimed to monitor the dispersion of the sediment plume generated during a trial of the DEME-GSR *Patania II* pre-prototype industrial mining vehicle in the Belgian and German exploration contract areas in the CCZ in 2019. This trial would offer a unique opportunity to investigate the environmental pressures and impacts arising from a sub-industrial-scale nodule mining operation on the seafloor. Monitoring of the *Patania II* plume was originally planned to be conducted during the RV *Sonne* cruise SO268 in spring 2019, carried out in parallel with the *Patania II* trial in the same area, but needed to be postponed until spring 2021 due to a technical problem associated with the mining vehicle's power supply (Haeckel and Linke, 2021). As an alternative experiment during SO268, we conducted a small-scale, plume monitoring experiment using a 1-m-wide dredge to produce a plume for a period of

approximately 12 hours. The dispersion of the sediment plume was monitored at high resolution with an array of different stationary platforms equipped with optical and acoustic sensors in combination with visual seafloor observations made during remotely operated vehicle (ROV) and towed camera deployments.

In this study, we present and discuss the visual- and sensor-based data of the dredge experiment and present a monitoring concept and strategy for deep-sea operations, including data management. The results of our study were already used to validate and calibrate a plume dispersion model (Purkiani et al., 2021) and the experiences and knowledge gained were used to construct and execute a detailed plume monitoring survey for the *Patania II* test-mining activities in spring 2021.

6.2. Working area

The CCZ in the north-eastern equatorial Pacific Ocean stretches from Hawaii to Mexico and is bounded by the Clarion Fracture Zone in the north (~15°N) and the Clipperton Fracture Zone in the south (~5°N) (Fig. 6.1A). The dredge experiment was conducted in the eastern German exploration contract area at ca. 11.86°N 117.01°W (Figs. 6.1A-C). This contract area features different geomorphological settings at water depths between 2000 and 4500 m, including gently sloping terrain (≤3° in our study area), NNW-SSE trending ridges and valleys and isolated and clustered seamounts occasionally rising to 2 kilometres above the surrounding abyssal plain (Rühlemann et al., 2011).

The surface sediment consists of a mixture of siliceous ooze and deep-sea clay, containing small amounts of detrital carbonate and volcanic material (BGR Bundanstalt für Geowissenschaften und Rohstoffe, 2018). Surface sediments have a median grain size of 20 µm and a size distribution of <10 µm (28%), 10-63 µm (57%), and >63 µm (15%) (Gillard et al., 2019). The porosity of the top 10 cm is about 84-93% and wet bulk density amounts to 1.2 g cm^{-3} (BGR Bundanstalt für Geowissenschaften und Rohstoffe, 2018). The surface of the seafloor at the dredge experiment location is covered with manganese nodules with a size range from 3 to 13.5 cm, covering about 49% of the seafloor (Schoening and Gazis, 2019a; Schoening and Gazis, 2019b).

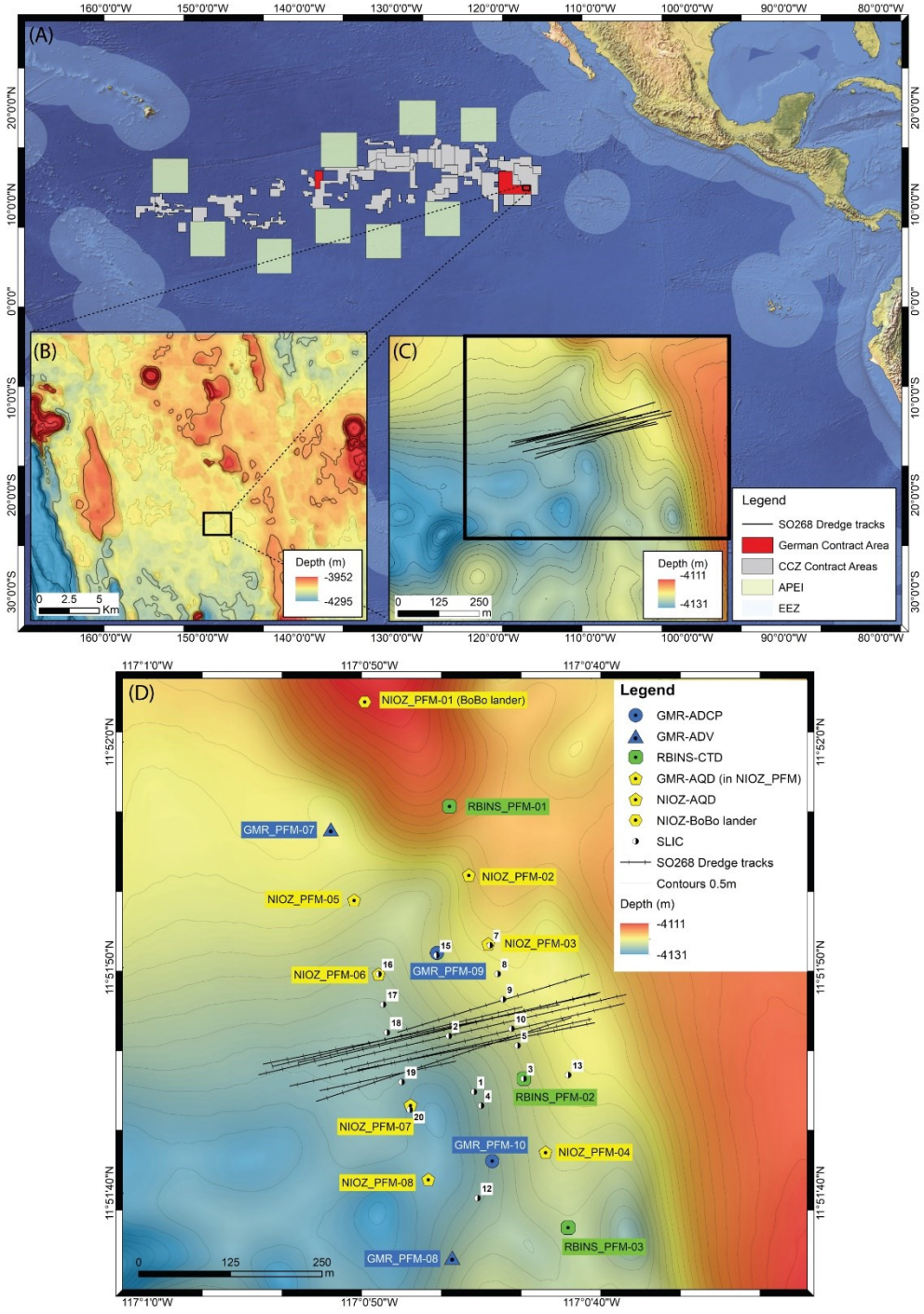
(A)
(B)
(C)
(D)
Legend
SO268 Dredge tracks
German Contract Area
CCZ Contract Areas
APEI
EEZ
Depth (m)
-3952
-4295
-4111
-4131
Km
m
NIOZ_PFM-01 (BoBo lander)
RBINS_PFM-01
GMR_PFM-07
NIOZ_PFM-02
NIOZ_PFM-05
NIOZ_PFM-03
GMR_PFM-09
NIOZ_PFM-06
RBINS_PFM-02
NIOZ_PFM-07
GMR_PFM-10
NIOZ_PFM-04
NIOZ_PFM-08
RBINS_PFM-03
GMR_PFM-08
GMR-ADCP
GMR-ADV
RBINS-CTD
GMR-AQD (in NIOZ_PFM)
NIOZ-AQD
NIOZ-BoBo lander
SLIC
Contours 0.5m

Figure 6.1: A) Map showing the overall location of the CCZ with the German exploration contract areas marked in red. The area of the dredge experiment is shown in more detail in the insets (B and C). The abbreviation APEI stands for Area of Particular Environmental Interest (source: https://isa.org.jm) and EEZ stands for Exclusive Economic Zone (source: https://marineregions.org). D) Locations of the sensor platforms and SLIC boxes in relation to the dredge tracks. The trajectory of the dredge on the bottom was measured during dredging using a USBL beacon mounted to the wire 500 m ahead of the dredge. Post-dredging visual inspection using USBL-navigated OFOS and ROV video footage improved the accuracy of the observed dredge track locations. Sensor platforms of the different scientific institutes involved have been allocated different colours. Bathymetric data were gathered during RV Sonne cruises SO239 (Martinez Arbizu and Haeckel, 2015; Peukert et al., 2018) and SO268 (Gazis, 2020; Haeckel and Linke, 2021). The isobath contour interval in B is 100 m for the darker contours and 25 m for the shaded contours, in figures C and D the isobath contour is 0.5 m.

The bottom currents are characterised by a semi-diurnal M2 tidal cycle, as well as a diurnal S1 tidal cycle (Aleynik et al., 2017). Generally, the bottom current speeds are low, with average speeds of approximately 3.5 cm s^{-1} and peak values usually below 10 cm s^{-1}. However, during the passage of mesoscale eddies, which have their clearest expression at the ocean surface but of which the effect occasionally extends to the seafloor at >4 km depth, average current speeds increase to ~8 cm s^{-1}, with peak values of up to 24 cm s^{-1} (Aleynik et al., 2017).

Whilst background bottom currents are probably not strong enough to resuspend surface sediment most of the time, resuspension might well occur under peak bottom currents associated with these mesoscale eddies (Purkiani et al., 2020). Direct observations of sediment resuspension by eddies do not exist from the area. However, the occurrence of intermittent resuspension events was inferred from the observation that nodules covered by sediment settled from a plume around an epibenthic sledge (EBS) track in 2015 (Peukert et al., 2018) were free of sediment cover when the EBS track was revisited in 2019 during the SO268 cruise (Haeckel and Linke, 2021). With several mesoscale eddies passing annually over the area (Purkiani et al., 2022), it is not unlikely that at least one eddy between 2015 and 2019 has been strong enough to remove and redistribute the sediment settled on the seafloor in 2015.

6.3. Methods

6.3.1. Monitoring plume dispersion and sediment redeposition

In this small-scale plume dispersion experiment, a 1 m wide chain dredge (Fig. 6.2) was deployed to generate a sediment plume. The dredge was dragged over the seafloor in 11 WSW-ENE trending hauls of ~500 m length each with an average speed of 0.2 m s^{-1} (Table 6.1). It took between 40 and 60 min to complete each haul. At the end of each haul, the dredge

was lifted 250-350 m above the seafloor to bring it vertically below the ship, and then lowered back to the seafloor for the next haul. The dredging was carried out on the 11th of April 2019 and lasted for 12.5 hours (06:30 – 19:00 UTC).

Table 6.1: Dredge times (UTC) and positions (longitude, latitude) of each haul on the 11th of April 2019. The trajectory of the dredge on the bottom was measured during dredging using a USBL beacon mounted to the wire 500 m ahead of the dredge. Post-dredging visual inspection using USBL-navigated OFOS and ROV video footage improved the accuracy of the observed dredge track locations.

Haul	Start time	End time	Start position	End position
1	08:03	08:42	-117.01419, 11.86264	-117.01126, 11.86331
2	09:03	09:45	-117.01122, 11.86321	-117.01400, 11.86277
3	10:07	10:40	-117.01346, 11.86299	-117.01055, 11.86372
4	11:02	11:42	-117.01063, 11.86363	-117.01414, 11.86291
5	12:08	12:37	-117.01436, 11.86299	-117.01132, 11.86371
6	13:02	13:29	-117.01208, 11.86341	-117.01496, 11.86282
7	13:50	14:15	-117.01504, 11.86284	-117.01242, 11.86345
8	14:35	15:03	-117.01278, 11.86336	-117.01547, 11.86283
9	15:27	15:49	-117.01505, 11.86285	-117.01268, 11.86348
10	16:18	16:41	-117.01202, 11.86304	-117.01428, 11.86250
11	17:02	17:23	-117.01393, 11.86249	-117.01173, 11.86303

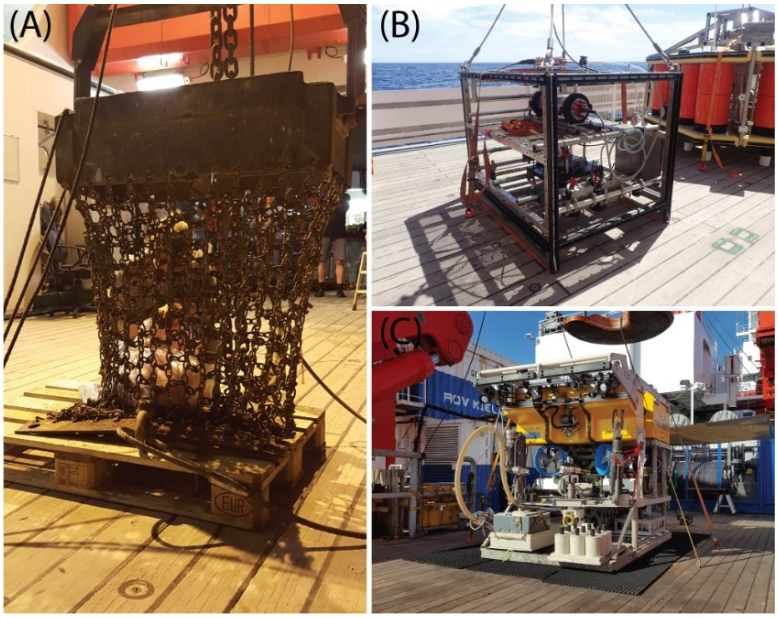

Figure 6.2: A) The 1-m-wide geological chain dredge that was used to create a sediment plume in our study (photo courtesy: Henko de Stigter). B) The Ocean Floor Observatory System (OFOS) of the RV Sonne (Photo courtesy: Yasemin Bodur). C) Remotely Operated Vehicle (ROV) GEOMAR KIEL 6000 (Photo courtesy: Henko de Stigter).

To monitor the dispersion of the generated sediment plume and mass concentration of suspended particulate matter (SPM), 15 sensor platforms were distributed around the dredge

tracks prior to dredge deployment (Fig. 6.1D). The sensor platforms were equipped with different types of optical and acoustic sensors for recording speed and direction of near-bottom currents, as well as bottom water turbidity. The platforms can be categorised into 5 different types:

1) Tripods equipped with an upward-looking Nortek Aquadopp 2 MHz current profiler recording current speed, current direction, and acoustic backscatter, and a JFE Advantech optical backscatter sensor (OBS) recording turbidity. NIOZ deployed seven of these platforms, named NIOZ_PFM-02 to -08.
2) Tripods equipped with a Nortek ADV current meter recording current speed and direction, together with a JFE Advantech OBS recording turbidity. GEOMAR deployed two of these platforms, named GMR_PFM-07 and -08.
3) Tripod frames with an upward-looking RDI Workhorse 300 kHz ADCP cardanically suspended in the frame, recording current speed, current direction, and acoustic backscatter. GEOMAR deployed two of these platforms, named GMR_PFM-09 and -10.
4) Frames holding a SeaBird 19+ CTD placed upright on the seafloor on a rectangular base plate, recording conductivity, temperature, and pressure as well as turbidity using two Seapoint OBSs recoding turbidity. RBINS deployed three of these platforms, named RBINS_PFM-01 to -03.
5) A Bottom Boundary (BoBo) lander (van Weering et al., 2000) equipped with an upward-looking RDI Workhorse 300 kHz ADCP and a downward-looking RDI Workhorse 1200 kHz ADCP, recording current speed and direction and acoustic backscatter, a SeaBird 16+ CTD recording conductivity, temperature, pressure, and turbidity through a WetLabs FLNTU OBS, and a stand-alone JFE Advantech OBS recording turbidity. One BoBo lander was deployed by NIOZ, named NIOZ_PFM-01.

A summary of the sensor platform specifications, including information on measuring range, sampling intervals and deployment and recovery times is provided in Table 6.2.

The initial sensor layout for monitoring the plume generated by *Patania II* was based on a plume dispersion probability map, produced on the basis of numerical simulation using the MITgcm hydrodynamic model combined with a sediment transport module (for a detailed description see Purkiani et al., 2021) (Fig. 6.3). The numerical model was driven by 10 years of

Table 6.2: Specifications of all sensors used in the monitoring array around the dredge experiment site.

Platform[1]	Type	Sensor	Mounted at	Settings	Location
NIOZ_PFM-01	5	CTD SBE16 + WetLabs FLNTU	2 mab	5 min interval, 40 cycles	475 m north
		JFE Advantech OBS	2 mab	10 min interval, 15 samples, 1 Hz	
		Teledyne RDI Workhorse Sentinel 1200 kHz	2 mab	5 min interval, 50 pings/ensemble, 15 bins, 0.2 m bin size, 0.67 m blanking distance	
		Teledyne RDI Workhorse Sentinel 300 kHz	0.75 mab	5 min interval, 80 pings/ensemble, 35 bins, 2 m bin size, 4.23 m blanking distance	
NIOZ_PFM-02	1	JFE Advantech OBS	1 mab	10 min interval, 15 samples, 1 Hz	200 m north
		Nortek Aquadopp 2 MHz	0.75 mab	5 min interval, 60 pings, 1 Hz, 20 bins, 0.5 m bin size, 0.5 m blanking distance	
NIOZ_PFM-03	1	JFE Advantech OBS	1 mab	10 min interval, 15 samples, 1 Hz	100 m north
		Nortek Aquadopp 2 MHz	0.75 mab	5 min interval, 60 pings, 1 Hz, 20 bins, 0.5 m bin size, 0.5 mblanking distance	
NIOZ_PFM-04	1	JFE Advantech OBS	1 mab	10 min interval, 15 samples, 1 Hz	200 m south
		Nortek Aquadopp 2 MHz	0.75 mab	5 min interval, 60 pings, 1 Hz, 20 bins, 0.5 m bin size, 0.5 m blanking distance	
NIOZ_PFM-05	1	JFE Advantech OBS	1 mab	2 min interval, 15 samples, 1 Hz	200 m north
		Nortek Aquadopp 2 MHz	0.75 mab	1 min interval, 60 pings, 1 Hz, 20 bins, 0.5 m bin size, 0.5 m blanking distance	
NIOZ_PFM-06	1	JFE Advantech OBS	1 mab	1 min interval, 15 samples, 1 Hz	100 m north
		Nortek Aquadopp 2 MHz	0.75 mab	1 min interval, 60 pings, 1 Hz, 20 bins, 0.5 m bin size, 0.5 m blanking distance	
NIOZ_PFM-07	1	JFE Advantech OBS	1 mab	2 min interval, 15 samples, 1 Hz	100 m south
		Nortek Aquadopp HR 2 MHz	0.75 mab	1 min interval, 14 pings, 1 Hz, 18 bins, 100 mm bin size, 0.5 m blanking distance	
NIOZ_PFM-08	1	JFE Advantech OBS	1 mab	2 min interval, 15 samples, 1 Hz	200 m south
		Nortek Aquadopp 2 MHz	0.75 mab	1 min interval, 60 pings, 1 Hz, 20 bins, 0.5 m bin size, 0.5 m blanking distance	
GMR_PFM-07	2	JFE Advantech OBS	1 mab	10 min interval, 15 samples, 1 Hz	300 m north
		Nortek Velocimeter 6 MHz	0.25 mab	1 min interval, 120 pings, 64 Hz	
GMR_PFM-08	2	JFE Advantech OBS	1 mab	10 min interval, 15 samples, 1 Hz	300 m south
		Nortek Velocimeter 6 MHz	0.25 mab	1 min interval, 120 pings, 64 Hz	
GMR_PFM-09	3	Teledyne RDI Workhorse Sentinel 300 kHz	0.75 mab	5 min interval, 80 pings/ensemble, 35 bins, 2 m bin size, 4.22 m blanking distance	120 m north
GMR_PFM-10	3	Teledyne RDI Workhorse Sentinel 300 kHz	0.75 mab	5 min interval, 80 pings/ensemble, 35 bins, 2 m bin size, 4.22 m blanking distance	175 m south
RBINS_PFM-01	4	CTD SBE19+ + 2 Seapoint OBS	1 mab	5 min interval, 40 cycles; 1 mab	300 m north
RBINS_PFM-02	4	CTD SBE19+ + 2 Seapoint OBS	1 mab	5 min interval, 40 cycles; 1 mab	100 m south
RBINS_PFM-03	4	CTD SBE19+ + 2 Seapoint OBS	1 mab	5 min interval, 40 cycles; 1 mab	300 m south

[1]Naming of the sensor platforms was based on the project partner's name who provided the platforms to ensure proper data management.

Table 6.2 continued: Specification of all sensors used in the monitoring array around the dredge experiment site.

Platform[1]	Type	Sensor	Deployment	Recovery	Valid measuring range turbidity	Valid measuring range currents
NIOZ_PFM-01	5	CTD SBE16 + WetLabs FLNTU JFE Advantech OBS Teledyne RDI Workhorse Sentinel 1200 kHz Teledyne RDI Workhorse Sentinel 300 kHz	07-04-2019 16:30	15-05-2019 21:54	2 mab 2 mab 0.13 – 1.33 mab (bins 1 – 6) 9.23 – 21.23 mab, 23.23 – 37.23 mab (bins 2 – 7, 9 – 15)	0.73 – 0.93 mab (bins 3 – 6) 17.23 - 21.23, 25.23 – 29.23 mab (bins 6, 7, 10 and 11)
NIOZ_PFM-02	1	JFE Advantech OBS Nortek Aquadopp 2 MHz	08-04-2019 18:21:32	14-05-2019 19:36:24	1 mab 1.25 – 6.25 mab (bins 1 – 10)	1.25 – 2.75 mab (bins 1 – 3)
NIOZ_PFM-03	1	JFE Advantech OBS Nortek Aquadopp 2 MHz	08-04-2019 17:55:30	14-05-2019 19:15:12	1 mab 1.25 – 6.25 mab (bins 1 – 10)	1.25 – 2.75 mab (bins 1 – 3)
NIOZ_PFM-04	1	JFE Advantech OBS Nortek Aquadopp 2 MHz	10-04-2019 19:21:33	12-05-2019 21:10:11	1 mab 1.25 – 7.25 mab (bins 1 – 12)	1.25 – 2.75 mab (bins 1 – 3)
NIOZ_PFM-05	1	JFE Advantech OBS Nortek Aquadopp 2 MHz	08-04-2019 18:41:02	14-05-2019 20:00:45	1 mab 1.25 – 6.25 mab (bins 1 – 10)	1.25 – 3.25 mab (bins 1 – 4)
NIOZ_PFM-06	1	JFE Advantech OBS Nortek Aquadopp 2 MHz	08-04-2019 17:38:58	13-04-2019 00:27:41	1 mab 1.25 – 7.25 mab (bins 1 – 12)	1.25 – 2.75 mab (bins 1 – 3)
NIOZ_PFM-07	1	JFE Advantech OBS Nortek Aquadopp HR 2 MHz	10-04-2019 19:50:47	14-05-2019 00:48:51	1 mab 1.35 – 3.05 mab (bins 1 – 18)	1.35 – 3.05 mab (bins 1 – 18)
NIOZ_PFM-08	1	JFE Advantech OBS Nortek Aquadopp 2 MHz	10-04-2019 19:00:24	12-05-2019 21:42:13	1 mab 1.25 – 6.55 mab (bins 1 – 8)	1.25 – 2.25 mab (bins 1 – 2)
GMR_PFM-07	2	JFE Advantech OBS Nortek Velocimeter	08-04-2019 19:14:27	14-05-2019 20:29:42	1 mab 0.25 mab	0.25 mab
GMR_PFM-08	2	JFE Advantech OBS Nortek Velocimeter	10-04-2019 21:29:19	12-05-2019 16:42:22	1 mab 0.25 mab	0.25 mab
GMR_PFM-09	3	Teledyne RDI Workhorse Sentinel 300 kHz	08-04-2019 17:13:26	14-05-2019 00:18:12	9 – 45 mab (bins 3 – 20)	17 – 29 mab (bins 7 – 12)
GMR_PFM-10	3	Teledyne RDI Workhorse Sentinel 300 kHz	08-04-2019 21:50:10	12-05-2019 22:09:11	15 – 61 mab (bins 6 – 28)	17 – 29 mab (bins 7 – 12)
RBINS_PFM-01	4	CTD SBE19+ + 2 Seapoint OBS	08-04-2019 19:43:01	14-05-2019 21:17:57	1 mab	
RBINS_PFM-02	4	CTD SBE19+ + 2 Seapoint OBS	08-04-2019 22:24:55	12-05-2019 20:12:52	1 mab	
RBINS_PFM-03	4	CTD SBE19+ + 2 Seapoint OBS	08-04-2019 22:54:51	12-05-2019 20:42:04	1 mab	

wind data, affecting the oceans' surface currents (2009-2019; Fig. 6.3A) and throughout the open boundaries with horizontal current velocities obtained from a reanalysis of model products of HYCOM (Purkiani et al., 2021). Model results were validated with long-term current data acquired through oceanographic mooring deployments by BGR (Fig. 6.3C). Based on the model prediction, sediment plume sensors were planned to be distributed over kilometres. For the dredge experiment, the sensor array had to be downscaled in extent to adjust to a much smaller plume generated over a shorter timeframe than anticipated for the *Patania II* trial (12 h vs. 4 days).

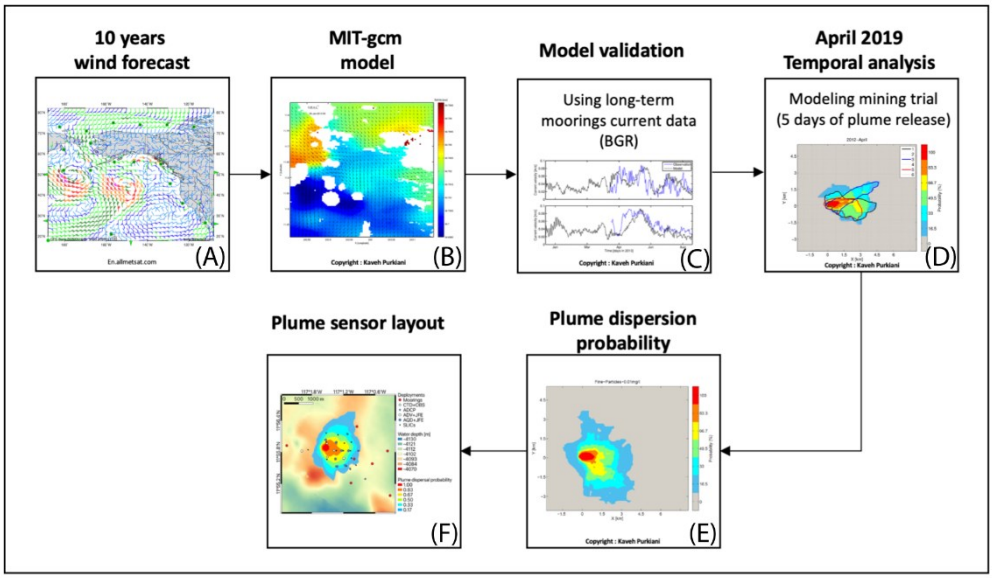

Figure 6.3: Development of plume dispersion probability map, used as a basis for determining the actual sensor layout for plume monitoring. A) Gathering 10-year wind forecast. B) Forcing data in the MIT-gcm hydrographic model. C) Validation of the model using long-term mooring current data as obtained by BGR. D) Temporal analysis of plume dispersion based on integration of a sediment transport module. E) Plume dispersion probability map. F) Plume sensor layout map.

The overall NNW-SSE spread of sensors as in the original layout was maintained, as this was based on the long-term prediction of current direction at the time during and after the experiment, but sensors were distributed much closer to each other and to the dredge area. Furthermore, sensors were not only placed SSE of the dredge area according to the most probable current direction, but also NNW of the dredge area to register plume dispersion in opposite direction. The different sensor platforms were distributed at distances of 100 to 475 m away from the planned dredge area (Fig. 6.1D). Despite that the experiment described in

Peukert et al. (2018) showed almost no blanketing beyond 100 m distance from the disturbance site (EBS track), the sensors were placed not closer than 100 m from the planned dredge tracks to allow some navigation inaccuracy in towing of the dredge in 4120 m water depth. The majority of the sensor platforms were distributed on two parallel lines spaced 200 m apart and perpendicular to the WSW-ENE trending dredge tracks.

This distribution provided replication of the plume signal recordings on either side of the dredge tracks and enabled for a more comprehensive monitoring of the spatial distribution of mobilised sediments. Along these two parallel lines the sensor platforms were placed 100, 200 and 300 m away from the dredge area, with platforms GMR_PFM-09 and GMR_PFM-10 located in the middle of the sensor array at respectively 120 m north and 175 m south of the dredge tracks (Fig. 6.1D). The BoBo lander (NIOZ_PFM-01) was placed 475 m north of the dredge tracks. This was because the lander was deployed free fall, making accurate positioning difficult. BoBo served as a reference for background conditions and to record the far-field plume in case the current direction would be towards the north. All other sensor platforms were deployed accurately by ROV, allowing to monitor gradients of SPM mass concentration at varying distances away from the dredge tracks. Most of the sensors along the western line were set to record the dredge plume at a relatively high sampling rate that allowed high temporal resolution but limited their battery lifetime to approx. 1 week (Table 6.2). Sensors along the eastern line were set to record at a lower sampling rate to extend battery lifetime to 6 weeks or more. This setting sacrificed temporal resolution during the plume monitoring experiment to extend the recording timeframe of the sensors, in order to potentially record resuspension of deposited plume sediment under the influence of a mesoscale eddy that was concomitantly passing over the German exploration contract area in a westward direction at this time (Purkiani et al., 2022). To increase spatial resolution two sensor platforms (NIOZ_PFM-03 and NIOZ_PFM-07) were relocated one day after dredging (12th of April) into the dredge tracks, to monitor potential resuspension at a place where the deposited sediment thickness was expected to be highest.

Visual inspection of sediment deposition was undertaken using video cameras on the towed Ocean Floor Observations System (OFOS) and on GEOMAR's KIEL 6000 ROV (Fig. 6.2). Video footage of both OFOS and ROV was manually annotated during the deployments using the

OFOP software package (Huetten and Greinert, 2008). Preliminary seafloor categories were "dredge track", "faint sediment coverage (<1 mm)", "thick sediment coverage (>1 mm)" and "no sediment coverage".

Additionally, 16 Sediment Level IndiCator (SLIC) boxes were deployed throughout the sensor array, with some only 50 m away from the dredge tracks (Fig. 6.1D). These SLIC boxes were originally intended to collect sediment from the *Patania II* induced plume, and then to be photographed by the ROV or an autonomous underwater vehicle (AUV). This would provide an estimation of the thickness of the sediment drape deposited from the plume. However, since the remobilised sediment from the small-scale dredge experiment was orders of magnitude lower than what was expected from a mining plume, the SLIC boxes only provided a qualitative impression of the sediment redeposition. The SLIC boxes were photographed by the ROV immediately after their deployment and revisited 24 to 30 hours after dredging to assess sediment deposition qualitatively (Fig. S6.1).

6.3.2. Data processing and quality assessment

Sensor data were averaged over the set ensemble interval either internally during the recording process (RDI Workhorse ADCP; Nortek Aquadopp profiler; WetLabs FLNTU OBS; Seapoint OBS) or externally during data evaluation (JFE Advantech OBS) (see Table 6.2). The quality of the turbidity data recorded by the optical sensors (JFE Advantech OBS; WetLabs FLNTU OBS; Seapoint OBS) was assessed by a feasibility check and showed no signs of spurious turbidity values or instrumental drift. Furthermore, data recorded during deployment, relocations and/or recovery of the sensor platforms was removed. The quality and reliability of the acoustic data (current speed and acoustic backscatter data) was checked for each acoustic bin of the respective ADCP. Current speed and direction data were generally discarded from bins for which the standard deviation of the u- and/or v-velocity was more than 0.050 m s^{-1}, as this value represents the upper limit of the background current velocities (Aleynik et al., 2017). This typically coincides with bins where the acoustic backscatter was lower than 25 counts or 40 counts for the Nortek Aquadopp and RDI Workhorse ADCP respectively, which are provided as a lower limit for good data by the manufacturers (Nortek, 2017; Deines, 1999). Table 6.2 specifies for each sensor which bins were regarded as valid for current speed and direction as well as backscatter intensity.

The recorded acoustic backscatter in counts for the RDI and Nortek sensors were converted to (uncalibrated) acoustic backscatter (*ABS*) in decibels using Eq. 6.1 (Lohrmann, 2001), correcting the recorded signal for loss by acoustic spreading and absorption by water (α_w):

$$ABS\ [dB] = 0.46 * ABS\ [counts] + 20 *\ log_{10}(R) + 2\alpha_w R + 20 * R \int \alpha_p dr \qquad \text{(Eq. 6.1)}$$

where the value of 0.46 represents the count-to-decibel conversion factor (k_c = 127/(T + 237.15)) (Manik et al., 2020), with *T* as seawater temperature, *R* represents the distance from the transducer head to the middle of the measurement bin in metres, and α_w and α_p represent the absorption coefficient by water and particles, respectively. The water absorption coefficient (α_w) was determined following the Ainslie and McColm (1998) model, with temperature, depth, and salinity values of 1.5 °C, 4.3 km and 34.7, respectively. This results in a water absorption coefficient of 1451.7 dB km^{-1} for the 2 MHz Nortek Aquadopp profilers and coefficients of 530.2 dB km^{-1} and 44.2 dB km^{-1} for the 1200 kHz and 300 kHz RDI Workhorse ADCPs, respectively. In our calculation we discarded particle absorption α_p, which is unknown but considered to be negligible at the measured low concentrations of SPM.

6.3.3. (Inter)calibration of turbidity sensors

Three different types of optical backscatter sensors were used in this study (JFE Advantech, WetLabs FLNTU and Seapoint OBS). For converting the sensor outputs to SPM mass concentration (mg dry weight L^{-1}), it is essential to (inter)calibrate the sensors for the type of sediment present in the area. To achieve this, sensors were immersed in sediment suspensions of stepwise increasing concentration contained in a 50 L container, after which sensor response in FTU, NTU or voltage was recorded for one or two minutes. The calibration was carried out on board the research vessel in a darkened, cold room at 4 °C. To avoid interference between instruments and provide sufficient sensor reading windows, each sensor was calibrated separately (Fig. S6.2). Stock suspensions had been prepared prior to the cruise from the top 10 cm sediment layer of a box corer sample taken in the German exploration contract area by BGR (sample KG-172, research cruise SO262) mixed with artificial seawater. By adding doses of stock suspension to the 50 L calibration container filled with unfiltered bottom water collected from the test site, the SPM mass concentration was increased in seven steps from 0 mg L^{-1} to 1640 mg L^{-1}. This SPM range was chosen to cover all sensor-specific

detection limits and to include one additional step to assure complete detection range coverage. The outlet of a pump system (3000 L h^{-1}) was placed at 45° onto the container bottom to assure complete mixing during calibration. The sensors recorded the turbidity at their highest sampling rate (1 to 10 seconds). To determine the SPM mass concentration of the successive calibration suspensions, triplicate samples (36.12 ± 0.57 mL) were taken from the suspension after each calibration step. After the cruise, the complete volume of these sub-samples was filtered through a dried, pre-weighed 25 mm diameter, 0.2 mm cellulose acetate filter (Sartorius). After each filtration, the filter was carefully rinsed twice with Milli-Q water to remove remaining salt and dried before it was weighed to obtain the sediment weight. The drying of the clean filter or the filtered sample occurred in an oven (Heraeus, Thermo Scientific) at 60 °C for 48 hours. The turbidity values recorded by the sensors showed a good linear relationship with the corresponding SPM mass concentrations for all the OBSs, with an R^2 of ~0.98 (Fig. 6.4A for the OBSs used on platforms NIOZ_PFM-08 and RBINS_PFM-03). The sensor-specific linear relation was used for the conversion of sensor output data to SPM mass concentration.

The acoustic backscatter recorded by the acoustic sensors could not be directly calibrated on board in a similar manner as done for the OBSs, due to the relatively large minimum measurement range of the acoustic sensors. Following a practice described in other studies (e.g., Fettweis et al., 2019; Haalboom et al., 2021), the Nortek Aquadopp sensors were calibrated in situ by reference to the SPM mass concentration derived from a calibrated OBS placed close to the first valid measurement bin of the Aquadopp. This is exemplarily shown for sensors of platform NIOZ_PFM-08. The lowermost bin of the Nortek Aquadopp was at 1.25 metres above bed (mab), while the JFE OBS was recording at 1 mab. As shown in Figure 6.7 the recorded turbidity patterns show similarities in terms of amplitude and timing on the 11th of April. The cross-comparison of these data points (SPM mass concentration on a linear scale, acoustic backscatter as decibels; Fig. 6.4B) revealed a significant ($p < 0.001$), though not particularly strong ($R^2 = 0.6855$) $\log_{10}$ relation between these two timeseries. Applying this relationship to convert the acoustic backscatter levels to SPM mass concentration results overall in a much higher estimate of the SPM mass concentration compared to what was inferred from the OBSs.

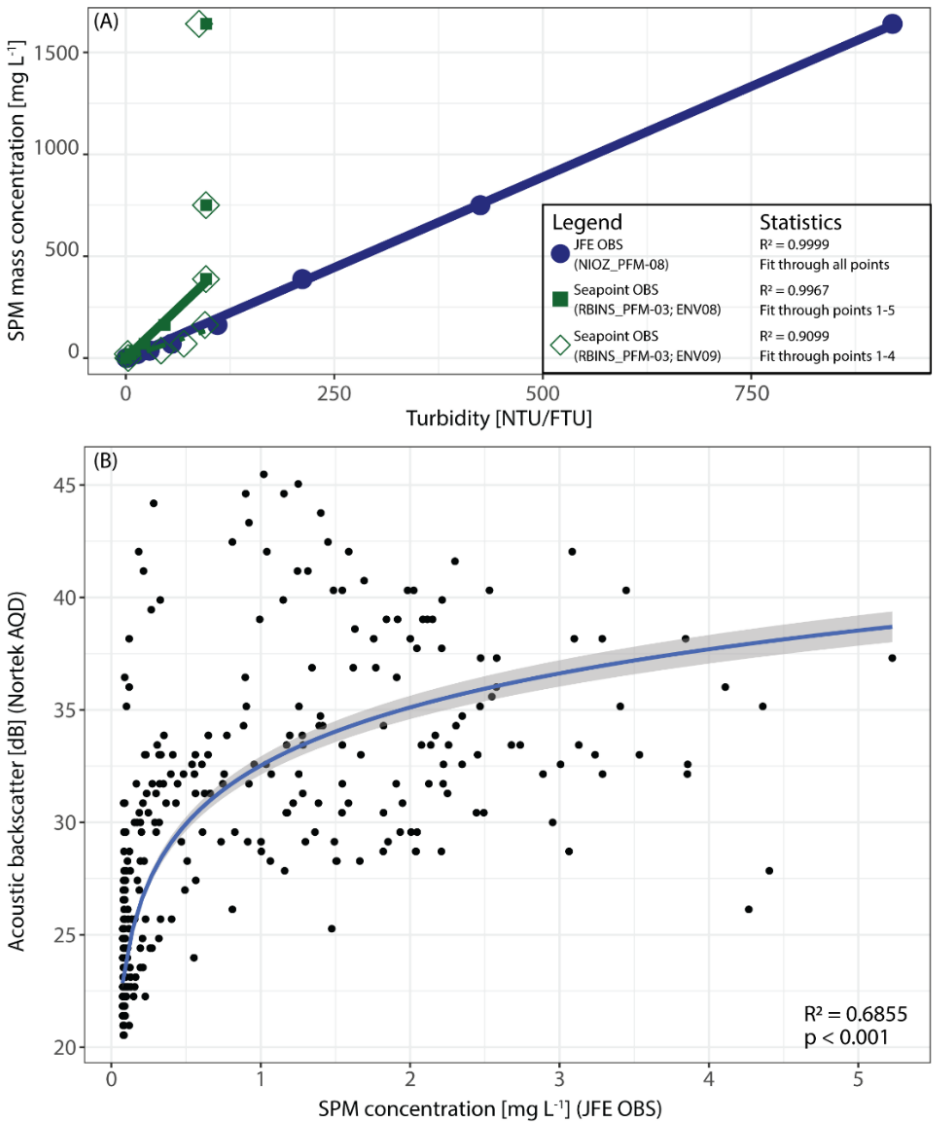

Figure 6.4: A) Correlation between recorded turbidity of several optical backscatter sensors (OBSs) as measured during onboard calibration and SPM mass concentration. Results are shown for the JFE Advantech OBS NIOZ_ENV14 as used on platform NIOZ_PFM-08 (blue) and the Seapoint OBS RBINS_ENV08 (SP1; green solid squares) and Seapoint OBS RBINS_ENV09 (SP2; green open squares), used on sensor platform RBINS_PFM-03. The linear regressions are used for the conversion of the recorded turbidity signal into SPM mass concentration. Note that for the Seapoint OBSs the regression line is only fitted to the first 4 or 5 points as the other higher calibration steps were beyond the saturation level of these OBSs, resulting in a constant response (saturation) of these sensors above 100 NTU. B) Correlation between SPM mass concentration as recorded at sensor platform NIOZ_PFM-08 (200 m south of the dredge tracks) by a JFE Advantech OBS (x-axis) and converted acoustic backscatter in dB as recorded by the Nortek Aquadopp profiler (y-axis) at the same site on the 11th of April.

Due to these large differences and uncertainties about what exactly caused them, we refrain from using the acoustic backscatter results in any quantitative analysis. Even so, the acoustic

backscatter data (converted to dB) provide valuable qualitative insight in the occurrence of sediment plumes in time and space, in particular regarding the vertical extent of these plumes above the seabed.

6.3.4. Different particle size sensitivity of turbidity sensors

Optical backscatter sensors are known to be more sensitive to fine-grained particles, whilst their sensitivity decreases with increasing particle size (e.g., Downing, 2006). For acoustic sensors, the sensitivity depends on the particle size and other particle parameters (e.g., density, shape; Fettweis et al., 2019 and references therein) as well as on the operating frequency of the acoustic device (e.g., Wilson and Hay, 2015). However, to gain a basic comparison of the particle size sensitivity of the used acoustic sensors, the simple approximation from Lohrmann (2001) can be used. The model states that the sensor response is at its maximum when $ka = 1$, with k being the acoustic wave number given as $k = \frac{2\pi f}{c}$, with f being the operating frequency and c the speed of sound, and a the particle radius. For particle radii of $ka < 1$ the acoustic sensitivity decreases proportionally to the particle radius to the fourth power, and for particle radii of $ka > 1$ the acoustic sensitivity is predicted to behave inversely proportional to the particle radius. Applying this to the acoustic sensors used in our plume monitoring experiment, operating at 300 kHz, 1200 kHz, and 2000 kHz (Table 6.2), these sensors have maximum sensitivity for particles of, respectively, 1618 µm, 404 µm, and 242 µm diameter, taking the speed of sound as in the study area at 4 km depth (1525 m s^{-1}). Already at a tenth of this diameter (162 µm, 40 µm, and 24 µm respectively), the sensitivity of these sensors decreases by approximately -40 dB (factor 10.000).

6.3.5. Water column SPM mass concentration

During the SO268 cruise, five CTD casts were performed in the dredge area to determine the SPM mass concentration in the water column. During each of the CTD casts, a bottom water sample (~4119 m water depth) was taken in duplicate using 11 L Niskin bottles. From the Niskin bottles, subsamples of either 4.5 L or 9 L were drawn (Table 6.3) and filtered on board over 47 mm diameter, 0.4 µm pre-weighed Millipore polycarbonate filters. The filters were rinsed with Milli-Q to remove salt and stored at -20 °C until further analysis. In the laboratory at NIOZ, the thawed filters were rinsed again with Milli-Q to remove still remaining salt, and subsequently freeze-dried and weighed to determine the weight of SPM per volume of filtered seawater.

Table 6.3: SPM mass concentration obtained from bottom water samples at five CTD stations during cruise SO268.

Station	Latitude	Longitude	Depth (m)	Volume (L)	SPM mass conc. (µg L^{-1})
SO268/2 – ST94 – CTD11	11°51.598 'N	117°00.839 'W	4119	4.5	15
SO268/2 – ST94 – CTD11	11°51.598 'N	117°00.839 'W	4119	4.5	15
SO268/2 – ST120 – CTD12	11°51.769 'N	117°00.739'W	4115	4.5	19
SO268/2 – ST120 – CTD12	11°51.769 'N	117°00.739'W	4115	4.5	9
SO268/2 – ST159 – CTD15	11°51.587 'N	117°00.842 'W	4120	9.0	10
SO268/2 – ST159 – CTD15	11°51.587 'N	117°00.842 'W	4120	9.0	17
SO268/2 – ST183 – CTD16	11°51.600 'N	117°00.839 'W	4120	9.0	13
SO268/2 – ST183 – CTD16	11°51.600 'N	117°00.839 'W	4120	9.0	24
SO268/2 – ST208 – CTD17	11°51.601 'N	117°00.834 'W	4118	9.0	18
SO268/2 – ST208 – CTD17	11°51.601 'N	117°00.834 'W	4118	9.0	31

6.4. Results

6.4.1. Bottom water background characteristics

Based on CTD data, the bottom water in the study area is characterised by a temperature of 1.5 °C, a salinity of 34.7, a density (σ-θ) of 27.8 kg m^{-3}, and SPM mass concentrations of 0.02 mg L^{-1}, as inferred from the JFE Advantech OBS (Fig. S6.3). Such low concentrations correspond to values obtained from the Niskin water samples collected in undisturbed, clear bottom water, which showed average SPM mass concentrations of 0.017 ± 0.006 mg L^{-1}. Low turbidity values were recorded throughout the water column below thermocline depth, and no increase in turbidity towards the seafloor that would indicate the presence of a bottom nepheloid layer was detected. Throughout the 6 weeks of monitoring, mean current speeds close to the seafloor (< 20 mab) were about 4 cm s^{-1}, predominantly in southeast direction, with alternations towards the north. Higher in the water column, between 20 and 30 mab, mean current speeds increased to 6 cm s^{-1}, still having the same dominant current direction. Spectral analysis showed that the current regime is dominated by the semidiurnal and diurnal tidal harmonic components M2 and K1 (Fig. S6.4).

6.4.2. Visual observations of the dredge's impact on the seafloor

Based on the ROV and OFOS images (Fig. 6.5) it could be confirmed that the dredge did not remove or stir up the sediment equally along its predefined tracks. The dredge was effectively dragged over the seafloor along some parts of the transects, with much of the sediment being pushed aside as a cohesive mass and thus not fully put into suspension. Along other parts of the dredge tracks, we found that the dredge had bounced over the seafloor and had hardly touched the seafloor at all, or only scratched the surface. Furthermore, lumps of cohesive

sediment were observed to be scattered outside of the dredge tracks, which most likely were dropped when the dredge was hauled up at the end of each track and moved into position to start the next track.

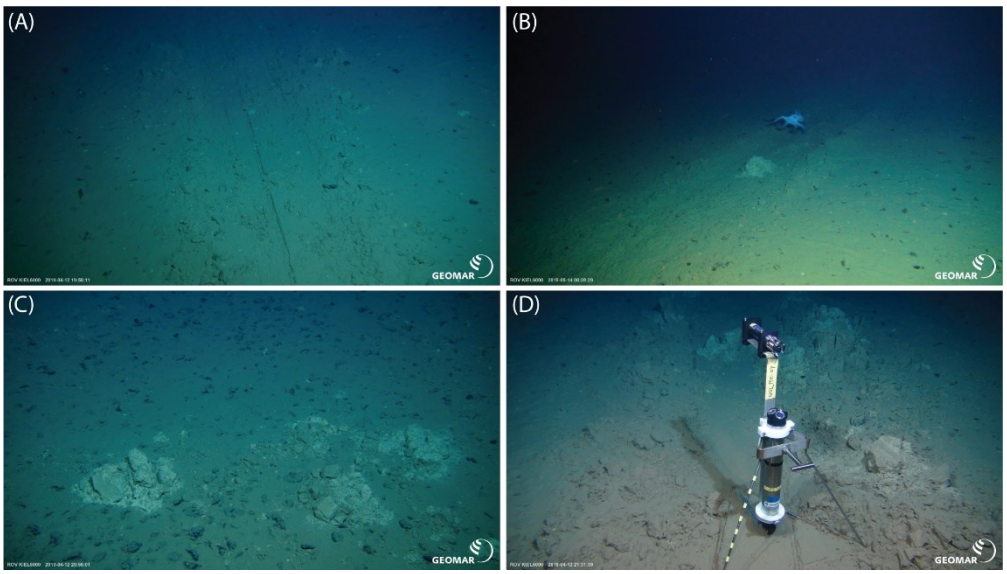

Figure 6.5: A) The 1-m-wide dredge track, with sediment pushed to the side. On both sides of the dredge track the blanketing of the polymetallic nodules is observed. B) Variability in depth of the dredge mark. In the foreground the 1-m-wide dredge only swept over the sediment surface but further down the dredge mark deepens and more sediment was pushed sideways. The photo also shows a churned-up sediment lump in the middle of the track and an octopus behind. C) Sediment lumps found outside of the dredge tracks, presumably fallen from the dredge as it was hoisted up from the seafloor. D) Photo showing NIOZ_PFM07 after it was repositioned into the dredge track on the 12th of April. More photos are found in the SO268 cruise report (Haeckel and Linke, 2021). (Photo courtesy: GEOMAR, ROV Team Kiel 6000).

6.4.3. Sensor data on sediment plume dispersion

During the dredging (11th of April 06:30 – 19:00 UTC), the recorded current patterns were generally consistent between all sensors (Fig. 6.6). At the start of the dredging (between 06:30 and 11:00 UTC), the currents were directed towards the southeast, with average current speeds of 2 to 3 cm s^{-1} (Fig. 6.6). From 11:00 UTC onwards until the end of the dredging at 19:00 UTC, the currents turned clockwise towards the south, with maximum current speeds reaching 7 cm s^{-1}. This pattern of initial flow towards the southeast turning more to the southwest at a later stage is depicted in progressive vector diagrams showing cumulative displacement (Fig. S6.5), where differences between the platforms become apparent from the diverging trajectories.

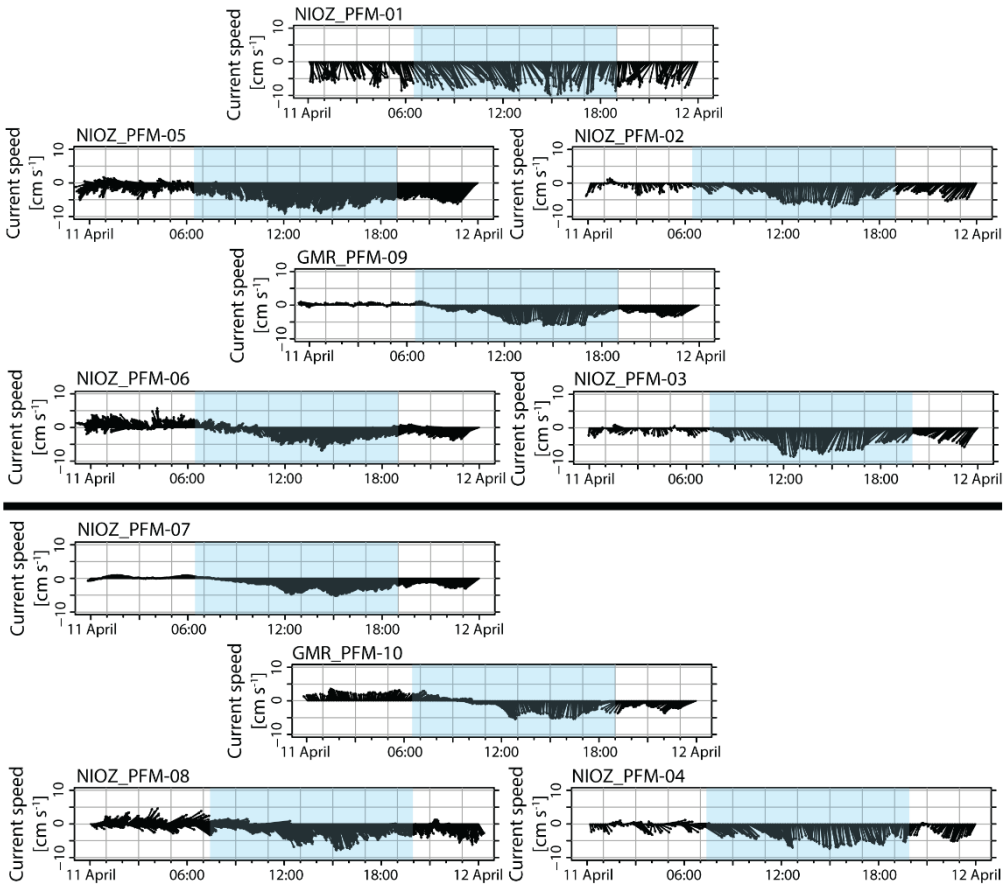

Figure 6.6: Time series of current speed and direction recorded on the 11th of April by the Nortek Aquadopp profilers (bin 1 at 1.25 mab, NIOZ_PFM-02 to -08) and the RDI Workhorse ADCPs (bin 7 at 19 mab, GMR_PFM-09 and -10, and bin 3 at 0.7 m, NIOZ_PFM-01) located north and south of the dredge tracks. The blue overlay indicates the time interval during which the dredging took place. The arrangement of the time series graphs corresponds with the geographical arrangement of the sensor platforms north and south of the dredge tracks (black line through the centre).

In agreement with the observed current directions, the time series of SPM mass concentration recorded at the different sensor platforms reflect a southward entrainment of the sediment plume. Both during and after the dredging, the sensors north of the dredge tracks did not record increased SPM mass concentrations but remained at the background SPM mass concentration of 0.02 mg L^{-1} (Fig. 6.7). In contrast, the sensors south of the dredge tracks recorded repeated increases in SPM mass concentration well above background level. The recorded maximum SPM mass concentrations decreased with increasing distance from the dredge area. At platforms NIOZ_PFM-07 and RBINS_PFM-02, both 100 m south of the dredge tracks, 5 intervals of enhanced SPM mass concentrations of ~3 mg L^{-1}, with maxima going up

to 11 mg L^{-1}, were recorded between 09:00 and 18:00 UTC, and between 10:00 and 18:00 UTC, respectively (Fig. 6.7). At sensor platforms NIOZ_PFM 08 and NIOZ_PFM-04, located 200 m south of the dredge tracks, the passing plumes were recorded between 10:00 and 19:30 UTC, and between 10:00 and 14:00 UTC, respectively, with SPM mass concentrations of ~2 mg L^{-1}. At platforms GMR_PFM-08 and RBINS_PFM-03, both located 300 m south of the dredge area, the plumes were recorded from 11:30 to 20:00 UTC, and from 11:00 to 14:30 UTC, respectively, with lower SPM mass concentrations of ~1 mg L^{-1}, still clearly exceeding the background SPM mass concentration.

The drift speed of the plumes away from the dredge area, as inferred from the arrival times of the plume at the different sensor platforms, is in good agreement with the current speeds recorded close to the seafloor at that time. For example, the maximum recorded SPM mass concentration of the first plume, indicating the main body of the first plume, was recorded at 10:30, 11:00 and 12:00 UTC, at sensor platforms NIOZ_PFM-07 (100 m), NIOZ_PFM-08 (200 m) and GMR_PFM-08 (300 m), respectively. This gives current speeds ranging from 2.8 to 5.6 cm s^{-1}, in line with the currents measured between 10:30 and 12:00 UTC by NIOZ_PFM-07 (ranging from 2.8 cm s^{-1} to 5.3 cm s^{-1}).

The acoustic backscatter recorded from the lowermost measurement bin of the Nortek Aquadopp profilers at platforms NIOZ_PFM-07, NIOZ_PFM-08 and NIOZ_PFM-04 was compared to the OBS data from the same platforms. As shown in Figure 6.7, the acoustic backscatter recorded at those platforms displayed several sharp increases, and subsequent decreases to background level, predominantly in parallel with SPM mass concentration changes recorded by the OBSs. However, we observe some differences between the acoustic and optical data in the arrival time, peak value, and end of successive plume events. Typically, the acoustic sensors detected the initial increase in turbidity marking the arrival of the plume considerably earlier than the optical sensor on the same platform, in some cases up to one hour earlier. The maximum turbidity within successive plume events was usually also recorded first by the acoustic sensor, by up to an hour earlier than the corresponding OBS sensor.

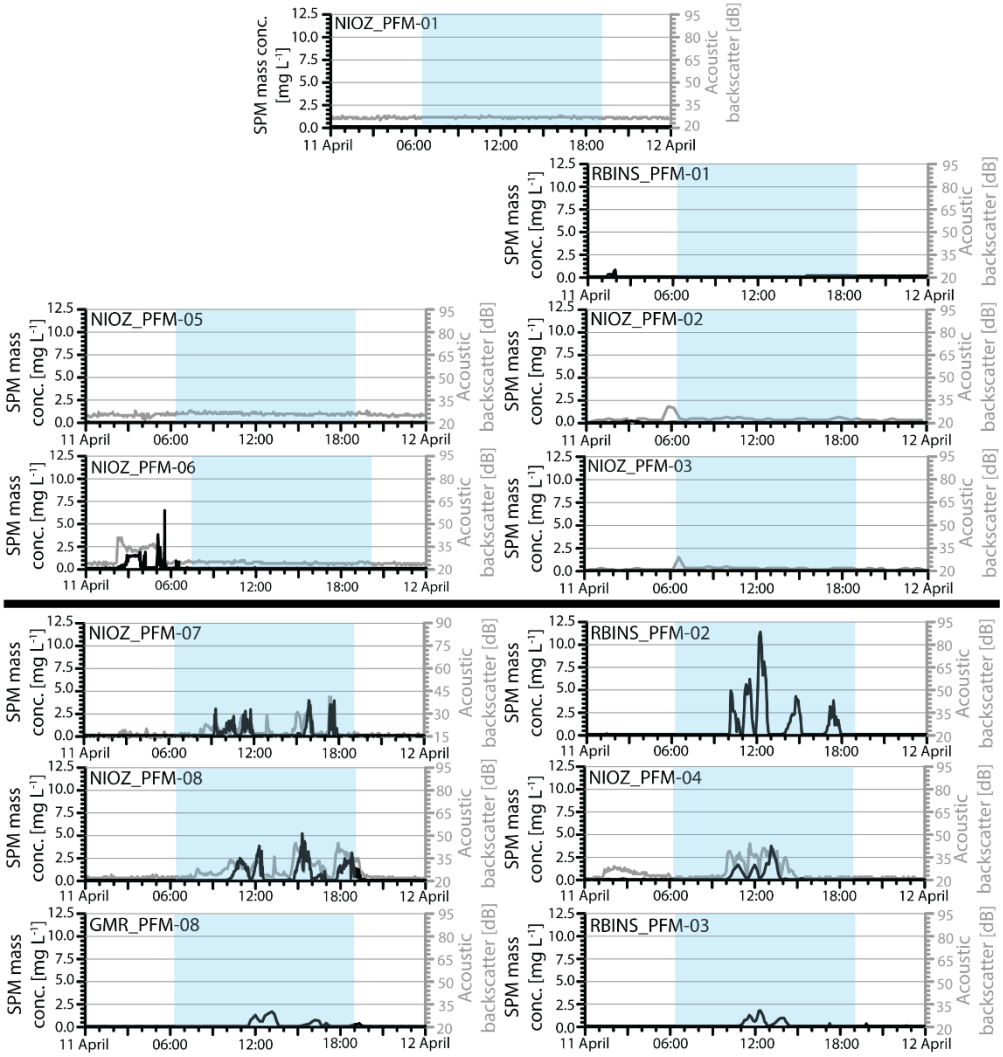

Figure 6.7: Time series of SPM mass concentration as inferred from OBS measurements at 1 mab (black) and acoustic backscatter at 1.25 mab (red) recorded on the 11th of April. The blue overlay indicates the time interval during which the dredging took place. The arrangement of the time series graphs corresponds with the geographical arrangement of the sensor platforms north and south of the dredge tracks (black line through the centre). It should be noted that in the representation of relative turbidity using a decibel scale, variation in the low concentration range appears disproportionally enhanced compared to variation in the high concentration range. The observed increase in recorded turbidity by both the optical and acoustic sensors of platforms NIOZ_PFM-06 in the hours before dredging took place, can be attributed to the sediment plume produced by lift-off of the elevator that was used for transferring sensor platforms from the ship to the seafloor. The elevator was located 800 m NE of the platform, while current at the moment of lift-off was in southwesterly direction.

The return to background turbidity levels, however, was usually recorded at the same time by both sensor types. This mismatch between the simultaneously measured acoustic and optical backscatter is also evident in the broad scatter seen in Figure 6.4B.

Inspection of the entire turbidity profile obtained from the Nortek Aquadopp profilers allows estimation of the height of the plume. The densest part of the plume stayed within 2 m above the seafloor, but occasionally rose to 6 mab, as shown in Figure 6.8 for NIOZ_PFM-08 and NIOZ_PFM-04 that were located 300 m south of the dredge tracks. The 300 kHz ADCP at platform GMR_PFM-10, which due to its lower frequency has a larger detection range, was installed to predominantly record coarser-grained (aggregated) particles. Unfortunately, this sensor also has a larger blanking distance and only started recording at 5 mab. Furthermore, the lowermost bins did not provide trustworthy data so that good data could only be obtained from 19 mab upwards. Thus, the RDI 300 kHz ADCPs missed the lower part of the plume, but the 300 kHz ADCP sensor at platform GMR_PFM-10 (Fig. 6.8) did show a peculiar backscatter pattern up to 60 mab close to the end of the dredging at 18:00 UTC.

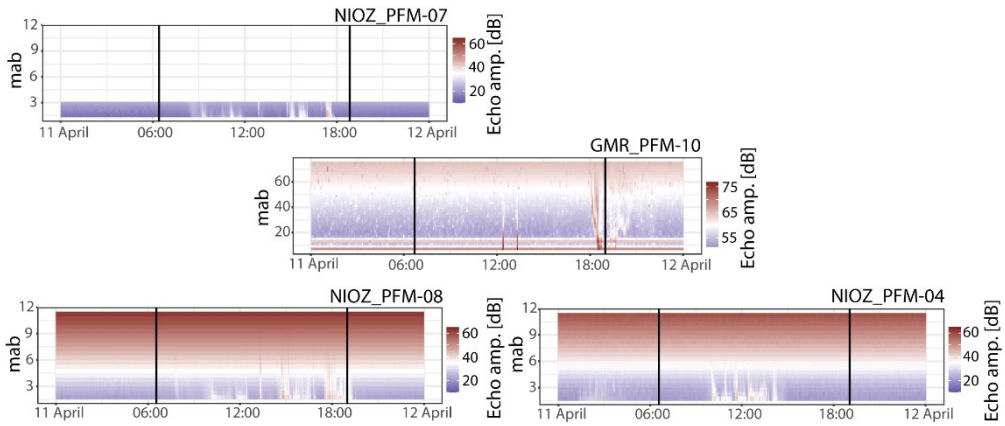

Figure 6.8: Times series of acoustic backscatter (converted to dB) in the lower metres or tens of metres above the seabed (mab) recorded with Nortek Aquadopp profilers (on NIOZ_PFM-04, -07, and -08) and the RDI Workhorse ADCP (on GMR_PFM-10) in the southern part of the sensor array, showing the vertical extent of the sediment plume and particle swarms above the seabed. The two black lines in the figures represent the start and the end time of the dredging. The arrangement of the time series graphs corresponds with the geographical arrangement of the sensor platforms. Note the different scale of the vertical axis for platform GMR_PFM-10. The range-dependent gradual increase in background echo amplitude level is caused by acoustic loss correction for spreading and absorption, which amplify the raw signal with increasing distance from the transducer (Eq 6.1). Since the acoustic absorption is frequency dependent, this increase in more pronounced for NIOZ_PFM-4, -07 and -08 (Nortek Aquadopp with 2 MHz), compared to GMR_PFM-10 (RDI ADCP with 300 kHz).

During the weeks after the dredging was carried out (11th April to 13th May), we observed variable current speeds and directions, as shown exemplarily for sensor platform NIOZ_PFM-04 in Figure 6.9 (and for all sensor platforms in Fig. S6.6). Currents were predominantly directed southward, occasionally alternating towards the north. After the plumes had passed, we occasionally recorded enhanced SPM mass concentrations at some of the sensor platforms (e.g., NIOZ_PFM-04; Fig. 6.9; Fig. S6.7). These events can be linked to our own sampling and monitoring activities at or close to the seafloor in the near vicinity of these sensor platforms.

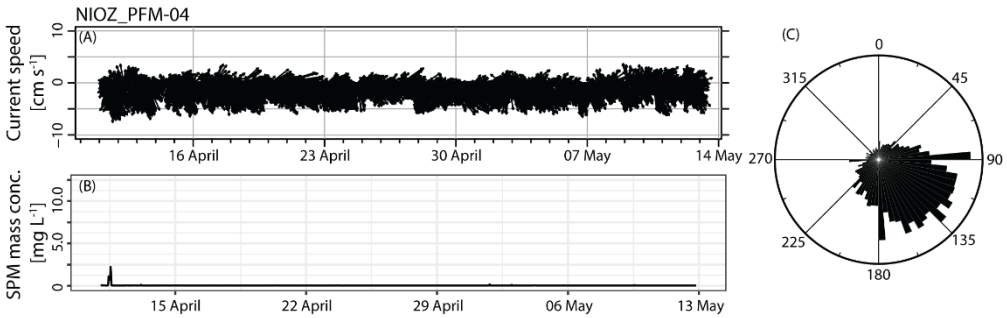

Figure 6.9: Longer-term variability of current speed and direction and SPM mass concentration at sensor platform NIOZ_PFM-04, recorded between the 11th of April and the 13th of May 2019, 200 m south of the dredge tracks. A) Current speed and direction, showing predominant southeast current direction, alternating with northerly direction. B) Recorded SPM mass concentrations during the entire deployment period. C) Rose diagram display of the recorded current directions.

6.4.4. Visual observations of plume sediment deposition from the plume

OFOS and ROV imagery showed a drape of up to a few mm of resettled sediment (Fig. 6.10). Observations of SLIC boxes by ROV confirmed this observation (Fig. 6.11 and Fig. S6.1). These sediment drapes were only found in close proximity to the dredge tracks, and were just sufficient to cover the nodules, but not completely bury them (Fig. 6.10C). Furthermore, we saw more resettled material in SLIC boxes 02, 05, 10 and 19 (in between or close to the dredge tracks; Fig. 6.11 and Fig. S6.1). The thickness of the drape rapidly diminished in a southward direction, as shown by still images taken from SLIC boxes 01, 03, 04 and 20 (Fig. 6.11 and Fig. S6.1), as well as in OFOS imagery (Fig. 6.10B). No sediment cover related to the dredge experiment was visually discernible at distances of 100 m or more south of the dredge tracks (Figs. 6.10A and 6.11). North of the dredge tracks, a faint coverage was only found in SLIC boxes 16 and 18, whereas the other SLIC boxes did not show any coverage (Fig. 6.11).

6.4.5. Virtual 4D Data visualisation

We compiled all gathered data for visualisation in 4D using the web-based Digital Earth Viewer tool (Buck et al., 2021). A freely accessible example can be found here: https://digitalearthviewer-plume.geomar.de. This tool allows easy navigation through time and space, and an eye-catching visualisation of the dispersion of the sediment plume of the dredge experiment described here.

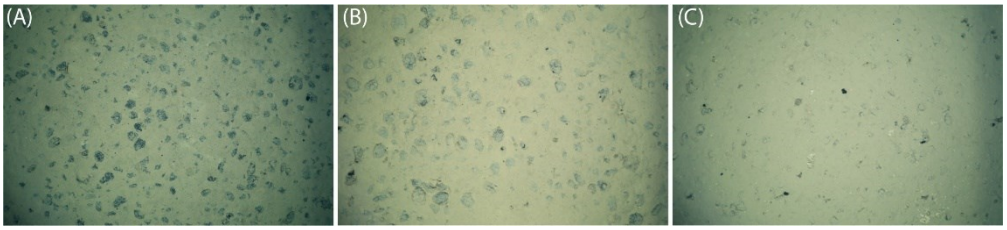

Figure 6.10: Still images acquired during seafloor imagery surveys using the OFOS. A) No sediment coverage. B) Faint sediment coverage. C) Thick sediment coverage. Data availability: Purser et al. (2021).

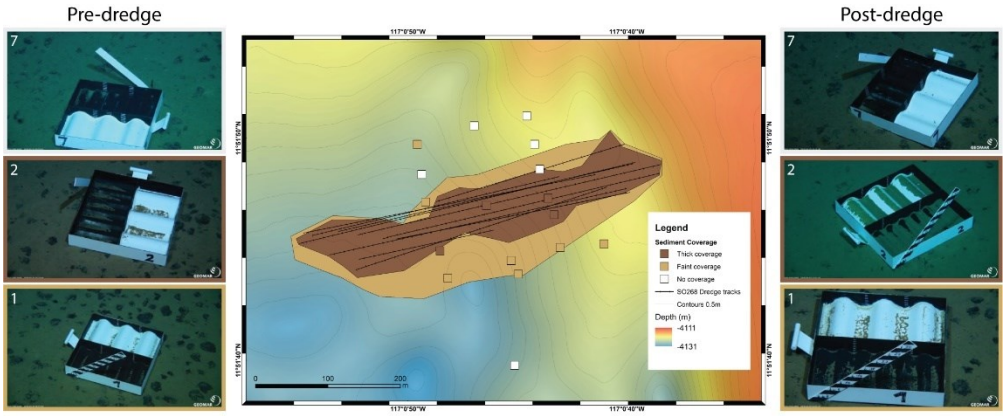

Figure 6.11: Map showing the visually assessed sediment coverage of the nodules, distinguishing "no coverage" (with/no colour), "faint coverage" (light brown) and "thick coverage" (dark brown) (Schoening et al., submitted). The isobath contour interval is 0.5 m. Pre- and post-dredge photos (left and right) of three SLIC boxes illustrate different amounts of sediment accumulation: no coverage (box 7, top), thick coverage (box 2, middle) and faint coverage (box 1, bottom). From these images it is clear that sediment has resettled in the throughs of the SLIC boxes, but especially in case of SLIC box 2, also forms a drape on the crests. These SLIC boxes, designed by GEOMAR, consist of two 25x50 cm sections of corrugated iron painted white and black, contained in a 50x50x8 cm iron frame. An oblique measuring stick was mounted on one side of each box (Photo courtesy: GEOMAR, ROV Team Kiel 6000).

6.5. Discussion

Our monitoring array has provided an unprecedented insight into the spatial and temporal dispersion of anthropogenic sediment plumes in the abyssal ocean. Compared to impact

experiments that were carried out in the past (e.g., Lavelle et al., 1982; Peukert et al., 2018; Spearman et al., 2020; Baeye et al., 2022), we placed many more sensors close to each other at well-defined locations in a large spatial array around the disturbance area. We were able to clearly detect the dispersion of the generated plume up to at least 300 m from the disturbance site. Using visual inspection, we observed sediment deposition up to 100 m away from the source. The combination of methodologies that inspect both plume sediment in suspension and plume sediment deposition is important, as both represent environmental pressures impacting the deep-sea ecosystem surrounding disturbed or mining sites (Jones et al., 2017; Washburn et al., 2019). In the following we will discuss the observed plume dispersion and sediment deposition as well as the strengths and weaknesses of our monitoring setup. We conclude with thoughts and recommendations on how to improve monitoring approaches for future larger-scale, deep-sea mining trials.

6.5.1. Sediment mobilisation and dispersion of the plume

Our data show that the plume produced by the dredge experiment initially dispersed south of the dredge tracks, as also predicted using modelled plume dispersion probability analysis undertaken for the time of the experiment (Fig. 6.3E). The sensor data show that the dredge activities of 11 hauls in total were neither recorded by the sensors as 11 discrete plume events, nor as a continuous plume of varying intensity. The irregular series of separate plume events, separated by shorter or longer intervals when turbidity dropped back to background values, suggests that plumes produced by some of the dredge hauls have merged, whereas some of the hauls may not have produced significant plumes. During the initial hours of dredging, the near-bottom current had an easterly component, due to which the initial plumes may have bypassed the southern sensor platforms. From the collected imagery, showing discontinuous dredge hauls of variable depth (Fig. 6.5), it appears that the dredge did not scrape the seafloor evenly, but rather moved in a bouncing manner, at times flying over the seafloor, and at times digging more than 10 cm deep into the seafloor. In part, this could be due to a blocking of the dredge mouth with the very sticky deep-sea sediment, preventing further pick-up of nodules and sediment. This has certainly affected the amount of sediment that went into suspension, as was also observed during a small-scale disturbance experiment by Becker et al. (2001), who found that 80% of the sediment mobilised by a propeller-generated water jet remained on the seafloor. Based specifically on the field data of our study, Purkiani et al. (2021) deduced by

numerical modelling that only approximately 4% of the sediment mobilised by the dredge was actually brought into suspension and reached the southern sensor platforms. Another 25% of the mobilised sediment was deposited at short distance from the track, leaving about 70% of the mobilised sediment in the dredge tracks as cohesive sediment that was only pushed aside. Both the optical and the acoustic sensors on the seafloor detected a sequence of plume events caused by the dredging activities. However, the patterns of recorded turbidity differ between these two sensor types, even though the sensors were placed less than half a metre apart on the same platform and measured the turbidity simultaneously (Fig. 6.7). It should be noted that initial minor increases in acoustic backscatter, marking the arrival of the plume and preceding the increase in optical backscatter, may have been disproportionately emphasised by being presented in a decibel scale. However, differences in the response of optical and acoustic sensors have been observed previously (e.g. Haalboom et al., 2021) and might be related to the differing sensitivity of optical and acoustic sensors to varying particle sizes of suspended material. We found that OBSs are most sensitive to fine-grained particles, while the acoustic sensors, depending on their operating frequency, tend towards higher sensitivity for coarser particles (Section 3.4).

Given that the median particle size in the local seafloor surface sediment is around 20 µm (Gillard et al., 2019), non-aggregated suspended sediment particles would be close to or below the wavelength limit of the Nortek Aquadopp profilers operating at 2 MHz, and even more so for the 1200 kHz and 300 kHz ADCPs. Despite this, the acoustic profilers detected clear plume signals, indicating that the plume carried sufficiently large particles to cause measurable backscatter. The sediment plume certainly contained primary sediment particles at the coarse end of the particle size spectrum but very likely also aggregated fine-grained sediment. Recent laboratory experiments by Gillard et al. (2019) have shown that under typical deep-sea flow conditions, aggregation of CCZ sediment particles occurs rapidly. Particle aggregation, producing larger-sized particles at the cost of smaller-sized particles, results in an increased intensity in the acoustic backscatter but a decrease in optical backscatter. Settling of larger particles would result in a decrease in acoustic backscatter, whilst there might be no change in optical backscatter. Aggregation occurring in the plumes as they drifted southwards may thus account for differences in intensity with which the plume was recorded by optical and acoustic sensors.

The differences in arrival times of plume events as registered by optical and acoustic sensors are, however, not explained by differences in aggregation state of the suspended particles in the plume. Fine-grained primary particles and coarser-grained aggregates are both passively transported with the currents and thus have the same horizontal velocity. Different clock times or sampling rates of the sensors can be excluded, as all sensors were programmed with the same UTC time and sampling rate and observed drift in clock times amounted to less than 50 seconds over the entire 6 weeks of the deployments. In addition, optical and acoustic sensors recorded some of the plume events almost simultaneously.

One possible explanation might be that the larger particles detected acoustically before the sediment plume was detected optically represent nektobenthos like amphipods, swarming ahead of the advancing sediment plume, but we do not know of any visual observations reported in the literature that might confirm this hypothesis. Alternatively, the acoustic sensors could have recorded a rain of sediment lumps falling out of the sediment-laden dredge as it was lifted from the seafloor at the end of each haul. Video imagery revealed many lumps of cohesive sediment scattered closely around the dredge tracks (Fig. 6.5), but smaller parts may have been carried further away by the currents. Released at several tens of metres above the seafloor, where current speed is higher than at the seafloor, small bits of cohesive sediment raining out from the dredge may have reached the sensor platforms earlier than the plume moving southwards close to the seafloor. In this light, the peculiar reflection noted in the backscatter profile recorded by the 300 kHz ADCP on GMR_PFM-10 shortly after 18:00 UTC might also be explained in this way. In the acoustic backscatter profile recorded by the 2 MHz Aquadopp profilers at NIOZ_PFM-07, located at 135 m from GMR_PFM-10 but 50 m closer to the dredge tracks, a relatively intense vertical reflection was also observed just before 18:00 UTC.

While the hypotheses above try to explain what may be merely a side-effect of our dredge experiment, they highlight an important advantage of using acoustic profilers over optical sensors for recording turbidity. While optical sensors produce point measurements of turbidity, the acoustic sensors allow monitoring turbidity over a distance of metres to tens of metres away from the sensor head. Upward-looking acoustic profilers detect the vertical extent of the plumes. With a caveat that some of the backscatter signals may in fact represent

showers of sediment falling out of the dredge, we postulate that the sediment plumes 300 m south of the dredge tracks extended 2-6 m above the seafloor (Fig. 6.8). This is higher than the 0.96 to 1.6 m inferred by Peukert et al. (2018) for a plume produced with an epibenthic sledge (EBS) in the same study area, or the 1.5 to 2 m height of an EBS plume reported by Greinert (2015) in the Peru Basin. But these previous estimates were based on observations made at short distances of maximum 50 m from the plume source, where the plume had little time to extend vertically into the water column by turbulent mixing, while our monitoring setup spread over a distance of 300 m.

Our time series of turbidity extend until 13th May, covering a period of one month after the dredging was performed (Fig. 6.9). Data from this period do not show any signals of enhanced turbidity which cannot be explained by nearby ROV operations or bottom sampling gear. We have not recorded additional signals of plume dispersion even when the near-bottom current turned to a northerly direction in the day following dredging. We assume that the plume had already largely settled out at this stage and had been diluted with ambient water and was no longer detectable by the sensors, or that tails of the plumes may have bypassed the area where our sensors were positioned. By exponential extrapolation of the decrease in observed peak SPM mass concentrations with increasing distance from the dredge tracks, we estimate that the plume concentration dropped below the detection limit of our sensors within a distance of one kilometre from the source. With an average current speed of 4 cm s^{-1} this corresponds to a transit time of less than 7 hours.

From the lack of any natural increase in turbidity in the weeks after the dredging, and the lack of a notable increase in near-bed current velocity, it can be inferred that the mesoscale eddy which was observed passing over our study area either had not reached the seafloor within the time interval that our sensors were deployed, or that it did not affect the deep water column and seafloor. Observed near-bottom current speeds in the CCZ generally do not exceed the critical threshold of 15 cm s^{-1} required for resuspension of unconsolidated sediment from the seafloor (Thomsen and Gust, 2000). During the passage of strong eddies, current speeds near the bottom have been observed to increase significantly (up to 24 cm s^{-1}; Aleynik et al., 2017). This would be high enough to resuspend freshly deposited plume sediment and spread it out over a larger area than where it had initially settled. The eddy that

passed the study area after our experiment was only of moderate size. The centre of the eddy at the sea surface passed the area at the beginning of May (Purkiani et al., 2022). According to Purkiani et al. (2020), the effect of the eddy at the seafloor in ~4 km depth would be expected 2 to 4 weeks later, which in our case would mean a date when our sensors had already been recovered from the seafloor. Even so, a model simulation by Purkiani et al. (2022), shows that the effect of this specific eddy most likely only reached down to 1500 m water depth.

6.5.2. Visual observations of plume sediment deposition

In agreement with the pattern of decreasing turbidity with distance from the dredge tracks, the photos of SLIC boxes and the OFOS and ROV imagery indicate a successive decrease in thickness of sediment deposition away from the dredge tracks, reflecting successive sediment resettlement. Although not quantitative, this proved helpful to illustrate the likely spatial distribution of visible sediment deposition on the seafloor (Fig. 6.11), which is complementary to the information on the dispersion of the sediment plume as derived from sensor records. However, while the sensors recorded plume dispersion at least to a distance of 300 m to the south of the dredge tracks, seafloor imagery only tracked sediment deposition to 100 m from the source. Deposition became too thin to be observed visually beyond that.

Our results indicate that low-tech tools to measure sediment deposition, such as SLIC boxes, could be useful to assess the thickness of sediment blanketing after mining activities, when combined with large-scale seafloor imaging activities. However, these tools can only map and quantify strong sediment deposition of ca. 1 mm and more. Therefore, with the small amount of mobilised sediment in our study, these SLIC boxes could only be used for a qualitative assessment of sediment resettlement. Furthermore, the resettled sediment did not only fill the troughs of the corrugated iron bottom plate of the SLIC boxes, but also settled on the crests, which additionally impedes quantitative assessment of deposited sediment thickness. Optimally, imaging of SLIC boxes could be combined with efficient AUV image mapping surveys, enabling the reconstruction of seafloor mosaics at square-kilometre-scale. Such mosaics allow the establishment of a complete, yet qualitative, picture of sediment deposition. In contrast, ROV and OFOS imaging surveys are ineffective due to their low cruising speed. As

a towed system, OFOS additionally suffers from reduced navigation control, potentially missing the targeted SLIC box locations.

6.5.3. Quantification of the suspended material load

For the dispersion of mobilised sediment in suspension, it is important that at any given location the variability in mass concentration through time can be properly quantified from the different acoustic and optical turbidity measurements. In order to obtain estimates of SPM mass concentration we (inter)calibrated the sensors (Section 3.3) that had differing measurement ranges (0-25 NTU, 0-125 NTU, 0-500 NTU, 0-1000 FTU) using a seven-step approach from 0 mg L^{-1} to 1640 mg L^{-1} providing a sufficient range for the broad-range JFE Advantech and Seapoint sensors. The results showed a very convincing linear relationship between SPM mass concentrations and corresponding turbidity recorded by these optical sensors (Fig. 6.4A). However, only the 4 lowest calibration steps were in the measuring range of the most sensitive sensors, such as the WetLabs FLNTU sensors mounted on the BoBo lander and the Seapoint OBSs on the RBINS platforms (Table 6.2), whilst all higher steps were beyond their saturation level. In general, it is challenging to perform calibration at very low SPM mass concentrations in a multipurpose lab onboard a research vessel, as small amounts of dirt contaminating the water compromised the measurement in the low turbidity range. As a result, the SPM mass concentrations measured by filtration of the water of the lowest calibration level was 5.4 mg L^{-1}, which is significantly higher than the 0.017 mg L^{-1} ± 0.006 mg L^{-1} measured by filtration of Niskin samples of the local near-bottom water. Even though the regression lines were forced through zero, inaccuracies still produced a lowermost SPM mass concentration as inferred from the OBSs of 0.1 mg L^{-1}.

Better calibration results might have been obtained by mounting turbidity sensors on the CTD and lowering these into water masses of different turbidity and SPM mass concentration, whilst simultaneously taking water samples for filtering and later lab analyses. As shown by Haalboom et al. (2021), this approach produced good results in the Whittard submarine canyon, where widely differing turbidity levels have been encountered over an extent of hundreds of metres in the vertical water column. In our study, turbidity levels were extremely low from the base of the permanent thermocline at 1 km down to the seafloor at more than 4 km water depth. Unfortunately, it was not possible to lower the CTD into the plume

generated by the dredge, mainly because the plume had already drifted away before the dredge was brought back on board and the CTD could be lowered to the seafloor (ca. 4 h). Furthermore, taking water samples very close to the seafloor in more than 4 km depth with a conventional CTD lowered by a winch is practically very difficult without touching the seafloor and stirring up additional sediment from the seafloor. Even with good real-time depth and altimeter readings from the CTD and heave compensated winch, standard practice is to lower the CTD not closer than 5 m above the seafloor. Therefore, the ex-situ calibration as performed in this study is a good method for the calibration of the optical backscatter sensors but can still be improved in the future. We infer that more calibration steps are needed, and that the calibration exercise should ideally be performed in a clean room to prevent contamination, especially in the low turbidity range. It needs to be ensured that surface sediment from the same location is used, as physical properties of the suspended material will influence the recorded turbidity signal (Guillén et al., 2000). A drawback is that physical characteristics of sampled surface sediment will be slightly different from the suspended sediment, as coarser-grained particles settle out rapidly. Moreover, inhomogeneity of the suspension in the calibration container might also have introduced a larger variability in the determined SPM mass concentration, especially as only small sample sizes were taken (36.12 ± 0.57 mL). Using a larger sample volume size could reduce this variability.

Whereas establishment of a regression function for OBS turbidity records was straightforward, the quantification of the acoustic backscatter signal proved to be difficult. In a study on SPM dynamics in the Whittard Canyon, Haalboom et al. (2021) found a clear correlation between optical backscatter recorded with WetLabs FLNTU and JFE Advantech OBSs and the acoustic backscatter recorded by a Nortek Aquadopp 1 MHz current profiler. After converting the optical backscatter signal to SPM mass concentration, the acoustic backscatter signal could be correlated via a logarithmic function. Such an approach does not appear to be appropriate in the case of our dredge plume experiment, due to the widely differing responses of the optical and acoustic sensors (Fig. 6.7). This lack of correlation is likely related to the same unknown effect that caused the acoustic sensors to record a signal one hour prior to the OBS sensors (Section 5.1). Thus, it was not possible to convert the acoustic backscatter to SPM mass concentration, although this signal did prove very useful in determining the plume height. For monitoring purposes of mining plumes, it remains important to quantify SPM mass

concentration within the water column, highlighting the need for calibration of acoustic sensors and/or setting up vertical lines of multiple optical sensors e.g., using a mooring approach.

6.5.4. Recommendation for future mining-related plume monitoring

The sensors and setup approaches used worked well in our small-scale dredge experiment and provided insight in the dispersion of a relatively small and short-lived suspended sediment plume in an abyssal setting. The collected data formed the basis for validating and calibrating a numerical model that provides a more comprehensive insight into the dispersion of the suspended sediment in the plume and its subsequent deposition (Purkiani et al., 2021). In this last section of the discussion, we evaluate the monitoring setup and provide recommendations for the monitoring of future, larger-scale disturbance experiments and potential mining activities. When doing so, it should be borne in mind that the ~0.03 km^2 of seafloor in which we deployed our dredge is only a fraction of the area of seafloor expected to be directly impacted by mining tests and full-scale mining, not counting the surrounding areas under influence of sediment plumes. The DEME-GSR trials of the *Patania II* pre-prototype nodule collector conducted in spring 2021 were directly impacting a seafloor area of max 0.1 km^2 in the German and Belgian contract areas in the CCZ (GSR, 2018; BGR Bundanstalt für Geowissenschaften und Rohstoffe, 2018), while future full-scale mining is expected to impact several hundreds of km^2 of ocean seafloor per mining operation per year (Smith et al., 2008; Weaver et al., 2022). In addition to the much larger spatial scale of future mining operations, the amount of sediment mobilised and dispersed by industrial nodule collectors will also be much larger than by our dredge. Whereas the thickness of the sediment layer mobilised by the dredge and by industrial collectors may be comparable, the different width and operational speed of the dredge (1 m, 0.2 m s^{-1}) compared to industrial mining equipment (*Patania II* pre-prototype nodule collector vehicle; 4 m, 0.5 m s^{-1}; full-scale nodule collector vehicle 16 m, 0.5 m s^{-1}; GSR, 2018) will result in a 10-40 times larger sediment mobilisation. While we observed that the dredge tended to push much of the sediment in its path aside as a cohesive mass rather than dispersing it in the water, the hydraulic nodule collector systems currently developed for industrial mining will mix the sediment taken up with the nodules with water and discharge it as a thoroughly dispersed suspension. This will result in much higher SPM mass concentrations within the initial sediment plume as compared

to the dredge plume. Unless solutions are found for effectively retaining the spreading of sediment plumes, industrial mining plumes will disperse orders of magnitude more sediment over much larger distances than observed in our dredge experiment.

6.5.4.1. Sensor array layout

6.5.4.1.1. Static sensor layout

We found that a realistic and integrated modelling effort on plume dispersion, including a module for sediment transport and aggregation as described by Purkiani et al. (2021) and illustrated in Fig. 6.3, is a prerequisite to determine the most effective sensor layout. Based on probability maps for plume dispersion and deposition, sensors can be distributed along the main axes or gradients of plume transport and SPM mass concentration. However, we also recommend deploying sensors in the less probable direction of plume transport, as current directions are highly variable especially on short time scale (e.g., Aleynik et al., 2017; Fig. 6.9 of this study). Furthermore, such sensors are required to register and ensure that no sediments dispersed in those directions.

6.5.4.1.2. Dynamic sensor layout

During future larger-scale impact experiments or mining activities, sensor deployments will require more flexibility as compared to the static sensor array used in our study. Here, a minimum distance of 100 m from the dredge tracks was deemed relatively safe for the deployment of the sensor platforms. In a larger-scale (test) mining operation, however, the distance at which fixed sensor platforms can be considered safe at all times may be hundreds of metres or even one or more kilometres from the disturbance site. Despite the larger size of the plume, much of its suspended load will already have settled before the plume reaches the first sensor platforms, and thus important information on how the plume develops from the near field to the far field will be lost. Therefore, in scenarios for future monitoring of deep-sea extractive activities (e.g., Aguzzi et al., 2019), AUVs with integrated turbidity sensors are envisioned as a suitable tool for dynamic monitoring of the seafloor and sediment plumes. Since AUVs do not produce a synoptic image of plume dispersion but will create short-term single spot measurements, it is recommendable to combine AUV plume mapping with the deployment of fixed sensors that produce continuous timeseries of current speed and direction as well as turbidity close to the seafloor.

Multibeam systems mounted on AUVs could also help to monitor the dispersion of sediment plumes over larger spatial scales. Generally, multibeam systems are used to map the bathymetry or roughness of the seafloor (e.g., Lurton, 2002), but water column reflection may also be used for the detection of suspended material (e.g., Best et al., 2010; Simmons et al., 2010; Fromant et al., 2021). During the SO268 expedition, a small experiment was carried out in which a multibeam system was mounted on the ROV, together with an OBS. The ROV thrusters were used to stir up sediment from the seafloor, which served as a target for the multibeam systems (Fig. S6.8). Although the principle of the approach could be proved, ship time constraints did not allow for optimisation of the method.

6.5.4.2. Types of monitoring tools

6.5.4.2.1. Visual monitoring

Seafloor imagery obtained by both ROV and OFOS deployments proved to be useful to visualise plume-related sediment deposition on the seafloor. The SLIC boxes provided qualitative information on the amount of settled sediment, and we infer that they may be especially efficient to assess the amount of sediment deposition associated with larger-scale (mining) activities. Moreover, time-lapse cameras may prove to be useful in the case that a gravity flow forms (dependent on sediment concentration and topography), or if the plume stays below the lowermost mounted sensors, to complement to the overall picture of the plume dispersion. Furthermore, the usage of AUVs for visual monitoring is recommended, as larger distances can be covered more easily.

6.5.4.2.2. Sensor-based monitoring

Optical backscatter sensors are a good choice for monitoring of the SPM mass concentration, as the recorded signal of these sensors is more easily quantified. Moreover, as demonstrated, upward-looking acoustic profilers provided useful information on plume height and turbidity gradients. The choice of the type of acoustic profilers is not trivial, however, as the acoustic frequency at which the sensor operates determines its sensitivity for a certain range in particle sizes. Ideally, acoustic profilers operating at different frequencies should be combined: high frequency for profiling of dispersed fine-grained suspended sediment and low frequency for profiling of the larger (aggregated) particles, as well as plankton and nekton. Alternatively, a multifrequency acoustic sensor could be used for this purpose. To corroborate the particle-

size dependency of optical and acoustic backscatter sensors, in situ particle sizers such as LISST (Laser In Situ Scattering and Transmissometry) and particle cameras could probably be helpful (e.g., Sternberg et al., 1996; Mikkelsen et al., 2005; Roberts et al., 2018). Furthermore, the blanking distance of the acoustic signal received from close to the sensor head should be taken into account. When upwardly mounted at the seafloor, low frequency profilers, such as the 300 kHz ADCP used in our study, will always miss the lowermost metres above the seafloor where SPM mass concentration of the plume is highest. Alternatively, the profilers could be mounted to look down at several metres height above the seafloor. However, in this configuration interference of the acoustic beams with the seafloor could potentially lead to invalid data in the lowermost bins.

6.5.4.3. Calibration of the recorded backscatter signal

For all types of turbidity sensors used, both optical and acoustic, calibration to the specific type of suspended material relevant for the experiment or mining site is necessary to convert relative units of optical and acoustic backscatter to absolute SPM mass concentration. Ideally, sensors should be mounted on a CTD-Rosette and lowered into plume waters of different SPM mass concentration. However, this might prove to be difficult, due to uncertainties related to the location of the mining plume or the low height of the plume above the seafloor. Onboard calibration in suspensions made of local surface sediment and bottom water are a suitable alternative, at least for optical sensors that can be immersed in a relatively small volume of suspension. However, the particle size distribution in the suspension may not be completely comparable to that of the in situ sediment plume produced at the seafloor, thereby affecting the amount of optical backscatter. If the local surface sediment contains a significant fraction of coarse silt and sand, the coarse fraction will settle out rapidly leaving only the finer fraction in suspension, whereas in the calibration container vigorous stirring will keep the coarser fraction in suspension. Furthermore, in the plume at the seafloor, the suspended sediment will rapidly aggregate, whereas this is prevented during the lab calibration.

Acoustic sensors, which in practice cannot be calibrated in the lab, may be calibrated by reference to simultaneously recorded optical backscatter converted to SPM mass concentration. However, the relationship between optical backscatter and SPM mass concentration is probably not as constant as is often assumed, as optical backscatter is also

dependent on suspended particle size distribution (e.g., Downing, 2006). Whereas this approach worked well in other settings (Haalboom et al., 2021), we suspect that the presence of non-plume sediment particles shed from the dredge interfered with plume-related signals in our present study. In view of the advantages that acoustic profilers can potentially offer for plume monitoring, further efforts towards a proper calibration of these sensors are certainly needed.

6.6. Conclusion

A small-scale dredge experiment was carried out in the German contract area for polymetallic nodule exploration in the CCZ in April 2019 to test a setup strategy for the monitoring of sediment plumes produced by deep-sea mining machinery. The monitoring strategy included the placement of an array of turbidity sensors and current meters on the seafloor at different distances and in different directions from the plume source, in combination with seafloor photo and video surveying. The collected data provided valuable insights into the dispersion of the plume of sediment mobilised by the dredge by bottom currents and subsequent deposition on the seafloor. Our findings in brief:

- Against the close-to-zero natural background turbidity in the dredge area, the plume of suspended sediment produced a distinct signal in recorded optical and acoustic backscatter, which was likely detectable to greater distances from the source than the 300 m at which our most distal sensors were placed. However, redeposited sediment could be discerned visually from seafloor imagery to no more than 100 m from the source.
- Calibration of optical backscatter sensors on board the research vessel, using suspensions made with local seafloor sediment and bottom water, allowed conversion of recorded optical backscatter measurements into absolute mass concentration of suspended sediment. It should be noted, however, that aggregation of fine-grained suspended sediment into larger aggregates may result in a reduction of optical backscatter.
- Acoustic backscatter recorded with upward-looking current profilers gave insight into the vertical extent of the dredge plume above the seafloor. In comparison to optical sensors, current profilers have the distinct advantage that they produce profiles of

backscatter (suspended matter) over a range of metres in the case of high-frequency profilers, to potentially hundreds of metres in the case of low-frequency profilers. However, there a noticeable differences in the detection and sensitivity of acoustic and optical backscatter sensors to different sizes of suspended particles.

- Acoustic backscatter sensors cannot be easily calibrated to obtain SPM mass concentration due to the long range of the emitted acoustic signal. High-frequency acoustic profilers, which have a particle-size sensitivity overlapping that of optical backscatter sensors, may be calibrated indirectly by reference to optical backscatter recorded simultaneously in an overlapping spatial range. In our dredge plume experiment, however, this indirect calibration did not produce satisfying results, likely due to interference by larger sediment particles produced unintentionally during the dredging process.
- In situ particle sizers and/or particle cameras need to be deployed simultaneously with optical and acoustic sensors to further establish the particle-size dependency of optical and acoustic backscatter.
- The optical and acoustic sensors used in our small-scale dredge experiment proved suitable for plume monitoring, but upscaling of the monitoring array will be necessary to encompass the much larger area affected by test- or full-scale mining. A more dynamic deployment of sensors would be preferable, for example on platforms that can be placed forward or retracted backward dependent on the retreat or advance of the frontline of active mining. In addition, AUVs appear well-suited for such dynamic plume monitoring, especially when equipped with acoustic profilers capable of recording vertical profiles of turbidity.

Data availability

CTD data gathered during cruise SO268 is available in PANGAEA under DOI: 10.1594/PANGAEA.944351, and the additional CTD turbidity data recorded by the JFE OBSs is available in PANGAEA under DOI: 10.1594/PANGAEA.943313. Filter weights for SPM sampling, gathered during the CTD casts are available in PANGAEA under DOI: 10.1594/PANGAEA.942058. Data recorded by the optical and acoustic sensors on the sensor platforms and landers are available in PANGAEA under DOI's: 10.1594/PANGAEA.943396, 10.1594/PANGAEA.943402 (NIOZ sensors), 10.1594/PANGAEA.943331 (GEOMAR sensors),

and 10.1594/PANGAEA.942065 (RBINS sensors). Ocean current data to force the numerical model can be obtained online from HYCOM data server at http://www.hycom.org/dataserver. The data on the onboard calibration of the OBSs is available upon request.

Author contributions

SH contributed to the design of the field experiment and conducted the field experiment, analysed, and interpreted the data and wrote the first draft of the manuscript. TS, PU, I-ZG, HS, KP, LT, MHa, AV, and JG contributed to the design of the field experiment, with KP conducting the long-term numerical simulation for the determination of the sensor layout and TS, PU, I-ZG, HS, and MHa conducted the field experiment during cruise SO268. MHa planned and coordinated the SO268 field work. TS, PU, I-ZG, HS, BG, KP, MB, MHo, G-JR, LT, AV, and JG contributed to the data analysis and interpretation. All authors contributed to manuscript revision, read, and approved the submitted version.

Funding

This research was carried out in the framework of the European collaborative project MiningImpact and received funding through the Joint Programming Initiative Healthy and Productive Seas and Oceans (JPI Oceans): German Ministry of Research grant no. 03F0812A-H; Dutch Research Council grant no. 856.18.002. SH received funding from the Blue Nodules project (EC grant agreement no. 688785). Additional funds for representing the data within the 4D Digital Earth Viewer came through the Helmholtz Project "Digital Earth" grant ZT-0025.

Acknowledgments

We gratefully acknowledge the support of the captain and crew of RV Sonne for their essential assistance during cruise SO268. We thank the GEOMAR ROV KIEL 6000 team for the endless ROV dives, without which we would not have been able to deploy our gear and obtain images of the SLIC boxes. We also thank Yasemin Bodur and the OFOS team, as the images they acquired greatly contributed to tracing back the dredge tracks, as well as mapping the sediment coverage. We thank reviewers Xavier Durrieu De Madron and Jeroen Ingels for their constructive feedback, which helped to improve the manuscript.

Supplementary material

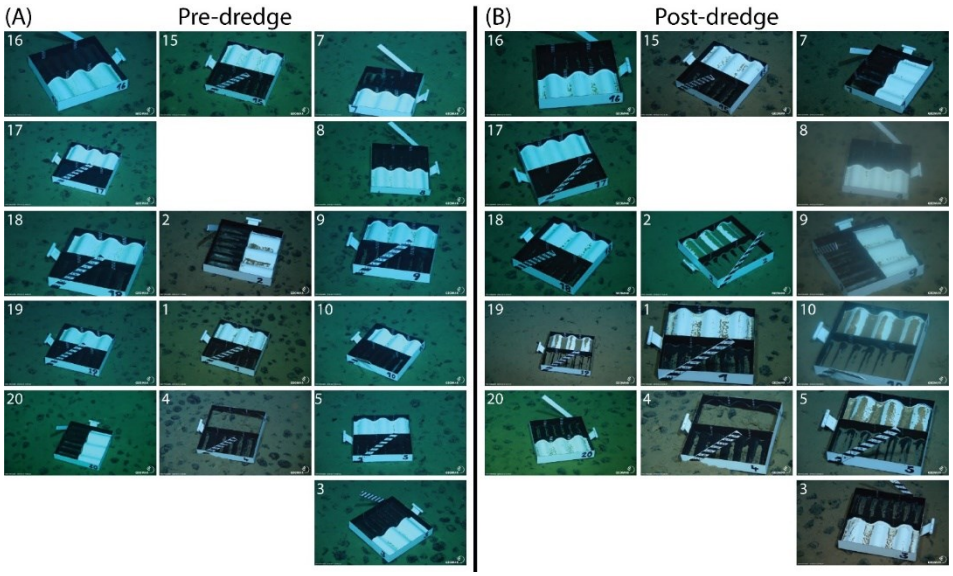

Figure S6.1: (A) Pre-dredge photos of the SLIC boxes. (B) Post-dredge photos of the SLIC boxes. Please note that SLIC box 04 lost its white bottom part, therefore showing the underlying seafloor Numbers on the top left of the photos show the number of the individual SLIC box. Photo courtesy: GEOMAR, ROV Team Kiel 6000.

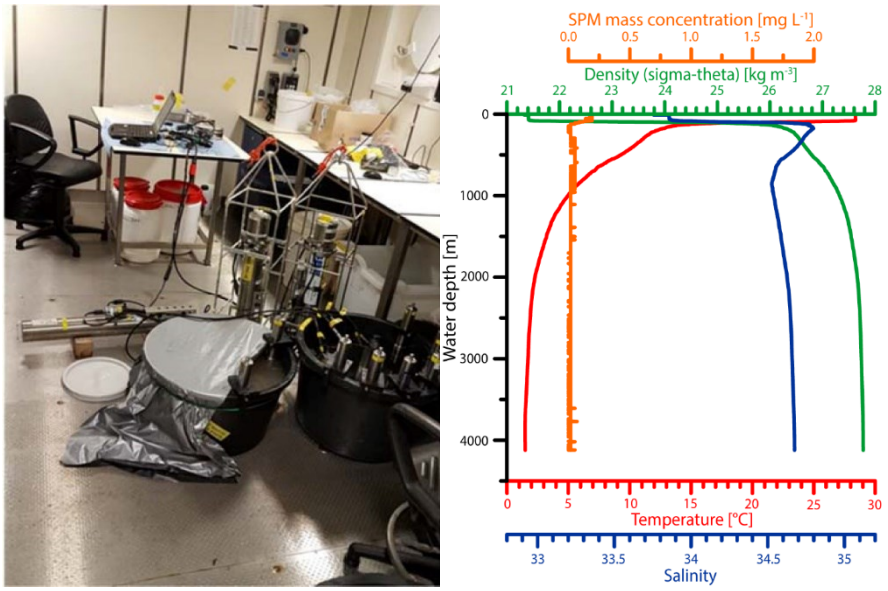

Figure S6.2 (left): Onboard calibration setup in the cold lab. Calibration of the OBSs were carried out with lights dimmed (photo courtesy: Henko de Stigter). Figure S6.3 (right): Water column profiles of temperature (red), salinity (blue), density (green) and SPM mass concentration as inferred from the JFE Advantech OBS (orange) obtained with the CTD in the dredge experiment area (SO268/2-ST208-CTD17).

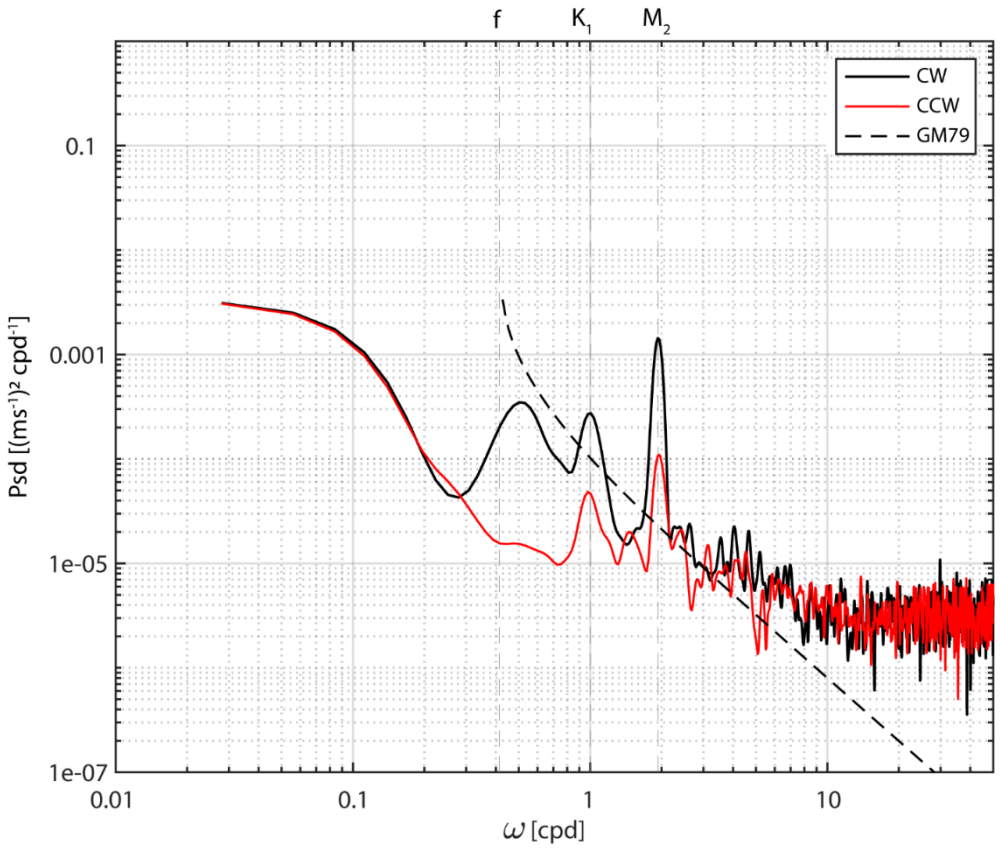

Figure S6.4: Power spectral density (PSD) inferred from the current velocities of bin 3 of the Nortek Aquadopp profilers on NIOZ_PFM-02 from the 9th of April until the 14th of May 2019. The spectra are calculated from each 5-min segment in order to show the most prominent frequency. The current velocity is considered as a complex rotary velocity vector (u+iy) (e.g. Alfrod et al., 2012). The energy spectrums of other sensors at different stations show very similar patterns). The clockwise (CW) and counterclockwise (CCW) rotations relating to negative and positive frequencies are shown by the black and red lines.

Motions at near inertial frequencies are strongly polarized, with clockwise energy around two orders of magnitude larger than counterclockwise energy. Similar differences have been observed in the northern hemisphere in previous studies (Alfrod, 2003). The magnitude of the counterclockwise motion is in good agreement with the Garret and Munk (1972) predictions, expect for the high frequency motions, which are most likely attributable to noise in the measurements.

The relatively short time series of data did not allow lower frequency motions to be resolved. The high-frequency motion is dominated by different semidiurnal and diurnal tidal harmonic components M2 and K1. Note that the dominant high-frequency signals are evident in both clockwise and counterclockwise rotations, while the near-inertial oscillation is only depicted in the clockwise rotations. Inertial motion f is well below other dominant frequencies and therefore can be clearly seen. Although an individual peak does not occur at inertial frequency, a wide near-inertial peak results in a remarkable energy content in the data.

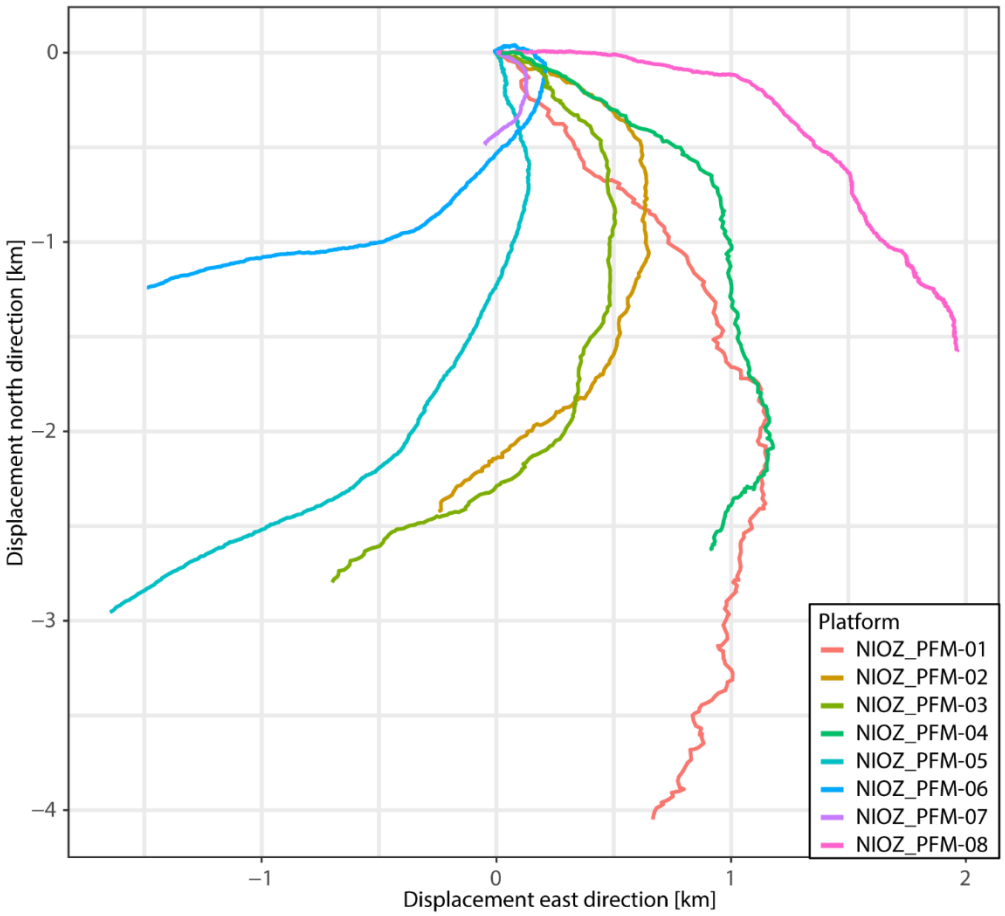

Figure S6.5: Progressive vector diagrams of cumulative water displacement at different sensor platforms between the 11th of April 06:30 UTC and 12th of April 00:00 UTC. The current at SO268/2-NIOZ_PFM-01 was measured at 0.7 mab, at all other NIOZ platforms at 1.25 mab.

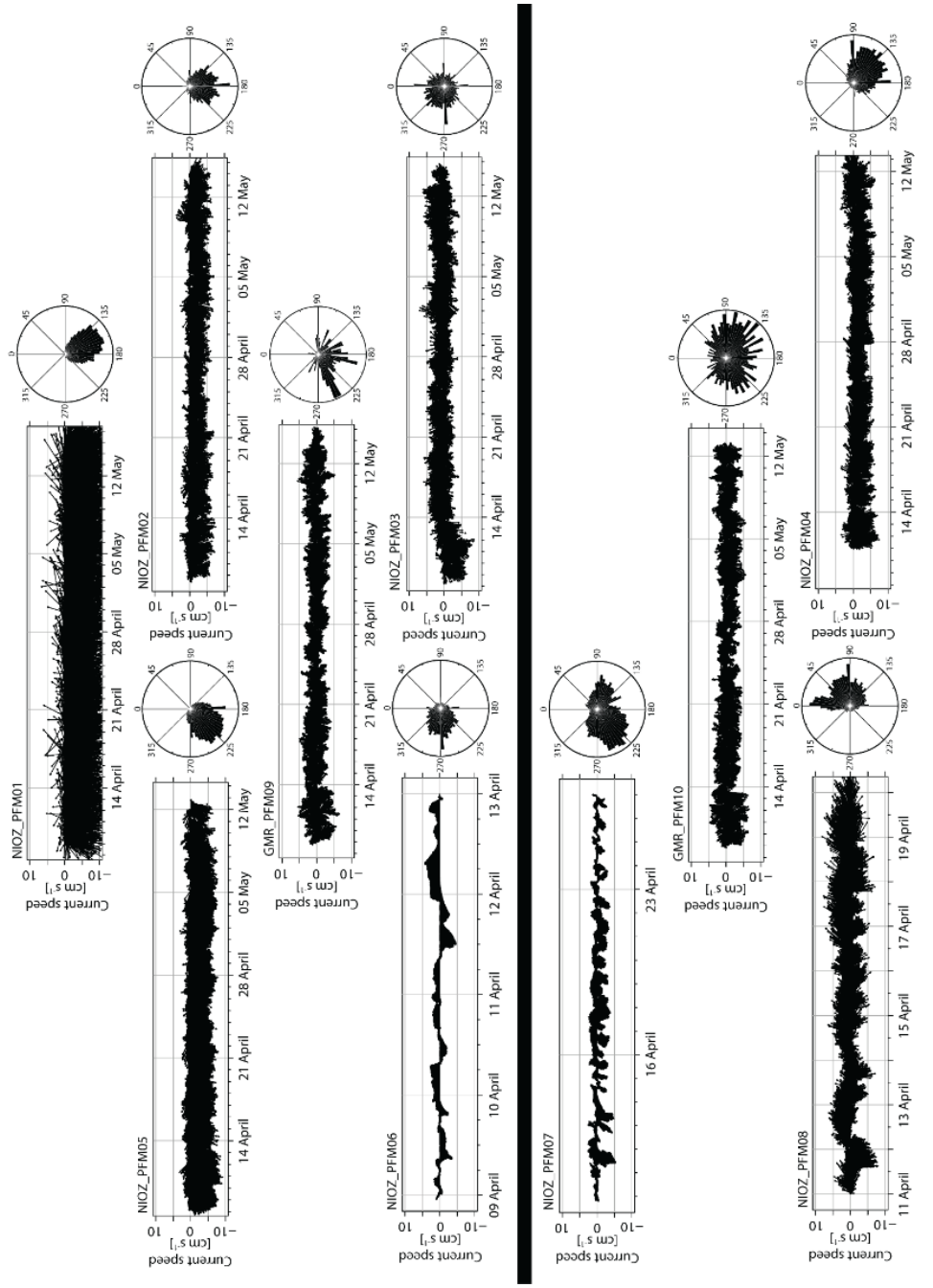

Figure S6.6: Feather plots and rose diagrams of current speed and directions as recorded by the Nortek Aquadopp profilers (bin 1 at 1.25 mab, NIOZ_PFM-02 and -08) and RDI workhorse ADCPs (bin 7 at 19 mab, GMR_PFM-09 and -10, bin 3, 0.7 mab, NIOZ_PFM-01) for the entire duration of the deployments. Note that time scales are different, with platforms NIOZ_PFM-06, NIOZ_PFM-07 and NIOZ_PFM-08 having a shorter time span. The arrangement of the time series graphs corresponds with the geographical arrangement of the sensor platforms north and south of the dredge tracks (black line through the centre).

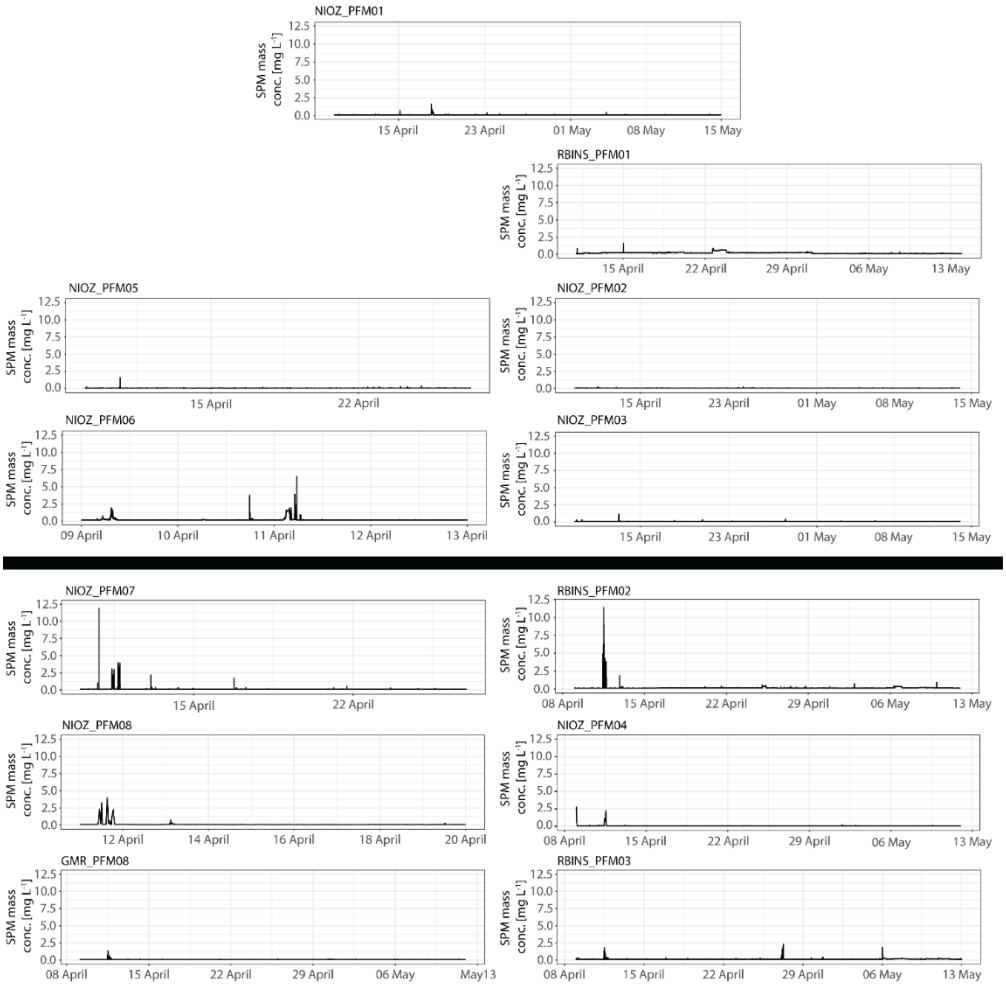

Figure S6.7: Time series of SPM mass concentration as recorded by the OBSs for the entire duration of the deployment. Note that time scales are different, with platforms NIOZ_PFM-05, NIOZ_PFM-06, NIOZ_PFM-07 and NIOZ_PFM-08 represent a shorter time span. The arrangement of the time series graphs corresponds with the geographical arrangement of the sensor platforms north and south of the dredge tracks (black line through the centre).

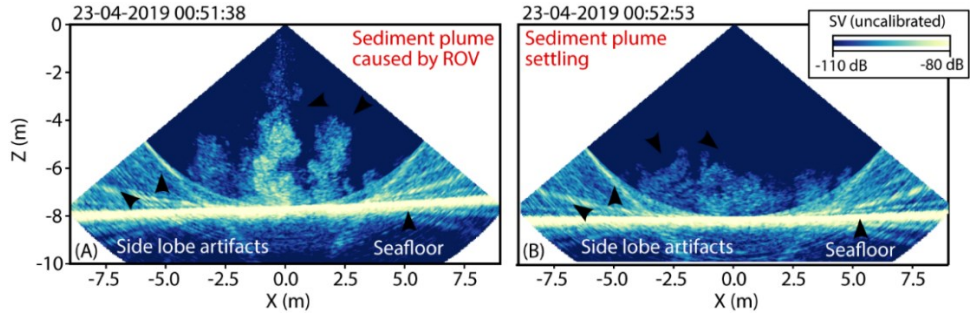

Figure S6.8: Multibeam images of the lower metres of water column and underlying seafloor showing a sediment plume generated by the thrusters of the ROV. (A) Sediment plume extending up to 6 mab. (B) Settling of the generated sediment plume 1 minute later.

References

Agogue, H., Lamy, D., Neal, P. R., Sogin, M. L., and Herndl, G. J., 2011. Water mass-specificity of bacterial communities in the North Atlantic revealed by massively parallel sequencing, Mol. Ecol., 20, 258–274. https://doi.org/10.1111/j.1365-294X.2010.04932.x.

Agrawal, Y.C., Pottsmith, H.C., 2000. Instruments for particle size and settling velocity observations in sediment transport. Mar. Geol. 168, 89–114. https://doi.org/10.1016/S0025-3227(00)00044-X.

Aguzzi, J., Chatzievangelou, D., Marini, S., Fanelli, E., Danovaro, R., Flögel, S., et al., 2019. New High-Tech Interactive and Flexible Networks for the Future Monitoring of Deep-Sea Ecosystems. Environ. Sci. Technol. 53, 6616–6631. https://doi.org/10.1021/acs.est.9b00409.

Ainslie, M. A., and McColm, J. G., 1998. A Simplified Formula for Viscous and Chemical Absorption in Sea Water. J. Acoust. Soc. America 103 (3), 1671–1672. https://doi.org/10.1121/1.421258.

Aleynik, D., Inall, M. E., Dale, A., and Vink, A., 2017. Impact of Remotely Generated Eddies on Plume Dispersion at Abyssal Mining Sites in the Pacific. Sci. Rep. 7 (1), 16959. https://doi.org/10.1038/s41598-017-16912-2.

Alimba, C.G., Faggio, C., 2019. Microplastic in the marine environment: Current trends in environmental pollution and mechanisms of toxicological profile. Environmental toxicology and pharmacology, v. 68, 61-74. https://doi.org/10.1016/j.etap.2019.03.001.

Allison, E.H., and Bassett, H.R., 2015. Climate change in the oceans: Human impacts and responses. Science 350, 778-782. https://doi.org/10.1126/science.aac8721.

Amaro, T., de Stigter, H., Lavaleye, M., Duineveld, G., 2015. Organic matter enrichment in the Whittard Channel; its origin and possible effects on benthic megafauna. Deep-Sea Res. Part I – Oceanogr. Res. Papers 102, 90–100. https://doi.org/10.1016/j.dsr.2015.04.014.

Image: Lighthouse at Point Atkinson Battery in West-Vancouver with the North Shore mountains in the back, as seen while approaching Vancouver at the end of RV *Sonne* cruise SO268, May 2019.

Amaro, T., Huvenne, V.A.I., Allcock, A.L., Aslam, T., Davies, J.S., Danovaro, R., DeStigter, H.C., Duineveld, G.C.A., Gambi, C., Gooday, A.J., Gunton, L.M., Hall, R., Howell, K.L., Ingels, J., Kiriakoulakis, K., Kershaw, C.E., Lavaleye, M.S.S., Robert, K.,Stewart, H., Van Rooij, D., White, M., Wilson, A.M., 2016. The Whittard Canyon – a case study of submarine canyon processes. Prog. Oceanogr. 146, 38–57. https://doi.org/10.1016/j.pocean.2016.06.003.

Amin, M., Huthnance, J.M., 1999. The pattern of cross-slope depositional fluxes. Deep- Sea Res. Part I-Oceanogr. Res. Papers 46 (9), 1565–1591. https://doi.org/10.1016/S0967-0637(99)00020-5.

Anantharaman, K., Breier, J. A., and Dick, G. J., 2016. Metagenomic resolution of microbial functions in deep-sea hydrothermal plumes across the Eastern Lau Spreading Center, Isme J., 10, 225–239. https://doi.org/10.1038/ismej.2015.81.

Article 145 UNCLOS.
https://www.un.org/depts/los/convention_agreements/texts/unclos/unclos_e.pdf.

Aslam, T., Hall R.A., Dye, S.R., 2018. Internal tides in a dendritic submarine canyon. Progress in Oceanography 169, 20–23. https://doi.org/10.1016/j.pocean.2017.10.005.

Bárcenas, P., 2011. Spatial variability of surficial sediment on the northern shelf of the Alboran Sea: the effects of hydrodynamic forcing and supply of sediment by rivers. J. Iber. Geol. 37 (2), 195–214. https://doi.org/10.5209/revJIGE.2011.v37.n2.8.

Baeye, M., Fettweis, M., 2015. In situ observations of suspended particulate matter plumes at an offshore wind farm, southern North Sea. Geo-Mar. Lett. 35 (4), 247–255. https://doi.org/10.1007/s00367-015-0404-8.

Baeye, M., Purkiani, K., de Stigter, H. C., Gillard, B., Fettweis, M., and Greinert, J., 2022. Tidally Driven Dispersion of a Deep-Sea Sediment Plume Originating From Seafloor Disturbance in the DISCOL Area (SE Pacific Ocean). Geosciences 12, 8. https://doi.org/10.3390/geosciences12010008.

Baker, E.T., Lavelle, J.W., 1984. The effect of particle size on the light attenuation coefficient of natural suspensions. J. Geophys. Res. 89 (C5). https://doi.org/10.1029/JC089iC05p08197.

Baker, E., Beaudoin, Y., 2013. Deep-sea minerals. Cobalt-rich ferromanganese crusts. A physical, biological, environmental and technical review.

Baraza, J., Ercilla, G., Lee, H.J., 1992. Geotechnical properties and preliminary assessment of sediment stability on the continental slope of the northwestern Alboran Sea. Geo-Mar. Lett. 12, 150–156. https://doi.org/10.1007/BF02084926.

Barnett, B. G., and Suzuki, T., 1997. The use of kriging to estimate resedimentation in the JET experiment. In: Proceedings of the International Symposium on Environmental Studies for Deep-Sea Mining, pp. 143–151.

Becker, H. J., Grupe, B., Oebius, H. U., and Liu, F., 2001. The Behaviour of Deep- Sea Sediments Under the Impact of Nodule Mining Processes. Deep-Sea. Res. Part II. -Top. Stud. Oceanogr. 48 (17-18), 3609–3627. https://doi.org/10.1016/S0967-0645(01)00059-5.

Berelson, W. M., Anderson, R. F., Dymond, J., Demaster, D. J., Hammond, E., Collier, R., et al., 1997. Biogenic Budgets of Particle Rain, Benthic Remineralization and Sediment Accumulation in the Equatorial Pacific. Deep-Sea. Res. II. 44 (9-10), 2251–2282. https://doi.org/10.1016/S0967-0645(97)00030-1.

Best, J., Simmons, S., Parsons, D., Oberg, K., Czuba, J., and Malzone, C., 2010. A New Methodology for the Quantitative Visualization of Coherent Flow Structures in Alluvial Channels Using Multibeam Echo-Sounding (MBES). Geophys. Res. Lett. 37 (6), L06405. https://doi.org/10.1029/2009GL041852.

BGR Bundanstalt für Geowissenschaften und Rohstoffe, 2018. Environmental Impact Assessment 827 for the Testing of a Pre-Protoype Manganese Nodule Collector Vehicle in the Eastern German License 828 Area (Clarion-Clipperton Zone) in the Framework of the European JPI-O MiningImpact 2 Research 829 Project. https://isa.org.jm/minerals/environmental-impact-assessments.

Bishop, J.K.B., 1986. The correction and suspended particulate matter calibration of sea tech transmissometer data. Deep-Sea Res. Part A-Oceanogr. Res. Papers 33 (1), 121–134. https://doi.org/10.1016/0198-0149(86)90111-1.

Blue Nodules, 2016. https://blue-nodules.eu/vision-and-objectives/.

Boetius, A. and Haeckel, H., 2018. Mind the seafloor. Research and regulations must be integrated to protect seafloor biota from future mining impacts. Science, v. 359, issue 6371, p34-36, https://doi.org/10.1126/science.aap7301.

Boschen, R. E., Rowden, A. A., Clark, M. R., and Gardner, J. P. A., 2013. Mining of deep-sea seafloor massive sulfides: A review of the deposits, their benthic communities, impacts from mining, regulatory frameworks and management strategies, Ocean Coast. Manage., 84, 54–67. https://doi.org/10.1016/j.ocecoaman.2013.07.005.

Boschen, R., de Stigter, H.C., Tayman, C., Mravak, Z., 2020. Blue Nodules Deliverable Report D1.7: Environmental Impact Assessment (EIA) component for test mining up to prototype level (TRL 6). https://blue-nodules.eu/download/public_reports/publ_ic_reports/Blue-Nodules-688975-D1.7-Report-EIA-Assessment-FINAL.pdf.

Boss, E., Guidi, L., Richardson, M.J., Stemmann, L., Gardner, W., Bishop, J.K.B., Anderson, R.F., Sherrell, R.M., 2015. Optical techniques for remote and in-situ characterization of particles pertinent to GEOTRACES. Prog. Oceanogr. 133, 43–54. https://doi.org/10.1016/j.pocean.2014.09.007.

Breier, J. A., Toner, B. M., Fakra, S. C., Marcus, M. A., White, S. N., Thurnherr, A. M., and German, C. R., 2012. Sulfur, sulfides, oxides andorganic matter aggregated in submarine hydrothermal plumes at 9500 N East Pacific Rise, Geochim. Cosmochim. Ac., 88, 216– 236. https://doi.org/10.1016/j.gca.2012.04.003.

Brennan, M., Canals, M., Coleman, D., Austin Jr., J., Amblas, D., 2015. Bathymetric Extent of recent Trawl damage to the Seabed Captured by an ROV Transect in the Alboran Sea. Oceanography 28 (4), 8–10. http://www.jstor.org/stable/24861922.

Bricaud, A., Morel, A., Babin, M., Allali, K., Claustre, H., 1998. Variations of light absorption by suspended particles with chlorophyll a concentration in oceanic (case 1) waters: Analysis and implications for bio-optical models. J. Geophys. Res. Oceans 103 (C13), 31033–31044. https://doi.org/10.1029/98JC02712.

Briseño-Avena, C., Franks, P.J.S., Roberts, P.L.D., Jaffe, J.S., 2018. A diverse group of echogenic particles observed with a broadband, high frequency echosounder. J. Mar.Sci. 75, 471–482. https://doi.org/10.1093/icesjms/fsx171.

Brockett, T., and Richards, C. Z., 1994. Deep Sea Mining Simulator for Environmental Impact Studies. Sea. Technol. 35 (8), 77–82.

Brooke, S.D., Watts, M.W., Heil, A.D., Rhode, M., Mienis, F., Duineveld, G.C.A., Davies, A.J., Ross, S.W., 2017. Distributions and habitat associations of deep-water corals in Norkfolk and Baltimore Canyons, Mid-Atlantic Bight, USA. Deep-Sea Research Part II – Topical Studies in Oceanography 137, 131–147. https://doi.org/10.1016/j.dsr2.2016.05.008.

Buck, V., Stäbler, F., González, E., and Greinert, J. (2021). Digital Earth Viewer: A 4d Visualisation Platform for Geoscience Datasets. Worksh. Visual. Environ. Sci. (EnvirVis), 33–37. https://doi.org/10.2312/envirvis.20211081.

Bunt, J.A.C., Larcombe, P., Jago, C.F., 1999. Quantifying the response of optical backscatter devices and transmissometers to variations in suspended particulate matter. Cont. Shelf Res. 19 (9), 1199–1220. https://doi.org/10.1016/S0278-4343(99)00018-7.

Burd, B.J., Thomson, R.E., 2019. Seasonal patterns in deep acoustic backscatter layers near vent plumes in the northeastern Pacific Ocean. Facets 4, 183–209. https://doi.org/10.1139/facets-2018-0027.

Burns, R.E., 1980. Assessment of environmental effects of deep ocean mining of manganese nodules. Helgoländer Meeresunters. 33, 433-442.

Caetano, M., Vale, C., Anes, B., Raimundo, J., Drago, T., Schimdt, S., Nogueira, M., Oliveira, A., and Prego, R., 2013. The Condor seamount at Mid-Atlantic Ridge as a supplementary source of trace and rare earth elements to the sediments, Deep-Sea Res. Pt. II, 98, 24–37. https://doi.org/10.1016/j.dsr2.2013.01.009.

Canals, M., Puig, P., de Madron, X.D., Heussner, S., Palanques, A., Fabres, J., 2006. Flushing submarine canyon. Nature 444 (7117), 354–357. https://doi.org/10.1038/nature05271.

Canals, M., Company, J.B., Martín, D., Sànchez-Vidal, A., Ramírez-Llodrà, E., 2013.Integrated study of Mediterranean deep canyons. Novel results and future challenges. Prog. Oceanogr 118, 1–27. https://doi.org/10.1016/j.pocean.2013.09.004.

Cave, R. R., German, C. R., Thomson, J., and Nesbitt, R.W., 2002. Fluxes to sediments underlying the Rainbow hydrothermal plume at 36 140 N on the Mid-Atlantic Ridge, Geochim. Cosmochim. Ac., 66, 1905–1923. https://doi.org/10.1016/S0016-7037(02)00823-2.

Cerqueira, T., Barroso, C., Froufe, H., Egas, C., and Bettencourt, R., 2018. Metagenomic Signatures of Microbial Communities in Deep-Sea Hydrothermal Sediments of Azores Vent Fields, Microb. Ecol., 76, 387–403. https://doi.org/10.1007/s00248-018-1144-x.

Charlou, J. L., Donval, J. P., Fouquet, Y., Jean-Baptiste, P., Holm, N., 2002. Geochemistry of high H2 and CH4 vent fluids issuing from ultramafic rocks at the Rainbow hydrothermal field (36140 N, MAR), Chem. Geol., 191, 345–359. https://doi.org/10.1016/S0009-2541(02)00134-1.

Chavagnac, V., German, C. R., Milton, J. A., and Palmer,M. R., 2005. Sources of REE in sediment cores from the Rainbow vent site (36 140 N, MAR), Chem. Geol., 216, 329–352. https://doi.org/10.1016/S00092541(02)00134-1.

Clarke, K. R. and Gorley, R. N., 2006. PRIMER v6: User Manual/ Tutorial (Plymouth Routines in Multivariate Ecological Research), PRIMER-E, Plymouth.

Collins, P. C., Croot, P., Carlsson, J., Colaço, A., Grehan, A., Hyeong, K., Kennedy, R., Mohn, C., Smith, S., and Yamamoto, H., 2013. A primer for the Environmental Impact Assessment of mining at seafloor massive sulfide deposits, Mar. Policy, 42, 198 – 209. https://doi.org/10.1016/j.marpol.2013.01.020.

Connell, J. H. and Slayter, R. O., 1977. Mechanisms of Succession in Natural Communities and Their Role in Community Stability and Organization, Am. Nat., 111, 1119–1144. https://doi.org/10.1086/283241.

Cunha, M.R., Paterson, G.L.J, Amaro, T., Blackbird, S., de Stigter, H.C., Ferreira, C., Glover, A., Hilario, A., Kiriakoulakis, K., Neal, L., Ravara, A., Rodrigues, C.F., Tiago, A., Billett, D.S.M., 2011. Biodiversity of macrofaunal assemblages from three Portuguese submarine canyons (NE Atlantic). Deep-Sea Research Part II – Topical Studies in Oceanography, 58 (23-24), 2433–2447. https://doi.org/j.dsr2.2011.04.007.

Cowen, J. P. and Bruland, K. W., 1985. Metal Deposits Associated with Bacteria – Implications for Fe and Mn Marine Biogeochemistry, Deep-Sea Res., 32, 253–272. https://doi.org/10.1016/0198-0149(85)90078-0.

Cowen, J. P., Massoth, G. J., and Feely, R. A., 1990. Scavenging Rates of Dissolved Manganese in a Hydrothermal Vent Plume, Deep-Sea Res., 37, 1619–1637. https://doi.org/10.1016/0198-0149(90)90065-4.

Dahl, M.P., Pereyra, R.T., Lundalv, T., Andre, C., 2012. Fine-scale spatial genetic structure and clonal distribution of the cold-water coral Lophelia Pertusa. Coral Reefs, 31 (4), 1135–1148. https://doi.org/10.1007/s00338-012-0937-5.

Daly, E., Johnson, M.P., Wilson, A.M., Gerritsen, H.D., Kiriakoulakis, K., Allcock, A.L., White, M., 2018. Bottom trawling at Whittard Canyon: evidence for seabed modification, trawl plumes and food source heterogeneity. Prog. Oceanogr. 169, 227–240. https://doi.org/10.1016/j.pocean.2017.12.010.

Davies, E.J., Nimmo-Smith, W.A.M., Agrawal, Y.C., Souza, A.J., 2012. LISST-100 response to large particles. Mar. Geol. 307-310, 117–122. https://doi.org/10.1016/j. margeo.2012.03.006.

Davison, J.J., van Haren, H., Hosegood, P., Piechaud, N., Howell, K.L., 2019. The distribution of deep-sea sponge aggregations (Porifera) in relation to oceanographic processes in the Faroe-Shetland Channel. Deep Sea Res. Part I: Oceanogr. Res. Papers 146, 55–61. https://doi.org/10.1016/j.dsr.2019.03.005.

De Leo, F.C., Smith, C.R., Rowden, A.A., Bowden, D.A., Clark, M.R., 2010. Submarine canyons: hotspots of benthic biomass and productivity in the deep sea. Proc. Biol. Sci. 277 (1695), 2783–2792. https://doi.org/10.1098/rspb.2010.0462.

De Leo, F.C., Ogata, B., Sastri, A.R., Heesemann, M., Mihály, S., Galbraith, M., Morley, M.G., 2018. High-frequency observations from a deep-sea cabled observatory reveal seasonal overwintering of Neocalanus ssp. in Barkley Canyon, NE Pacific: Insights into particulate organic carbon flux. Prog. Oceanogr. 169, 120–137. https://doi.org/10.1016/j.pocean.2018.06.001.

de Stigter, H.C., Boer, W., de Jesus Mendes, P.A., Jesus, C.C., Thomsen, L., van den Bergh, G.D., van Weering, T.C.E., 2007. Recent sediment transport and deposition in the Nazaré Canyon, Portuguese continental margin. Mar. Geol. 246 (2–4), 144–164. https://doi.org/10.1016/j.margeo.2007.04.011.

de Stigter, H.C., Jesus, C.C., Boer, W., Richter, T.O., Costa, A., van Weering, T.C.E., 2011. Recent sediment transport and deposition in the Lisbon–Setúbal and Cascais submarine canyons, Portuguese continental margin. Deep-Sea Res. II Top. Stud. Oceanogr. 58 (23–24), 2321–2344. https://doi.org/10.1016/j.dsr2.2011.04.001.

Dell'Anno, A. and Corinaldesi, C., 2004. Degradation and turnover of extracellular DNA in marine sediments: Ecological and methodological considerations, Appl. Environ. Microbiol., 70, 4384–4386, https://doi.org/10.1128/AEM.70.7.4384– 4386.2004.

DEME Group, 2021. https://www.deme-group.com/news/metal-rich-nodules-collected-seabed-during-important-technology-trial.

Dick, G. J., Anantharaman, K., Baker, B. J., Li, M., Reed, D. C., and Sheik, C. S., 2009. The microbiology of deep-sea hydrothermal vent plumes: ecological and biogeographic linkages to seafloor and water column habitats, Front. Microbiol., 4, 124. https://doi.org/10.3389/fmicb.2013.00124.

Dick, G. J., Clement, B. G., Webb, S. M., Fodrie, F. J., Bargar, J. R., and Tebo, B. M., 2009. Enzymatic microbial Mn(II) oxidation and Mn biooxide production in the Guaymas Basin deep-sea hydrothermal plume, Geochim. Cosmochim. Ac., 73, 6517–6530. https://doi.org/10.1016/j.gca.2009.07.039.

Dick, G. J. and Tebo, B. M., 2010. Microbial diversity and biogeochemistry of the Guaymas Basin deep-sea hydrothermal plume, Environ. Microbiol., 12, 1334–1347. https://doi.org/10.1111/j.1462-2920.2010.02177.x.

Dickson, R.R., Mccave, I.N., 1986. Nepheloid layers on the continental-slope west of Porcupine Bank. Deep-Sea Res. Part A-Oceanogr. Res. Papers 33 (6), 791–818. https://doi.org/10.1016/0198-0149(86)90089-0.

Djurhuus, A., Mikalsen, S. O., Giebel, H. A., and Rogers, A. D., 2017. Cutting through the smoke: the diversity of microorganisms in deep-sea hydrothermal plumes, Roy. Soc. Open Sci., 4. 160829, https://doi.org/10.1098/rsos.160829.

Douville, E., Charlou, J. L., Oelkers, E. H., Bienvenu, P., Colon, C. F. J., Donval, J. P., Fouquet, Y., Prieur, D., and Appriou, P., 2002. The rainbow vent fluids (36 140 N, MAR): the influence of ultramafic rocks and phase separation on trace metal content in Mid- Atlantic Ridge hydrothermal fluids, Chem. Geol., 184, 37–48. https://doi.org/10.1016/S0009-2541(01)00351-5.

Downing, J.P., Sternberg, R.W., Lister, C.R.B., 1981. New instrumentation for the investigation of sediment suspension processes in the shallow marine environment. Marine Geology, 42, 19-34.

Downing, J.P., Beach, R.A., 1989. Laboratory apparatus for calibrating optical suspended-solids sensors. Mar. Geol. 86 (2–3), 243–249. https://doi.org/10.1016/0025-3227(89)90053-4.

Downing, J., 2006. Twenty-five years with OBS sensors: the good, the bad, and the ugly. Cont. Shelf Res. 26 (17–18), 2299–2318. https://doi.org/10.1016/j. csr.2006.07.018.

Drake, D.E., 1976. Suspended sediment transport and mud deposition on continental shelves. Marine sediment transport and environmental management, pp. 127-158.

Drazen, J. C., Smith, C. R., Gjerde, K. M., Haddock, S. H. D., Carter, G. S., Choy, C. A., et al., 2020. Opinion: Midwater Ecosystems Must be Considered When Evaluating Environmental Risks of Deep-Sea Mining. Proc. Natl. Acad. Sci. U.S.A. 117 (30), 17455–17460. https://doi.org/10.1073/pnas.2011914117.

Duineveld, G.C.A., Lavaleye, M.S.S., Berghuis, E.M., de Wilde, P., 2001. Activity and composition of the benthic fauna in the Whittard Canyon and the adjacent slope. Oceanol. Acta 24 (1), 69–83. https://doi.org/10.1016/S0399-1784(00)01129-4.

Duineveld, G.C.A., Lavaleye, M.S.S., Berghuis, E.M., 2004. Particle flux and food supply to a seamount cold-water coral community (Galicia Bank, NW Spain). Marine Ecology Progress Series, 277, 13–23. https://doi/org/10.3354/meps277013.

Durrieu de Madron, X., 1994. Hydrography and nepheloid structures in the Grand-Rhone canyon. Cont. Shelf Res. 14 (5), 457–477. https://doi.org/10.1016/0278-4343(94)90098-1.

Durrieu de Madron, X., Ferré, B., Le Corre, G., Grenz, C., Conan, P., Pujo-Pay, M., Buscail, R., Bodiot, O., 2005. Trawling-induced resuspension and dispersal of muddy sediments and dissolved elements in the Gulf of Lion (NW Mediterranean). Cont. Shelf Res. 25, 2387–2409. https://doi.org/10.1016/j.csr.2005.08.002.

Edmond, J. M. Campell, A. C., Palmer, M. R., Klinkhammer, G. P., German, C. R., Edmonds, H. N., Elderfield, H., Thompson, G., and Rona, P., 1995. Time series studies of vent fluids from the TAG and MARK sites (1986, 1990) Mid-Atlantic Ridge: a new solution chemistry model and a mechanisms for Cu/Zn zonation in massive sulphide orebodies, Geol. Soc. Spec. Publ., 87, 77–86. https://doi.org/10.1144/GSL.SP.1995.087.01.07.

Edmonds, H. N. and German, C. R., 2004. Particle geochemistry in the Rainbow hydrothermal plume, Mid-Atlantic Ridge, Geochim. Cosmochim. Ac., 68, 759–772. https://doi.org/10.1016/S0016-7037(03)00498-8 .

Emery, W.J. and Meincke, J., 1986. GlobalWater Masses – Summary and Review, Oceanol Acta, 9, 383–391.

Epping, E., van der Zee, C., Soetaert, K., Helder, W., 2002. On the oxidation and burial of organic carbon in sediments of the Iberian margin and Nazaré Canyon. Prog. Oceanogr 52, 399–431. https://doi.org/10.1016/S0079-6611(02)00017-4.

Ercilla, G., Juan, C., Hernández-Molina, F.J., Bruno, M., Estrada, F., Alonso, B., Casas, D., Farran, M., Llave, E., García, M., Vázquez, J.T., D'Acremont, E., Gorini, C., Palomino, D., Valencia, J., El Moumni, B., Ammar, A., 2016. Significance of bottom currents in deep-sea morphodynamics: an example from the Alboran Sea. Mar. Geol. 378, 157–170. https://doi.org/10.1016/j.margeo.2015.09.007.

Fettweis, M., Francken, F., Pison, V., Van den Eynde, D., 2006. Suspended particulate matter dynamics and aggregate sizes in a high turbidity area. Mar. Geol. 235 (1–4), 63–74. https://doi.org/10.1016/j.margeo.2006.10.005.

Fettweis, M., Lee, B., 2017. Spatial and seasonal variation of biomineral suspended particulate matter properties in high-turbid nearshore and low-turbid offshore zones. Water 9 (9). https://doi.org/10.3390/w9090694.

Fettweis, M., Riethmüller, R., Verney, R., Becker, M., Backers, J., Baeye, M., Chapalain, M., Claeys, S., Claus, J., Cox, T., Deloffre, J., Depreiter, D., Druine, F., Flöser, G., Grünler, S., Jourdin, F., Lafite, R., Nauw, J., Nechad, B., Röttgers, R., Sottolichio, A., Van Engeland, T., Vanhaverbeke, W., Vereecken, H., 2019. Uncertainties associated with in situ high-frequency long-term observations of suspended particulate matter concentration using optical and acoustic sensors. Prog. Oceanogr. 178, article 102162. https://doi.org/10.1016/j.pocean.2019.102162.

Fielding, S., Griffiths, G., Roe, H.S.J., 2004. The biological validation of ADCP acoustic backscatter through direct comparison with net samples and model predictions based on acoustic-scattering models. J. Mar. Sci. 61, 184–200. https://doi.org/10.1016/j.icesjms.2003.10.011.

Findlay, A. J., Gartman, A., Shaw, T. J., and Luther, G. W., 2015. Trace metal concentration and partitioning in the first 1.5m of hydrothermal vent plumes along the Mid-Atlantic Ridge: TAG, Snakepit, and Rainbow, Chem. Geol., 412, 117–131. https://doi.org/10.1016/j.chemgeo.2015.07.021.

Firing, E., Ranada, J., Caldwell, P., 1995. Processing ADCP Data with the CODAS Software System Version 3.1. Joint Institute for Marine and Atmospheric Research, University of Hawaii & National Oceanographic Data Center.

Firing, E., Hummon, J.M., 2010. Shipboard ADCP Measurements.

Flagg, C.N., Smith, S.L., 1989. On the use of the acoustic Doppler current profiler to measure zooplankton abundance. Deep Sea Res. Part A 36, 455–474. https://doi.org/10.1016/0198-0149(89)90047-2.

Foote, K.G., 2001. Acoustic scattering by marine organisms. In: Encyclopedia of Ocean Sciences, 1. Academic Press, London, pp. 44–53.

Fouquet, Y., Barriga, F., Charlou, J. L., Elderfield, H., German, C. R., Ondréas, H., Parson, L., Radford-Knoery, J., Relvas, J., Ribeiro, A., Schultz, A., Appriou al, R., Cambon, P., Costa, I., Donval, J. P., Douville, E., Landuré, J. Y., Normund, A., Pellé, H., Ponsevera, E., Riches, S., Santana, H., and Stephan, M., 1998. Flores diving cruise with the Nautile near the Azores. First dives on the Rainbow field: hydrothermal seawater/mantle interaction, Inter Ridge News, 7, 24–28.

Frank, K. L., Rogers, D. R., Olins, H. C., Vidoudez, C., and Girguis,P. R., 2013. Characterizing the distribution and rates of microbial sulfate reduction at Middle Valley hydrothermal vents, Isme J.,7, 1391–1401. https://doi.org/10.1038/ismej.2013.17.

Frischknecht, M., Munnich, M., Gruber, N, 2018. Origin, Transformation, and Fate: The Three-Dimensional Biological Pump in the California Current System. Journal of Geophysical Research-Oceans, 123 (11), 7939–7962. https://doi.org/10.1029/2018jc013934.

Fromant, G., Le Dantec, N., Perrot, Y., Floc'h, F., Lebourges-Dhaussy, A., and Delacourt, C., 2021. Suspended Sediment Concentration Field Quantified From a Calibrated MultiBeam EchoSounder. Appl. Acoust. 180, 108107. https://doi.org/10.1016/j.apacoust.2021.108107.

Fugate, D.C., Friedrichs, C.T., 2002. Determining concentration and fall velocity of estuarine particle populations using ADV, OBS and LISST. Cont. Shelf Res. 22 (11–13), 1867–1886. https://doi.org/10.1016/S0278-4343(02)00043-2.

Fukushima, T., 1995. Overview "Japan Deep-sea Impact Experiment = JET", ISOPE-M-95-008, ISOPE.

García, R., Thomsen, L., 2008. Bioavailable organic matter in surface sediments of the Nazaré canyon and adjacent slope (Western Iberian Margin). J. Mar. Syst. 74 (1–2), 44–59. https://doi.org/10.1016/j.jmarsys.2007.11.004.

García, R., van Oevelen, D., Soetaert, K., Thomsen, L., de Stigter, H.C., Epping, E., 2008. Deposition rates, mixing intensity and organic content in two contrasting submarine canyons. Progress In Oceanography, 76 (2), 192–215. https://doi.org/j.pocean.2008.01.001.

Gardner, W.D., 1989a. Baltimore Canyon as a Modern Conduit of Sediment to the Deep-Sea. Deep-Sea Res. Part A-Oceanogr. Res. Papers 36 (3), 323–358. https://doi.org/10.1016/0198-0149(89)90041-1.

Gardner, W.D., 1989b. Periodic resuspension in Baltimore Canyon by focusing of internal waves. Journal of Geophysical Research – Oceans, 94, 18185–18194. https://doi.org/10.1029/JC094iC12p18185.

Gardner, W.D., Richardson, M.J., Mishonov, A.V., Biscaye, P.E., 2018a. Global comparison of benthic nepheloid layers based on 52 years of nephelometer and transmissometer measurements. Prog. Oceanogr. 168, 100–111. https://doi.org/10.1016/j.pocean.2018.09.008.

Gardner, W.D., Richardson, M.J., Mishonov, A.V., 2018b. Global assessment of benthic nepheloid layers and linkage with upper ocean dynamics. Earth Planet. Sci. Lett. 482, 126–134. https://doi.org/10.1016/j.epsl.2017.11.008.

Gausepohl, F., Hennke, A., Schoening, T., Köser, K., and Greinert, J., 2020. Scars In the Abyss: Reconstructing Sequence, Location and Temporal Change of the 78 Plough Tracks of the 1989 DISCOL Deep-Sea Disturbance Experiment in the Peru Basin. Biogeosciences, 17, 1463–1493. https://doi.org/10.5194/bg-17-1463-2020.

Gazis, I.-Z., 2020. Processed EM122 Multibeam Swath Bathymetry Collected During SONNE Cruise SO268/1 Inside the German License Area In The Clarion Clipperton Zone, Pacific (GEOMAR - Helmholtz Centre for Ocean Research Kiel, Germany PANGAEA). https://doi.org/10.1594/PANGAEA.915764.

German, C. R., Campbell, A. C., and Edmond, J. M., 1991. Hydrothermal Scavenging at the Mid-Atlantic Ridge – Modification of Trace Element Dissolved Fluxes, Earth Planet. Sc. Lett., 107, 101–114. https://doi.org/10.1016/0012-821X(91)90047-L.

German, C. R., Klinkhammer, G. P., and Rudnicki, M. D., 1996. The Rainbow hydrothermal plume, 140 N, MAR, Geophys. Res. Lett., 23, 2979–2982. https://doi.org/10.1029/96GL02883.

German, C.R., Richards, K.J., Rudnicki, M.D., Lam, M.M., Charlou, J.L., Party, F.S., 1998. Topographic control of a dispersing hydrothermal plume. Earth Planet. Sci. Lett. 156 (3–4), 267–273. https://doi.org/10.1016/S0012-821X(98)00020-X.

Gibbs, R.J., 1978. Light-scattering from particles of different shapes. J. Geophys. Res. Oceans Atmosph. 83 (Nc1), 501–502. https://doi.org/10.1029/JC083iC01p00501.

Gibbs, R.J., Wolanski, E., 1992. The effect of flocs on optical backscattering measurements of suspended material concentration. Mar. Geol. 107 (4), 289–291. https://doi.org/10.1016/0025-3227(92)90078-V.

Gillard, B., Purkiani, K., Chatzievangelou, D., Vink, A., Iversen, M.H., Thomsen, L., 2019. Physical and hydrodynamic properties of deep sea mining-generated, abyssal sediment plumes in the Clarion Clipperton Fracture Zone (eastern-central Pacific). Elementa – Sci. Anthropocene 7. https://doi.org/10.1525/elementa.343.

Gjerde, K.M., Reeve, L.L.N., Harden-Davies, H., Ardron, J., Dolan, R., Durussel, C., et al., 2016. Protecting Earth's last conservation frontier: scientific, management and legal priorities for MPAs beyond national boundaries. Aquat. Conserv.: Mar. Freshw. Ecosyst. 26, 45–60. https://doi.org/10.1002/aqc.2646.

Glover, A.G., Smith, C.R., 2003. The deep-sea floor ecosystem: current status and prospects of anthropogenic change by the year 2025. Environ. Conserv. 30 (3), 219–241. https://doi.org/10.1017/S0376892903000225.

Gollner, S., Kaiser, S., Menzel, L., Jones, D.O.B., Brown, A., Mestre, N.C., et al., 2017. Resilience of benthic deep-sea fauna to mining activities. Mar. Environ. Res. 129, 7 6-101. https://doi.org/10.1016/j.marenvres.2017.04.010.

Gostiaux, L., van Haren, H., 2010. Extracting meaningful information from uncalibrated backscattered echo intensity data. J. Atmos. Ocean. Technol. 27 (5), 943–949. https://doi.org/10.1175/2009JTECHO704.1.

Greinert, J., 2015. RV SONNE Cruise Report SO242-1: JPI OCEANS Ecological Aspects of Deep-Sea Mining, DISCOL Revisited, Guayaquil – Guayaquil (Equador), 28.07.-25.08.2015. https://doi.org/10.3289/GEOMAR_REP_NS_26_2015.

GSR, 2018. Environmental Impact Statement. Small-Scale Testing of Nodule Collector Component on the Seafloor of the Clarion-Clipperton Fracture Zone and its Environmental Impact. https://www.isa.org.jm/minerals/environmental-impact-assessments.

Gruber, P., Felix, D., Storti, G., Lattuada, M., Fleckenstein, P., Deschwanden, F., 2016. Acoustic measuring techniques for suspended sediment. In: IOP Conference Series: Earth and Environmental Science, p. 49. https://doi.org/10.1088/1755-1315/49/12/122003.

Guerrero, M., Szupiany, R.N., Amsler, M., 2011. Comparison of acoustic backscattering techniques for suspended sediments investigation. Flow Meas. Instrum. 22 (5), 392–401. https://doi.org/10.1016/j.flowmeasinst.2011.06.003.

Guillén, J., Palanques, A., Puig, P., De Madron, X.D., Nyffeler, F., 2000. Field calibration of optical sensors for measuring suspended sediment concentration in the western Mediterranean. Sci. Mar. 64 (4), 427–435. https://doi.org/10.3989/scimar.2000.64n4427.

Gwyther, D. and Wright, M., 2008. Environmental Impact Statement: Solwara 1, Coffey Natural Systems Pty Ltd, 47–65.

Haalboom, S., Price, D.M., Mienis, F., van Bleijswijk, J.D.L., de Stigter, H.C., Witte, H.J., Reichart, G.-J., Duineveld, G.C.A., 2020. Patterns of (trace) metals and microorganisms in the Rainbow hydrothermal vent plume at the Mid-Atlantic Ridge. Biogeosciences 17 (9), 2499–2519. https://doi.org/10.5194/bg-17-2499-2020.

Haalboom, S., de Stigter, H., Duineveld, G., van Haren, H., Reichart, G.-J., Mienis, F., 2021. Suspended particulate matter in a submarine canyon (Whittard Canyon, Bay of Biscay, NE Atlantic Ocean): assessment of commonly used instruments to record turbidity. Mar. Geol. 434 https://doi.org/10.1016/j.margeo.2021.106439.

Haalboom, S., Schoening, T., Urban, P., Gazis, I.-Z., de Stigter, H.C., Gillard, B., et al., 2022. Monitoring of anthropogenic sediment plumes in the Clarion-Clipperton Zone, NE equatorial Pacific Ocean. Front. Mar. Sci. – Deep-Sea Environ. Ecol. 9, 882155. https://doi.org/10.3389/fmars.2022.882155.

Haeckel, M., and Linke, P., 2021. RV SONNE Cruise Report SO268 – Assessing the Impacts of Nodule Mining on the Deep-Sea Environment: Nodule Monitoring, Manzanillo (Mexico) – Vancouver (Canada), 17.02. – 27.05.2019 (GEOMAR Report 59. GEOMAR Helmholtz-Zentrum für Ozeanforschung Kiel, Kiel, Germany), 802. https://doi.org/10.3289/GEOMAR_REP_NS_59_20.

Halbach, P., and Fellerer, R., 1980. The Metallic Minerals of the Pacific Seafloor. GeoJournal 4 (5), 407–422. https://doi.org/10.1007/BF01795925.

Halbach, P., Friedrich, G., von Stackelberg, U. (Eds.), 1988. The Manganese Nodule Belt of the Pacific Ocean. Enke, Stuttgart.

Hall, R.A., Aslam, T., Huvenne, V.A.I., 2017. Partly standing internal tides in a dendritic submarine canyon observed by an ocean glider. Deep Sea Res. Part I: Oceanogr. Res. Papers 126, 73–84. https://doi.org/10.1016/j.dsr.2017.05.015.

Han, Y. C., Gonnella, G., Adam, N., Schippers, A., Burkhardt, L., Kurtz, S., Schwarz-Schampera, U., Franke, H., and Perner, M., 2018. Hydrothermal chimneys host habitat-specific microbial communities: analogues for studying the possible impact of mining seafloor massive sulfide deposits, Sci. Rep.-UK, 8, 10386. https://doi.org/10.1038/s41598-018-28613-5.

Harris, P.T., Whiteway, T., 2011. Global distribution of large submarine canyons: Geomorphic differences between active and passive continental margins. Mar. Geol. 285 (1–4), 69–86. https://doi.org/10.1016/j.margeo.2011.05.008.

Hatcher, A., Hill, P., Grant, J., Macpherson, P., 2000. Spectral optical backscatter of sand in suspension: effects of particle size, composition and colour. Mar. Geol. 168 (1–4), 115–128. https://doi.org/10.1016/S0025-3227(00)00042-6.

Hatcher, A., Hill, P., Grant, J., 2001. Optical backscatter of marine flocs. J. Sea Res. 46 (1), 1–12. https://doi.org/10.1016/S1385-1101(01)00066-1.

Hawley, N., 2004. A comparison of suspended sediment concentrations measured by acoustic and optical sensors. J. Great Lakes Res. 30 (2), 301–309. https://doi.org/10.1016/S0380-1330(04)70348-2.

Hedges, J.I., Keil, R.G., 1995. Sedimentary organic matter preservation: an assessment and speculative synthesis. Marine Chemistry, 49 (2), 81–115. https://doi.org/10.1016/0304-4203(95)00008-F.

Heijnen, M.S., Mienis, F., Gates, A.R., Bett, B.J, Hall, R.A., Hunt. J., Kane, I.A., Pebody, C., Huvenne, V.A.I., Soutter, E.L., Clare, M.A., 2022. Challenging the highstand-dormant paradigm for land-detached submarine canyons. Nature Communications, 13 (1), 3448. https://doi.org/10.1038/s41467-022-31114-9.

Hein, J.R., Conrad, T.A., Dunham, R.E., 2009. Seamount characteristics and mine-site model applied to exploration- and mining-lease-block selection for cobalt-rich ferromanganese crusts. Mar. Geores. Geotech., 27, 160-176. https://doi.org/10.1080/10641190902852485.

Hein, J. R., Mizell, K., Koschinsky, A., Conrad, T. A., 2013. Deep-Ocean Mineral Deposits as a Source of Critical Metals for High- and Green- Technology Applications: Comparison With Land-Based Resources. Ore. Geolog. Rev. 51, 1–14. https://doi.org/10.1016/j.oregeorev.2012.12.001.

Hill, P.S., Boss, E., Newgard, J.P., Law, B.A., Milligan, T.G., 2011. Observations of the sensitivity of beam attenuation to particle size in a coastal bottom boundary layer. J. Geophys. Res. 116 (C2). https://doi.org/10.1029/2010JC006539.

Hoagland, P., Beaulieu, S., Tivey, M. A., Eggert, R. G., German, C., Glowka, L., and Lin, J., 2010. Deep-sea mining of seafloor massive sulfides, Mar. Policy, 34, 728–732, https://doi.org/10.1016/j.marpol.2009.12.001.

Holt, J.T., Thorpe, S.A., 1997. Propagation of high frequency internal waves in the Celtic Sea. Deep-Sea Res. I 44 (12), 2087–2116. https://doi.org/10.1016/S0967-0637(97)00091-5.

Hosegood, P., Bonnin, J., van Haren, H., 2004. Solibore-induced sediment resuspension in the Faeroe-Shetland Channel. Geophys. Res. Lett. 31, L09301 https://doi.org/ 10.1029/2004GL019544. https://doi.org/10.1016/0012-821X(91)90047-L.

Huber, J. A., Butterfield, D. A., and Baross, J. A., 2003. Bacterial diversity in a subseafloor habitat following a deepsea volcanic eruption, FEMS Microbiol. Ecol., 43, 393–409. https://doi.org/10.1111/j.1574-6941.2003.tb01080.x.

Huetten, E., and Greinert, J., 2008. "Software Controlled Guidance, Recording and Post-Processing of Seafloor Observations by ROV and Other Towed Devices: The Software Package OFOP," in EGU General Assembly 2008, Vienna, Austria, 13-18.04. 2008.

Hunter, T.N., Darlison, L., Peakall, J., Biggs, S., 2012. Using a multi-frequency acoustic backscatter system as an in situ high concentration dispersion monitor. Chem. Eng. Sci 80, 409–418. https://doi.org/10.1016/j.ces.2012.06.038.

Hunter, W.R., Jamieson, A., Huvenne, V.A.I., Witte, U., 2013. Sediment community responses to marine vs. terrigenous organic matter in a submarine canyon. Biogeosciences, 10 (1), 67–80. https://doi.org/10.5194/bg-10-67-2013.

Huvenne, V.A., Tyler, P.A., Masson, D.G., Fisher, E.H., Hauton, C., Huhnerbach, V., Le Bas, T.P., Wolff, G.A., 2011. A picture on the wall: innovative mapping reveals coldwater coral refuge in submarine canyon. PLoS One 6 (12), e28755. https://doi.org/10.1371/journal.pone.0028755.

Jahnke, R.A., Reimers, C.E., Craven, D.B., 1990. Intensification of recycling of organic matter at the sea-floor near ocean margins. Nature 348 (6296), 50–54. https://doi.org/10.1038/348050a0.

JAMSTEC – Japan Agency for Marine-Earth Science and Technology (CC-BY 4.0). "Cobalt-rich ferromanganese crust found at depths of 4.500 m".

Jankowski, J.A., Malcherek, A., Zielke, W., 1996. Numerical modeling of suspended sediment due to deep-sea mining. J. Geophys. Res. Oceans 101 (C2), 3545–3560. https://doi.org/10.1029/95JC03564.

Jankowski, J. A., and Zielke, W., 2001. The Mesoscale Sediment Transport Due to Technical Activities in the Deep Sea. Deep-Sea. Res. II. 48, 3487–3521. https://doi.org/10.1016/S0967-0645(01)00054-6.
Jannasch, H. W. and Mottl, M. J., 1985. Geomicrobiology of Deep-Sea Hydrothermal Vents, Science, 229, 717–725. https://doi.org/10.1126/science.229.4715.717.

Jerlov, N.G., 1976. Marine Optics, Chapter 3. Elsevier, New York.

Jones, D. O., Kaiser, S., Sweetman, A. K., Smith, C. R., Menot, L., Vink, A., et al., 2017. Biological Responses to Disturbance From Simulated Deep-Sea Polymetallic Nodule Mining. PloS One 12 (2), 171750. https://doi.org/10.1371/journal.pone.0171750.

Jones, D. O. B., Amon, D. L., and Chapman, A. S. A., 2018. Mining Deep-Ocean Mineral Deposits: What are the Ecological Risks?, Elements, 14, 325–330. https://doi.org/10.2138/gselements.14.5.325.

Jones, D.O.B., Ardon, J.A., Colaco, A., Durden, J.M., 2020. Environmental considerations for impact and preservation reference zones for deep-sea polymetallic nodule mining. Mar. Policy 118, 103312. https://doi.org/10.1016/j.marpol.2018.10.025.

Ibáñez-Tejero, L., Ladah, L.B., Sánchez-Velasco, L., Barton, E.D., Filonov, A., 2018. Vertical distribution of zooplankton biomass during internal tidal forcing under mesoscale conditions of upwelling and relaxation. Continental Shelf Res 171, 1–11. https://doi.org/10.1016/j.csr.2018.10.003.

Ifremer (2013). Cheminées hydrothermales actives. Ifremer. https://image.ifremer.fr/data/00702/81434/

Inthorn, M., Wagner, T., Scheeder, G., Zabel, M., 2006. Lateral transport controls distribution, quality and burial of organic matter along continental slopes in high-productivity areas. Geology, 34 (3), 205–208. https://doi.org/10.1130/g22153.1.

ISA - International Seabed Authority, 2019. Recommendations for the Guidance of Contractors for the Assessment of the Possible Environmental Impacts Arising From Exploration for Marine Minerals in the Area. https://isa.org.jm/files/files/document s/26ltc-6-rev1-en_0.pdf.

ISA, 2024. https://www.isa.org.jm/exploration-contracts/.

Khripounoff, A., Vangriesheim, A., Crassous, P., Segonzac, M., Colaço, A., Desbruyères, D., Barthelemy, R., 2001. Particle flux in the Rainbow hydrothermal vent field (Mid-Atlantic Ridge), Dynamics, mineral and biological composition. J. Mar. Res. 59 (4), 633–656. https://doi.org/10.1357/002224001762842217.

Khripounoff, A., Caprais, J.-C., Crassous, P., Etoubleau, J., 2006. Geochemical and biological recovery of the disturbed seafloor in polymetallic nodule fields of the Clipperton-Clarion Zone Fracture Zone (CCFZ) at 5,000-m depth. Limnol. Oceangr. 51, 2033-2041. https://doi.org/10.4319/lo.2006.51.5.2033.

Kineke, G.C., Sternberg, R.W., 1992. Measurements of high concentration suspended sediment using the optical backscatterance sensor. Mar. Geol 108, 253–258. https://doi.org/10.1016/0025-3227(92)90199-R.

Kiriakoulakis, K., Blackbird, S., Ingels, J., Vanreusel, A., Wolff, G.A., 2011. Organic geochemistry of submarine canyons: the Portuguese Margin. Deep-Sea Res. II Top. Stud. Oceanogr. 58 (23–24), 2477–2488. https://doi.org/10.1016/j.dsr2.2011.04.010.

Klindworth, A., Pruesse, E., Schweer, T., Peplies, J., Quast, C., Horn, M. and Glöckner, F. O., 2023. Evaluation of general 16S ribosomal RNA gene PCR primers for classical and next-generation sequencing-based diversity studies, Nucleic Acids Res., 41, e1. https://doi.org/10.1093/nar/gks808.

Klunder, L., de Stigter, H., Lavaleye, M. S. S., van Bleijswijk, J. D. L., van der Veer, H. W., Reichart, G.-J., and Duineveld, G. C. A., 2020. A Molecular Approach to Explore the Background Benthic Fauna Around a Hydrothermal Vent and Their Larvae: Implications for Future Mining of Deep-Sea SMS Deposits, Front. Mar. Sci., 7, 134. https://doi.org/10.3389/fmars.2020.00134.

Kulkarni, C.S., Haley, P.J., Lermusiaux, P.F.J., Dutt, A., Gupta, A., Mirabito, C., et al., 2018. Real-Time Sediment Plume Modeling in the Southern California Bight. OCEANS 2018 MTS/IEEE Charleston, 2018, pp. 1–10. https://doi.org/10.1109/OCEANS.2018.8653642.

Kutti, T., Bannister, R. J., Fosså, J. H., Krogness, C. M., Tjensvoll, I., Søvik, G., 2015. Metabolic Responses of the Deep-Water Sponge Geodia Barretti to Suspended Bottom Sediment, Simulated Mine Tailings and Drill Cuttings. J. Exp. Mar. Biol. Ecol. 473, 64–72. https://doi.org/10.1016/j.jembe.2015.07.017.

Lal, D., 1977. The Oceanic Microcosm of Particles. Sci. New Series 198 (4321), 997–1009. https://doi.org/10.1126/science.198.4321.997.

Lavelle, J.W., Ozturgut, E., Baker, E.T., 1982. Discharge and surface plume measurements during manganese nodule mining tests in the north equatorial pacific. Mar. Environ. Res. 7, 51–70. https://doi.org/10.1016/0141-1136(82)90050-2.

Levin, L. A., Mengerink, K., Gjerde, K. M., Rowden, A. A., Van Dover, C. L., Clark, M. R., Ramirez-Llodra, E., Currie, B., Smith, C. R., Sato, K. N., Gallo, N., Sweetman, A. K., Lily, H., Armstrong, C. W., and Brider, J., 2016a. Defining "Serious Harm" to the Marine Environment in the Context of Deep-Seabed Mining, Mar. Policy, 74, 245–259. https://doi.org/10.1016/j.marpol.2016.09.032.

Levin, L.A., Baco, A.R., Bowden, D.A., Colaco, A., Cordes, E.E., Cunha, M.R., et al., 2016b. Hydrothermal vents and methane Seeps: rethinking the sphere of influence. Front. Mar. Sci. 3 https://doi.org/10.3389/fmars.2016.00072.

Lewis, J., Eads, R., Klein, R., 2007. Comparisons of Turbidity Data Collected with Different Instruments. California Department of Forestry and Fire Protection USDA Forest Service - Pacific Southwest Research Station.

Lin, J., He, Q., Guo, L., van Prooijen, B.C., Wang, Z.B., 2020. An integrated optic and acoustic (IOA) approach for measuring suspended sediment concentration in highly turbid environments. Mar. Geol. 421, 106062. https://doi.org/10.1016/j.margeo.2019.106062.

Lohrmann, A., 2001. Monitoring Sediment Concentration With Acoustic Backscattering Instruments. Tech. Note. Nortek. 1–5.

Lo Iacono, C., Guillen, J., Guerrero, Q., Duran, R., Wardell, C., Hall, R.A., Aslam, T., Carter, G.D.O., Gales, J.A., Huvenne, V.A.I., 2020. Bidirectional bedform fields at the head of a submarine canyon (NE Atlantic). Earth and Planetary Science Letters, 542. https://doi.org/10.1016/j.epsl.2020.116321.

Lurton, X., 2002. An Introduction to Underwater Acoustics: Principles and Applications (London Springer Science & Business Media).

López-García, P., Duperron, S., Philippot, P., Foriel, J., Susini, J., and Moreira, D., 2003. Bacterial diversity in hydrothermal sediment and epsilonproteobacterial dominance in experimental microcolonizers at the Mid-Atlantic Ridge, Environ. Microbiol., 5, 961– 976. https://doi.org/10.1046/j.1462-2920.2003.00495.x.

Lucieer, P., Boomsma, W., Broere, B., van Dalfsen, A., de Bruyne, K., Smit, M., de Jonge, L., 2017. Initial design of vehicle propulsion and propulsion test performance. Blue Nodules Public Rep. D2, 4. https://blue-nodules.eu/download/public_report s/public_summary_reports/Blue-Nodules-688975-D2.4-Updated-Initial-design-of-vehicle-propulsion-and-propulsion-test-performanc-FINAL-publishable-summary.pdf.

Ludford, E. M., Palmer, M. R., German, C. R., and Klinkhammer, G. P., 1996. The geochemistry of Atlantic hydrothermal particles, Geophys. Res. Lett., 23, 3503–3506. https://doi.org/10.1029/96GL02078.

Maa, J.P.Y., Xu, J.P., Victor, M., 1992. Notes on the performance of an optical backscatter sensor for cohesive sediments. Mar. Geol. 104 (1–4), 215–218. https://doi.org/10.1016/0025-3227(92)90096-Z.

Maier, K.L., Gales, J.A., Paull, C.K., Rosenburger, K., Talling, P.J., Simmons, S.M., Gwiazda, R., McGann, M., Cartigny, M.J.B., Lundsten, E., Anderson, K., Clare, M.A., Xu, J.P., Parsons, D., Barry, J.P., Wolfson-Schwehr, M., Nieminski, N.M., Summer, E.J., 2019a. Linking direction measurements of turbidity currents to submarine canyon-floor deposits. Frontiers in Earth Science, 7. https://doi.org/10.3389/feart.2019.00144.

Maier, K.L., Rosenberger, K.J., Paull, C.K., Gwiazda, R., Gales, J., …, Cartigny, M.J.B., 2019b. Sediment and organic carbon transport and deposition driven by internal tides along Montery Canyon, offshore California. Deep-Sea Research Part I, 53, 103108. https://doi.org/10.1016/j.dsr.2019.103108.

Maier, S.R., Brooke, S., De Clippele, L.H., de Froe, E., van der Kaaden, A.S., Kutti, T., Mienis, F., van Oevelen, D., 2023. On the paradox of thriving cold-water coral reefs in the food-limited deep sea. Biological Reviews. https://doi.org/10.1111/brv.12976.

Mandernack, K. W. and Tebo, B. M., 1993. Manganese Scavenging and Oxidation at Hydrothermal Vents and in Vent Plumes, Geochim. Cosmochim. Ac., 57, 3907–3923. https://doi.org/10.1016/0016-7037(93)90343-U.

Manik, H. M., Gultom, D. A., Firdaus, Elson, L., 2020. Evaluation of ADCP Backscatter Computation for Quantifying Suspended Sediment Concentration. Earth Environ. Sci. 249, 12035. https://doi.org/10.1088/1755-1315/429/1/012035.

Manning, A.J., Dyer, K.R., 1999. A laboratory examination of floc characteristics with regard to turbulent shearing. Mar. Geol. 160, 147–170. https://doi.org/10.1016/S0025-3227(99)00013-4.

Markussen, T.N., Andersen, T.J., 2014. Flocculation and floc break-up related to tidally induced turbulent shear in a low turbidity, micro tidal estuary. J. SeaRes. 89, 111. https://doi.org/10.1016/j.seares.2014.02.001.

Marques, A. F. A., Barriga, F., Chavagnac, V., and Fouquet, Y., 2006. Mineralogy, geochemistry, and Nd isotope composition of the Rainbow hydrothermal field, Mid-Atlantic Ridge, Miner. Deposita, 41, 52–67. https://doi.org/10.1007/s00126-005-0040-8.

Martín, J., Puig, P., Palanques, A., Giamportone, A., 2014. Commercial bottom trawling as a driver of sediment dynamics and deep seascape evolution in the Anthropocene. Anthropocene 7, 1–15. https://doi.org/10.1016/j.ancene.2015.01.002.

Martínez Arbizu, P., and Haeckel, M., 2015. RV SONNE Fahrtbericht / Cruise Report SO239: EcoResponse Assessing the Ecology, Connectivity and Resilience of Polymetallic Nodule Field Systems, Balboa (Panama) – Manzanillo (Mexico,) 11.03.-30.04.2015 Vol. 204 (Kiel, Germany: GEOMAR Helmholtz-Zentrum für Ozeanforschung). https://doi.org/10.3289/GEOMAR_REP_NS_25_2015.

MARUM – Center for Marine Environmental Sciences, University of Bremen (CC-BY 4.0). "The "Candelabra" black smoker at a water depth of 3.300 meters in the Logatchev Hydrothermal Field on the Mid-Atlantic Ridge".

Masqué, P., Fabres, J., Canals, M., Sanchez-Cabeza, J.A., Sanchez-Vidal, A., Cacho, L., et al., 2003. Accumulation rates of major constituents of hemipelagic sediments in the deep Alboran Sea: a centennial perspective of sedimentary dynamics. Mar. Geol. 193, 207–233. https://doi.org/10.1016/S0025-3227(02)00593-5.

Masson, D.G., Huvenne, V.A.I., de Stigter, H.C., Wolff, G.A., Kiriakoulakis, K., Arzola, R.G., Blackbird, S., 2010. Efficient burial of carbon in a submarine canyon. Geology, 38 (9), 831–834. https://doi.org/10.1130/g30895.1.

Mayer, L.M., 1994. Surface area control of organic carbon accumulation in continental shelf sediments. Geochimica et Cosmochiminca Acta, 58 (4), 1271–1284. https://doi.org/10.1016/0016-7037(94)90381-6.

McAnally, W.H., Mehta, A.J., 2002. Significance of aggregation of fine sediment particles in their deposition. Estuar. Coastal Shelf Sci. 54, 643–653. https://doi.org/10.1006/ecss.2001.0847.

McCave, I.N., 1986. Local and global aspects of the bottom nepheloid layers in the world ocean. Neth. J. Sea Res. 20 (2/3), 167–181. https://doi.org/10.1016/0077-7579(86)90040-2.

McCollom, T. M., 2000. Geochemical constraints on primary productivity in submarine hydrothermal vent plumes, Deep-Sea Res. Pt. I, 47, 85–101. https://doi.org/10.1016/S0967-0637(99)00048-5.

Mengual, B., Cayocca, F., Le Hir, P., Draye, R., Laffargue, P., Vincent, B., Garlan, T., 2016. Influence of bottom trawling on sediment resuspension in the 'Grande-Vasière' area (Bay of Biscay, France). Ocean Dyn. 66 (9), 1181–1207. https://doi.org/10.1007/s10236-016-0974-7.

Merckelbach, L.M., Ridderinkhof, H., 2005. Estimating suspended sediment concentration using backscatterance from an acoustic Doppler profiling current meter at a site with strong tidal currents. OceanDyn.56(34), 153168. https://doi.org/10.1007/s10236-005-0036-z.

Mero, J.L., 1965. The mineral resources of the sea. Elsevier, Amsterdam.

Michard, G., Albarède, F., Michard, A., Minister, J. F., Charlou. J. L., and Tan, N., 1984. Chemistry of Solution from the 13 N East Pacific Rise Hydrothermal Site, Earth Planet. Sc. Lett. 67, 297– 307. https://doi.org/10.1016/0012-821X(84)90169-9.

Mienis, F., de Stigter, H.C., White, M., Duineveld, G., de Haas, H., van Weering, T.C.E.,2007. Hydrodynamic controls on cold-water coral growth and carbonate-mound development at the SW and SE Rockall Trough Margin, NE Atlantic Ocean. Deep-SeaRes. I Oceanogr. Res. Pap. 54 (9), 1655–1674. https://doi.org/10.1016/j.dsr.2007.05.013.

Mikkelsen, O.A., Hill, P.S., Milligan, T.G., Chant, R.J., 2005. In situ particle size distributions and volume concentrations from a LISST-100 laser particle sizer and a digital floc camera. Cont. Shelf Res. 25 (16), 1959–1978. https://doi.org/10.1016/j.csr.2005.07.001.

Miller, K.A., Thompson, K.F., Johnston, P., Santillo, D., 2018. An overview of seabed mining including the current state of development, environmental impacts, and knowledge gaps. Frontiers in Marine Science, v.4, article 418. https://doi.org/10.3389/fmars.2017.00418.

Millot, C., 1999. Circulation in the Western Mediterranean Sea. J. Mar. Syst. 20,423–442. https://doi.org/10.1016/S0924-7963(98)00078-5.

Millot, C., 2009. Another description of the Mediterranean Sea outflow. Prog. Oceanogr. 82 (2), 101–124. https://doi.org/10.1016/j.pocean.2009.04.016.

Mino, S., Nakagawa, S., Makita, H., Toki, T., Miyazaki, J., Sievert, S. M., and Watanabe, H., 2017. Endemicity of the cosmopolitan mesophilic chemolithoautotroph Sulfurimonas at deep-sea hydrothermal vents, ISME J., 11, 909. https://doi.org/10.1038/ismej.2016.178.

Moate, B.D., Thorne, P.D., 2012. Interpreting acoustic backscatter from suspended sediments of different and mixed mineralogical composition. Continental Shelf Res 46, 67–82. https://doi.org/10.1016/j.csr.2011.10.007.

Mohn, C., Denda, A., Christiansen, S., Kaufmann, M., Peine, F., Springer, B., Turnewitsch, R., Christiansen, B., 2018. Ocean currents and acoustic backscatter data from shipboard ADCP measurements at three North Atlantic seamounts between 2004 and 2015. Data Brief. 17, 237–245. https://doi.org/10.1016/j.dib.2018.01.014.

Morris, K.J., Tyler. P.A., Masson, D.G., Huvenne, V.I.A., Rogers, A.D., 2013. Distribution of cold-water corals in the Whittard Canyon, NE Atlantic Ocean. Deep-Sea Research Part II – Topical Studies in Oceanography, 92, 136–144. https://doi.org/10.1016/j.dsr2.2013.03.036.

Mullison, J., 2017. Backscatter Estimation Using Broadband Acoustic Doppler Current Profilers Application Note (FSA-031), Teledyne RD Instruments. In: ASCE Hydraulic Measurements and Experimental Methods Conference, Durham, NH.

Murray, J., Renard, A.F., 1891. Deep-sea deposits (based on the specimens collected during the voyage of HMS Challenger in the years 1872 to 1876). Report on the scientific results of the voyage of H.M.S. Challenger during the years 1873-76; John Menzies and Co., Edinburgh, United Kingdom.

Nakagawa, S., Takai, K., Inagaki, F., Hirayama, H., Nunoura, T., Horikoshi, K., and Sako, Y., 2005. Distribution, phylogenetic diversity and physiological characteristics of epsilon-Proteobacteria in adeep-sea hydrothermal field, Environ. Microbiol., 7, 1619–1632. https://doi.org/10.1111/j.1462-2920.2005.00856.x.

Nakata, K., Kubota, M., Aoki, S., and Taguchi, K., 1997. Dispersion of Resuspended Sediment by Ocean Mining Activity - Modelling Study, Proceedings of the International Symposium on Environmental Studies for Deep-Sea Mining, Tokyo, Japan, November 20-21.

Nortek, A. S., 2017. The Comprehensive Manual. https://www.nortekgroup.com/assets/documents/ComprehensiveManual_Oct2017__compressed.pdf.

Nittrouer et al., 1986. Concentration and flux of suspended sediment on the Amazon continental shelf. Contintental Shelf Research, v. 6, n. 2, pp. 151-174. https://doi.org/10.1016/0278-4343(86)90058-0.

Ohnemus, D.C., Lam, P.J., Twining, B.S., 2018. Optical observation of particles and responses to particle composition in the GEOTRACES GP16 section. Mar. Chem. 201, 124–136. https://doi.org/10.1016/j.marchem.2017.09.004.

Olins, H. C., Rogers, D. R., Preston, C., Ussler, W., Pargett, D., Jensen, S., Roman, B., Birch, J. M., Scholin, C. A., Haroon, M. F., and Girguis, P. R., 2017. Co-registered Geochemistry and Metatranscriptomics Reveal Unexpected Distributions of Microbial Activity within a Hydrothermal Vent Field, Front. Microbiol., 8, 1042. https://doi.org/10.3389/fmicb.2017.01042.

Opatkiewicz, A. D., Butterfield, D. A., and Baross, J. A., 2009. Individual hydrothermal vents at Axial Seamount harbor distinct subseafloor microbial communities, Fems Microbiol. Ecol., 70, 413– 424. https://doi.org/10.1111/j.1574-6941.2009.00747.x.

Orcutt, B. N., Sylvan, J. B., Knab, N. J., and Edwards, K. J., 2011. Microbial ecology of the dark ocean above, at, and below the seafloor, Microbiol. Mol. Biol. Rev., 75, 361–422. https://doi.org/10.1128/MMBR.00039-10.

Osborne, P.D., Vincent, C.E., Greenwood, B., 1994. Measurement of suspended sand concentrations in the nearshore - field intercomparison of optical and acoustic backscatter sensors. Cont. Shelf Res. 14 (2–3), 159–174. https://doi.org/10.1016/0278-4343(94)90011-6.

Palanques, A., Puig, P., Latasa, M., Scharek, R., 2009. Deep sediment transport induced by storms and dense shelf-water cascading in the northwestern Mediterranean basin. Deep Sea Research Part I: Oceanographic Research Papers, 56 (3), 425–434. https://doi.org/10.1016/j.dsr.2008.11.002.

Palanques, A., Puig, P., Guillen, J., de Madron, X.D., Latasa, M., Scharek, R., Martin, J., 2011. Effects of storm events on the shelf-to-basin sediment transport in the southwestern end of the Gulf of Lions (Northwestern Mediterranean). Natural Hazards and Earth System Sciences, 11 (3), 843–850. https://doi.org/10.5194/nhess-11-843-2011.

Paull, C.K., Talling, P.J., Maier, K.L., Parsons. D., Xu, J.P., Caress, D.W., Gwiazda, R., Lundsten, E.M., Anderson, K., Barry, J.P., Chaffey, M., O'Reilly, T., Rosenberger, K.J., Gales, J.A., Kieft, B., McGann, M., Simmons, S.M., McCann, M., Sumner, E.J., Clare, M.A., Cartigny, M.J., 2018. Powerful turbidity currents driven by dense basal layers. Nature Communications, 9. https://doi.org/10.1038/s41467-018-06254-6.

Pearman, T.R.R., Robert, K., Callaway, A., Hall, R.A., Mienis, F., Huvenne, V.A.I., 2023. Spatial and temporal environmental heterogeneity induced by internal tides influences faunal patterns on vertical walls within a submarine canyon. Frontiers in Marine Science, 10. https://doi.org/10.3389/fmars.2023.1091855.

Perkey, D., Pratt, T., Ganesh, N., 2010. Comparison of SSC measurements with acoustic backscatter data: West Bay sediment diversion, Mississippi River. In: 2nd Joint Federal Interagency Conference: Las Vegas. Perlin, A., Moum, J.N., Klymak, J.M., Levine, M.D., Boyd, T., Kosro, P.M., 2007. Organization of stratification, turbulence, and veering in bottom Ekman layers. J. Geophys. Res. 112 https://doi.org/10.1029/2004JC002641.C05S90.

Peukert, A., Schoening, T., Alevizos, E., Köser, K., Kwasnitschka, T., Greinert, J., 2018. Understanding Mn-nodule distribution and evaluation of related deep-sea mining impacts using AUV-based hydroacoustic and optical data. Biogeosciences 15 (8), 2525–2549. https://doi.org/10.5194/bg-15-2525-2018.

Phillips, B. T., 2017. Beyond the vent: New perspectives on hydrothermal plumes and pelagic biology, Deep-Sea Res. Pt. II, 137, 480–485. https://doi.org/10.1016/j.dsr2.2016.10.005.

Pingree, 1980. Physical Oceanography of the Celtic Sea and English Channel. In: Elsevier Oceanography Series, volume 24, part B, pp. 415–465. https://doi.org/10.1016/S0422-9894(08)71358-8.

Pingree, R.D., Sihna, B., Griffiths, C.R., 1999. Seasonality of the European slope current (Goban Spur) and ocean margin exchange. Continental Shelf Research, 19 (7), 929–975. https://doi.org/10.1016/S0278-4343(98)00116-2.

Plueddemann, A.J., Pinkel, P., 1989. Characterization of the patterns of diel migration using a Doppler sonar. Deep Sea Res., Part A 36, 509–530. https://doi.org/10.1016/0198-0149(89)90003-4.

Porter, M., Inall, M.E., Hopkins, J., Palmer. M.R., Dale, A.C., Aleynik, D., Barth, J.A., Mahaffey, C., Smeed, D.A., 2016. Glider observations of enhanced deep water upwelling at a shelf break canyon: A mechanisms for cross-slope carbon and nutrient exchange. Journal of Geophysical Research – Oceans, 121 (10), 7575–7588. https://doi.org/10.1002/2016jc012087.

Poulin, P.-M., Menna, M., Gerin, R., 2018. Mapping Mediterranean tidal currents with surface drifters. Deep-Sea Res. I Oceanogr. Res. Pap. 138, 22–33. https://doi.org/10.1016/j.dsr.2018.07.011.

Prouty, N.G., Mienis, F., Campell-Swarzenski, P., Roark, E.B., Davies, A.J., Robertson, C.M., Duineveld, G., Ross, S.W., Rhode, M., Demopoulos, A.W.J., 2017. Seasonal variability in the source and composition of particulate matter in the depositional zone of Baltimore Canyon, U.S. Mid-Atlantic Bight. Deep Sea Research Part I: Oceanographic Research Papers, 127, 77–89. https://doi.org/10.106/j.dsr/2017.08.004.

Puig, P., Palanques, A., 1998. Nepheloid structure and hydrographic control on the Barcelona continental margin, northwestern Mediterranean. Mar. Geol. 149 (1–4), 39–54. https://doi.org/10.1016/S0025-3227(98)00037-1.

Puig, P. Ogston, A.S., Mullenbach, B.L., Nittrouer, C.A., Parsons, J.D., Sternberg, R.W., 2004. Storm-induced sediment gravity flows at the head of the Eel submarine canyon, northern California margin. Journal of Geophysical Research – Oceans, 109, https://doi.org/10.1029/2003JC001918.

Puig, P., Canals, M., Company, J.B., Martin, J., Amblas, D., Lastras, G., Palanques, A., 2012. Ploughing the deep sea floor. Nature 489 (7415), 286–289. https://doi.org/10.1038/nature11410.

Puig, P., de Madron, X.D., Salat, J., Schroeder, K., Martin, J., Karageorgis, A.P., Palanques, A., Roullier, F., Luis Lopez-Jurado, J., Emelianov, M., Moutin, T., Houpert, L., 2013. Thick bottom nepheloid layers in the western Mediterranean generated by deep dense shelf water cascading. Progress in Oceanography, 111, 1–23. https://doi.org/10.1016/j.pocean.2012.10.003.

Puig, P., Palanques, A., Martin, J., 2014. Contemporary sediment-transport processes in submarine canyons. Ann. Rev. Mar. Sci. 6, 53–77. https://doi.org/10.1146/annurevmarine-010213-135037.

Purkiani, K., Paul, A., Vink, A., Walter, M., Schulz, M., and Haeckel, M., 2020. Evidence of Eddy-Related Deep-Ocean Current Variability in the Northeast Tropical Pacific Ocean Induced by Remote Gap Winds. Biogeosciences 17 (24), 6527–6544. https://doi.org/10.5194/bg-17-6527-2020.

Purkiani, K., Gillard, B., Paul, A., Haeckel, M., Haalboom, S., Greinert, J., et al., 2021. Numerical simulation of Deep-Sea Sediment Transport Induced by a Dredge Experiment in the northeastern Pacific Ocean. Front. Mar. Sci. 8, 719463. https://doi.org/10.3389/fmars.2021.719463.

Purkiani, K., Haeckel, M., Haalboom, S., Schmidt, K., Urban, P., Gazis, I.-Z, et al., 2022. Impact of a Long-Lived Anticyclonic Mesoscale Eddy on Seawater Anomalies in the Northeastern Tropical Pacific Ocean: A Composite Analysis From Hydrgraphic Measurement, Sea Level Altimetry Data and Reanalysis Model Products. Ocean. Sci. Discuss. https://doi.org/10.5194/os18-1163-2022.

Purser, A., Bodur, Y., Ramalo, S., Stratmann, T., and Schoening, T., 2021. Seafloor Images of Undisturbed and Disturbed Polymetallic Nodule Province Seafloor Collected During RV SONNE Expeditions So268/1+2 (PANGAEA). https://doi.org/10.1594/PANGAEA.935856.

Quaresma, L.S., Vitorino, J., Oliveira, A., da Silva, J., 2007. Evidence of sediment resuspension by nonlinear internal waves on the western Portuguese mid-shelf. Mar. Geol. 246 (2–4), 123–143. https://doi.org/10.1016/j.margeo.2007.04.019.

R Core Team, 2020. R: A Language and Environment for Statistical Computing. R Foundation for Statistical Computing, Vienna, Austria. https://www.R-project.org/.

Rabouille, C., Caprais, J.C., Lansard, B., Crassous, P., Dedieu, K., Reyss, J.L., Khripounoff, A., 2009. Organic matter budget in the Southeast Atlantic continental margin close to the Congo Canyon: In situ measurements of sediment oxygen consumption. Deep-Sea Research Part II – Topical Studies in Oceanography, 56 (23), 2223–2238. https://doi.org/10.1016/j.dsr2.2009.04.005.

Radziejewska, T., 2002. Response of deep-sea meiobenthic communities to sediment disturbance simulating effects of polymetallic nodule mining. Int. Rev. Hydrobiol. 87, 457-477. https://doi.org/10.1002/1522-2632(200207)87:4<457::AID-IROH457>3.0.CO;2-3.

Ramirez-Llodra, E., Tyler, P. A., Baker, M. C., Bergstad, O. A., Clark, M. R., Escobar, E., Levin, L. A., Menot, L., Rowden, A. A., Smith, C. R., and Van Dover, C. L., 2011. Man and the Last Great Wilderness: Human Impact on the Deep Sea, Plos One, 6, e2258, https://doi.org/10.1371/journal.pone.0022588.

Reed, D. C., Breier, J. A., Jiang, H. S., Anantharaman, K., Klausmeier, C. A., Toner, B. M., Hancock, C., Speer, K., Thurnherr, A. M., and Dick, G. J., 2015. Predicting the response of the deep-ocean microbiome to geochemical perturbations by hydrothermal vents, Isme J., 9, 1857–1869, https://doi.org/10.1038/ismej.2015.4.

Renault, L., Oguz, T., Pascual, A., Vizoso, G., Tintore, J., 2012. Surface circulation in the Alborán Sea (western Mediterranean) inferred from remotely sensed data. J. Geophys. Res. 117, C08009. https://doi.org/10.1029/2011JC007659.

Resing, J. A., Sedwick, P. N., German, C. R., Jenkins,W. J., Moffett, J. W., Sohst, B. M., and Tagliabue, A., 2015. Basin-Scale Transport of Hydrothermal Dissolved Metals across the South Pacific Ocean, Nature, 523, 200–203. https://doi.org/10.1038/nature14577.

Roberts, E.M., Mienis, F., Rapp, H.T., Hanz, U., Meyer, H.K., Davies, A.J., 2018. Oceanographic setting and short-timescale environmental variability at an Arctic seamount sponge ground. Deep Sea Res. Part I: Oceanogr. Res. Papers 138, 98–113. https://doi.org/10.1016/j.dsr.2018.06.007.

Robertson, C.M., Demopoulos, A.W.J., Bourque, J.R., Mienis, F., Duineveld, G.C.A., Lavaleye, M.S.S., Koivisto, R.K.K., Brooke, S.D., Ross, S.W., Rhode, M., Davies, A.J., 2020. Submarine canyons influence macrofaunal diversity and density patterns in the deep-sea benthos. Deep Sea Res. Part I, Oceanogr. Res. Papers, volume 159. https://doi.org/10.1016/j.dsr.2020.103249.

Rolinski, S., Segschneider, J., Südermann, J., 2001. Long-term propagation of tailings from deep-sea mining under variable conditions by means of numerical simulations. Deep-Sea Res. II 48, 3469–3485. https://doi.org/10.1016/S0967-0645(01)00053-4.

ROV KIEL 6000, GEOMAR (CC BY 4.0). "Manganese Nodules of the seafloor in the Clarion-Clipperton Zone. Photo taken with ROV KIEL 6000 during cruise SO239 with RV Sonne in April 2015".

ROV KIEL 6000, GEOMAR (CC BY 4.0). "Sensor frame deployed in the Clarion-Clipperton Zone. Photo taken with ROV KIEL 6000 during cruise SO268 with RV Sonne in April 2019".

ROV KIEL 6000, GEOMAR (CC BY 4.0). "Manganese nodules on the seafloor in the Clarion-Clipperton Zone, with a dredge track in between. Photo taken with ROV KIEL 6000 during cruise SO268 with RV Sonne in April 2019".

Rühlemann, C., Kuhn, T., Wiedicke, M., Kasten, S., Mewes, K., and Picard, A., 2011. Current Status of Manganese Nodule Exploration in the German License Area, Proceedings of the Ninth (2011) ISOPE Ocean Mining Symposium. 168–173.

Rymszewicz, A., O'Sullivan, J.J., Bruen, M., Turner, J.N., Lawler, D.M., Conroy, E., Kelly-Quinn, M., 2017. Measurement differences between turbidity instruments, and their implications for suspended sediment concentration and load calculations, A sensor inter-comparison study. J. Environ. Manage 199, 99–108. https://doi.org/10.1016/j.jenvman.2017.05.017.

Sala, E., Mayorga, J., Bradley, D., Cabral, R.B., Atwood, T.B., …, Lubchenco, J., 2019. Protecting the global ocean for biodiversity food and climate. Nature, 592, 397-402. https://doi.org/10.1038/s41586-021-03371-z.

Sánchez-Garrido, J.C., Sannino, G., Liberti, L., García Lafuente, J., Pratt, L., 2011.Numerical modeling of three-dimensional stratified tidal flow over Camarinal Sill, Strait of Gibraltar. J. Geophys. Res. 116 (C12). https://doi.org/10.1029/2011JC007093.

Sahin, C., Ozturk, M., Aydogan, B., 2020. Acoustic doppler velocimeter backscatter for suspended sediment measurements: Effects of sediment size and attenuation. Appl. Ocean Res. 94, 101975. https://doi.org/10.1016/j.apor.2019.101975.

Santos, A.I., Oliveira, A., Carinhas, D., Pinto, J.P., Zacarias, N., Freitas, M.C., 2020. The acoustic properties of in-situ measured suspended sediments and their implications on concurrent ADCP response – Case studies of the Portuguese inner shelf. Mar. Geol. 419, 106079. https://doi.org/10.1016/j.margeo.2019.106079.

Schaafsma, A.S., Hay, A.E., 1997. Attenuation in suspensions of irregularly shaped sediment particles: a two-parameter equivalent spherical scatterer model. J. Acoustical Soc. Am. 102 (3), 1485–1502. https://doi.org/10.1121/1.420063.

Schoellhamer, D.H., 1993. Biological interference of optical backscatterance sensors in Tampa Bay, Florida. Mar. Geol. 110, 303–313. https://doi.org/10.1016/0025-3227(93)90090-I.

Schoening, T., and Gazis, I.-Z., 2019a. Sizes, Weights and Volumes of Poly- Metallic Nodules From Box Cores Taken During SONNE Cruises SO268/1 and SO268/2 (GEOMAR - Helmholtz Centre for Ocean Research Kiel, Germany PANGAEA). https://doi.org/10.1594/PANGAEA.904962.

Schoening, T., and Gazis, I.-Z., 2019b. Summary of Sizes, Weights, Counts and Coverage of Poly-Metallic Nodules From Box Cores Taken During SONNE Cruises SO268/1 and SO268/2 (GEOMAR - Helmholtz Centre for Ocean Research Kiel, Germany PANGAEA). https://doi.org/10.1594/PANGAEA.904967.

Severmann, S., Johnson, C. M., Beard, B. L., German, C. R., Edmonds, H. N., Chiba, H., Green, D. R. H., 2004. The effect of plume processes on the Fe isotope composition of hydrothermally derived Fe in the deep ocean as inferred from the Rainbow vent site, Mid-Atlantic Ridge, 36 140 N, Earth Planet. Sc. Lett., 225, 63–76. https://doi.org/10.1016/j.epsl.2004.06.001.

Sheik, C. S., Anantharaman, K., Breier, J. A., Sylvan, J. B., Edwards, K. J., and Dick, G. J., 2015. Spatially resolved sampling reveals dynamic microbial communities in rising hydrothermal plumes across a back-arc basin, Isme J., 9, 1434–1445. https://doi.org/10.1038/ismej.2014.228.

Simmons, S. M., Parsons, D. R., Best, J. L., Orfeo, O., Lane, S. N., Kostaschuk, R., et al., 2010. Monitoring Suspended Sediment Dynamics Using MBES. J. Hydraulic. Engineering-Asce. 136, 45–49. https://doi.org/10.1061/(ASCE)HY.1943-7900.0000110.

Simon-Lledo, E., Bett, B.J., Huvenne, V.A.I., Koser, K., Schoening, T., Greinert, J., Jones, D.O.B., 2019. Biological effects 26 years after simulated deep-sea mining. Sci. Rep. 9 (1), 8040. https://doi.org/10.1038/s41598-019-44492-w.

Smith, C. R., and Demopoulos, A. W. J., 2003. The Deep Pacific Ocean Floor. Ecosyst. World, 179–218.

Smith, C. R., Levin, L. A., Koslow, A., Tyler, P. A., and Glover, A. G., 2008. The Near Future of the Deep Seafloor Ecosystems, Aquatic Ecosystems: Trends and Global Prospects.

Smith, S.J., Friedrichs, C.T., 2011. Size and settling velocities of cohesive flocs and suspended sediment aggregates in a trailing suction hopper dredge plume. Cont. Shelf Res. 31 (10), S50–S63. https://doi.org/10.1016/j.csr.2010.04.002.

Spearman, J., Taylor, J., Crossouard, N., Cooper, A., Turnbull, M., Manning, A., Lee, M., Murton, B., 2020. Measurement and modelling of deep sea sediment plumes and implications for deep sea mining. Sci. Rep. 10, 5075. https://doi.org/10.1038/s41598-020-61837-y.

Stetten, E., Baudin, F., Reyss, J.L., Martinez, P., Charlier, K., Schnyder, J., Rabouille, C., Dennielot, B., Coston-Guarini, J., Pruski, A.M., 2015. Organic matter characterisation and distribution in sediments of the terminal lobes of the Congo deep-sea fan: Evidence for the direct influence of the Congo River. Marine Geology, 369, 182–195. https://doi.org/10.1016/j.margeo.2015.08.020.

Stramma, L., Schmidtko, S., Levin, L.A., Johnson, G.C., 2010. Ocean oxygen minima expansions and their biological impacts. Deep-Sea Research I, 57, 587-595. https://doi-org.proxy.library.uu.nl/10.1016/j.dsr.2010.01.005.

Stratmann, T., Voorsmit, I., Gebruk, A. et al., 2018. Recovery of Holothuroidea population density, community composition, and respiration activity after a deep-sea disturbance experiment. Limnol Oceanogr 63:2140–2153. https://doi.org/10.1002/lno.10929.

Sternberg, R.W., Ogston, A., Johnson, R., 1996. A video system for in situ measurement of size and settling velocity of suspended particles. J. Sea Res. 36, 127–130. https://doi.org/10.1016/S1385-1101(96)90782-0.

Sunamura, M., Higashi, Y., Miyako, C., Ishibashi, J., and Maruyama, A., 2004. Two bacteria phylotypes are predominant in the Suiyo Seamount hydrothermal plume, Appl. Environ. Microb., 70, 1190–1198. https://doi.org/10.1128/AEM.70.2.1190-1198.2004.

Sylvan, J. B., Pyenson, B. C., Rouxel, O., German, C. R., and Edwards, K. J., 2012. Time-series analysis of two hydrothermal plumes at 9 500 N East Pacific Rise reveals distinct, heterogeneous bacterial populations, Geobiology, 10, 178–192, https://doi.org/10.1111/j.1472-4669.2011.00315.x.

Tesi, T., Puig, P., Palanques, A., Goni, M.A., 2010. Lateral advection of organic matter in cascading-dominated submarine canyons. Progress In Oceanography, 84 (3-4), 185–203. https://doi.org/10.1016/j.pocean.2009.10.004.

Tessier, C., Le Hir, P., Lurton, X., Castaing, P., 2008. Estimation de la matiére en suspension à partir de l'intensité rétrodiffusée des courantomètres acoustiques à effet Doppler (ADCP). Compt. Rendus Geosci. 340 (1), 57–67. https://doi.org/10.1016/j.crte.2007.10.009.

Thiel, H., Schiever, G., 1989. Cruise report DISCOL 1, Sonne – cruise 61. Berichte aus dem Zentrum für Meeres- und Klimaforschung 3. Zentrum für Meeres- und Klimaforschung der Universität Hamburg, Institut für Hydrobiologie und Fischereiwissenschaft, 75 pp.

Thiel, H., 2001. Evaluation of the environmental consequences of polymetallic nodule mining based on the results of the TUSCH Research Association. Deep-Sea Research II 48, 3433–3452. https://doi.org/10.1016/S0967-0645(01)00051-0.

Thomsen, L., van Weering, T.C.E., 1998. Spatial and temporal variability of particulate matter in the benthic boundary layer at the N.W. European Continental Margin (Goban Spur). Prog. Oceanogr. 42, 61–76. https://doi.org/10.1016/S0079-6611(98)00028-7.

Thomsen, L., 1999. Processes in the benthic boundary layer at continental margins and their implications for the benthic carbon cycle. J. Sea Res. 41, 73–86. https://doi.org/10.1016/S1385-1101(98)00039-2.

Thomsen, L., and Gust, G., 2000. Sediment Erosion Thresholds and Characteristics of Resuspended Aggregates on the Western European Continental Margin. Deep-Sea Res. I 47, 1881–1897. https://doi.org/10.1016/S0967-0637(00)00003-0.

Thomsen, L., van Weering, T., Gust, G., 2002. Processes in the benthic boundary layer at the Iberian continental margin and their implication for carbon mineralization. Prog. Oceanogr. 52 (2–4), 315–329. https://doi.org/10.1016/S0079-6611(02)00013-7.

Thorne, P.D., Hanes, D.M., 2002. A review of acoustic measurement of small-scale sediment processes. Cont. Shelf Res. 22 (4), 603–632. https://doi.org/10.1016/S0278-4343(01)00101-7.

Trueblood, D.D., Ozturgut, E., 1997. The benthic impact experiment: A study of the ecological impacts of deep seabed mining on abyssal benthic communities. Proc. Of the 7th ISOPE conference, Honolulu, Hawaii.

Thurnherr, A. M. and Richards, K. J., 2001. Hydrography and high temperature heat flux of the Rainbow hydrothermal site (36140 N, Mid-Atlantic Ridge), J. Geophys. Res.-Oceans, 106, 9411–9426. https://doi.org/10.1029/2000JC900164.

Thurnherr, A. M., Richards, K. J., German, C. R., Lane-Serff, G. F., and Speer, K. G., 2002. Flow and mixing in the rift valley of the Mid-Atlantic Ridge, J. Phys. Oceanogr., 32, 1763–1778. https://doi.org/10.1175/1520-0485(2002)032.

Trocine, R. P. and Trefry, J. H., 1998. Distribution and chemistry of suspended particles from an active hydrothermal vent site on the Mid-Atlantic Ridge at 26 N, Earth Planet. Sc. Lett. 88, 1–15. https://doi.org/10.1016/0012-821X(88)90041-6.

Van Aken, H.M., Becker, G., 1996. Hydrography and through-flow in the north-eastern North Atlantic Ocean: the NANSEN project. Progress in Oceanography, 38 (4), 297–346. https://doi.org/10.1016/S0079-6611(97)00005-0.

Van Aken, H.M., 2000. The hydrography of the mid-latitude Northeast Atlantic Ocean: The intermediate water masses. Deep Sea Research Part I: Oceanographic Research Papers, 47 (5), 789–824. https://doi.org/10.1016/s0967-0637(99)00112-0.

van Bleijswijk, J. D. L., Whalen, C., Duineveld, G. C. A., Lavaleye, M. S. S., Witte, H. J., and Mienis, F., 2015. Microbial assemblages on a cold-water coral mound at the SE Rockall Bank (NE Atlantic): interactions with hydrography and topography, Biogeosciences, 12, 4483–4496. https://doi.org/10.5194/bg-12-4483-2015.

van den Eynde, D., Baeye, M., Fettweis, M., Francken, F., Naudts, L., Van Lancker, V., 2014. Sediment Plume Monitoring in the Clarion-Clipperton Zone, 2nd Deep-Water Circulation Congress, Ghent, Belgium.

van Haren, H., 2007. Monthly periodicity in acoustic reflections and vertical motions in the deep ocean. Geophys. Res. Lett. 34, L12603. https://doi.org/10.1029/2007GL029947.

van Haren, H., Laan, M., Buijsman, D.-J., Gostiaux, L., Smit, M.G., Keijzer, E., 2009. NIOZ3: Independent temperature sensors sampling year-long data at a rate of 1 Hz. IEEE J. Oceanic Eng 24, 315–322.

van Haren, H., Compton, T.J., 2013. Diel vertical migration in deep sea plankton is finely tuned to latitudinal and seasonal day length. PLoS One 8 (5), e64435. https://doi.org/10.1371/journal.pone.0064435.

van Haren, H., 2014. Internal wave–zooplankton interactions in the Alboran Sea (W Mediterranean). J. Plankton Res. 36 (4), 1124–1134. https://doi.org/10.1093/plankt/fbu031.

van Haren, H., Cimatoribus, A.A., Gostiaux, L., 2015. Where large deep-ocean waves break. Geophys. Res. Lett. 42, 2351–2357. https://doi.org/10.1002/2015GL063329.

van Haren, H., Duineveld, G., and de Stigter, H., 2017. Prefrontal bore mixing, Geophys. Res. Lett., 44, 9408–9415, https://doi.org/10.1002/2017GL074384.

van Haren, H., Mienis, F., Duineveld, G., 2022. Contrasting internal tide turbulence in a tributary of the Whittard Canyon. Continental Shelf Research, 236, 104679. https://doi.org/10.1016/j.csr.2022.104679.

van de Hulst, H.C., 1957. Light Scattering by Small Particles. Wiley, New York.

van Leussen, W., 1988. Aggregation of particles, settling velocity of mud flocs - a review. In: Dronkers, J., van Leussen, W. (Eds.), Physical Processes in Estuaries. Springer Verlag, pp. 347–403.

van Weering, T. C. E., Thomsen, L., van Heerwaarden, J., Koster, B., and Viergutz, T., 2000. A Seabed Lander and New Techniques for Long Term in Situ Study of Deep-Sea Near Bed Dynamics. Sea. Technol. 41, 17–27.

Vanreusel, A., Hilario, A., Ribeiro, P.A., Menot, L., Arbizu, P.M., 2016. Threatened by mining, polymetallic nodules are required to preserve abyssal epifauna. Sci. Rep. 6, 26808. https://doi.org/10.1038/srep26808.

Vare, L. L., Baker, M. C., Howe, J. A., Levin, L. A., Neira, C., Ramirez-Llodra, E. Z., Reichelt-Brushett, A., Rowden, A. A., Shimmield, T. M., Simpson, S. L., and Soto, E. H., 2018. Scientific Considerations for the Assessment and Management of Mine Tailings Disposal in the Deep Sea, Front. Mar. Sci., 5, 17. https://doi.org/10.3389/fmars.2018.00017.

Vargas-Yanaz, M., Plaza, F., García-Lafuenta, J., Sarhan, T., Vargas, J.M., Vélez- Belchi, P., 2002. About the seasonal variability of the Alboran Sea circulation. J. Mar. Syst. 35, 229–248. https://doi.org/10.1016/S0924-7963(02)00128-8.

Verney, R., Lafite, R., Brun-Cottan, J.C., Le Hir, P., 2011. Behaviour of a floc population during a tidal cycle: laboratory experiments and numerical modelling. Cont. Shelf Res. 31, S64–S83. https://doi.org/10.1016/j.csr.2010.02.005.

Vetter, E.W., Smith, C.R., De Leo, F.C., 2010. Hawaiian hotspots: enhanced megafaunal abundance and diversity in submarine canyons on the oceanic islands of Hawaii. Marine Ecology – an Evolutionary Perspective, 31 (1), 183–199. https://doi.org/10.1111/j.1439-0485.2009.00351.x.

Walsh, J.J., 1991. Importance of continental margins in the marine biogeochemical cycling of carbon and nitrogen. Nature 350, 53–55. https://doi.org/10.1038/350053a0.

Wanis, P., 2013. Design and Applications of a Vertical Beam in Acoustic Doppler Current Profilers. OCEANS – San Diego, San Diego, CA, pp. 1–5. https://doi.org/10.23919/OCEANS.2013.674107.

Washburn, T.W., Turner, P.J., Durden, J.M., Jones, D.O.B., Weaver, P., Van Dover, C.L., 2019. Ecological risk assessment for deep-sea mining. Ocean Coast. Manag. 176, 24–39. https://doi.org/10.1016/j.ocecoaman.2019.04.014.

Weaver, P. P., Billett, D. S., and Van Dover, C. L., 2018. Environmental risks of deep-sea mining, in: Handbook on Marine Environment Protection, Springer, 215–245. https://doi.org/10.1007/978-3- 319-60156-4_11.

Weaver, P. P. E., Aguzzi, J., Boschen-Rose, R. E., Colaço, A., de Stigter, H., Gollner, S., et al., 2022. Assessing Plume Impacts Caused by Polymetallic Nodule Mining Vehicles. Mar. Policy 139, 105011. https://doi.org/10.1016/j.marpol.2022.105011.

Wedding, L. M., Reiter, S. M., Smith, C. R., Gjerde, K. M., Kittinger, J. N., Friedlander, A. M., et al., 2015. Managing Mining of the Deep Seabed. Science 349 (6244), 144–145. https://doi.org/10.1126/science.aac6647.

Welschmeyer, N.A., 1994. Fluorometric analysis of chlorophyll-a in the presence of chlorophyll-b and pheopigments. Limnology and Oceanography, 39 (8), 1985–1992. https://doi.org/10.4319/lo.1994.39.8.1985.

Wetzel, L. R. and Shock, E. L., 2000. Distinguishing ultramafic- from basalt-hosted submarine hydrothermal systems by comparing calculated vent fluid compositions, J. Geophys. Res.-Sol. Ea., 105, 8319–8340. https://doi.org/10.1029/1999JB900382.

Willford, W.A., Mac, M.J., Hesselberg, R.J., 1987. Assessing the bioaccumulation of contaminants from sediments by fish and other aquatic organisms. Hydrobiologia, 149, 107-111. https://doi.org/10.1007/BF00048651.

Wilson, G.W., Hay, A.E., 2015. Acoustic backscatter inversion for suspended sediment concentration and size: a new approach using statistical inverse theory. Continental Shelf Res. 106, 130–139. https://doi.org/10.1016/j.csr.2015.07.005.

Wilson, A.M., Kiriakoulakis, K., Raine, R., Gerritsen, H.D., Blackbird, S., Allcock, A.L., White, M., 2015a. Anthropogenic influence on sediment transport in the Whittard Canyon, NE Atlantic. Marine Pollution Bulletin, 101 (1), 320–329. https://doi.org/j.marpolbul.2015.10.067.

Wilson, A.M., Raine, R., Mohn, C., White, M., 2015b. Nepheloid layer distribution in the Whittard Canyon, NE Atlantic Margin. Mar. Geol. 367, 130–142. https://doi.org/10.1016/j.margeo.2015.06.002.

Yamazaki, T., Kajitani, Y., Barnett, B., Suzuki, T., 1997. Development of image analytical technique for resedimentation induced by nodule mining. In: Second ISOPE Ocean Mining Symposium, Seoul, Korea, November 1997.

Yang, C., Xu, D., Chen, Z., Wang, J., Xu, M., Yuan, Y., Zhou, M., 2019. Diel vertical migration of zooplankton and micronekton on the northern slope of the South China Sea observed by a moored ADCP. Deep-Sea Res. Part II 167, 93–104. https://doi.org/10.1016/j.dsr2.2019.04.012.

Yentsch, C.S., Menzel, D.W., 1963. A method for the determination of phytoplankton chlorophyll and phaeophytin by fluorescence. Deep-Sea Research, 10 (3), 221–231. https://doi.org/10.1016/0011-7471(63)90358-9.

Yilmaz, P., Parfrey, L. W., Yarza, P., Gerken, J., Pruesse, E., Quast, C., Schweer, T., Peplies, J., Ludwig, W., and Glöckner, F. O., 2014. The SILVA and "all-species living tree project (LTP)" taxonomic frameworks, Nucleic Acids Res., 42, 643 – 648. https://doi.org/10.1093/nar/gkt1209.

Ziegler, A.C., 2002. Issues related to use of turbidity measurements as a surrogate for suspended sediment. In: Turbidity and Other Sediment Surrogates Workshop, April 30 – May 2, 2002, Reno, NV.

Zinger, L., Amaral-Zettler, L. A., Fuhrman, J. A., Horner-Devine, M. C., Huse, S. M., Welch, D. B. M., Martiny, J. B. H., Sogin,M., Boetius, A., and Ramette, A., 2011. Global Patterns of Bacterial Beta-Diversity in Seafloor and Seawater Ecosystems, Plos One, 6, 63–76. https://doi.org/10.1371/journal.pone.0024570.

Photo taken onboard RV Sarmiento de Gamboa during the Blue Nodules cruise in 2019 by Laurens de Jonge.

About the author

Sabine Haalboom was born on the 1st of June 1992 in Ede, the Netherlands. Growing up on the Veluwe surrounded by forest, heathlands, and sand drifts, she developed an interest for the natural sciences. She started studying at Utrecht University in 2010 and completed a Bachelor in Earth Sciences and a Master in Earth, Structure and Dynamics, which she finished in 2016. As part of her master studies, she got the opportunity to perform a (first real) research project at Royal NIOZ, studying the chemical composition of the Rainbow hydrothermal plume. This experience sparked her interest in marine geology, which further manifested itself during her first research cruise, as part of a wonderful team onboard RV *Pelagia* in 2016. As the beautiful island of Texel charmed her, she moved to the less fabulous city of Den Helder (which actually turned out to be quite nice) and started her PhD at Royal NIOZ. During her PhD she joined another five research cruises onboard RV *Pelagia*, RV *Sarmiento de Gamboa* and RV *Sonne*, during which she spent a total of 19 weeks at sea (and by that missed out on watching several important football matches). She assisted during the yearly Marine Master Summer course and taught students about principles like the Doppler effect (thereby finding herself imitating a passing ambulance way too often) and its applications in the marine sciences. After her time at Royal NIOZ ended, she ventured out of the Netherlands and worked outside of the academic circle, while finishing her PhD thesis. During this time, she worked in the Science museum *Universum* in Bremen, Germany, where she made science more accessible for all generations. She assisted during classes for school kids in robotics, geology, and biology, and she performed science shows (with loud bangs) about rockets and the scientific principles of sound. Yet, trying the keep the kids in line was probably her most difficult task. She moved back to her home country in 2022 to work at *Aqua Vision*, a hydrographic- and oceanographic consultancy, where she continuous to apply her gained knowledge, especially on ADCPs and the quantification of SPM mass concentration.

Bibliography

Haalboom, S., de Stigter, H.C., Mohn, C., Vandorpe, T., Smit, M., de Jonge, L. & Reichart, G.-J., 2023. Monitoring of a sediment plume produced by a deep-sea mining test in shallow water, Málaga Bight, Alboran Sea (southwestern Mediterranean Sea). Marine Geology, 456, 106971. https://doi.org/10.1016/j.margeo.2022.106971

Purkiani, K., Haeckel, M., **Haalboom, S.**, Schmidt, K., Urban, P., Gazis, I.-Z., de Stigter, H.C., Paul, A., Walter, M. & Vink, A., 2022. Impact of long-lived anticyclonic mesoscale eddy on seawater anomalies in the northeastern tropical Pacific Ocean: a composite analysis from hydrographic measurements, sea level altimetry data, and reanalysis model products. Ocean Science, 18, 1163-1181. https://doi.org/10.5194/os-18-1163-2022

Haalboom, S., Schoening, T., Urban, P., Gazis, I.-Z., de Stigter, H.C., Gillard, B., Baeye, M., Hollstein, M., Purkiani, K., Reichart, G.-J., Thomsen, L., Haeckel, M., Vink, A. & Greinert, J., 2022. Monitoring of anthropogenic sediment plumes in the Clarion-Clipperton Zone, NE Equatorial Pacific Ocean. Frontiers in Marine Science, 9, 882115. https://doi.org/10.3389/fmars.2022.882155

Purkiani, K., Gillard, B., Paul, A., Haeckel, M., **Haalboom, S.**, Greinert, J., de Stigter, H.C., Hollstein, M., Baeye, M., Vink, A., Thomsen, L. & Schulz, M., 2021. Numerical simulation of deep-sea sediment transport induced by a dredge experiment in the northeastern Pacific Ocean. Frontiers in Marine Science, 8, 719463. https://doi.org/10.3389/fmars.2021.719463

Haalboom, S., de Stigter, H.C., Duineveld, G., van Haren, H., Reichart, G.-J. & Mienis, F., 2021. Suspended particulate matter in a submarine canyon (Whittard Canyon, Bay of Biscay, NE Atlantic Ocean): Assessment of commonly used instruments to record turbidity. Marine Geology, 434, 106439. https://doi.org/10.1016/j.margeo.2021.106439

Haalboom, S., Price, D.M., Mienis, F., van Bleijswijk, J.D.L., de Stigter, H.C., Witte, H.J., Reichart, G.-J. & Duineveld, G.C.A., 2020. Patterns of (trace) metals and microorganisms in the Rainbow hydrothermal vent plume at the Mid-Atlantic Ridge. Biogeosciences, 17, 2499-2519. https://doi.org/10.5194/bg-17-2499-2020

van Wijk, J.M., **Haalboom, S.**, de Hoog, E., de Stigter, H.C., Smit & M.G., 2019. Impact fragmentation of polymetallic nodules under deep ocean pressure conditions. Minerals Engineering, 134, 250-260. https://doi.org/10.1016/j.mineng.2019.02.015

Acknowledgements

This PhD thesis has been a team effort as I've been guided by many people all along this journey. Colleagues, family, and friends, who I could always turn to (despite sometimes having no clue what I was actually doing). This wonderful support system listened to me when I was talking nineteen to a dozen and always had my back. Here comes the shout-out to you!

Als eerste gaat mijn dank uit naar Gert-Jan, gezien ik zonder jou nooit bij het NIOZ terecht zou zijn gekomen. We leerden elkaar voor het eerst echt kennen in de zomer van 2015, toen ik bij je aanklopte met de vraag over een stage bij het NIOZ. Inmiddels zijn we zo'n 9 jaar verder en hebben we samen veel meegemaakt. Ik wil je bedanken voor het vertrouwen dat je in me had om me uit te nodigen de PhD te starten en voor al je begeleiding tijdens deze jaren. Het was altijd erg prettig om met je te sparren over onderzoeksideeën, maar ook om over niet-werk gerelateerde onderwerpen gesprekken te voeren. Je betrokkenheid en bezorgdheid over hoe het met mij en mijn PhD ging hebben ervoor gezorgd dat we dit mooie boek hebben kunnen afleveren.

Henko, we leerden elkaar al kennen tijdens mijn stage, maar ik leerde je echt goed kennen in de jaren die zouden volgen als mijn "dagelijkse begeleider". We zijn samen veel op pad geweest, meetdagen bij Deltares, conferenties in o.a. Parijs, Londen, Barcelona, Aken en Lissabon en we hebben samen veel tijd op zee doorgebracht tijdens verschillende vaartochten. Je passie voor het vak en je wil om alles tot in de puntjes uit te zoeken was erg aanstekelijk, maar soms ook een beetje overweldigend. Ik heb ontzettend veel van je geleerd, en ik zal je met rood gemarkeerde teksten (waar je je in het begin zelf soms voor verontschuldigde) absoluut gaan missen. Henko, ik wil je bedanken voor al je geduld met mij, voor je onvoorwaardelijke hulp (zowel werk- als niet-werk gerelateerd), voor je gezelschap en de ontzettend fijne samenwerking!

Furu, tijdens mijn PhD zou jij in eerste niet zo'n grote rol gaan spelen als dat je uiteindelijk gedaan hebt. Dit veranderde snel toen wat vaartochten verschoven werden en ik ook meeging met jouw vaartochten naar de Whittard Canyon. Zo werd ik toch jouw "extra" PhD-student en het was erg prettig om jou als mijn extra PhD-begeleider te hebben. Je keek altijd met een

kritisch oog naar het werk dat gedaan moest worden, naar het werk dat gedaan werd, en naar het werk dat op de planning stond. Dit gaf extra sturing in mijn jaren bij het NIOZ en ik heb er veel van geleerd. Je bent een prettig persoon om mee samen te werken, maar absoluut ook om in je vrije tijd om je heen te hebben voor een goed gesprek of feestje. Bedankt voor dit alles!

Gerard, na elkaar eens in de wandelgangen ontmoet te hebben, leerden we elkaar echt kennen op de Azoren, toen jij de chief scientist was op mijn eerste vaartocht. Met al jouw ervaring en geduld heb jij mij samen met Marc en Magda laten zien hoe het werk aan boord eraan toe ging. Ook in de jaren erna bleef je nauw betrokken bij de voortgang van mijn PhD en heeft je hulp bij het analyseren van de data en het schrijven van de manuscripten (maar ook je luisterende oor als ik even bij iemand anders dan mijn directe begeleiders mijn ei kwijt moest). Ook heb ik veel plezier beleefd aan het samen organiseren van een deel van de MaMa-cursus. Bedankt voor de fijne jaren!

Daarnaast zijn er nog veel meer mensen op het NIOZ te bedanken. Wim, in het lab hadden we eigenlijk weinig met elkaar te doen, maar de gezellige (tennis)avonden zal ik niet snel vergeten! Bob, mijn go-to persoon als ik hulp nodig had met een van de sensoren of er meer over wilde weten. Ik heb veel van je geleerd, maar ook altijd een gezellige tijd met je gehad in de vele weken die we samen op zee zijn geweest. Sharyn, ook wij hebben een aantal weken samen doorgebracht op zee, en ik kwam altijd graag even buurten in "jouw" container. Bedankt voor al je gezelligheid en de vele gesprekken die we gevoerd hebben! Jan-Berend, bedankt voor je hulp in de korrelgrootte-analyses, voor je adviezen over mijn PhD-traject en de gezelligheid die we o.a. samen hebben gehad in de PV. Daarnaast wil ik ook nog Meta, Rick, Hans, Loes, Piet, Patrick, Bas, Marck, Rob Witbaard, Sabine, Peter, Eric, Geert-Jan, Karel, Jan, Lennart, Femke en Rob Middag bedanken voor de prettige samenwerking en de fijne tijd. Maar ook de jongens in de werkplaats, Jan-Dirk, Lorendz, Leon, Edwin, Dave, Barry, en Yvo (en alle anderen die hebben bijgedragen), zonder jullie was dit proefschrift niet mogelijk geweest! En de mannen van de elektronica, Frank, Bas en Jeras, ik kwam altijd graag even langs voor een praatje en om te kijken waar jullie zo al mee bezig zijn.

In mijn jaren bij het NIOZ heb ik ook veel tijd doorgebracht bij de personeelsvereniging. Het was een fijne afwisseling tussen het PhD-werk door en heb hier samen met Jan-Dirk, Jan-Berend, Nicole, Darci, Rineke, Dennis, Denise en Siham een ontzettend leuke en gezellige tijd gehad met het organiseren van alle activiteiten.

Also a big shout-out to my office mates, Esmee and Sofia. We've spent most of the day together, which means you get to see all the good things that are happening, and some of the lesser good things. It was nice that we could always talk about anything, whether it was work-related or personal and the first (half an) hour on Monday morning was then also just meant for catching up. Uli, you were the first PhD-student I really got to meet, and I want to thank you for all the good times were had together. Dinners, swimming, climbing and parties, those evenings made my time in Den Helder much more enjoyable. Richard, mijn boot-buddy, klim-buddy, game-buddy, en nog veel meer! Met jou is het altijd gezellig en als iemand van een andere afdeling op het NIOZ, kon ik bij jou altijd makkelijk even mijn hart luchten. Marin, bedankt voor de gezellige avonden die we in restaurants, barretjes, op het strand of gewoon thuis hebben doorgebracht. Heerlijk om altijd even de gedachten te kunnen verzetten. Michèlle en Rob, bedankt voor jullie gastvrijheid sinds dag 1. We kenden elkaar nog geen 4 weken en ik was al welkom om Oud & Nieuw met jullie te komen vieren. Jullie hebben altijd voor me klaar gestaan, zowel in Den Helder, als toen ik in Duitsland woonde. Enorm bedankt hiervoor! Coral, we only really got to know each other when we learned we would go on the same cruise, and we absolutely made the best out of that! Thanks for all the wonderful times we've spent together! I also want to thank all the other PhD students in our group, that have made my time at NIOZ much more enjoyable! Mathijs, Stanley, Linda, Laura K, Inge, Alice, Saara, Indah, Kristin, Laura, Elodie, Louise, Nora and Szabina, thank you for the nice times we had together. It was a pleasure to share this journey with you all! And all the other people at NIOZ, thank you!

I also had the pleasure to work in two larger projects, during which I got to meet so many people from all over Europe. To everyone involved in the Blue Nodules and JPIO Mining Impact projects, it was great meeting you, sharing ideas and working together!

Mijn lieve paranimfen, Suus en Nina, zonder jullie waren deze 7.5 jaar nog zwaarder geweest. Jullie hebben altijd voor mij klaar gestaan, ook al was ik vele kilometers ver weg. Bezoekjes in Den Helder, Bremen en Ede, vele videogesprekken, en zelfs een verrassingsbezoek bij mijn ouders thuis als jullie doorhadden dat ik dat even nodig had. Jullie zijn de beste en ik ben erg dankbaar jullie ook nu nog aan mijn zijde te hebben.

Daarnaast de mensen uit "Jaartje '10", wat zijn jullie toch een fantastisch leuke groep. Pino, Daniël, Mathijs, Harry, Ivar, Quinten, Silvestre, Nikki, Chris, Erik, Maarten en Jesse, het was altijd goed jullie weer te zien in Utrecht, of tijdens jullie bezoek(en) in Den Helder. Serieke, bedankt voor de gezellige tijden en fijne gesprekken, die we in Den Helder, Groningen, Utrecht, of door corona en nog grotere afstanden, online hadden. Rijan en Tim, bedankt voor jullie betrokkenheid na al deze jaren. Jullie staan altijd voor me klaar en het was erg fijn met jullie als "buitenstaanders van de wetenschappelijke wereld" goede gesprekken te voeren, of gewoon een biertje te drinken. Mijn collega's van Aqua Vision, ik wil jullie allen bedanken voor jullie betrokkenheid en support de laatste 1.5 jaar! Also a big thank you to some of the people I've spent part of my free time in Germany with, Musti, Male and Anni, thank you for all the fun times while taking walks, going out for dinner, or grabbing (a) drink(s)! And Julia, even though we never lived in the same place, you have also become a part of my PhD journey. Thank you for all the good times!

Mijn familie, maar in het bijzonder mijn lieve ouders, Pappa en Marion, Mamma en Henk, ontzettend bedankt voor jullie onvoorwaardelijke steun deze jaren. Jullie hebben heel wat geklaag van mij moeten aanhoren, maar nu is het écht klaar.

And last but not least, Jessi. I'm so lucky that I got to know you during the RV *Sonne* cruise in 2019. What a ride it has been. Travelling back and forth between Den Helder and Bremen, living together in Germany, and then moving (back) together to the Netherlands. It hasn't always been easy, but all this time you were there for me. Thank you for all your patience with me, for all your advice and your guidance. I think I wouldn't have been able to finish this without you.